



Synthesis, molecular modeling and photochromic behaviour of polysiloxanes containing azo-groups with different geometries

Simona Ciobotarescu

► To cite this version:

Simona Ciobotarescu. Synthesis, molecular modeling and photochromic behaviour of polysiloxanes containing azo-groups with different geometries. General Physics [physics.gen-ph]. Université d'Angers; Universitatea tehnică "Gheorghe Asachi" (Iași, Roumanie), 2020. English. NNT : 2020ANGE0011 . tel-03270884

HAL Id: tel-03270884

<https://theses.hal.science/tel-03270884>

Submitted on 25 Jun 2021

HAL is a multi-disciplinary open access archive for the deposit and dissemination of scientific research documents, whether they are published or not. The documents may come from teaching and research institutions in France or abroad, or from public or private research centers.

L'archive ouverte pluridisciplinaire **HAL**, est destinée au dépôt et à la diffusion de documents scientifiques de niveau recherche, publiés ou non, émanant des établissements d'enseignement et de recherche français ou étrangers, des laboratoires publics ou privés.

THESE DE DOCTORAT DE

L'UNIVERSITE D'ANGERS
COMUE UNIVERSITE BRETAGNE LOIRE

L'UNIVERSITE TECHNIQUE « GHEORGHE ASACHI »
IASI

ECOLE DOCTORALE N° 596
Matière, Molécules, Matériaux
Spécialité : « Physique »

Par

« **Simona CIOBOTARESCU** »

« **Synthesis, molecular modeling and photochromic behaviour of polysiloxanes containing azo-groups with different geometries** »

Thèse présentée et soutenue à Iasi, Roumanie », le « 28 février 2020 »

Unité de recherche : Faculté de Ingénierie Chimique et Protection de l'Environnement, Bd. Prof. D. Mangeron, Iasi 700050, Roumanie

Laboratoire de Photonique d'Angers LPhiA EA 4464, 2 Boulevard de Lavoisier, 49000, Angers, France

Rapporteurs avant soutenance : Composition du Jury :

Aurelien PERERA Chercheur CNRS HDR
L'Université Pierre et Marie Curie
Ionel MANGALAGIU Professeur des universités HDR
L'Université « Alexandru Ioan Cuza » de Iasi

Président :
Teodor MALUTAN Professeur des universités HDR
L'Université Technique « Gheorghe Asachi » Iasi

Aurelien PERERA Chercheur CNRS HDR
L'Université Pierre et Marie Curie
Stephan CHAUSSEDENT Professeur des universités HDR
L'Université d'Angers
Ionel MANGALAGIU Professeur des universités HDR
L'Université « Alexandru Ioan Cuza » de Iasi

Directeurs de thèse :
Nicolae HURDUC Professeur des universités HDR
L'Université Technique « Gheorghe Asachi » Iasi
Victor TEBOUL Professeur des universités HDR
L'Université d'Angers

**SYNTHESIS, MOLECULAR MODELING AND PHOTOCHROMIC
BEHAVIOUR OF POLYSILOXANES CONTAINING AZO-GROUPS WITH
DIFFERENT GEOMETRIES**

Eng. Simona CIOBOTARESCU
Fields: Chemistry and Physics

President of the doctoral committee: Prof. Dr. Eng. Teodor MALUTAN

**Doctoral Supervisors: Prof. Dr. Eng. Nicolae HURDUC
Assoc. Prof. Dr. Victor TEBOUL**

**Official reviewers: Prof. Dr. Ionel MANGALAGIU
CNRS Researcher Dr. Aurelien PERERA
Prof. Dr. Stephan CHAUSSEDENT**

*To my sister,
Ramona*

Acknowledgements

[Insert inspirational quote here.]

I saved this for the last, even though it was the first thing I thought of.

Lots of things have changed since I first started my PhD. I changed.

If I were a molecular motor:

My two supervisors were the *light energy* that activated my ability to diffuse into the universe.

Prof. Hurduc, who first saw my isomerization capacity. He created the proper environment for me to develop my scientific interests and encouraged me to realize my potential. He inspired and supported me in creating a bridge towards the academic world.

Prof. Teboul, who guided me in setting up the initial conditions so to design my own trajectory. He offered me the much-cherished insight to form a computational vision. His input helped me elevate my critical thinking and enlarge my horizons.

The faculty were the *matrix* that enhanced my diffusion through induced cooperative motions. Luiza, who helped me overcome the boundary conditions. Prof. Scutaru, who made possible all the syntheses in the “impossible” organic chemistry. Prof. Lisa who always had a thermal approach towards me. Prof Ibanescu, who taught me “panta rhei”, everything is possible in the right time frame.

Mr. Petris and Petronela, who illuminated my experiments, enlightened me on matters of laser irradiation.

I always had along my colleagues friends to help each other, share ideas, dream, laugh, cry, cook, and all the boring stuff. Them girls: Dana, Diana, Elena, Mihaela, Roxana.

My dearest friends, thank you for dealing with me at my worst and at my best. Irina, you kill me with your kindness. Marcel, you bring me back down to earth.

The Ciobos: (nature & nurture_{in})/nurture_{out}

I wouldn't be *here* without you. I wouldn't be *me* without you.

If I were a polymer:

My long life partner, you were the *initiator*.

Maiengial, you are the *catalyst*.

SUMMARY

LITERATURE BACKGROUND	1
CHAPTER I. Introduction	1
I.1. Overview and motivation	1
I.2. Azobenzene	5
I.3. Isomerization mechanism	6
I.4. Azobenzene derivatives	9
I.5. Azopolymers	10
I.6. Mass transport in azopolymers	12
I.6.1. Thermal gradient model	15
I.6.2. Pressure gradient model	16
I.6.3. Translation diffusion model	17
I.6.4. Electromagnetic gradient force model	17
I.6.5. Mean field model	20
I.6.6. Thermodynamic deformation model	22
I.6.7. Microscopic theory of light induced deformation	24
I.6.8. Cage breaking model	27
I.7. Experimental study of SRG	29
I.7.1. Laser irradiation	29
I.7.2. Formation of surface relief gratings (SRG)	30
I.8. Molecular dynamics	33
I.8.1. Thermodynamics	38
I.8.1.1. Temperature and control methods	38
I.8.1.2. NVT Ensemble	40
I.8.2. Parameters evaluated in molecular dynamics	41
I.9. Bibliography	44
CHAPTER II. Thesis objectives	53

ORIGINAL CONTRIBUTIONS	55
<u>1st PART Experimental Studies</u>	56
CHAPTER III. Synthesis and characterization	58
III.1. Synthesis of studied azopolysiloxanes	58
III.1.1. Polysiloxane synthesis	58
III.1.2. Azo derivatives synthesis	61
III.1.2. Azopolysiloxane synthesis	65
III.2. Thermal characterization	70
III.2.1. Thermogravimetric studies	70
III.2.1. Differential thermal analysis	76
III.3. Liquid crystal state investigation	80
III.4. Surface characterization	82
III.5. Conclusions	85
CHAPTER IV. Photoisomerization studies	87
IV.1. Photoisomerization capacity of different azopolysiloxanes	87
IV.2. Isomerization under UV light	89
IV.3. Isomerization under Vis light	92
IV.4. Conclusions	95
CHAPTER V. Photochromic behavior	98
V.1. Strategy overview	98
V.2. Photochromic behavior of PFF3: polysiloxane with 4 – (phenylazo)phenol	99
V.2.1. Set 1	99
V.2.2. Set 2	105
V.3. Photochromic behavior of PDF: polysiloxane with 4– (4'- diphenylazo) phenol	108
V.4. Photochromic behavior of PNF1: polysiloxane with 4-(1'- naphthaleneazo) phenol	111

V.5. Photochromic behavior of PAF2: polysiloxane with 4-(2'- anthraceneazo) phenol	116
V.6. Conclusions	190
CHAPTER VI. Experimental technique	122
VI.1. Materials and methods	122
VI.1.1. Linear polysiloxane synthesis	122
VI.1.2. Azobenzene derivatives	124
VI.1.2.1. 4-(4'-biphenylazo)phenol	124
VI.1.2.2. 4 – (1'-naphthaleneazo)phenol synthesis	125
VI.1.2.3. 4-(2'-anthraceneazo)phenol synthesis	126
VI.1.2.4. Sodium salts	126
VI.1.3. Azopolysiloxanes synthesis	127
VI.2. Methods and instruments	127
VI.2.1. Spectroscopy	127
VI.2.1.1. ¹ H and ¹³ C NMR	127
VI.2.1.2. UV-Vis	128
VI.2.2. Spin coating technique	128
VI.2.3. Thermal analysis methods	129
VI.2.3.1. Thermal gravimetric analysis	129
VI.2.3.2. Differential thermal analysis	129
VI.2.4. Contact angle	129
VI.2.5. Optical microscopy with polarized light	130
VI.2.6. Laser irradiation	130

<u>2nd PART Simulation Studies</u>	133
CHAPTER VII. Simulation framework and calculations	135
VII.1. Framework	135
VII.2. Simulated systems	135
VII.2.1. Host molecules - the environment	135
VII.2.1.1. Diatomic host molecule model	136
VII.2.1.2. Methyl methacrylate coarse grained model	137
VII.2.2. Molecular motor – the isomerizing azobenzene	138
VII.3. Results validation	141
VII.3.1. Use of idealized molecules	141
VII.3.2. Time period between two successive trans – cis isomerizations τ_p	144
CHAPTER VIII. Diffusion studies on different motor sizes	147
VIII.1. Study framework	147
VIII.2. Influence of the motor's arm length on the host diffusion	149
VIII.3. Influence of motor width on the host's diffusion	167
VIII.4. Evaluation of different parameters concerning the host molecules	171
VIII.5. Threshold dependence on the host molecule size	174
VIII.6. Conclusions	176
CHAPTER IX. Isomerization rate influence on host's diffusion	178
IX.1. Study framework	178
IX.2. Diffusion behavior dependence on the isomerization rate	180
IX.3. Investigation on the forces acting on the motor	182
IX.4. Defining efficiency of the isomerization frequency	185
IX.5. Conclusions	182

CHAPTER X. Studies on the motor's motion	194
X.1. Study framework	194
X.2. Characteristic diffusion for motor and host molecules	195
X.3. Influence of the relative molecular masses on diffusion	197
X.4. Influence of the molecular sizes ratio on diffusion	200
X.5. Conclusions	211
 CHAPTER XI. Conclusions	 213

LITERATURE BACKGROUND

CHAPTER I. Introduction

I.1. Overview and motivation

The populations growing concern in raising life quality lead the scientific research towards continuous developing of new and better materials and technologies. Though there are various approaches to this challenge, we could say that they involve finding novel ways to exploit the chemical and physical properties of matter in relation to the desired functionality of final products. A particular manner to draw on designing intelligent materials is to use the materials' ability to response to different external stimuli, such as light, temperature, electromagnetic field, or to changes in their internal parameters, such as pH, ionic composition, and concentration. Moreover, targeted characteristics and specific functionalities represent an advantage that cannot be achieved through a common design. Progress in creating smart materials is constantly challenged by new discoveries and innovations and the research in this field varies widely.

In this frame, the subject of herein thesis is the study azo polymers that react to light stimuli with modifications into their spatial structure that have the ability to enable a mass displacement into the material. These materials own their specific behavior to a distinct property of the azobenzene molecules. Many aromatic azo molecules have bright colors due to their capacity to absorb visible light (400–700 nm). Through target molecular design, like extending the conjugation, incorporating various aromatic cycles, or introducing electron donor and acceptor groups, a wide spectral range of colors can be achieved. These colorful compounds are known as azo dyes and have been extendedly used as excellent colorants and pigments. The term “chromophore” is used to name an atom or a group of atoms that can act as a unit that absorbs light, being responsible for the colorful organic compounds. In

conclusion, light absorption groups and the structures that contain them are also referred to in literature as azo chromophores (Wang, 2017b).

As chromophores, azobenzenes and their derivatives undergo a reversible trans-cis photoisomerization, developing an impressive pressure of more than 1.5 GPa (Singleton *et al.*, 2012). When embedded into a material, they can serve as a driving force to induce motions that can eventually reshape the material at a nanoscale level, obtaining the so-called surface relief gratings (SRG). From a practical point of view, azobenzenes and azobenzene-like molecules can be seen as molecular motors. The resemblance comes from the way these molecules act when irradiated: the absorbed light energy is used to perform mechanical work.

Control of the chemical and physical properties of azobenzenes is the key in directing the mass transport in such way to obtain desirable features. Proceeding according to this strategy meets significant reservation because of the widely disputed mass transport process. Since the first report of SRG by two independent groups (Kim *et al.*, 1995; Rochon, Batalla and Natansohn, 1995), the mass transport mechanism that enables the obtaining of these nanostructures has been intensely studied. Several models have been proposed for the phenomenon, but they lack in consistency or omit important parameters.

The reasons behind the incitement in studying azo polymers revolve on the “cleanliness” of the method and the promising applications. Fabrication of SRG involve irradiation of the azo containing sample with light of certain wavelengths, polarization, and intensities. Luminous radiation is reliable energy source, the process can be remotely controlled and it doesn't involve any waste. As for applications, they are all connected to the low scale of the geometric features on the azopolymeric surfaces. Furthermore, varying the materials properties along with the experimental irradiation setup, a wide range of nanostructures can be obtained. For biological applications, a compulsory prerequisite is that the material must be bio inert, a thing which is solved through choosing polymers like polysiloxane or poly(methyl methacrylate). Using nanostructured azopolymeric films as support in cell cultures is a promising direction that is already studied within our research group (Hurduc, Macovei, Paius, Raicu, *et al.*, 2013a; Rocha *et al.*, 2014), as well as photosensitive micelles for controlled drug delivery (Rocha *et al.*, 2014). Literature shows more research in this field of biology and tissue engineering (Baac *et al.*, 2004; Lee *et al.*, 2004, 2005; Barille *et al.*, 2006; Barillé *et al.*, 2011).

I.2. Azobenzene

Azobenzene is a symmetric molecule that consists of two phenyl rings connected through the azo moiety --N=N-- , the chromophore group. By linking different substituents to the phenyl cycle, various derivatives can be obtained. For ease of discussion in the present thesis, some conventions will be used. The word azobenzene refers only to the diphenyldiazene, the representing molecule of the class. Whenever speaking about the whole class, the following names will be used: azobenzenes, azobenzene derivatives, azo molecules, and azo groups. To refer specifically to the double bond between the nitrogen atoms --N=N-- in the azobenzenes, chromophore group, azo moiety, or azo link is utilized.

By absorbing specific wavelengths of light, the chromophore enables a conformational change of the azobenzene molecule. The passing from one conformation to another is called isomerization. One of the configurations is the stable *trans* isomer, and the other is the metastable isomer *cis*.

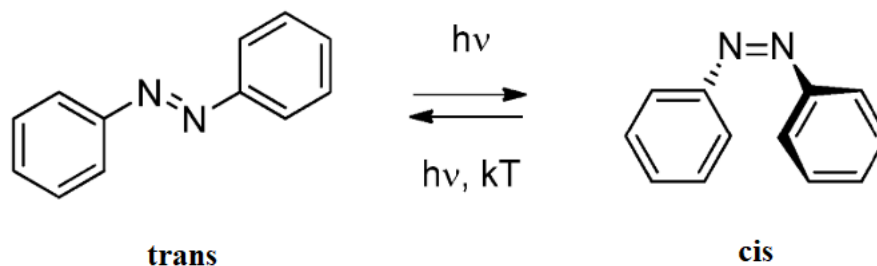


Figure I.1. Azobenzene isomerization (Bandara and Burdette, 2012).

The *cis* configuration of azobenzene has the two phenyl rings rotated with a 53.3° angle degree with respect to the N=N--C plane (Kurita, Ikegami and Ishikawa, 2002). Regarding the *trans* isomer, gas electron diffraction shows that the chemical bond between the phenyl cycle and azo moiety has a 1.41 \AA length, the N=N bond is 1.26 \AA long and the N--N--C bond angles are about 113° .

Due to the chromophore group, azo, azobenzene and its derivatives have long been used as dyes. Later, researchers began to study azo dyes focusing on the dichroism and birefringence properties. As azobenzenes possess dipole moment, they have the capacity to align when subjected to an electric field (Aleksejeva *et al.*, 2011). The first paper to report

observation of photoinduced anisotropy in a viscous solution containing an azo molecule was published in 1957 and the phenomenon was later attributed to photoinduced isomerization. After a few decades, the azobenzenes recapture researchers' interest starting with 1984, when two papers report on the inscription of polarization holograms in organic materials containing an azobenzene – like molecule. By using linearly two beams of polarized light perpendicular to each other, alternative areas of anisotropy (following the waves interference) (Todorov, Nikolova and Tomova, 1984a, 1984b; Hwang *et al.*, 2005). The third important discovery in the field comes from two independent groups in about the same time. They report the first application of azobenzene containing polymers to obtain surface relief gratings (SRG), using also polarized light interference. This moment marks an expanding interest to study azo materials, given the fact of the various applications foreseen.

Considering the isomerization as the driving force for fabricating SRG, different papers in the literature approach the matter from a theoretical point of view in order to gain insight into the molecules motion when it is provided with energy (Cattaneo and Persico, 1999). As it is always the case in simulations, models imply simplifications and an analogy with molecular switches is made.

I.3. Isomerization mechanism

Azobenzene molecules absorb light of appropriate wavelength through the azo moiety that enables trans-cis isomerization, passing through successive excitation states. For most azobenzenes, the isomerization process is completely reversible and severely precise experiments fail to prove any side reactions. Photocyclization and photoreduction are possible reactions, but very improbable because their low quantum yield in comparison with the isomerization (Wang, 2017b). While trans \leftrightarrow cis is enabled by light energy, cis \rightarrow trans can be driven by heat energy also (see Figure I.1.). The isomerization process is driven by the absorption of photons that determines electronic transitions. Thus, the change from the flat trans form to the folded cis form comes with modification of electronic and optical properties. There are two different pathways that describe isomerization i.e. rotation and inversion, including a mix of the two mechanisms and transient states. Over the course of the years, the subject has been researched, models have been proposed and new data from both

experiments and computation was continually added (Cattaneo and Persico, 1999; Kobayashi, Saito and Adachi, 2003; Schultz *et al.*, 2003; Cembran *et al.*, 2004; Dokić *et al.*, 2009; Ootani *et al.*, 2009; Xu *et al.*, 2018).

The model that describes the isomerization is schematized in Figure.I.2. Rotation around the azo moiety axis implies the breaking of the --N=N-- double bond in order to allow the two N atoms to spin relative to each other. This pathway completes with a modification of the C--N--N--C dihedral angle, maintaining the N--N--C angle value of $\sim 120^\circ$. In what concerns the inversion path, one “arm” of the azobenzene moves relatively to the other: one N=N--C angle widens to 180° , while the C--N=N--C dihedral stays at 0° . As specified from the beginning, two more complex paths are possible, namely the concerted rotation, when both N=N--C angles widen to 180° , when the molecule turns linear, and continues by bringing together the two arms, ending in the final cis conformation. The other mix course implies an inversion – assisted rotation described by a simultaneous modification in the C--N=N--C dihedral angle and a milder change in N=N--C angles. Very important to mention here is that the transient states that the azobenzenes pass through the isomerization between trans to cis (or vice versa), are all polar, except the linear conformation that forms during the concerted inversion. Thus, not surprisingly, the isomerization phenomenon causes, along with the geometrical change, a modification in the dipole moment.

The azobenzene molecule presents an absorption band with different maxima for the two isomers, i.e. $A_{\text{trans}} - \lambda = 365 \text{ nm}$ and $A_{\text{cis}} - \lambda = 440 \text{ nm}$. The $\text{trans} \leftrightarrow \text{cis}$ interconversion is controlled by using irradiation outside of two absorption maxima. For example, continuous irradiation with a $\lambda = 313 \text{ nm}$ light wavelength source or $\lambda = 436 \text{ nm}$ yields to a mix comprised of $\sim 20\%$ or $\sim 90\%$ respectively of trans isomer (this equilibrium is known as photostationary state). The isomerization is a very fast process, on the picoseconds range and although it differs with the solvent used and the solution viscosity, it stays in the picoseconds range.

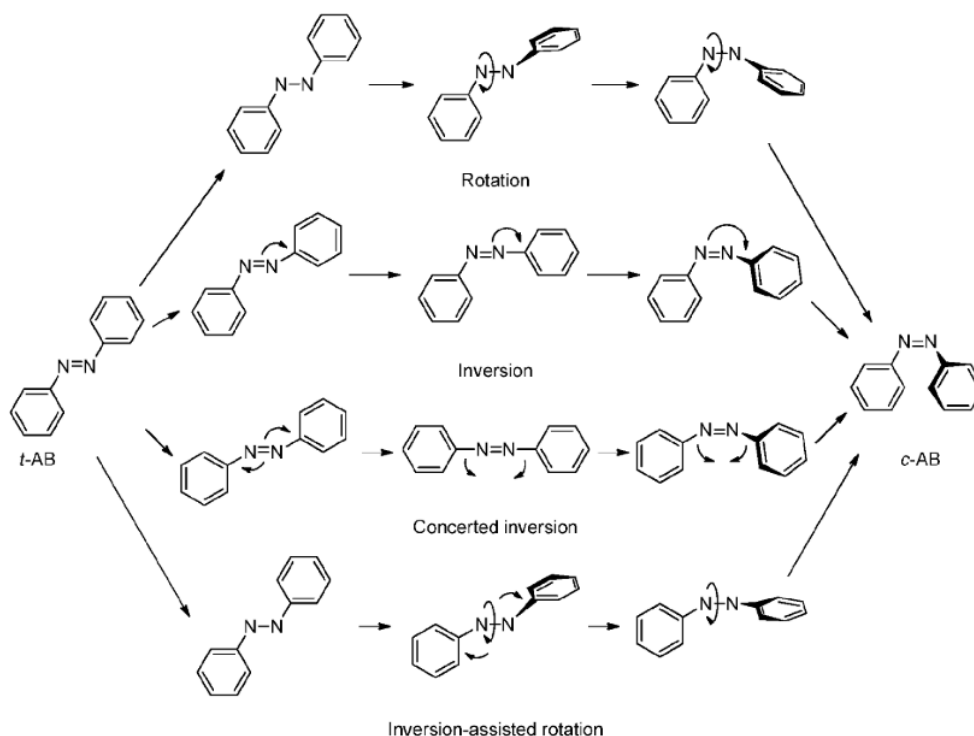


Figure I.2. Proposed mechanisms for *trans* – *cis* isomerization (Bandara and Burdette, 2012).

The exact pathways followed by the azobenzene when it changes its configuration through the electronic states is still under debate. While thermal isomerization (no light excitation) supposes the ground state to overcome the energetic barrier, the photoisomerization implies electronic excited states that follow certain paths in the process of configuration changing. Jablonski diagram shows (Figure II.3.) the possible electronic states and electronic transitions of azobenzene when irradiated. S_0 represents the singlet ground state and S_1 ($\pi - \pi^*$) and S_2 ($n - \pi^*$) are the first and second excited singlet state. *Trans* \rightarrow *cis* transition occurs by both $S_1 \leftarrow S_0$ and $S_2 \leftarrow S_0$ excitation, while *cis* \rightarrow *trans* isomerization occurs following the reversed path (relaxation with time constant 0.11 – 1 ps). Energetically evaluation assigns the four mechanisms (rotation, inversion, concerted inversion and inversion-assisted rotation) to the possible electronic state.

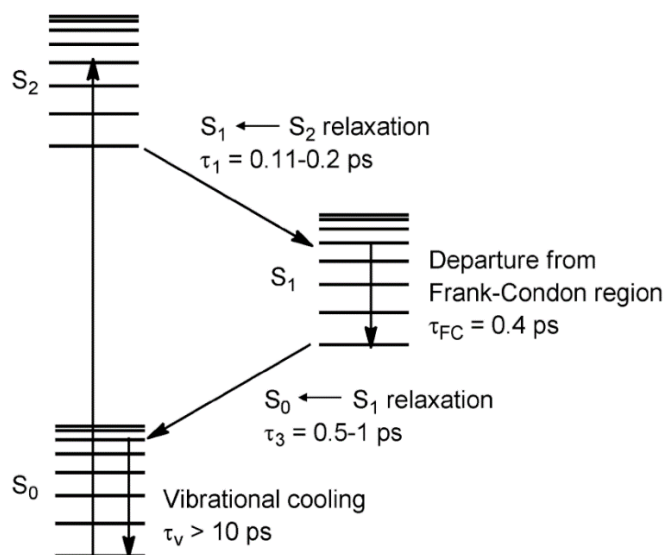


Figure I.3. Jablonski diagram of *trans* azobenzene depicting the singlet state S₀ and its excited states S₁ and S₂. (Bandara and Burdette, 2012).

Regarding the thermal *cis* → *trans* isomerization, the mechanisms proposed are rotation and inversion. The activation barrier for the phenomenon is lower in solution than in melt and the half-life of *cis* isomer at room temperature in solution is 2 days (Bandara and Burdette, 2012; Wang, 2017d).

I.4. Azobenzene derivatives

A simple azo compound is formed by two moieties connected through the azo bridging group. Its properties are influenced not only by the azo bond, but also by the groups found sideways of the azo bridge. If these groups are aryl and alkyl, the compounds are called aromatic and aliphatic azo molecules and their characteristics differ greatly due to the structural particularities (Wang, 2017b).

Azobenzene and its derivatives are widely used with polymers in order to obtain photosensitive materials. Considering the continuous development in this field, to fabricate azopolymers with different functions, a variety of derivatives are studied for improvement of materials and azobenzene itself is rarely used. Research on azo chromophores lead to the outgrowth of this functional group as being one of the most versatile in what regards its chemical and physical properties.

Azobenzene derivatives represent azobenzenes that have different substituents at one or both phenyl rings. These substituents have great influence on photochemical properties, absorption and emission, as well as the capacity to make the cis isomer more thermo- dynamically stable than the trans isomer.

Considering the absorption spectra of the derivatives, they can be parted in three different categories. First category is the *azobenzene type* and it is comprised of azobenzene substituted on one phenyl ring with one of the following groups: alkyl, aryl, halide, nitrile, amide, ester, carbonyl, carboxylic acid, nitro, 3-amino or 3-alkoxy¹. The absorption spectra of these derivatives are very similar to the azobenzene absorption spectrum. The p - p* transition takes place in the UV region, easy to distinguish from the n - p* transition, with the specification that most of these derivatives have higher rates of for the thermal isomerization. The second category is represented by the *aminoazobenzenes type* and their structure is the azobenzene substituted on one of the phenyl cycle with electron donating groups: 2- or 4-amino, 2- or 4-hydroxy, or 2- or 4-alkoxy. In these derivatives, the p - p* transition is shifted to higher wavelengths leading to overlapping of the two transitions. Third category is the *pseudo-stilbene type* and it is formed by two types of structures: the *protonated azobenzene* ($-NH=N-$) with no substituents on the phenyl rings, and the *push – pull azobenzenes* (substituted at one phenyl ring with electron donating groups like nitro or carboxylic acid, and at the other with electron accepting groups, such as amino or alkoxy). In this category, pseudostilbenes, the p - p* and n - p* transitions are nearly degenerate in energy. It is important to mention that just as the azobenzene, its derivatives too are influenced by the solvent on the matter of absorption spectrum (Bandara and Burdette, 2012; Wang, 2017d).

I.5. Azopolymers

Combining the advantages of high molecular weight molecules with the unique properties of azo compounds offers the opportunity to design photosensitive materials with targeted applications. For a few decades now, using light as an activator to fabricate intelligent materials has become one of the important research directions in the field of nanotechnology, azopolymers gained interest for study, and creative ideas are continuously

emerging. In general, these polymers can be classified in the same way as the azobenzenes, by taking into consideration their absorption spectra.

Besides the photonic and optical properties, other characteristics can be also ascribed to azobenzenes. Azo functional structures can also display large π -conjugated systems properties due to the π -conjugation between azo moieties and aromatic rings. Azobenzenes are typical examples of rigid molecular architectures with anisotropic geometry, such as disk-like or elongated shapes. The polymers that contain these azo cores can exhibit liquid crystal phases, if proper external conditions are provided (temperature and solvent). Azo containing architectures tuned with flexible spacers and tails are frequently used as building blocks to create liquid crystals azopolymers.

In the last decades, many azopolymers have been synthesized, studied and applied in various fields. These materials can have the azobenzenes embedded (in which case the polymer can be referred to as matrix), or chemically connected to the main chain or side chain of the polymer. One main reason for their investigation is represented by the will to understand the behavior of azopolymers when they interact with light at molecular and macroscopic level. After 1995, when the research in this field started booming, new studies began to emerge, investigating in novel domains, such as nonlinear optics (NLO), liquid crystals (LC), photorefractive materials, mono- and multilayer assemblies, or self-assembly in solutions, all based on the azopolymers photosensitivity (Wang, 2017b).

As other functional polymers, azopolymers can be obtained by polymerization and copolymerization of monomers that already contain azobenzenes. In what concerns radical polymerization, the drawback of this method relies on the strong inhibitory capacity of azobenzenes, a fact that challenges the initiators efficiency and the obtaining of high molecular mass azopolymers. Regarding the polycondensation of azo containing monomers, this method can be prone to side reaction. In order to avoid these disadvantages, an alternative way to synthesize azopolymers can be employed: synthesis of a suitable polymer and further modification with azobenzenes through chemical reactions. The type of polymerization reaction influences the polydispersity index. Between chain, step, and controlled radical polymerization, the latter gives the narrowest molecular weight distribution (Wang, 2017a).

Different monomers are used to obtain azopolymers, such as acrylates /methacrylates (Paterson *et al.*, 1996; Deshmukh, Bromberg and Hatton, 2006; Hubert *et al.*,

2007; Zhu and Wang, 2013), styrene (Soozandehfar *et al.*, 2000; Bai and Zhao, 2001; Fahmy, Ha and Ahmed, 2002; Li Cui, 2003; Cao *et al.*, 2008), or the less common siloxanes (Kazmierski *et al.*, 2004; Ene *et al.*, 2008; Enea *et al.*, 2008; Kulikovska *et al.*, 2008; Hurduc, Macovei, Paius, Raicu, *et al.*, 2013b; Luca *et al.*, 2014; Rocha *et al.*, 2014; Damian *et al.*, 2016) that make the subject of the present thesis. Literature shows also more complex structures, such as hyperbranched, dendritic or star azopolymers (Deng and Chen, 2004; Jankova, Bednarek and Hvilsted, 2005).

Polymers with different main-chain rigidity imprint different properties to the corresponding azopolymers. In view of the fact that polymers are macromolecules with numerous structural characteristics, leaving aside the azobenzenes influence, it is difficult to make comparisons between different azopolymers; to assign differences in the behavior to a specific factors is challenging. However, some studies addressing this issue report that higher chain flexibility is linked to an increased rate of SRG formation (He, Wang and Zhou, 2002; Zhou, Tang and Wang, 2015). The flexibility of the spacer, if any, between the azo molecule and the main-chain is to take into consideration also (Wang *et al.*, 2009). Adding to that, the polymer's crystallinity has also an effect on its SRG forming capacity; the majority of reports state that amorphous are more prone to give better results (Natansohn and Rochon, 2002a).

I.6. Mass transport in azopolymers

One of the most important characteristics of azopolymers is their capacity to enable photoinduced mass transport, challenging the previous technologies to obtain surface modulation that relies mostly on nanolithography. No other materials have been shown until present day to have this ability of mass displacement under light irradiation, forming nanostructures on the surface of azopolymer films. The first two reports on this subject in 1995 (Kim *et al.*, 1995; Rochon, Batalla and Natansohn, 1995) marked the beginning of intense research by different groups on the matter of mass migration in azopolymers, as a method to obtain SRG (Hvilsted *et al.*, 1998; Kim, Kumar and Kim, 2003; Ishitobi *et al.*, 2007).

The surface modulation on azopolymeric films is attained by the usage of light only and it is usually of a few hundreds of nanometers.

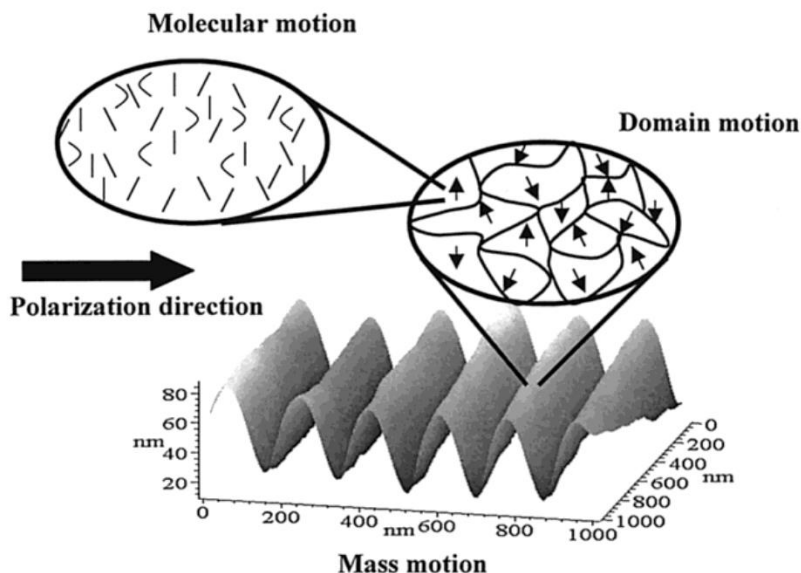


Figure I.4. Representation of photoinduced SRG formation in azopolymers illustrating the system motions on a bottom-up scale: i) molecular motion; ii) domain motion; iii) mass motion (Natansohn and Rochon, 2002b).

As one of the pioneers in the field (Natansohn and Rochon, 2002b) proposes, the mass transport in azopolymers can be split in three stages. First step is the molecular motion, meaning the trans – cis – trans photoisomerization. When the azo moiety’s longitudinal axis is parallel with the light polarization direction, it absorbs the luminous energy and undergoes isomerization, changing its spatial orientation along with the geometrical form. On the other hand, perpendicular positioning with respect to the polarization vector it is not favorable to light absorption. Because of this position restriction for azo moiety – light interaction, more and more chromophores end up in the “inert” perpendicular position relative to the polarization vector, creating domains of spatial oriented azobenzene molecules (Figure I.4.). This is when the second step comes into play. Creation of these nanoscale domains require spatial constraints, i.e. the photoisomerization can only enable development of oriented domains if azobenzene molecules are embedded in/connected to a tightly organized structure. For the azobenzene to affect the motion of neighboring molecules, optimal spatial restraints are necessary. The chromophores alignment with respect to the light polarization direction, that results from the molecular motion in the first step, hinder further isomerization, as it would conflict with the newly created order at the nanoscale level. Due to the high quantum

yield of photoisomerization, orientation of a larger region takes place. The ordered domains (liquid crystalline or crystalline) form through cooperative motions of azobenzenes and are orthogonally positioned with respect to the light polarization. The domains size varies, but the amount of displacement material is definitely greater than in the first step. The first two stages lead to a larger motion of the azopolymer, a material displacement – dependent of the light polarization and light beam interference – that forms the pattern on the film surface in the range of micrometers. The driving force responsible for the macroscopic movement is subject to a lot of discussion in the research field and various postulates have been made to account for the mass transport. From the gradient electric force, to isomerization pressure, asymmetric diffusion, intermolecular interaction, mechanical stress and permittivity gradient, etc., none of these proposed models explain all the experimental observations.

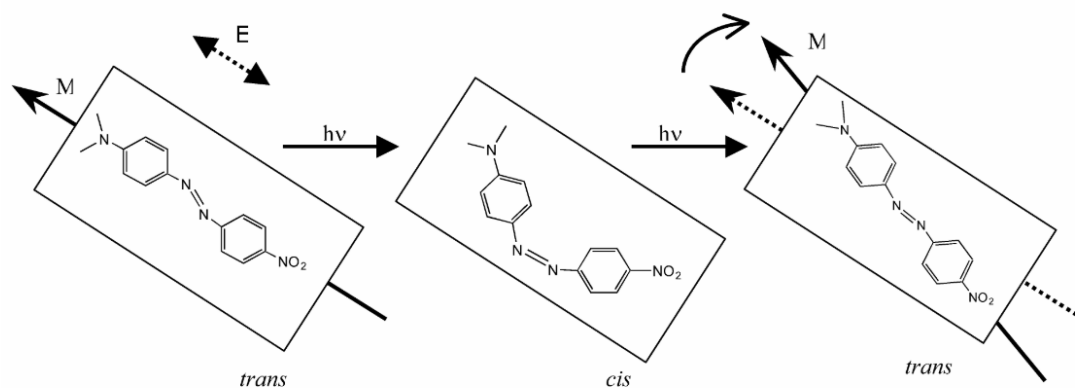


Figure I.5. Azobenzene photoinduced orientation with respect to the electric field vector E and showing the optical transition moment axis M (Cojocariu and Rochon, 2004).

Most of the research on SRG explore the ability of azopolymers to design modulated surfaces with certain features that required for specific applications. Thus, irradiation is tailored to fit the requirements, without much interest to grasp the process of obtaining the SRG. Thus, despite the multitude of studies on this field, the emphasis on applications makes it difficult to overthrow the influence of various factors implied in mass transport, i.e. studies from different papers cannot be compared to one another (Burke and Barrett, 2004; Mechau, Saphiannikova and Neher, 2006; Liu, He and Wang, 2010; Teboul *et al.*, 2015). Inconsistency of the findings by different researches complicate the aim to design a universal

model. Most models cannot be transferred from one azopolymer to another and show strong dependence on the laser setups.

Nevertheless, some research does focus on the mass migration phenomenon and several mechanisms have been proposed along the time, as new and new discoveries emerged. Most of the model deal with the driving force responsible for the mass transport, but the counterintuitive capacity of azopolymer chains to suffer microscale displacement at temperatures below T_g is another factor to pay regard to.

I.6.1. Thermal gradient model

The first report (Rochon, Batalla and Natansohn, 1995) of SRG formation, proposes an explanation for the phenomenon observed based on the thermal gradient. The model states that temperature varies across the light interference pattern according to its maxima and minima, and diffusion rate of the material is proportional to the thermal gradient. According to this explication, the SRG formation rate follows the heat flow in the material, but experiments (Yager and Barrett, 2004) conducted on substrates characterized by different coefficients of thermal conductivity conclude that results do not depend on the film temperature. Another finding that challenges this interpretation is that by simulating the heat flow along the interference pattern, the temperature between the maxima and minima reach almost the same values (difference on third decimal) in 2 μ s, a timeframe too short to account for the massive mass transport. Another approach to studying this model implies the use of pulsed light irradiation. Rather than a direct dependency between the thermal gradient and material's diffusion, an intermediary factor is considered to become effective: the permittivity gradient induced by the thermal variation. Besides the contradictory results from other studies, the principal drawback is that while it accounts for the light intensity (the SRG profile is proportional to the second derivative of light intensity) the influence of light polarization is not addressed to (Wang, 2017c).

I.6.2. Pressure gradient model

This model holds responsible for the formation of SRG the expansion of free volume in the confined space of a thin azopolymeric layer and it was proposed in the early stages of research on the field (Barrett, Natansohn and Rochon, 1996; Barrett, Rochon and Natansohn, 1998).

The model describes the process as taking place in two successive steps. Firstly, the photoisomerization occurs with different frequencies, according to the intensity fringes caused by interfering beams. The illuminated regions are reach in azobenzene molecules that undergo trans – cis isomerization, determining an expansion of the free volume in the azopolymeric film. The second step is thus triggered by isomerization and is expressed by a non-uniform pressure increase into the material. The material experiences a viscoelastic flow from high-pressure to lower-pressure regions. This flow is in conformity with the alternant illuminated/dark (high-/low-pressure) areas and consequently, the regular sinusoidal modulated surface (SRG) forms. In this interpretation, the model is often called isomerization-driven free volume expansion.

In the general frame of Newtonian fluid dynamics, the flow of incompressible fluids is described by Navier – Stokes relation. Without factoring into the particularities of the model, the equation applies to the flow of azopolymeric material in agreement with the pressure gradient. Hence, this model provides a generic view of SRG formation outside the of influence parameters from the laser setups and polymers characteristics. In accordance, the model can be used to evaluate the evolution in time of the film surface.

$$\frac{1}{h^2} = \frac{1}{h_0^2} - \frac{2}{3\eta} \frac{\partial^2 P(x)}{\partial x^2} t$$

Equation I.1.

where h represents the change in the film surface in time t , h_0 is a parameter for the initial film thickness, η is the kinematic viscosity and $P(x)$ is the pressure along x axis.

Forecast calculations using this model show good agreement with experimental results, with a few limitations. For example, absorption change in the azopolymeric film during (and due to) irradiation, is inconsistent with the assumption of thin film, a condition of the equation. Validation of the proposed mechanism comes also from two studies that

confirm the free volume expansion during irradiation. However, similar to the thermal gradient model, it does not show regard to light polarization (Wang, 2017c).

I.6.3. Translation diffusion model

The mass transport mechanism responsible for SRG is discussed (Lefin and Fiorini, 1998; Lefin, Fiorini and Nunzi, 1998) in terms of a unidimensional random motion along the excitation direction of azobenzene molecules, dragging the polymer chains with them. A trans – cis – trans photoisomerization cycle enables azobenzene to perform random walk steps in the direction parallel to its previous orientation, much like a worm, hence the *worm-like movement* name. Upon some necessary simplifications, a method to calculate the displacement of molecules in one step is developed. The photoinduced flux of azobenzenes moving in the direction positive z is evaluated, then diffusion of azobenzenes (the new position) and finally the concentration of trans molecules in a point r at time t .

$$\frac{\partial N}{\partial t} = -\text{div}J + D_0\Delta N$$

Equation I.2.

where N is the number of molecules, J is the photoinduced flux and D_0 is the spontaneous diffusion coefficient of azobenzenes in the environmental molecules.

Comparing to other models, the calculation (Equation I.2.) is applicable to two types light polarization, s- and p-polarization. Recent improvements have been made to this method, bringing about the photoinduced diffusion model, which takes into consideration the free space around the molecules (jumps from hole to hole). This new model can be used in Monte Carlo modeling method to successful simulate the molecular transport in the material and modifications of the surface topography, taking into account the interactions between molecular dipoles and electromagnetic field (Wang, 2017c).

I.6.4. Electromagnetic gradient force model

The statement of this model (Kumar *et al.*, 1998; Bian *et al.*, 1999) is that the azobenzenes' dipoles interact with the electric field and as a consequence of the latter's gradient, the migration of the azopolymeric chains occurs. Thus, the driving force of SRG formation is the electromagnetic gradient created by the optical field. Findings of the underlying experiments show that SRG form only in the presence of an intensity gradient

and the electric field has a component parallel to the plane of incidence on the film. The model is developed from prior studies of the proponents, which focus on light polarization. A first observation is that since the polarization is proven to have a strong influence on the SRG recording, thermal effects have to be negligible. Light fluence is a more suitable influence criterion to evaluate diffraction efficiency than the light intensity itself. Another study found that even though s-polarized light has the highest intensity modulation, it leads to SRG with lower amplitude than light, which contains p-polarization component (the experiment is performed with light beams of comparable intensities).

The model uses for the calculation of the time averaged gradient force density f induced by the optical field the following formula (Equation I.3.). The assumption that the polymer is an incompressible material is needed.

$$f = \langle [P(r, t) \cdot \nabla] E[r, t] \rangle = \langle [\varepsilon_0 E(r, t) \cdot \nabla] E(r, t) \rangle = 1/2 \varepsilon_0 \chi' E(r) \cdot \nabla E(r)$$

Equation I.3.

where P is p-polarization, r represents the position and t the time, E is the optical field, ε_0 is , χ and χ' are the polymer susceptibility and its real part.

The force induced mass transport is evaluated according to Equation I.4.

$$v(x, y, z) = \mu f(x, y, z)$$

Equation I.4.

where v is the flow velocity, x, y, z represent the Cartesian coordinates and μ is a proportionality factor for a particular polymer.

The model also provides a formula for the corresponding surface deformation $S(x, y, t)$ induced by a linearly polarized 1D beam with Gaussian distribution of intensity (Equation I.5.).

$$S(x, y, t) = \int_0^t v_z(X, y, 0) dt' = \frac{1}{4} h \mu \varepsilon_0 \chi' = \frac{\partial^2 I(x, y)}{\partial x^2} t$$

Equation I.5.

where h is the effective thickness of the moving layer in the film, and I is the optical intensity.

The relationship between the electromagnetic gradient force and optical field is portrayed in *Figure I.6.* and it shows the distribution of the $I(x)$ optical intensity's uni-dimensional component, $E(x)$ optical field, $dE(x)/dx$ gradient and $f(x)$ electromagnetic gradient force.

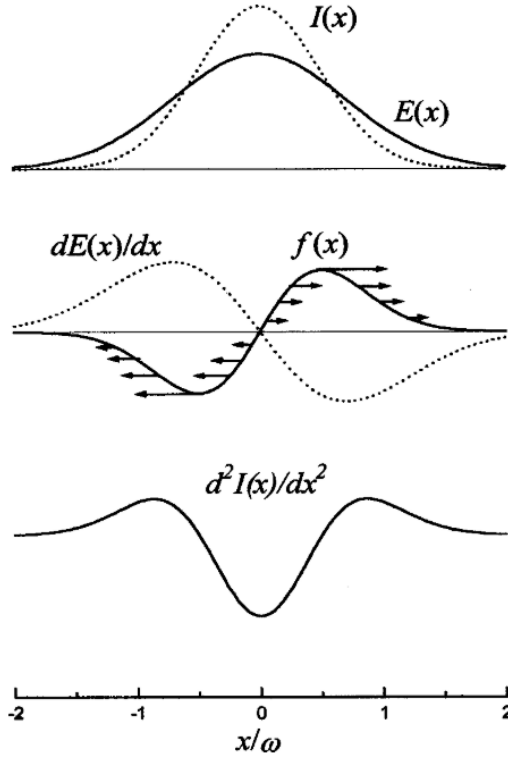


Figure I.6. The electromagnetic gradient force $f(x)$ in relation with optical field $E(x)$, where ω is the half width of incident beam's Gaussian distribution intensity and the arrows represent the force direction (Bian et al., 1999).

The model asserts the strong dependence of SRG inscription on the polarization and states that for the mass transport to occur, an electromagnetic gradient force with a polarization component parallel to the optical field. The inconvenience of this proposed mechanism is that the inconsistency regarding the force density: the estimated value in the model is two orders of magnitude lower than the gravitational force, thus too small to count as significant influence factor in the SRG inscription.

To note is that the studies underlying this model also indicate the existence of another mechanism that predominates in the SRG inscription process when higher light intensities are used. They attribute the erasing observed in the azopolymeric films to a

complex photo thermal effect and support the idea of some photochemical reactions, such as bleaching and crosslinking (Wang, 2017c).

I.6.5. Mean field model

The model (Pedersen *et al.*, 1998) is based on the azobenzenes rotational mobility induced by the isomerization phenomenon. The principle of mean field model is that the photoinduced orientation of azo chromophores is followed by anisotropic intermolecular interactions, which in turn enable mass transport. Attraction forces between the azobenzenes are considered to take place when the molecules are aligned in an end-to-end manner (y axis) or side-by-side (x axis) within the film plane and perpendicular to the grating vector.

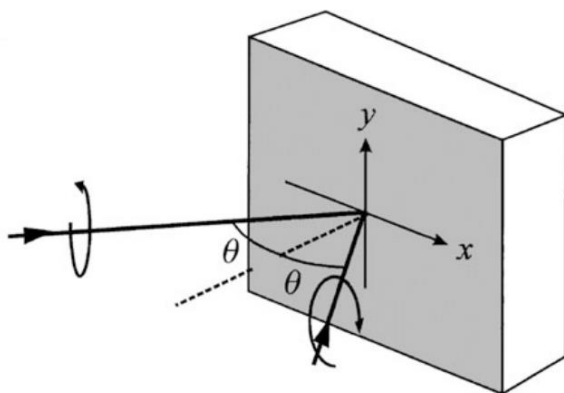


Figure I.7. Schematic illustration of the recording setup (Pedersen *et al.*, 1998).

The mean field approach must be carefully employed, as one constraint implies that the mean field potential considers contribution of molecules from an infinite sphere around the molecule in question. As part of the mean field theory, the Maier-Saupe assumption is to ignore the repulsive interactions, taking into consideration only the attractive ones. Given this circumstance, the side-by-side attractive interactions predominate, determining the azobenzenes to shift to areas of higher order. This translation in the x direction enables mass transport.

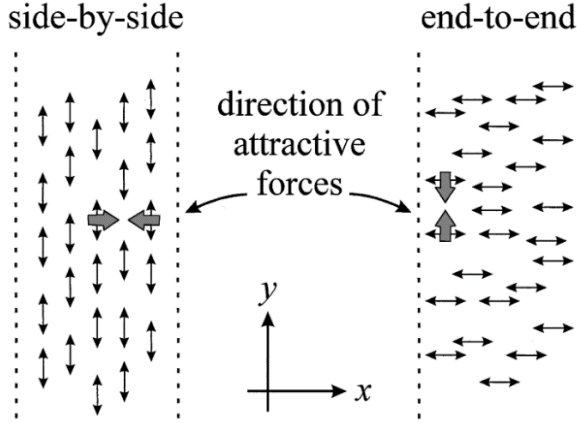


Figure I.8. Illustration of attractive interactions aligned with x axis (side-by-side), and y axis (end-to-end) (Pedersen *et al.*, 1998).

The proponents of the model develop a calculation method (Equation I.6.) for the energy functional $F[h]$ used to evaluate the effective height h of the SRG (the mobile layer) as a function of S_{eff} orientation order parameter. S_{eff} can be obtained from ellipticity of polarized light ϵ and electric field E .

$$F[h] = \int_{-\infty}^{\infty} \left\{ \sqrt{1 + \left[\frac{dh(x)}{dx} \right]^2} \right\} dx - K \int_{-\infty}^{\infty} S_{eff}^2(x) h(x) dx + \alpha \int_{-\infty}^{\infty} [h(x) - d] dx$$

Equation I.6.

where x represents the Cartesian coordinate axis s and K is a constant to express the relative strength between mean-field forces and surface tension. The calculation method is used in the model for three different light polarizations and the results are in agreement with experiments.

While the model is developed for liquid crystals, the authors affirm that it can be translated to amorphous materials also.

Irradiation with linearly polarized light orients the chromophores parallel to each other and thus their mutual attraction augments. Consequently, the azopolymeric film contracts in illuminated areas, and the ridges of the grating coincide with the interference band. Thus, particularity of the mechanism proposed is the statement that azobenzenes move from the low light intensity areas to the higher light intensity areas (unlike the other models) (Wang, 2017c).

I.6.6. Thermodynamic deformation model

The starting point in this model (Saphiannikova and Neher, 2005) resides in the plasticization phenomenon that would be needed for microscale mass transport to take place. A viscoelastic phase state, so above T_g , provides the necessary elasticity for mass migration to occur, but all experiments are performed at room temperature, well lower than T_g for most polymers. Moreover, previous tests show that light irradiation of azopolymeric films soften the material only a tenth of the softening achieved at T_g , the authors conclude that there must be a photoinduced force to compensate for this lack of plasticization in the film.

As previous research regarding the mass transport mechanism conclude that the azobenzenes photoinduced orientation with respect to the grating vector must be at the core of this phenomenon, the authors of this model use this finding as a commencement to propose a new mechanism that accounts for the system's free energy and translational symmetry in the material. They shift the focus point from the liquid crystalline systems where there is an inherent strong coupling between the azobenzene molecules to amorphous azopolymers. Starting from a material that already has a certain degree of order, the correct term in this case is photoinduced reorientation, and not orientation.

The principle behind this model is the need for entropy compensation: once the azobenzenes photoinduced reorientation takes place, the entropy drops because of the newly created order; thus, the system's disordering has to be restituted to reach its initial level at least, so that the entropy increases. This issue is solved by stretching of the sample along the polarization direction, which is the thermodynamic deformation that theorizes this model.

According to this idea, the entropy drop due to one azobenzene molecule due to photoinduced orientation can be evaluated for all types of light polarization. Adding to that, the sample deformation can be calculated in respect to the SRG amplitude and period. The following formula (Equation I.7.) is a general formalism for entropy drop/azobenzene S_{azo} .

$$S_{azo} = -k_B \iint f(\theta_E) \ln 4\pi[f(\theta_E)] d\Omega$$

Equation I.7.

where k_B is Boltzmann constant, θ_E is the angle between the vector of the azobenzene molecule and electric field vector E .

The free energy F_{azo} can be simply calculated, as it only depends on absolute temperature T and the entropy term:

$$F_{azo} = -TS_{azo}$$

Equation I.8.

Based on the previous formulas, the elastic stress's magnitude $\sigma(\varepsilon)$ can be evaluated from the derivative of free energy over deformation.

$$\sigma(\varepsilon) = n \frac{\partial F(\varepsilon)}{\partial \varepsilon}$$

Equation I.9.

where, n is the number density for azobenzenes, and ε is the elongation (deformation). The validity of this relation has been tested and lead to conclusion that the resulted elastic stress $\sigma(\varepsilon)$ is sufficiently high to induce plastic deformation in the azopolymeric film.

The strength of the photoinduced alignment is expressed through α parameter, where $\alpha < 4$ denotes weak alignment and $\alpha > 15$ strong alignment. The higher the α parameter, the narrower the orientational distribution function $f(\theta)$ that peaks at $\theta = 90^\circ$, meaning that most azobenzenes are found in a perpendicular (or very close to) position with respect to the direction of electric field vector.

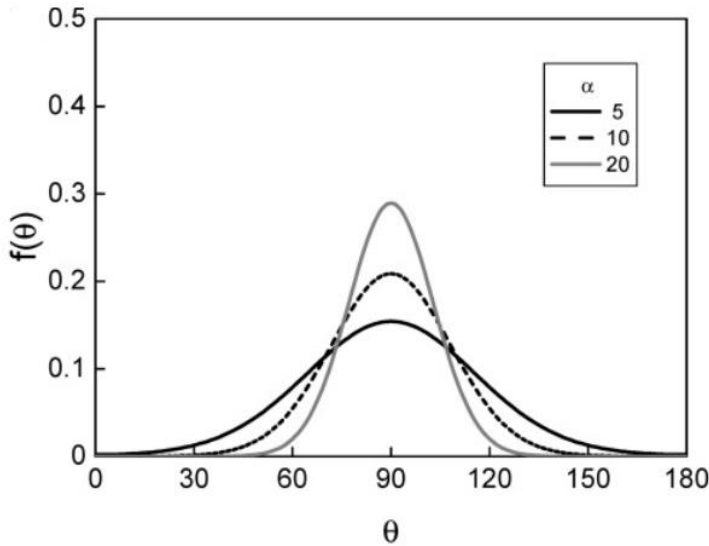


Figure I.9. Orientational distribution function $f(\theta)$ at different strengths of light-induced alignment: $\alpha = 5, 10$, and 20 (Saphiannikova and Neher, 2005).

One aspect left unexplained in this theory's frame is the dependency of alignment strength on the writing light intensity.

The model's prediction for *p-p*, *s-s*, and *circ-circ* polarized light is in agreement with most experiments from literature, namely the material is displaced from the high light intensity areas to the low energy ones. In the same time, a contraction of the material from dark regions is not indicated by the model's theory to occur. Regarding the efficiency of the SRG inscription, the model forecasts that *circ-circ* geometry has an intermediary value between *s-s* and *p-p* geometries. However, experiments show that *circ-circ* polarized light has the best results.

I.6.7. Microscopic theory of light induced deformation

In the frame of the microscopic theory (Toshchevnikov, Saphiannikova and Heinrich, 2009) SRG formation relies on the internal structure of azopolymers: polymers with side-chain azobenzene. The reasoning is that azobenzenes' orientation anisotropy (cause by their interaction with polarized light) is followed by mechanical stress. According to the theory, the photoinduced stress in the azopolymeric film is larger than the yield stress, implying that the material suffers both plastic and elastic deformation under light exposure. This approach provides an explanation for SRG inscription in amorphous azopolymers. In this viscoelastic picture, the theory's prediction is that the irreversible strain left after irradiation downsizes with temperature increase; at certain temperature below T_g , it can even completely vanish. Regarding the structural particularities accounted by the model, some azopolymer samples show nonmonotonic behavior, the elongation can turn to uniaxial compression. These findings are in good agreement with experiments carried in the literature.

The model studies polymers with side chain azobenzenes connected through a short or long spacer. The orientation distribution of azobenzenes with respect to the main chain is the parameter evaluated in order to find connections between the azopolymer's architectures and SRG inscription.

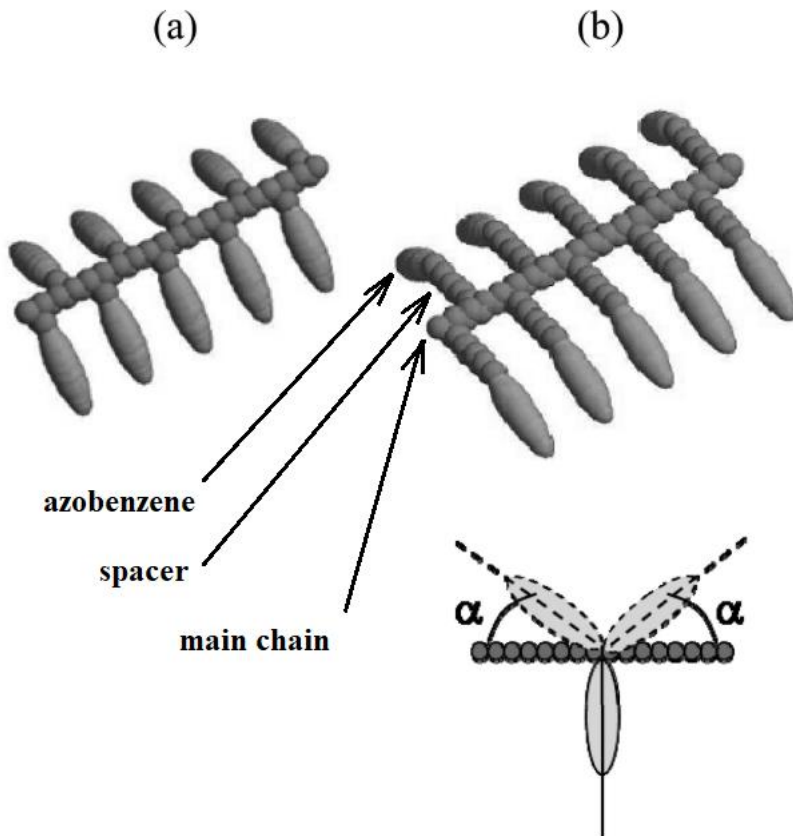


Figure I.10. Molecular architecture of a side chain azobenzene polymer with (a) short and (b) long spacers. Below, illustration of possible arrangement (Toshchevnikov, Saphiannikova and Heinrich, 2009).

In this model's theory, the authors develop a complex formalism for a polymer with side chain azobenzene irradiated with linearly polarized light. In addition to their previous model, thermodynamic deformation (Saphiannikova and Neher, 2005), the polymer backbone plays a major role here. To quantify the influence of the azopolymer's structure, they provide a mathematical description of the architecture: the backbone is formed from "oligomers", meaning stiff rods equivalent to Kuhn segments (common practice in computer simulation) that interact through the effective potential U . The potential U of a Kuhn segment subjected to an electrical field E represents a sum of energies and its orientation in space is described by two parameters: θ – the angle between the segment's long axis and electrical field E , and ψ – the segment's rotation around its own long axis.

$$U(\theta\psi) = N_{azo} V_0 u(\theta\psi)$$

Equation I.10.

where N_{azo} is the number of azobenzenes on one Kuhn segment, V_0 is the electric field strength and $u(\theta, \psi)$ is a function to describe orientation distribution of azobenzenes inside the Kuhn segment, averaged over multiple runs. In this context, the model provides new mathematical expressions for Helmholtz free energy, equilibrium elongation, and striction (deformation stress) at low and high light intensities.

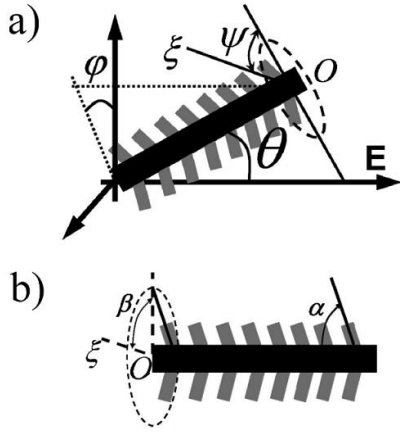


Figure I.11. *a) Spatial orientation of a Kuhn segment with azobenzene in side chains. Axis $O\xi$ is perpendicular to the main chain and defines the frame of reference related to the oligomer. b) Internal orientation of azobenzenes inside an oligomer; α is the angle between an azobenzene molecule and the main chain, β is the angle between a projection of azobenzene on a plane orthogonal to the main chain and the axis $O\xi$ (Toshchevnikov, Saphiannikova and Heinrich, 2009).*

In the model, results are interpreted in the viscoelastic picture. The critical temperature T^* (temperature at which the irreversible elongation disappears) is generally independent on T_g . On the other hand, it is determined by the following parameters: electrical field vector E , yield stress σ_y , number density of azobenzenes n_o , laser intensity I_p , activation energy trans \leftrightarrow cis E_a (term in Arrhenius equation), and spatial orientation of azobenzenes (α^* – the angle between the azobenzene's long axis and the Kuhn segment, and β^* – the angle between a reference axis placed perpendicularly to the long axis of azobenzene and the segment's axis).

I.6.8. Cage breaking model

The cage breaking model is first proposed (Saiddine, Teboul and Nunzi, 2010) following research to determine the responsible component that drives the SRG mechanism: the host or the azobenzene. To note is that often in computer simulation the preferred term for the polymer or monomer that contains the azobenzene molecules is *host* or *matrix*. According to the model, there are two scenarios: i) the azobenzene isomerization enables its motion inside the host, which further induces molecular motions of the host; ii) the azobenzene isomerization induces changes in the diffusion process of host, which in turn induces the azobenzene's motion inside the host.

In this context, the dynamics of both host and azobenzene are studied under different thermodynamic conditions. The authors find that when the azobenzene isomerizes, the host molecules around it move faster than the azobenzene itself. This result is sustained by the following findings. The host has a faster structural relaxation and a larger diffusion than the azobenzene. Consequently, it is the host's motions that drive the dynamics of the system. The model's frame supposes the host molecules surrounding the azobenzene as a shell that can be considered as having various radiuses. At large enough time scales, the azobenzene diffuses faster due to the fact that while the azobenzene remains inside the diffusive shell, the hosts are constantly pushed away by the azobenzene's isomerization motion. Thus, without the azobenzene around to modify their dynamics, the hosts diffuse less – thermal diffusion.

After the idea of a cage formed from the surrounding molecules around the azobenzene is iterated, the model is further developed to focus on the motions that lead the azobenzene to escape its cage (Teboul *et al.*, 2011). The starting point is the isomerization process that can push host molecules in the immediate vicinity of azobenzene. This can happen during both trans to cis conversion and cis to trans conversion, as the two *arms* of the azobenzene move to reach the corresponding configuration. Following the displacement of host molecules, a rearrangement that can be cooperative or not. Investigating the host molecules diffusion in relation with the isomerization, the authors show that the host diffuses after trans to cis motion and stops after cis to trans conversion. As the diffusion continues after trans to cis conversion and it doesn't stop immediately, it is the rearrangement process that is responsible for this behavior. This observation is in good agreement with the

dynamical heterogeneities proved by both experiments and simulations. In conclusion, the isomerization induced rearrangement of the host molecules is a cooperative process that leads to their further diffusion.

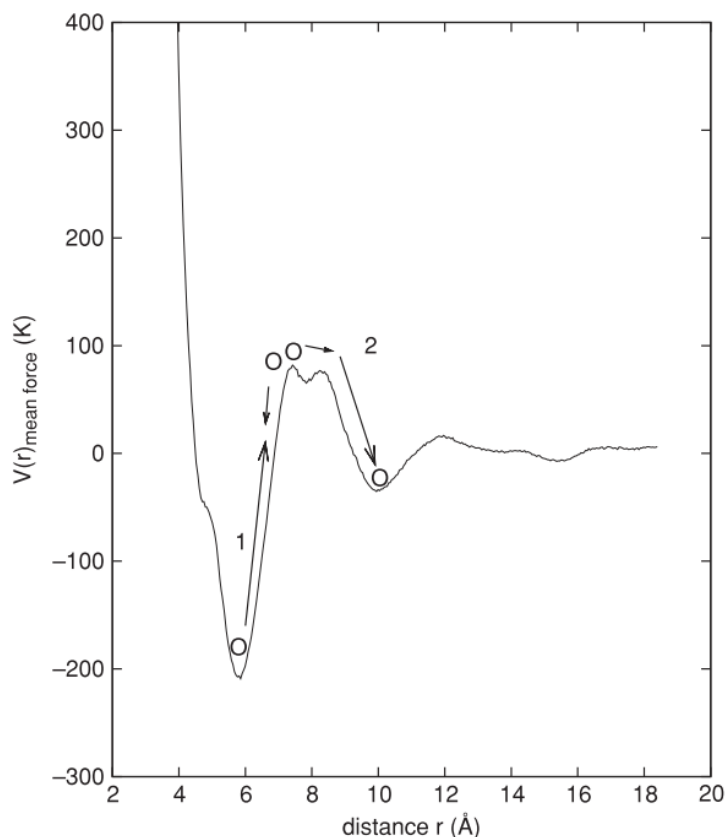


Figure I.12. Mean force potential between host molecules $V = -T \log(g(r))$ in Kelvin. The first ball represents the mean position of hosts trapped in the potential well. The *cis*–*trans* isomerization pushes the molecule to the second position (the second ball). From this point, the molecule will can either return to its initial position or continue to the second potential well. If the host continues moving forward, it escapes the cage formed by its neighbors, leading to induced diffusion (Teboul *et al.*, 2011).

Evaluation of the mean force potential (Figure I.12.) shows that after *trans* to *cis* isomerization, the host molecules can reach to an unstable position that followed by its return to the first well potential. If the first peak of the mean potential is surpassed, the molecules continues its trajectory to the second potential well. This point marks the host’s escaping from the cage formed by neighboring molecules. Conclusively, diffusion arises from these cage breaking steps which imply a reorganization of the host molecules in the considered

system. A chronological examination of this cage breaking process confirms that the diffusion takes place during and after trans to cis conversion, because it is during this time that the host is pushed by the azobenzene. Similarly, the induced diffusive motions stop during cis to trans isomerization, because the host molecules are kept in stable positions during this time laps.

I.7. Experimental study of SRG

I.7.1. Laser irradiation

Surface patterning is performed through laser irradiation. Two laser beams meet on the film surface and form an interference pattern that translates into a sinusoidal relief pattern (the SRG) with specific amplitude and period, characteristics that depend on the interference angle between the two beams. Regarding the experimental setup, the light wavelength, polarization, and intensity bring additional contribution to the SRG formation. The wavelength has to match the azopolymer absorption spectrum, thus most of the used light sources are Ar⁺ lasers (for $\lambda = 488.2$ and 514.5 nm wavelength) or diode-pumped solid-state lasers such as Nd:YAG and Nd:YVO₄ ($\lambda = 532$ nm wavelength).

A typical laser setup is described as follows. The light source for SRG inscription is a Ar⁺ laser that emits a beam (also called *writing beam*) with $\lambda = 514.5$ nm wavelength. The laser beam is linearly polarized by L1 and L2 lens and D diaphragm regulates the radius beam. As SRG inscription needs interference, the laser beam is split in two equal beams by BS beam splitter, then each beam is reflected by M1 and M2 mirrors to meet on the film surface. Position of M1 and M2 mirrors can be modified in order to control the angle between the two interfering beams. A second light source, He-Ne laser is used to monitor the SRG inscription by sending a laser beam (also called *reading beam*) of $\lambda = 632.8$ nm wavelength and on the film surface close to the normal incidence (it is not coplanar with the writing beams).

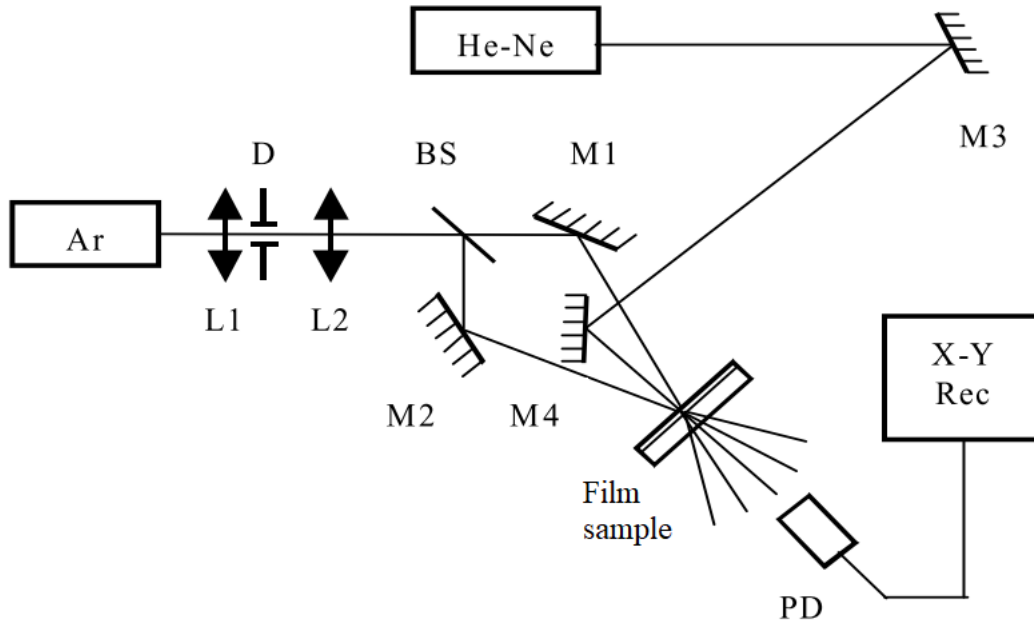


Figure I.13. Experimental setup for laser irradiation (Petrís and Vlad, 2001).

Research in the field explored not only continuous wave, but also pulse irradiation (≤ 7 ns pulse duration) (Baldus *et al.*, 2001; Damian *et al.*, 2014, 2016; Sava *et al.*, 2016) and shows that the irradiation regime plays an important role in the obtaining process of SRG. Experiments reveal that the surface relief peaks can also appear on the illuminated regions, not only in the dark areas, like for the continuous laser. In addition, the formation of SRG takes less time to complete (in some cases just one 5 ns pulse) than when continuous wave irradiation is used. This finding along with the different SRG stabilities obtained by the two methods, indicate that different mechanisms are to be held responsible.

I.7.2. Formation of surface relief gratings (SRG)

Formation of SRG is usually evaluated by characterizing the surface profile, grating features (amplitude and period), and the dynamics of inscribing process. The topographic morphology is commonly analyzed by AFM technique or, with its inherent drawbacks, classical microscopy. The evolution of the relief formation is evaluated through diffraction efficiency. Without a specific system that couples AFM with the laser setup (Yadavalli and Santer, 2013), live investigation of the topography is not possible, thus AFM investigate the samples post irradiation. Along with the writing (that inscribes the SRG) beams, there is also

a reading beam (usually He–Ne laser at 633 nm), whose diffraction power is registered during the whole process. Consequently, with the proper software, diffraction efficiency, expressed as the ratio between the non-diffracted power (initially transmitted power) and the 1st order of diffraction power, can be quantified during the sample irradiation. Although live monitoring of diffraction efficiency offers information about the formation process of surface gratings, the method is somewhat inscrutable because the diffraction reflects more processes that can take place into the material, besides the surface grating, like the polarization grating. Thus, pairing the AFM or microscopy with the lasers is the optimum setup. However, for some materials that have been characterized before, connections can be made between surface topography and diffraction efficiency and results can be extrapolated.

Irradiation of azobenzene containing materials leads to a phase grating. In a uniformly optic azopolymeric film with variations in the surface profile, a transmission phase grating appears. The temporal evolution of phase modulation depends on the temporal dependence of intensities of diffraction orders. Depending on the grating thickness, there are more diffraction regimes. These are ordained by the phase correlation between the diffraction orders, the Q parameter of Klein and Cook, and the amplitude $\Delta\Phi$ of phase correlation. The most used criterion to describe the different diffraction behaviors is the Q parameter, which is defined through a normalized expression to express the grating thickness. In an ideal case, the Raman – Nath formalism describes the behavior of thin gratings, where $Q \ll 1$ and $Q\Delta\Phi \ll 1$. Practically, it was observed that for $Q < 0.5$ and $Q\Delta\Phi \leq 1$, the regime's expression can be used to calculate the diffraction orders intensities with good accuracy. *Equation I.11.* expresses the intensity of 1th diffraction order according to Raman – Nath formula.

$$I_l = TI_R J_l^R(\Delta\Phi)$$

Equation I.11.

where l is the number of diffraction order, I_R is the light beam intensity, T is the sample's transmittance, and $J_l(\Delta\Phi)$ is the first kind Bessel function of 1th diffraction order of the light beam with $(\Delta\Phi)$ argument (Petrís and Vlad, 2001).

Depending on the profile of the surface grating, the diffraction orders have different efficiencies. The ideal blaze has 40.5 % 1st order efficiency, and the rest of the intensities is divided to the rest of diffraction orders. Consequently, the linear binary grating

(approximation of sinusoidal profile), has twice the efficiency in 1st order, meaning 81 % (O'Shea *et al.*, 2009).

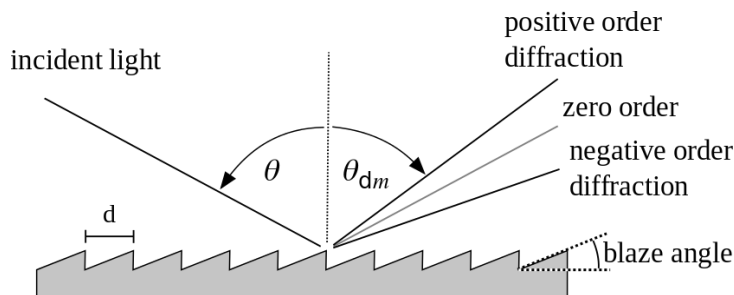


Figure.I.14. Light diffraction on an ideal blaze profile (https://commons.wikimedia.org/wiki/File:Diffraction_from_a_blazed_grating.svg).

The diffraction efficiency η_D is defined by the rate between the diffracted intensity and the initial intensity (transmitted through the sample prior irradiation, which equals the non-diffracted light, 0th order diffraction) . According to this expression, the 1st order efficiency in Raman – Nath regime is described by the following formula:

$$\eta_D = I_1 / T I_R$$

Equation I.12.

where I_1 is the 1st order diffraction intensity.

The polarization grating process is enabled by the orthogonal orientation of the azo moieties with regard to the polarization plane of the incident light beam. Photoinduced dichroism and birefringence cause local optical anisotropy, tracking the interference pattern of the two polarized light beams. Following the photo orientation of azobenzenes, a correlated motion of the polymer chains takes place, also in according to the light interference pattern. While the illuminated areas of the azopolymer surface are depleted in material, the dark regions are filled, thus the topography of the surface grating is characterized by a sinusoidal profile. The photoinduced orientation process and the mass transport from bright to dark regions effect two superimposed gratings: the polarization grating (also called birefringence grating) and the surface relief grating (SRG) respectively (Laguné Labarhet, Buffeteau and Sourisscau, 1998; Wang, 2017c). Research on this subject (Laguné Labarhet, Buffeteau and Sourisscau, 1998) shows that the two processes have different

contribution proportions for different azopolymers. In addition, the paper provides a Jones's formalism to calculate the diffraction intensities corresponding to the two gratings.

I.8. Molecular dynamics

Molecular dynamics combines theoretical methods and computational techniques to study molecules and molecular systems at the atomic level. The most used methods for studying molecular systems are the molecular mechanics ones, which are grounded on the laws of classical mechanics for minimizing potential energy. Energy minimization is useful for refining the structure that is being studied, especially for finding the optimal conformation of a molecule (Lewars, 2003; Piela, 2007).

Once the energy terms were established and the structure was minimized, the system can then be subjected to a molecular dynamics simulation. At the core of this simulation are the classical Newtonian equations for motion, which are modified, if required, for simulating the effects that temperature and pressure can have on the system. The main result of a molecular dynamics simulation run is a trajectory file which records atomic configuration, atomic velocities, and other parameters, outlined in sequential time steps that can be subsequently analyzed. Usually, the system is simulated under high-temperature conditions, for facilitating molecular collisions, which can increase the reaction time and can sustain the whole simulation within an acceptable timeframe (Catlow, 2005; Clementi, 2005).

The movement of the atoms is essential to the understanding of many physical processes that take place within materials. Molecular dynamics implies thus applying Newton's laws of motion to all the atoms in the system; the movement constantly being correlated with the potential energy of the system. The first step performed is establishing the initial configuration, that can be obtained from experimental results (NMR spectroscopy or X-ray crystallography), from a theoretical model (modeling), or a combination of both. The system has to be at least partially minimized to eliminate exaggerated interactions or distortions, which can appear when generating the initial configuration. Usually, setting the initial velocity values is performed statistically, in concordance with the imposed temperature. The velocity values are then corrected, such that the total momentum value to be zero (Ciccotti, Kapral and Sergi, 2005; Leach and Gillet, 2007).

$$P = \sum_{i=1}^N m_i v_i = 0$$

Equation I.13.

where m_i is the mass of atom i and N is the number of atoms. The v_i velocities are chosen from the Maxwell-Boltzmann or Gauss distributions, which give the probability of an atom i to have the velocity v_x in the direction x at a temperature T .

$$p(v_{ix}) = \left(\frac{m_i}{2\pi k_B T} \right)^{\frac{1}{2}} \exp \left[-\frac{1}{2} \frac{m_i v_{ix}^2}{k_B T} \right]$$

Equation I.14.

The temperature can be computed from the velocity values using the following relationship:

$$T = \frac{1}{3N} \sum_{i=1}^N \frac{|p_i|^2}{2m_i}$$

Equation I.15.

After attributing the system of coordinates, the second law of Newton, or the law of motion, is applied.

$$F_i(t) = m_i a_i(t)$$

Equation I.16.

where F_i represents the force that acts on the atom i at time t , a_i is the acceleration of atom i .

The atoms interact between themselves through chemical and physical bonds. The system is given a specific potential energy value. The force can be expressed as a gradient of the potential energy.

$$F_i = -\nabla_i V = -\frac{dE_p}{dr_i(t)}$$

Equation I.17.

where E_p is the potential energy of the system.

Combining the two equations, we obtain:

$$a_i(t) = -\frac{1}{m_i} \frac{dE_p}{dr_i(t)}$$

Equation I.18.

where r_i is the position of atom i .

Thus, for computing the trajectory, the following are required: the initial positions of the atoms, the initial distribution of the velocity and acceleration, which is determined as the gradient of potential energy's function (Keffer, 2002; Guedes, 2015).

The classical equation of motion is deterministic, meaning that the positions and velocities at time $t = 0$ determine the positions and velocities at any given time t . As such, the successive configurations of the system will be established by integrating the classical law of motion. The result of a full dynamics run is a *trajectory* that specifies the ways in which the atom's position and velocities change over time. Trajectories are responsive to the initial conditions. The regular method for numerically solving common differential equations is the finite-difference method. The underlying idea can be comprised in the following statement. Given the initial velocities and coordinates along with supplementary dynamic information at time t , the velocities and positions at time $t+\Delta t$ are computed. The time step Δt is dependent on both the system itself as well as the integration method (J.M.HAILE, 1992; Allen, 2004; Kapral and Ciccotti, 2005; Tsolou, Harmandaris and Mavrantzas, 2008).

Even though initial coordinates draw values from the input file (or a prior operation like minimization), the initial velocities are generated randomly at the start of a dynamics run, in accordance with the targeted temperature. As such, dynamics runs cannot be repeated in a complete manner, excluding force field engines that permit you to set the random number seed to the value that was utilized in a subsequent run (Hermans, Mark and Skeel, 1997; Michel Le Bellac, Fabrice Mortessagne, 2004; Schlick, 2010; González, 2011).

Molecular dynamics is regularly applied to models of large sizes. Evaluating the energy is time-consuming, and the memory resources required are significant. For correctness of statistical ensembles, the conservation of energy is of crucial importance (Macpherson, Borg and Reese, 2007; Anderson, Lorenz and Travesset, 2008; Tsolou, Harmandaris and Mavrantzas, 2008; Chang *et al.*, 2010).

Thus, the fundamental criteria for an efficient integrator in molecular simulations are the following:

- Optimized, fast run-time (ideally, one energy evaluation per time step);
- Low memory requirements;
- Possibility to use relatively long time steps;
- Energy conservation.

All integration algorithms imply that the speeds, velocities, and positions can be approximated as a Taylor series (Frenkel, Daan; Smith, 2008; Cavagna, 2009).

Molecular dynamics is a computational simulation method that can be used for analyzing the evolution of molecular systems over time and enables the prediction of static and dynamic properties of the simulated systems taking into account the various ways the molecules can interact (Gupta *et al.*, 1996; Somer, 2004; Kobayashi and Yamamoto, 2011). Molecular dynamics is also used for studying non-equilibrium processes and is an efficient instrument for structure optimization, overstepping the local minima of energies (a technique called simulated annealing) (Hedman, 2006; Piela, 2007).

The molecular dynamics method was first introduced by Alder and Wainwright, at the end of the 50s ('57, '59), and was initially used for studying the interactions of hard spheres. From their research, important characteristics related to the behavior of simple liquids have been obtained. Another historically important step was realized in 1964, when Rahman first simulated the behavior of liquid argon. The first protein simulation was first done in 1977 and used 500 atoms of the Bovine Pancreatic Trypsin Inhibitor protein, under a simulation time of $9.2 \text{ ps} = 0.00092 \text{ ns}$, using CHARMM's precursor. Presently, most of the simulations are usually done with solvated proteins, protein-DNA complexes, lipidic systems, enzymatic reactions, etc. The number of simulation techniques has grown considerably over the years, such as that in the present, there are multiple specialized techniques fine-tuned for particular problem spaces, including simulations that combine classical and quantum mechanics (Hermans, Mark and Skeel, 1997; Jensen F., 1999; Rapaport, 2004; Somer, 2004; Gupta, Tiwari and Yadav, 2012; Meunier, 2012).

The following are some relevant areas of interests where molecular dynamics bring important contributions:

- Liquids – using non-equilibrium techniques, transport phenomena, such as viscosity;
- Structural defects - point defects (vacancies, interstitial) linear defects, planar defects (packing defects);
- Surfaces – surface diffusion, important for understanding phenomena such as surface construction;
- Shear, adhesion, cohesion – studies have been extended from macro levels to microscopic characterizations done through MD modeling;
- Clusters – conglomerates of atoms - a bridge between molecular systems and solids; often, a number of different configurations have similar energies which increases the difficulty of determining stable structures.;
- Biomolecules – MD enables analysis of the dynamics of macromolecules, such as proteins, nucleic acids (ADN, ARN), and membranes;
- Electronic properties – the development of Car-Parrinello method, in which the atomic forces are obtained from solving the electronic structure rather than from the inter-atomic potential, enables the study of electronic properties (Kapral and Ciccotti, 2005).

Simulating complex systems (ex: solvated proteins) is done for run times higher than nanoseconds range; the reports being made are at the order of milliseconds. Simulations for long-running processes (around the order of 1 microsecond) are extremely costly, because they require the calculation of a very high number of steps in time. In these cases, the approach for solving these problems is to use simplified, reduced representations, which are called coarse-grained models. These models reunite atoms on criteria like functional groups and treat them like one pseudo-atom (they are used in simulations for proteins, lipids, nucleic acids, and biological membranes). The polar hydrogen atoms are normally kept in the system, because the treatment itself of the hydrogen bonds requires a reasonable accuracy for describing the direction and electrostatic interactions between the donor and acceptor groups. A hydroxyl group, for example, can be both donor and an acceptor of hydrogen a fact that makes it impossible to consider it as a single O-H pseudo-atom. One thing to be noted is that usually approx. half of the atoms of a molecule are nonpolar hydrogen atoms, so using the coarse-grained mode allows saving substantial computing time.

Compared to the Monte-Carlo method, molecular dynamics is a deterministic technique, meaning that, given an initial set of positions and velocities, the evolution in time is entirely determined. The atoms move, colliding with each other, float (if the system is fluid), oscillate in concerted waves with their neighbors, etc., similarly to how atoms behave within a real substance (Allen, 2004).

I.8.1. Thermodynamics

The integration of Newton's equations for motion allows exploring the constant energy surface of the system. Even so, most of the natural phenomena occur within conditions where the system is exposed to external pressures and / or heat exchanges with the surrounding environment. In these situations, the total energy of the system cannot be conserved, and extended forms of molecular dynamics are required.

Molecular dynamics simulations generate information pertaining to the microscopic level, including positions and velocities of atoms. Converting this information from the microscopic level to observable macroscopic properties like pressure, energy, caloric capacity, etc., requires the use of mechanical statistics.

Through molecular dynamics simulations, thermodynamic properties, and/or time-dependent (kinetic) phenomena can be studied. To connect the macroscopic and the microscopic systems, time-independent statistical averages are used (Frenkel, Daan; Smith, 2008).

I.8.1.1. Temperature and control methods

The temperature is computed according to the equipartition principle: each freedom degree in the system is attributed to a kinetic energy.

$$E_c = 3Nk_B T / 2$$

Equation I.19.

$$E_c = E(m_i v_i^2(t)) / 2$$

Equation I.20.

Thermostats are normally used for simulating interactions of vibrational modes in a macroscale system at the atomic level. A well-judged choice of a thermostat depends on the system and the properties that are of interest. Whereas some thermostats compare the

system's temperature and adjust the speed of the particles, other couple the movement of each particle with the vibrational modes of the heat bath. In systems coupled to infinite thermostats, any temperature variation is absorbed by the thermostat in such manner that the mean temperature of the system constant.

Even though the initial velocities are produced such that a Maxwell-Boltzmann distribution is generated at the desired temperature, the distribution is not constant during the simulation run. This is particularly true when the system does not start from a structure with minimum-energy configuration. This is a common situation, since structures are regularly minimized just to rule out eventual hot spots.

Throughout dynamics runs, exchanges between potential energy and kinetic energy, cause differences in temperature. To keep the temperature at constant value, computed velocities require proper adjustment. Additionally, to maintain the desired temperature, the right statistical ensemble must be generated through the temperature-control mechanism. This implies that the probability of a specific configuration to occur is subjected to the laws of statistical mechanics. As an example, in canonical ensemble, $P(E)$ (i.e., the probability of a configuration with energy E to occur) needs to be proportional to $\exp(-E/k_B T)$, the Boltzmann factor.

Post-equilibration, a milder thermal energy exchange between system and heat bath can be implemented with the Berendsen method, where each velocity is multiplied by the factor λ .

$$\lambda = \sqrt{1 - \frac{\Delta t}{\tau} \left(\frac{T_{instan} - T_0}{T_{instan}} \right)}$$

Equation I.21.

where τ is a characteristic relaxation time, Δt represents the size of the time step, T_{instan} is the instantaneous temperature, and T_0 represents the target temperature.

This treatment provides a constant-temperature ensemble, which can be controlled by both by modifying the relaxation time τ (usually between 0.1 - 0.4 ps) and by adjusting the target temperature T_0 , to a good approximation.

The thermodynamic state of a system is typically defined as a small set of parameters, for example, the temperature T , the pressure P , and the number of particles, N . Other thermodynamic properties can be derived from the thermodynamic equations of state.

The mechanical or microscopic state of a system is defined by the atomic positions \mathbf{r} and the momentum \mathbf{p} . These can be considered coordinates in a multidimensional space, called *phase space*. For a system with N particles, this space has $6N$ dimensions. A single point, noted with Γ , describes the state of a system.

An ensemble is a collection of all the possible systems that have different microscopic states but also have identical macroscopic states or thermodynamics. There are different ensembles that have different characteristics:

- Constant temperature, constant pressure (NPT);
- Constant energy, constant volume (NVE);
- Constant pressure, constant enthalpy (NPH);
- Constant temperature, constant volume (NVT).

Multiple methods are available for the control of temperature and pressure. Depending on the state variables that are fixed (energy E , enthalpy H – meaning $E + PV$ -, the number of particles N , the pressure P , stress S , temperature T , and volume V), different statistical ensembles can be generated. A variety of structural, energetic, and dynamic properties can then be computed from the mean values of the fluctuations of these quantities for the generated ensemble (Hedman, 2006; Frenkel, Daan; Smith, 2008; Harrison, 2012).

I.8.1.2. NVT Ensemble

The NVT ensemble, also known as the canonical ensemble, is obtained from the thermodynamic control of temperature. The thermodynamic state is characterized by a constant number of atoms, volume $V = \text{const}$, temperature $T = \text{const}$.

This ensemble is appropriate for simulating models in a void, without periodic conditions of simulation. Without this constraint, volume, density, and pressure are not defined, and the constant-pressure dynamics cannot be carried out. When systems with periodic boundaries conditions are simulated, and the pressure is not considered a significant factor, the NVT ensemble has the advantage of a minimal disturbance of the trajectory due to the lack of coupling to the pressure bath (Rapaport, 1999).

I.8.2. Parameters evaluated in molecular dynamics

A molecular dynamics calculation involves the existence of three phases: heating, equilibrium, data collection. Initially, the system is considered to be at absolute zero temperature. In consequence, in the first phase, we need to increase the temperature of the system to the value we want the simulation to be executed at. The heating process will cause an increase in the system's kinetic energy. Depending on the simulation's purpose, the heat process can be done fast or gradually. If the process is too fast, the constant temperature required for the equilibrium phase cannot be reached. If the system is of large size, equilibrium is slowly attained.

The main problem of molecular dynamics derives from the fact that the total simulation time, even using massive parallel computing systems, cannot breach the value of 1000-20000 ps. This is often the reason why the time spent in the equilibrium phase might not be enough to reach complete relaxation.

Following the molecular dynamics calculations, several parameters are evaluated, such as mean square displacement MSD , diffusion coefficient D , radial distribution function $g(r)$, alpha relaxation $\alpha_2(R, \tau_p, t)$ and alpha relaxation time τ_p .

Molecules moving through a medium, encounter other molecules in their path that results in collisions between them. This events force molecules to change their moving direction, so the molecules do not follow a rectilinear trajectory. Although the motion is uncoordinated, a molecule does not remain around its initial position an indefinite time. Generally speaking, the motion of a particle inside a liquid is considered to be like the moving of a pedestrian random walk. From mathematical perspective, the Markovian process explain this walk is a series of consecutive steps, each in a different direction, completely random, and in a different direction than the previous one. Considering a unidimensional space, a right line, the particle's motion is a step frontwards (+) or backwards (-) with equal probability to occur. In conclusion, the shift distance of a particle is almost equal to zero. However, adding the square of the shift distance in each step, a sum of the squared roots of the displacements is obtained (Tsolou, Harmandaris and Mavrantzas, 2008; Chen *et al.*, 2012).

The mean square displacement is a measure of the mean distance a molecule shifts in a given medium and is defined by the following relation (*Equation I.22*)

$$MSD = \langle r(t) \rangle = \langle \Delta r_i(t)^2 \rangle = \langle (r_i(t) - r_i(0))^2 \rangle$$

Equation I.22.

where $r_i(t)-r_i(0)$ is the distance vector of a path distance of molecule i in a time interval t . the angular parentheses represent the fact that the parameter is averaged over all molecules in the system. MSD gives information about the diffusion of molecules in the system. In a solid medium, the kinetic energy is not sufficient to enable diffusion. But if the system is fluid, diffusion increases linearly with time and the phenomena can be investigated through the MSD slope, which represents the diffusion coefficient, D and is expressed through the following equation.

$$D = \lim_{t \rightarrow \infty} \frac{1}{6t} \langle r^2(t) \rangle$$

Equation I.23.

The molecular diffusion describes the scattering, the distribution of molecules in the system through random moves. The diffusion coefficient characterizes the rate of components diffusing in a mixture, measuring the area covered by a molecule in the time unit. Einstein analyzed the random trajectory of particles in a system in the frame of Brownian motion and conceded that the average's distance square of the particle's movement in its random trajectory is equal to the time used (*Equation I.24*)

$$\langle r^2(t) \rangle = 6D + C$$

Equation I.24.

where C is a constant.

The Einstein-Smoluchowski equation (*Equation II.*) for diffusion coefficient shows the importance of some characteristics, such as the system's viscosity, form and dimension of particles, comprised in the friction coefficient ξ .

$$D = \frac{kT}{\xi}$$

Equation I.25.

where T is the temperature in Kelvin and k is the rate constant.

The above presented parameters represent just a small part of the parameters that can be evaluated in molecular dynamics. The resulting files from a calculation run can be

processed to obtain a variety of functions, depending on the followed objective (Hoover and Hoover, 2005; Frenkel, Daan; Smith, 2008).

I.9. Bibliography

- Accary, J. B. and Teboul, V. (2013) 'How does the isomerization rate affect the photoisomerization-induced transport properties of a doped molecular glass-former?', *Journal of Chemical Physics*, 139(3). doi: 10.1063/1.4813410.
- Aleksejeva, J. *et al.* (2011) 'Photoinduced birefringence in azo-dye doped polyurethane', *Latvian Journal of Physics and Technical Sciences*, 48(4), pp. 5–14. doi: 10.2478/v10047-011-0022-9.
- Allen, M. (2004) 'Introduction to molecular dynamics simulation', *Computational Soft Matter: From Synthetic Polymers to ...*, 23(2), pp. 1–28. doi: 10.1016/j.cplett.2006.06.020.
- Anderson, J. A., Lorenz, C. D. and Travesset, A. (2008) 'General purpose molecular dynamics simulations fully implemented on graphics processing units', *Journal of Computational Physics*, 227(10), pp. 5342–5359. doi: 10.1016/j.jcp.2008.01.047.
- Baac, H. *et al.* (2004) 'Submicron-scale topographical control of cell growth using holographic surface relief grating', *Materials Science and Engineering C*, 24(1–2), pp. 209–212. doi: 10.1016/j.msec.2003.09.009.
- Bai, S. and Zhao, Y. (2001) 'Azobenzene-containing thermoplastic elastomers: Coupling mechanical and optical effects', *Macromolecules*, 34(26), pp. 9032–9038. doi: 10.1021/ma011299o.
- Baldus, O. *et al.* (2001) 'Surface relief gratings generated by pulsed holography: A simple way to polymer nanostructures without isomerizing side-chains', *Journal of Chemical Physics*, 114(3), pp. 1344–1349. doi: 10.1063/1.1332789.
- Bandara, H. M. D. and Burdette, S. C. (2012) 'Photoisomerization in different classes of azobenzene', *Chemical Society Reviews*, 41(5), pp. 1809–1825. doi: 10.1039/c1cs15179g.
- Barille, R. *et al.* (2006) 'Neuron growth engineering on a photoinduced surface relief grating: a tool for plastic neuroelectronics', *Biophotonics and New Therapy Frontiers*, 6191(2006), p. 61911Q. doi: 10.1117/12.663527.
- Barillé, R. *et al.* (2011) 'Photo-responsive polymer with erasable and reconfigurable micro- and nano-patterns: An in vitro study for neuron guidance', *Colloids and Surfaces B: Biointerfaces*, 88(1), pp. 63–71. doi: 10.1016/j.colsurfb.2011.06.005.
- Barrett, C. J., Natansohn, A. L. and Rochon, P. L. (1996) 'Mechanism of Optically Inscribed High-Efficiency Diffraction Gratings in Azo Polymer Films', *The Journal of Physical Chemistry*, 100(21), pp. 8836–8842. doi: 10.1021/jp953300p.
- Barrett, C. J., Rochon, P. L. and Natansohn, A. L. (1998) 'Model of laser-driven mass transport in thin films of dye-functionalized polymers', *Journal of Chemical Physics*, 109(4), pp. 1505–1516. doi: 10.1063/1.476701.
- Bian, S. *et al.* (1999) 'Photoinduced surface deformations on azobenzene polymer films', *Journal of Applied Physics*, 86(8), p. 4498. doi: 10.1063/1.371393.

- Burke, S. E. and Barrett, C. J. (2004) ‘Controlling the physicochemical properties of weak polyelectrolyte multilayer films through acid/base equilibria’, *Pure and Applied Chemistry*, 76(7–8), pp. 1387–1398. doi: 10.1351/pac200476071387.
- Cao, H. Z. *et al.* (2008) ‘Azo polymers with electronical push and pull structures prepared via RAFT polymerization and its photoinduced birefringence behavior’, *Express Polymer Letters*, 2(8), pp. 589–601. doi: 10.3144/expresspolymlett.2008.71.
- Catlow, C. R. A. (2005) ‘ENERGY MINIMIZATION TECHNIQUES IN MATERIALS MODELING’, pp. 547–564.
- Cattaneo, P. and Persico, M. (1999) ‘An ab initio study of the photochemistry of azobenzene’, *Physical Chemistry Chemical Physics*, 1(20), pp. 4739–4743. doi: 10.1039/a905055h.
- Cavagna, A. (2009) ‘Supercooled liquids for pedestrians’, *Physics Reports*, 476(4–6), pp. 51–124. doi: 10.1016/j.physrep.2009.03.003.
- Cembran, A. *et al.* (2004) ‘On the Mechanism of the cis-trans Isomerization in the Lowest Electronic States of Azobenzene: S0, S1, and T1’, *Journal of the American Chemical Society*, 126(10), pp. 3234–3243. doi: 10.1021/ja038327y.
- Chang, K.-S. *et al.* (2010) ‘A molecular dynamics simulation of a homogeneous organic-inorganic hybrid silica membrane.’, *Chemical communications (Cambridge, England)*, 46(48), pp. 9140–9142. doi: 10.1039/c0cc02531c.
- Chen, X. *et al.* (2012) ‘Molecular modeling of temperature dependence of solubility parameters for amorphous polymers’, *Journal of Molecular Modeling*, 18(6), pp. 2333–2341. doi: 10.1007/s00894-011-1249-3.
- Ciccotti, G., Kapral, R. and Sergi, A. (2005) ‘Methods and Models’, in *Handbook of Materials Modeling*, pp. 1–17.
- Clementi, E. (2005) ‘Computational chemistry : attempting to simulate large molecular systems’, in *Theory and Applications of Computational Chemistry: The First Forty Years*, pp. 89–111.
- Cojocariu, C. and Rochon, P. (2004) ‘Light-induced motions in azobenzene- containing polymers’, *Pure Applied Chemistry*, 76(7–8), pp. 1479–1497. doi: 10.1351/pac200476071479.
- Damian, V. *et al.* (2014) ‘Surface relief gratings induced by pulsed laser irradiation in low glass-transition temperature azopolysiloxanes’, *Journal of Applied Polymer Science*, 131(24). doi: 10.1002/app.41015.
- Damian, V. *et al.* (2016) ‘Optical analyses of pulsed interferometric patterning of azopolysiloxanes’, in *PROCEEDINGS OF SPIE - THE INTERNATIONAL SOCIETY FOR OPTICAL ENGINEERING*. doi: 10.1117/12.966848.
- Deng, G. and Chen, Y. (2004) ‘A Novel Way To Synthesize Star Polymers in One Pot by

ATRP of N - [2- (2-Bromoisobutyryloxy) ethyl] maleimide and Styrene', pp. 18–26.

Deshmukh, S., Bromberg, L. and Hatton, T. A. (2006) 'Photo- and Thermoinduced Sol-Gel Transitions in Blends of Azobenzene Copolymers and Pluronic Surfactants'. Available at: <http://18.7.29.232/handle/1721.1/30390>.

Dokić, J. *et al.* (2009) 'Quantum chemical investigation of thermal cis-to-trans isomerization of azobenzene derivatives: substituent effects, solvent effects, and comparison to experimental data', *Journal of Physical Chemistry A*, 113(24), pp. 6763–6773. doi: 10.1021/jp9021344.

Ene, R. *et al.* (2008) 'The capacity of nucleobases containing azo-polysiloxanes to generate a surface relief grating', 10(3), pp. 541–544.

Enea, R. *et al.* (2008) 'Photo-sensible (thymine containing) azo-polysiloxanes: Synthesis and light induced effects', *Journal of Physics: Conference Series*, 100(1), pp. 11–15. doi: 10.1088/1742-6596/100/1/012022.

Fahmy, T., Ha, H. R. and Ahmed, M. T. (2002) 'Structural and relaxation aspects in azodye-doped ABS films: TDSC study', *International Journal of Polymeric Materials*, 51(10), pp. 875–889. doi: 10.1080/00914030290046408.

Frenkel, Daan; Smith, B. (2008) 'Understanding Molecular Simulations.pdf'.

González, M. A. (2011) 'Force fields and molecular dynamics simulations', *EDP Sciences*, 12, pp. 169–200.

Guedes, R. (2015) 'Molecular Dynamics', *Aula de Modelação Molecular, MQFT*, (Md). doi: 10.1007/978-3-319-16375-8.

Gupta, R., Tiwari, A. and Yadav, M. (2012) 'Molecular Dynamics : Basic Study', *International Journal*, 4(1), pp. 245–248. doi: 10.9735/0975-3087.4.1.245-248.

Gupta, S. a *et al.* (1996) 'A Nonequilibrium Molecular Dynamics Study of the Rheology of Alkanes I Introduction', pp. 1–9.

Harrison, C. (2012) *Computational chemistry: Crowd-based enhancement of chemical diversity*, *Nature Reviews Drug Discovery*. doi: 10.1038/nrd3646.

He, Y., Wang, X. and Zhou, Q. (2002) 'Epoxy-based azo polymers : synthesis , characterization and photoinduced surface-relief-gratings', 43, pp. 7325–7333.

Hedman, F. (2006) *Algorithms for Molecular Dynamics Simulations*, *Biopolymers*. doi: 10.1080/00268979100100101.

Hermans, P., Mark, B. and Skeel, S. (1997) *Computational Molecular Dynamics: Challenges, Methods, Ideas, Wriggers.Biomachina.Org*. doi: 10.1007/978-3-642-58360-5.

Hoover, W. G. and Hoover, C. G. (2005) 'Nonequilibrium molecular dynamics', *Condensed Matter Physics*, 8(2), pp. 247–260.

- Hubert, C. *et al.* (2007) 'Spontaneous photoinduced patterning of azo-dye polymer films: the facts', *Journal of the Optical Society of America B*, 24(8), p. 1839. doi: 10.1364/JOSAB.24.001839.
- Hurduc, N., Macovei, A., Paius, C., Raicu, A., *et al.* (2013a) 'Azo-polysiloxanes as new supports for cell cultures', *Materials Science and Engineering C*, 33(4), pp. 2440–2445. doi: 10.1016/j.msec.2013.01.012.
- Hurduc, N., Macovei, A., Paius, C., Raicu, A., *et al.* (2013b) 'Azo-polysiloxanes as new supports for cell cultures', *Materials Science and Engineering C*. Elsevier B.V., 33(4), pp. 2440–2445. doi: 10.1016/j.msec.2013.01.012.
- Hurduc, N., Macovei, A., Paius, C., Ibanescu, C., *et al.* (2013) 'DIRECT OBSERVATION OF ATHERMAL PHOTOFLUIDISATION IN AZO-POLYMER FILMS', *Journal of Materials Chemistry*, 2(2), p. 303. doi: 10.1039/x0xx00000x.
- Hvilsted, S. *et al.* (1998) 'Azobenzene side-chain liquid crystalline polyesters with outstanding optical storage properties', *Turkish Journal of Chemistry*, 22(1), pp. 33–45.
- Hwang, U. J. *et al.* (2005) 'Photoinduced birefringence in an azo polymer film', *Journal of the Korean Physical Society*, 46(SUPPL. II), pp. 218–223.
- Ishitobi, H. *et al.* (2007) 'The anisotropic nanomovement of azo-polymers.', *Optics express*, 15(2), pp. 652–659. doi: 10.1364/OE.15.000652.
- J.M.HAILE (1992) 'Molecular dynamics simulation, elementary methods', *Journal of Molecular Structure: THEOCHEM*, pp. 287–288. doi: 10.1016/0166-1280(93)87060-Q.
- Jankova, K., Bednarek, M. and Hvilsted, S. (2005) 'Star Polymers by ATRP of Styrene and Acrylates Employing Multifunctional Initiators', pp. 3748–3759. doi: 10.1002/pola.20834.
- Jensen F. (1999) 'An Introduction to Computational Chemistry'.
- Kapral, R. and Ciccotti, G. (2005) 'Molecular dynamics : an account of its evolution', in *Theory and Applications of Computational Chemistry: The First Forty Years*, pp. 425–441.
- Kazmierski, K. *et al.* (2004) 'Polysiloxanes with chlorobenzyl groups as precursors of new organic-silicone materials', *Journal of Polymer Science, Part A: Polymer Chemistry*, 42(7), pp. 1682–1692. doi: 10.1002/pola.11066.
- Keffer, D. (2002) *The working person's guide to MD simulations*.
- Kim, D. Y. *et al.* (1995) 'Laser-induced holographic surface relief gratings on nonlinear optical polymer films', *Applied Physics Letters*, 66(10), pp. 1166–1168. doi: 10.1063/1.113845.
- Kim, M. J., Kumar, J. and Kim, D. Y. (2003) 'Photofabrication of superhelix-like patterns on azobenzene polymer films', *Advanced Materials*, 15(23), pp. 2005–2008. doi: 10.1002/adma.200305682.
- Kobayashi, H. and Yamamoto, R. (2011) 'Implementation of Lees-Edwards periodic

boundary conditions for direct numerical simulations of particle dispersions under shear flow', *Journal of Chemical Physics*, 134(6). doi: 10.1063/1.3537974.

Kobayashi, T., Saito, T. and Adachi, S. (2003) 'Sub-5-fs real-time spectroscopy of several molecular systems', *Journal of Luminescence*, 102–103(SPEC), pp. 722–726. doi: 10.1016/S0022-2313(02)00631-2.

Kulikovska, O. *et al.* (2008) 'Smart ionic sol-gel-based azobenzene materials for optical generation of microstructures', *Chemistry of Materials*, 20(10), pp. 3528–3534. doi: 10.1021/cm800106x.

Kumar, J. *et al.* (1998) 'Gradient force: The mechanism for surface relief grating formation in azobenzene functionalized polymers', *Applied Physics Letters*, 72(17), pp. 2096–2098. doi: 10.1063/1.121287.

Kurita, N., Ikegami, T. and Ishikawa, Y. (2002) 'Ab initio study of the minimum-energy structure of trans-azobenzene', *Chemical Physics Letters*, 360(3–4), pp. 349–354. doi: 10.1016/S0009-2614(02)00854-0.

Lagugné Labarhet, F., Buffeteau, T. and Sourisscau, C. (1998) 'Analyses of the diffraction efficiencies, birefringence, and surface relief gratings on azobenzene-containing polymer films', *Journal of Physical Chemistry B*, 102(15), pp. 2654–2662. doi: 10.1021/jp980050e.

Leach, A. R. and Gillet, V. J. (2007) *An introduction to Chemoinformatics*.

Lee, J. K. *et al.* (2004) 'The topographical guidance of neurons cultured on holographic photo-responsive polymer', *Annual International Conference of the IEEE Engineering in Medicine and Biology - Proceedings*. IEEE, 26 VII, pp. 4970–4973. doi: 10.1109/iembs.2004.1404374.

Lee, J. K. *et al.* (2005) 'Spatial patterning of fibroblast cells with fabricating holographic patterning on the photoresponsive polymer', *Annual International Conference of the IEEE Engineering in Medicine and Biology - Proceedings*. IEEE, 7 VOLS, pp. 4107–4110. doi: 10.1109/iembs.2005.1615366.

Lefin, P. and Fiorini, C. (1998) 'Anisotropy of the photoinduced translation diffusion of azo-dyes', 9(January), pp. 323–328.

Lefin, P., Fiorini, C. and Nunzi, J.-M. (1998) 'Anisotropy of the photo-induced translation diffusion of azobenzene dyes in polymer matrices', *Pure and Applied Optics: Journal of the European Optical Society Part A*, 7(1), pp. 71–82. doi: 10.1088/0963-9659/7/1/011.

Lewars, E. (2003) 'Computational Chemistry'.

Li Cui, Y. Z. (2003) 'Synthesis of azobenzene-containing diblock copolymers using atom transfer radical polymerization and the photoalignment behavior', *Macromolecules*, pp. 8246–8252.

Liu, J., He, Y. and Wang, X. (2010) 'Influence of chromophoric electron-withdrawing groups on photoinduced deformation of azo polymer colloids', *Polymer*. Elsevier Ltd,

51(13), pp. 2879–2886. doi: 10.1016/j.polymer.2010.04.048.

Luca, A. R. *et al.* (2014) ‘Mass transport in low Tg azo-polymers: Effect on the surface relief grating induction and stability of additional side chain groups able to generate physical interactions’, *Applied Surface Science*, 290, pp. 172–179. doi: 10.1016/j.apsusc.2013.11.027.

Macpherson, G. B., Borg, M. K. and Reese, J. M. (2007) ‘Generation of initial molecular dynamics configurations in arbitrary geometries and in parallel’, *Molecular Simulation*, 33(December), pp. 37–41. doi: 10.1080/08927020701730724.

Mechau, N., Saphiannikova, M. and Neher, D. (2006) ‘Molecular tracer diffusion in thin azobenzene polymer layers’, *Applied Physics Letters*, 89(25), pp. 2006–2008. doi: 10.1063/1.2405853.

Meunier, M. (2012) ‘Introduction to Materials Studio’, *EPJ Web of Conferences*, 30, p. 04001. doi: 10.1051/epjconf/20123004001.

Michel Le Bellac, Fabrice Mortessagne, G. B. (2004) *Equilibrium and Non-Equilibrium Statistical Thermodynamics*. cambridge university press.

Natansohn, A. L. and Rochon, P. (2002a) ‘Photoinduced motions in azo-containing polymers’, *Chemical Reviews*, 102(11), pp. 4139–4175. doi: 10.1021/cr970155y.

Natansohn, A. L. and Rochon, P. (2002b) ‘Photoinduced motions in azo-containing polymers’, *Chemical Reviews*, 102(11), pp. 4139–4175. doi: 10.1021/cr970155y.

O’Shea, D. C. *et al.* (2009) ‘Design of Diffraction Gratings’, in *Diffraction Optics*, pp. 83–113. doi: 10.1117/3.527861.ch5.

Ootani, Y. *et al.* (2009) ‘Ab initio molecular dynamics simulation of photoisomerization in azobenzene in the n^{??} state’, *Journal of Chemical Physics*, 131(19). doi: 10.1063/1.3263918.

Paterson, J. *et al.* (1996) ‘Optically inscribed surface relief diffraction gratings on azobenzene-containing polymers for coupling light into slab waveguides’, *Applied Physics Letters*, 69(22), pp. 3318–3320. doi: 10.1063/1.117292.

Pedersen, T. G. *et al.* (1998) ‘Mean-field theory of photoinduced formation of surface reliefs in side-chain azobenzene polymers’, *Physical Review Letters*, 80(1), pp. 89–92. doi: 10.1103/PhysRevLett.80.89.

Petris, A. and Vlad, V. I. (2001) ‘Diffraction in laser induced gratings on thin As₂S₃ films’, *Journal of Optoelectronics and Advanced Materials*, 3(3), pp. 769–776.

Piela, L. (2007) *Ideas of Quantum Chemistry*.

Rapaport, D. C. (1999) ‘Molecular dynamics simulation’, *Computing in Science Engineering*, 1(1), pp. 537–542. doi: 10.1080/0892702042000212821.

Rapaport, D. C. (2004) *The Art of Molecular Dynamics*.

- Rocha, L. *et al.* (2014) 'Azobenzene based polymers as photoactive supports and micellar structures for applications in biology', *Journal of Photochemistry and Photobiology A: Chemistry*, 291(January 2016), pp. 16–25. doi: 10.1016/j.jphotochem.2014.06.018.
- Rochon, P., Batalla, E. and Natansohn, A. L. (1995) 'Optically induced surface gratings on azoaromatic polymer films', *Applied Physics Letters*, 66(2), pp. 136–138. doi: 10.1063/1.113541.
- Saiddine, M., Teboul, V. and Nunzi, J. M. (2010) 'Isomerization-induced surface relief gratings formation: A comparison between the probe and the matrix dynamics', *Journal of Chemical Physics*, 133(4), pp. 1–4. doi: 10.1063/1.3465577.
- Saphiannikova, M. and Neher, D. (2005) 'Thermodynamic theory of light-induced material transport in amorphous azobenzene polymer films', *Journal of Physical Chemistry B*, 109(41), pp. 19428–19436. doi: 10.1021/jp053249h.
- Sava, E. *et al.* (2016) 'Considerations on the surface relief grating formation mechanism in case of azo-polymers, using pulse laser irradiation method', *Optical Materials*. Elsevier B.V., 53, pp. 174–180. doi: 10.1016/j.optmat.2016.01.055.
- Schlick, T. (2010) *Molecular Modeling and Simulation: An Interdisciplinary Guide*. doi: 10.1007/978-1-4419-6351-2.
- Schultz, T. *et al.* (2003) 'Mechanism and dynamics of azobenzene photoisomerization', *Journal of the American Chemical Society*, 125(27), pp. 8098–8099. doi: 10.1021/ja021363x.
- Singleton, T. A. *et al.* (2012) 'Azobenzene photoisomerization under high external pressures: Testing the strength of a light-activated molecular muscle', *Journal of Physical Chemistry B*, 116(32), pp. 9860–9865. doi: 10.1021/jp3060872.
- Somer, F. L. (2004) 'Molecular Modelling for Beginners (Alan Hinchliffe)', *J. Chem. Educ.*, 81(11), pp. 1573--.. doi: 10.1021/ed081p1573.
- Soozandehfar, S. H. *et al.* (2000) 'Synthesis and bacterial degradation of an azopolymer', *International Journal of Pharmaceutics*, 198(1), pp. 71–82. doi: 10.1016/S0378-5173(99)00454-8.
- Teboul, V. *et al.* (2011) 'An isomerization-induced cage-breaking process in a molecular glass former below T_g', *Journal of Chemical Physics*, 134(11), pp. 1–7. doi: 10.1063/1.3563548.
- Teboul, V. *et al.* (2015) 'Light mediated emergence of surface patterns in azopolymers at low temperatures', *Soft Matter*, 11(32), pp. 6444–6449. doi: 10.1039/C5SM00846H.
- Todorov, T., Nikolova, L. and Tomova, N. (1984a) 'Polarization holography. 1: A new high-efficiency organic material with reversible photoinduced birefringence.', *Applied optics*, 23(23), pp. 4309–4312. doi: 10.1364/AO.23.004309.
- Todorov, T., Nikolova, L. and Tomova, N. (1984b) 'Polarization holography. 2:

Polarization holographic gratings in photoanisotropic materials with and without intrinsic birefringence.’, *Applied optics*, 23(24), p. 4588. doi: 10.1364/AO.23.004588.

Toshchevnikov, V., Saphiannikova, M. and Heinrich, G. (2009) ‘Microscopic theory of light-induced deformation in amorphous side-chain azobenzene polymers’, *Journal of Physical Chemistry B*, 113(15), pp. 5032–5045. doi: 10.1021/jp8078265.

Tsolou, G., Harmandaris, V. a. and Mavrantzas, V. G. (2008) ‘Molecular dynamics simulation of temperature and pressure effects on the intermediate length scale dynamics and zero shear rate viscosity of cis-1,4-polybutadiene: Rouse mode analysis and dynamic structure factor spectra’, *Journal of Non-Newtonian Fluid Mechanics*, 152(1–3), pp. 184–194. doi: 10.1016/j.jnnfm.2007.10.011.

Wang, D. *et al.* (2009) ‘Photoinduced Mass-Migration behavior of two amphiphilic Side-Chain azo diblock copolymers with different length flexible spacers’, *Macromolecules*, 42(7), pp. 2651–2657. doi: 10.1021/ma8026063.

Wang, X. (2017a) ‘Azo Polymer Syntheses’, in *Azo Polymers*. Berlin, Heidelberg: Springer Soft and Biological Matter, pp. 57–115. doi: 10.1007/978-3-662-53424-3_3.

Wang, X. (2017b) ‘Introduction’, in *Azo Polymers*. Berlin, Heidelberg: Springer Soft and Biological Matter, pp. 1–17. doi: 10.1007/978-3-662-53424-3.

Wang, X. (2017c) ‘Photoinduced Mass Transport’, in *Azo Polymers*. Berlin, Heidelberg: Springer Soft and Biological Matter, pp. 151–195. doi: 10.1007/978-3-662-53424-3_5.

Wang, X. (2017d) ‘Trans–Cis Isomerization’, in *Azo Polymers*. Berlin, Heidelberg: Springer Soft and Biological Matter, pp. 19–56. doi: 10.1007/978-3-662-53424-3.

Xu, C. *et al.* (2018) ‘Probing the $\pi \rightarrow \pi^*$ photoisomerization mechanism of trans-azobenzene by multi-state ab initio on-the-fly trajectory dynamics simulations’, *Physical Chemistry Chemical Physics*, 20(37), pp. 23885–23897. doi: 10.1039/c8cp02767f.

Yadavalli, N. S. and Santer, S. (2013) ‘In-situ atomic force microscopy study of the mechanism of surface relief grating formation in photosensitive polymer films’, *Journal of Applied Physics*, 113(22). doi: 10.1063/1.4809640.

Yager, K. G. and Barrett, C. J. (2004) ‘Temperature modeling of laser-irradiated azo-polymer thin films’, *Journal of Chemical Physics*, 120(2), pp. 1089–1096. doi: 10.1063/1.1631438.

Zhou, Y., Tang, B. and Wang, X. (2015) ‘Photoinduced deformation behavior of a series of newly synthesized epoxy-based polymers bearing push-pull azo chromophores’, *Polymer*. Elsevier Ltd, 60, pp. 292–301. doi: 10.1016/j.polymer.2015.01.033.

Zhu, Y. and Wang, X. (2013) ‘Photoresponsive diblock copolymers bearing strong push-pull azo chromophores and mesogenic biphenyl groups’, *Dyes and Pigments*. Elsevier Ltd, 97(1), pp. 222–229. doi: 10.1016/j.dyepig.2012.12.014.

CHAPTER II. Thesis objectives

The present thesis, **Synthesis, molecular modeling and photochromic behaviour of polysiloxanes containing azo-groups with different geometries**, represents a complex study of photosensitive azopolysiloxanes and rejoins both theoretical and experimental techniques.

The thesis subject revolves around the azopolymer's mass transport phenomenon induced by the photoisomerization of azobenzenes. Studies are directed to comprehension of this complex mechanism. Azobenzenes isomerize when exposed to light from the *trans* form, to the less stable form *cis* and vice-versa. To note is that the *cis-trans* isomerization can also be actuated by temperature. The isomerization is a reversible process that, along with the geometrical change, also enables a modification of dielectric momentum. The azobenzenes photoisomerization property is explored to obtain surface relief gratings *SRG* on azopolymeric films. Azobenzenes are chemically linked to polysiloxanes and provide the azopolymer with the force needed to perform a translation motion, as a result of their isomerization. Despite the fact that the photoinduced mass transport has been long investigated and several mechanisms have been proposed, none succeeds explaining all the experimental observations that are linked to various influence factors.

To investigate how the photochromic behavior is dependent on the azobenzene derivative, several azopolysiloxanes are synthesized and characterized. The obtained materials are tested for their capacity to generate *SRG* under light irradiation. Continuing on this path, assistance light is provided during the nanostructuration process to enhance the photoisomerization.

To determine the relevant parameters that enhance the mass transport process of the azobenzene containing materials, molecular modeling is employed. The molecular dynamics simulations investigate the influence of the azobenzene's shape (length and width dimensions) relative to the size of the material embedded in. Also, the effect of the characteristic folding times (related to isomerization rate) on the material's diffusion is studied. Another direction that the thesis approaches is the possibility to increase the motor's diffusion.

ORIGINAL CONTRIBUTIONS

1st PART

Experimental Studies

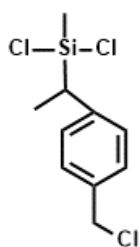
CHAPTER III. Synthesis and characterization

III.1. Synthesis of studied azopolysiloxanes

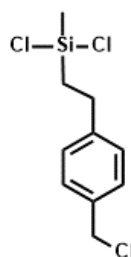
Azopolysiloxanes synthesis starts with the obtaining of the support polymer, linear polysiloxane. Then, the azo derivatives, separately obtained, are connected to the polysiloxane through a substitution of the chlorobenzyl side groups.

III.1.1. Polysiloxane synthesis

The polysiloxane is prepared in a two-step reaction, starting from dichloro-4-[(chloromethyl)-phenyl]ethyl-methylsilane monomer. First, a mixture of cyclic and linear oligomers is obtained by polycondensation through hydrolysis. Then, the hydrolysate's cationic equilibration catalyzed by triflic acid and regulated by a chain blocker (1,3-divinyl-1,1,3,3-tetramethyldisiloxane) leads to formation of linear polysiloxane.



α isomer



β isomer

Figure III.1. Dichloro-4-[(chloromethyl)-phenyl]ethyl-methylsilane monomer in α and β form.

The monomer is a mix of α and β forms (α – isomer $27 \% \pm 3 \%$) that stays the same throughout the whole set of following reactions. Presence of these two forms of structural units in the starting monomer counteracts the high stacking capacity of azo derivatives. This characteristic is favorable to our application, since we need amorphous films for nanostructuration.

The hydrolysis leads to the mixture of linear and cyclic oligomers (mostly cyclotetrasiloxane) (*Figure III.2.*). Please note that for ease of representation, we only show the β – isomer which is majoritarian.

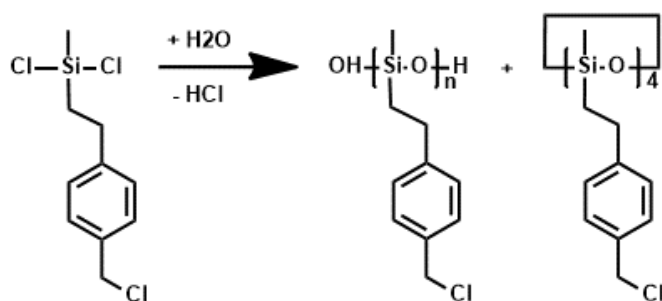


Figure III.2. The hydrolysis reaction scheme

Next step in obtaining the polysiloxane is the cationic equilibration reaction catalyzed by triflic acid. Chain blocker 1,3-divinyl-1,1,3,3-tetra- methylidisiloxane (DVDS) is used. A few vinyl end groups of the polysiloxane, remain untransformed during the reaction so there is also a low fraction of silanol end groups (*Figure III.3.*) It is important to specify here that these groups react during precipitation of the linear polysiloxane in methanol and become $\text{Si}-\text{OCH}_3$. Following this reaction, the average polymerization degree rises to values around $\langle P_d \rangle \approx 50$. The chain blocker plays an important role in stabilizing the P_d , and the molecular weight implicitly, because the $\text{Si}-\text{OH}$ groups can lead to post polymerization. The DVDS to hydrolysate rate allows, thus, to control the polysiloxane's molecular weight.

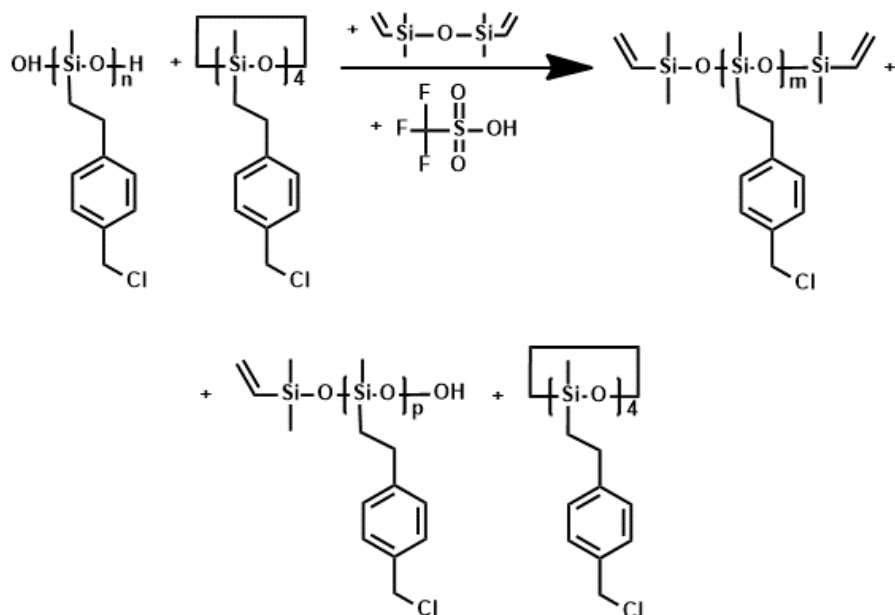


Figure III.3. The equilibration of hydrolysate reaction scheme

The cyclic polysiloxane is separated from the final product, as we only use the linear polysiloxane in this study. The chlorobenzyl side group is further substituted with sodium salts of the azo derivatives to obtain azopolysiloxane.

We present ^1H -NMR spectrum of a typical polysiloxane sample (Figure III.4.)

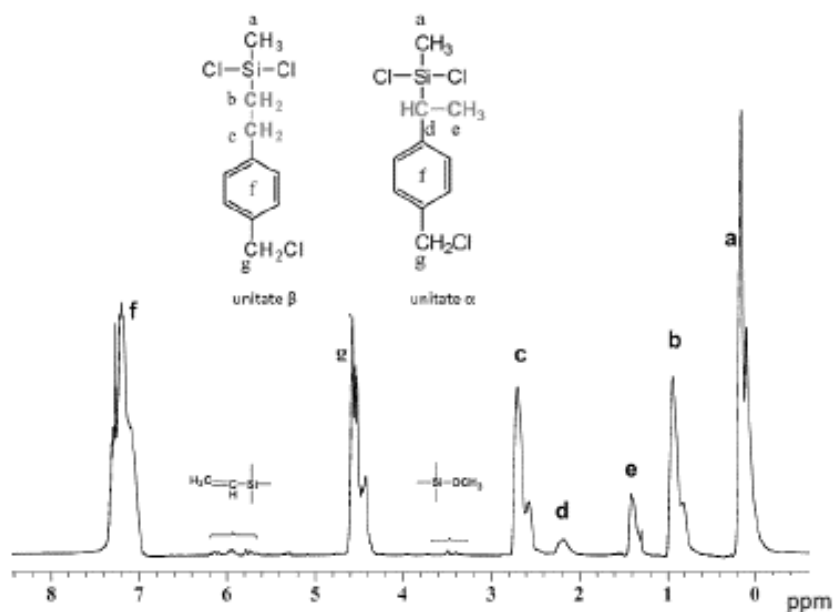


Figure III.4. ^1H -NMR spectrum of polysiloxane.

The spectrum indicates all the polysiloxane signals, as follows:

- 0.15 ppm: 3 H, main chain $-\text{CH}_3$ groups (a);
- 0.5 – 2.8 ppm: 4 H, α and β side groups
 - 0.5 – 1 ppm: 2 H, $-\text{CH}-$ group linked to Si from β isomers (b);
 - 2.5 – 2.8 ppm: 2 H, $-\text{CH}-$ group linked to aromatic ring from β isomers (c);
 - 1.25 – 1.5 ppm: 3 H, $-\text{CH}_3$ groups from α isomer (d);
 - 2 – 2.3 ppm: 1 H, $-\text{CH}-$ groups linked to Si and aromatic ring from α isomer (e);
- 3 – 4 ppm: 3 H, $\text{Si}-\text{OCH}_3$ end chain group;
- 4.5 ppm: 2 H, $-\text{CH}_2\text{Cl}$ (chlorobenzyl) side groups (g);
- 5.5 – 6.5 ppm: 3 H, $-\text{CH}=\text{CH}_2$ end chain group;
- 6.9 – 7.4 ppm: 4 H, aromatic rings (f).

III.1.2. Azo derivatives synthesis

We use a classical diazotization and coupling reaction scheme to obtain different azobenzene derivatives (*Figure III.5.*).

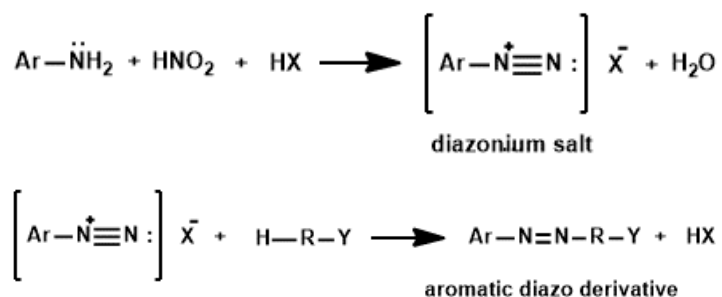
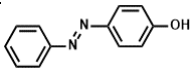
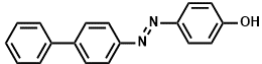
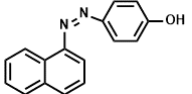
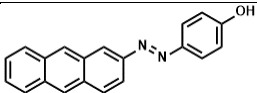


Figure III.5. General reaction scheme of diazotization and coupling.

A primary aromatic amine reacts with nitrous acid in aqueous media, when the diazonium salt is formed. As nitrous acid is not stable, it is prepared in situ from a sodium nitrite NaNO_2 solution in water under acid pH conditions (X represents the anion of a strong acid, like HCl). Further, the obtained diazonium salt is coupled with phenol (Y represents the electro donor group, $-\text{OH}$).

Apart from 4-phenylazophenol which is commercially available we obtain the azo derivatives using the above reaction plan. To link them to the polysiloxane, we modify the azophenols in sodium salts which can react with the chlorobenzyl side group through nucleophilic substitution.

Table III.1. The starting primary aromatic amine and the corresponding azophenol obtained.

Primary aromatic amine	Azophenol	Azophenol structure
-	4 – (phenylazo)phenol	
4 – aminobiphenyl	4 – (4'-diphenylazo)phenol	
1 – aminonaphthalene	4 – (1'-naphthaleneazo)phenol	
2 – aminoanthracene	4 – (2'-anthraceneazo)phenol	

We note here that the 4 – aminobiphenyl, unlike the other amines which were purchased as such, was synthesized by nitration of biphenyl, followed by reduction of formed 4 – nitrobiphenyl (*Figure III.6.*).

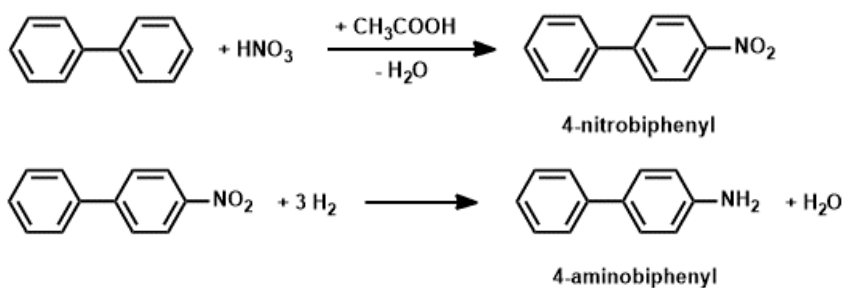


Figure III.6. Scheme reaction for 4 – aminobiphenyl synthesis.

Hydrogen and Carbon spectra are presented in the following pictures (*Figures III.7. – 11.*) along with the detailed magnetic field displacement.

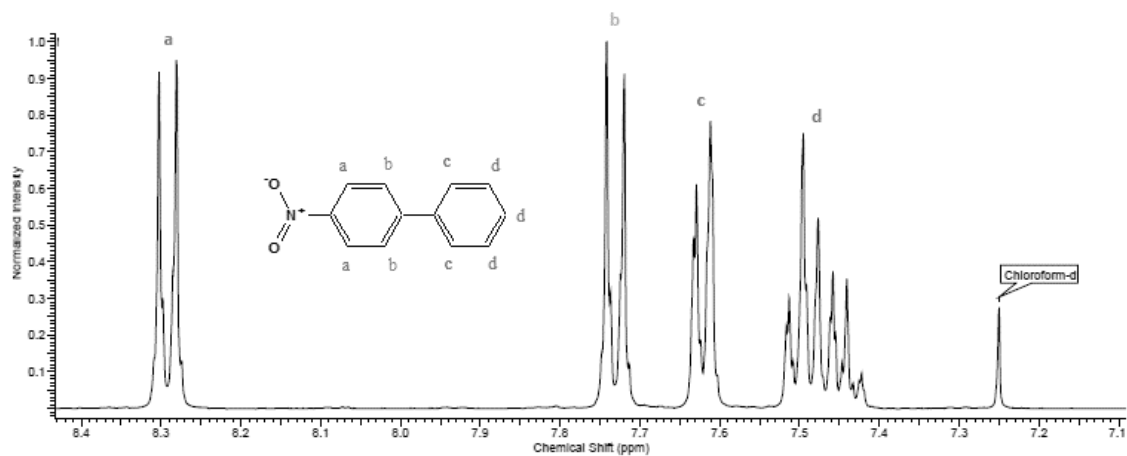


Figure III.7. ^1H -NMR spectrum of 4 – nitrobiphenyl

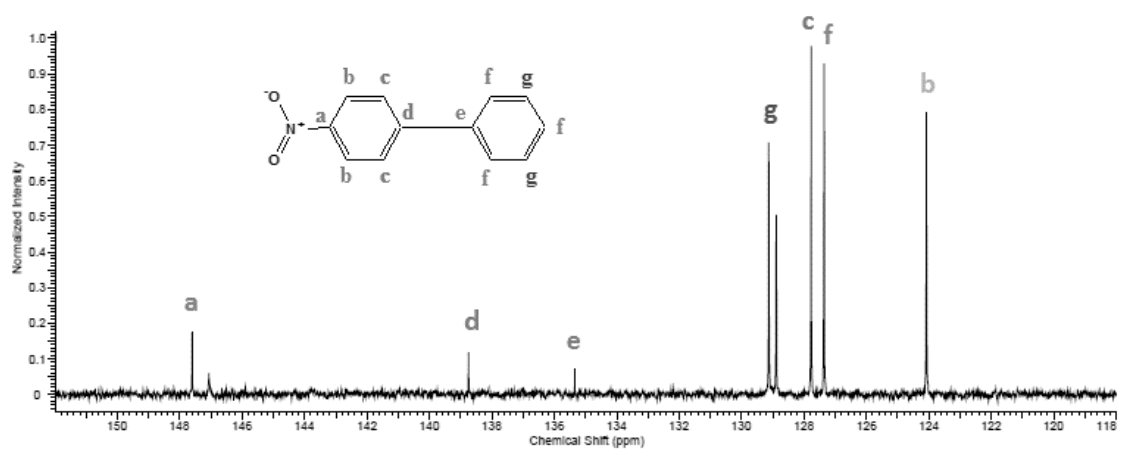


Figure III.8. ^{13}C -NMR spectrum of 4 – nitrobiphenyl

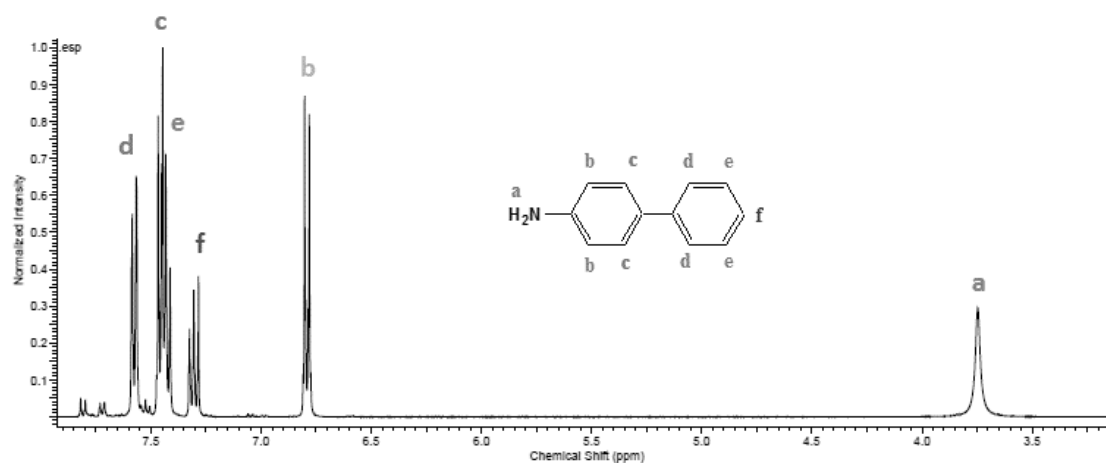


Figure III.9. ^1H -NMR spectrum of 4 – aminobiphenyl

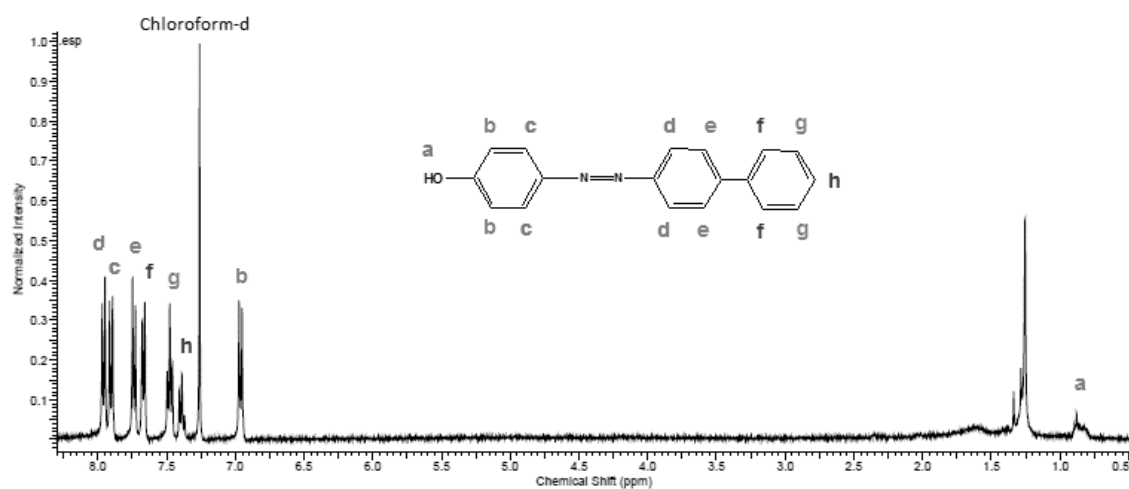


Figure III.10. ^1H -NMR spectrum of 4 – (4'-diphenylazo)phenol

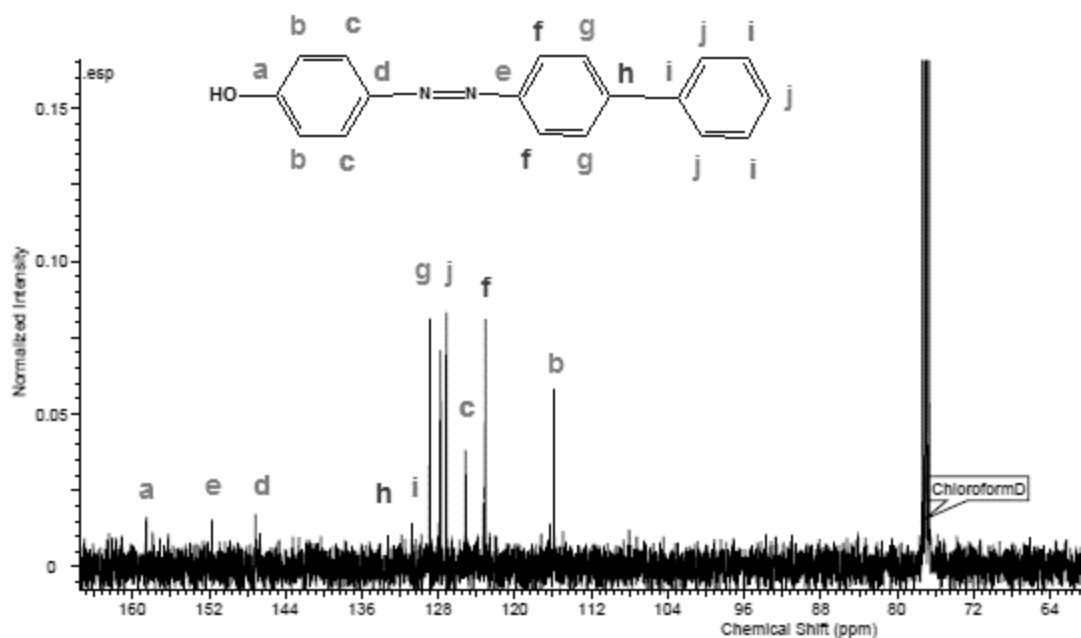


Figure III.11. ^{31}C -NMR spectrum of 4 – (4'-diphenylazo)phenol

III.1.2. Azopolysiloxane synthesis

Polysiloxane is modified by nucleophilic substitution $\text{S}_{\text{N}}2$ of the chlorobenzyl side group with the azo derivatives. We present the general reaction scheme, where R represents the azobenzenes in the form of sodium salts (Figure III.12.).

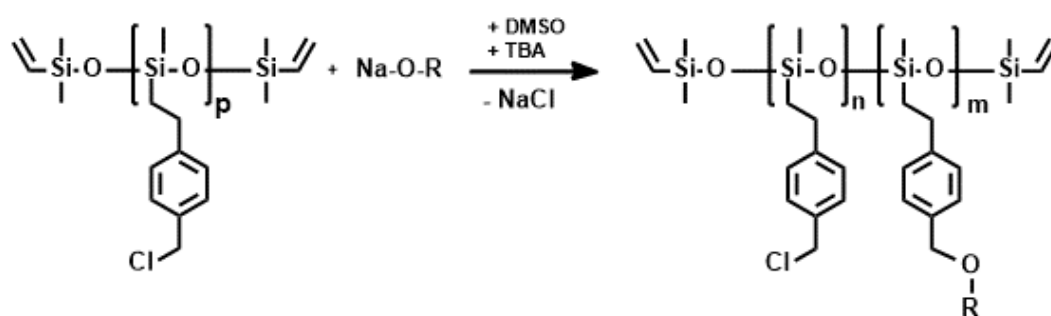


Figure III.12. General scheme of azopolysiloxane reaction.

The reaction takes place in dimethyl sulfoxide (DMSO) and is catalyzed by tetrabutylammonium bromide (TBA). Azopolysiloxane with different degrees of substitution are obtained by controlling the azo polysiloxane – azo derivative ratio. The next image (Figure III.13.) shows the azopolysiloxanes we obtained.

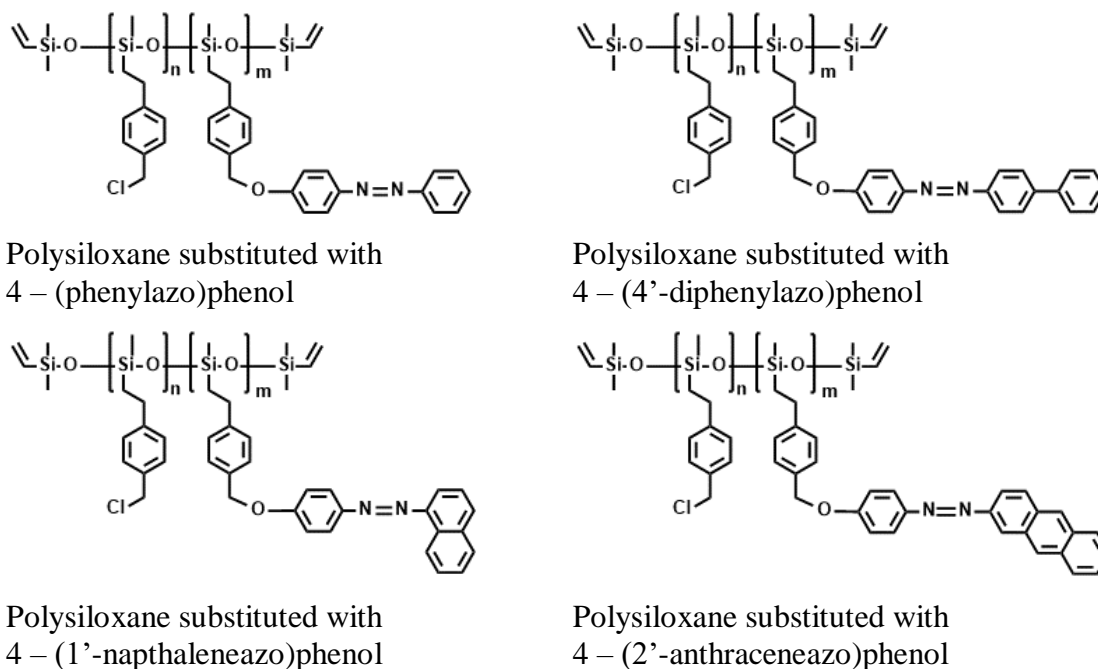


Figure III.13. Chemical structures of the obtained azopolysiloxanes

Table III.2. Synthesized azopolysiloxanes and their structural characteristics

Sample code	Azo substituent	S _d (%)	<P _d >	<M _n > (Da)
PFF1	4 – (phenylazo)phenol	61	43	13 628
PFF2		52	40	12 062
PFF3		99	*	*
PDF1	4 – (4'-diphenylazo)phenol	84	34	14 212
PDF2		58	60	20 951
PDF3		31	72	20 737
PDF4		32	57	16 731
PNF1	4 – (1'-naphthaleneazo)phenol	72	50	18 285
PNF2		31	27	7 763
PAF1	4 – (2'-anthraceneazo)phenol	84	*	*
PAF2		43	61	20 014
PAF3		43	55	18 031
PAF4		28	46	13 352
PAF5		30	49	14 315

We confirm the azopolysiloxanes' chemical structures through ^1H -NMR spectroscopy. We also evaluate the substitution degree S_d , polymerization degree P_d and numeric molecular weight M_n . the last two characteristics are mere estimation of the real values, as the NMR spectra cannot give accurate information on this matter. The star sign (*) in the table marks the cases where the NMR method did not allowed for a proper evaluation of the polymerization degree and numeric molecular weight.

S_d is calculated based on the chlorobenzyl side groups $-\text{CH}_2\text{Cl}$ (indicated on the spectrum at about 5 ppm) and the ones that have reacted with azo derivatives $-\text{CH}_2-\text{O}-\text{R}$ (indicated on the spectrum at about 4.5 ppm), according to the following formula (*Equation III.1.*).

$$S_d \% = \frac{\int -\text{CH}_2\text{Cl}}{\int -\text{CH}_2\text{Cl} + \int -\text{CH}_2\text{O}-\text{R}} \cdot 100$$

Equation III.1.

Average molecular weight is evaluated based on the signals for the both types of end chains, $-\text{CH}=\text{CH}_2$ and $\text{Si}-\text{OCH}_3$.

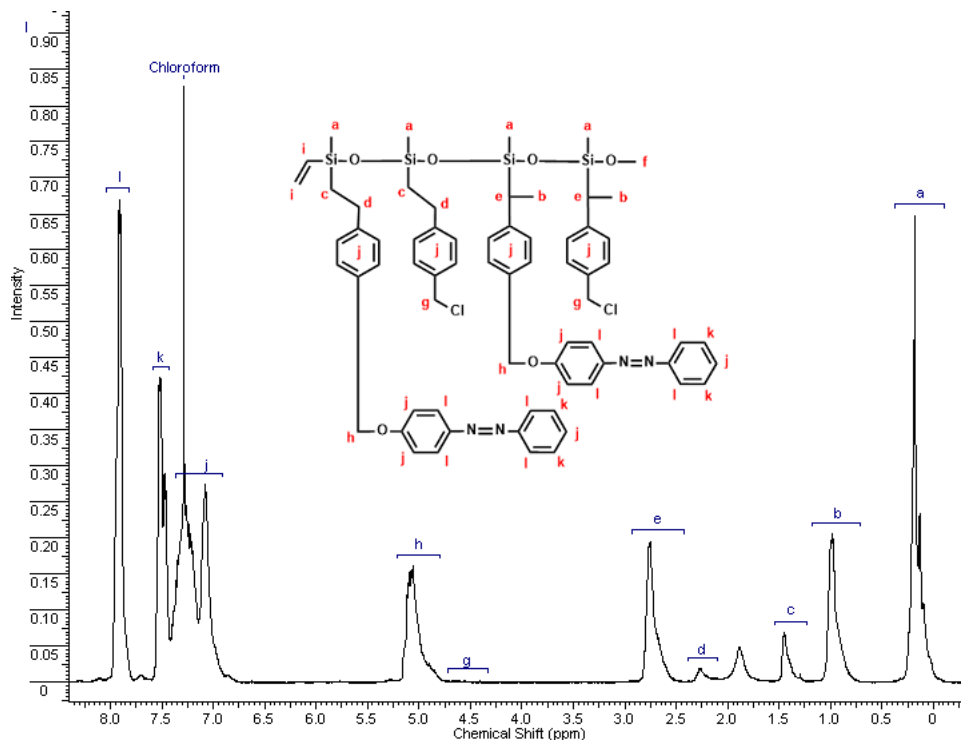


Figure III.14. ^1H -NMR spectrum of sample polysiloxane substituted with 99 % 4 – (phenylazo)phenol

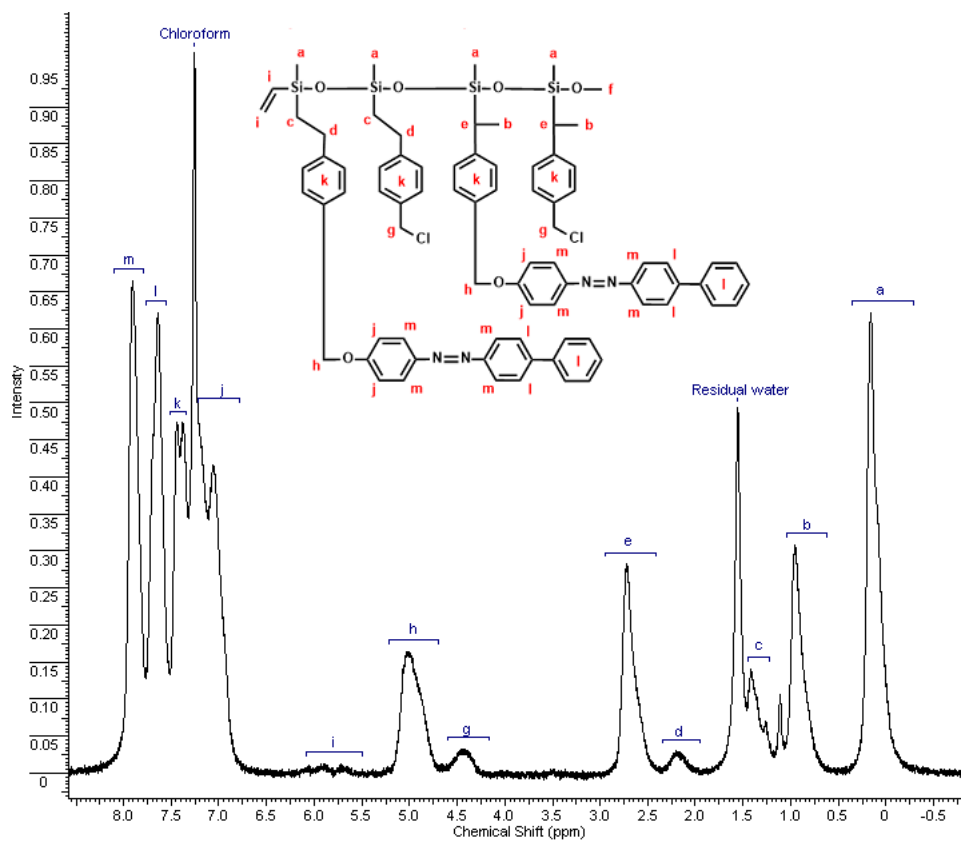


Figure III.15. ^1H -NMR spectrum of sample polysiloxane substituted with 84 % 4 – (4'-diphenylazo)phenol

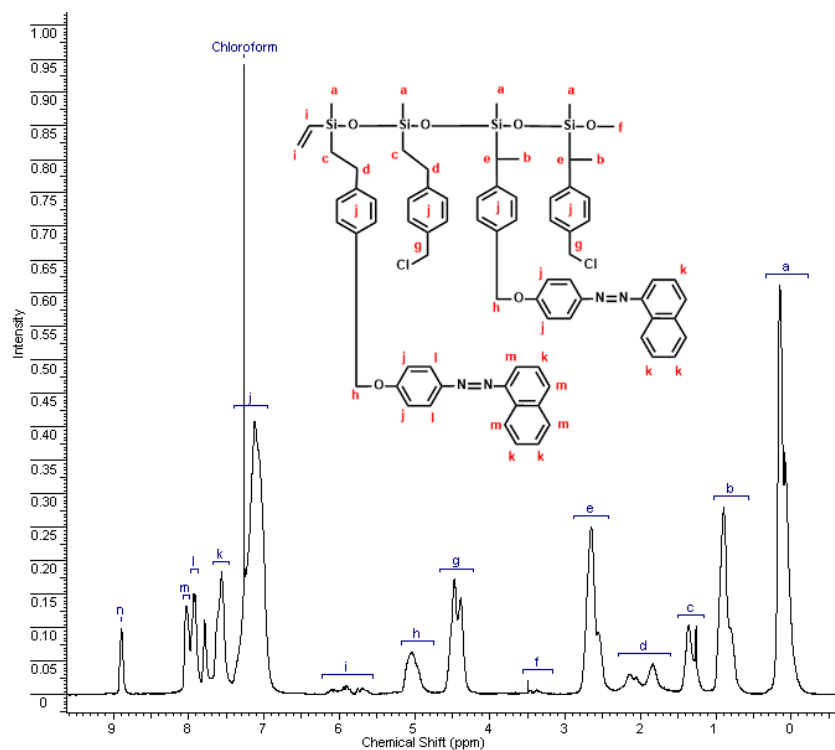


Figure III.16. ^1H -NMR spectrum of sample polysiloxane substituted with 31 % 4 – (1'-naphthaleazo)phenol

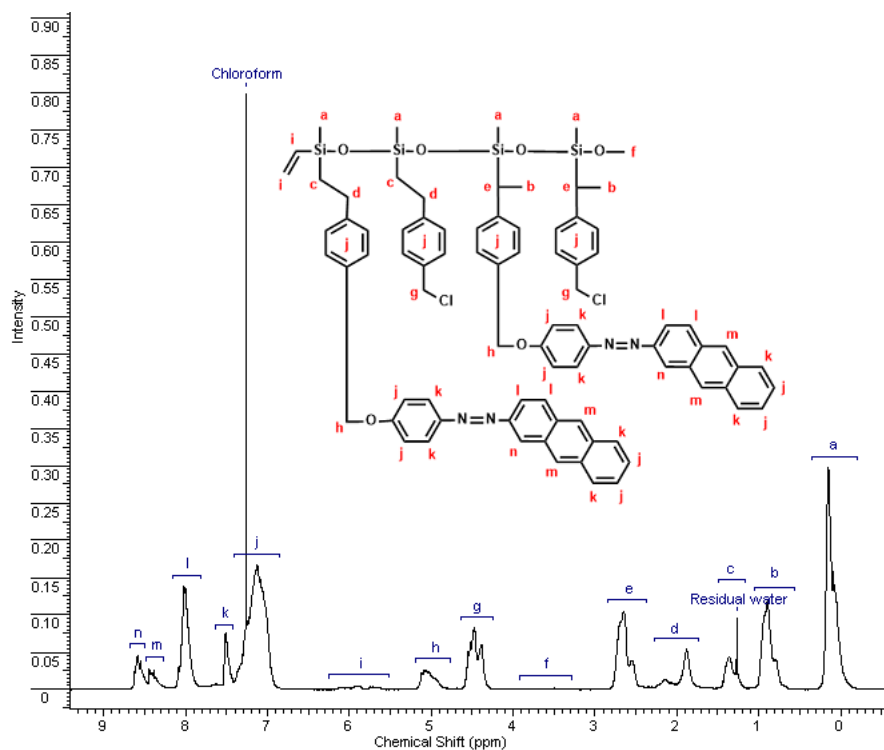


Figure III.17. ^1H -NMR spectrum of sample polysiloxane substituted with 28 % 4 – (2'-anthraceneazo)phenol

III.2. Thermal characterization

Both thermogravimetric and thermoanalytic studies are performed on a Mettler Toledo TGA – Star System instrument on samples of 2.5 – 4.5 mg weight in N₂ atmosphere (15 mL/min).

III.2.1. Thermogravimetric studies

The tests are performed on a range of temperature $T = 25 - 890$ °C with a heating rate of 10 and 15 K/min. We investigate the thermal stability of azopolysiloxanes which is important for applications, as well as the gradual decomposition.

We display in the next figure (*Figure III.20.*) the thermal gravimetric *TG* curves of polysiloxanes substituted with the 4 different azo derivatives for comparison.

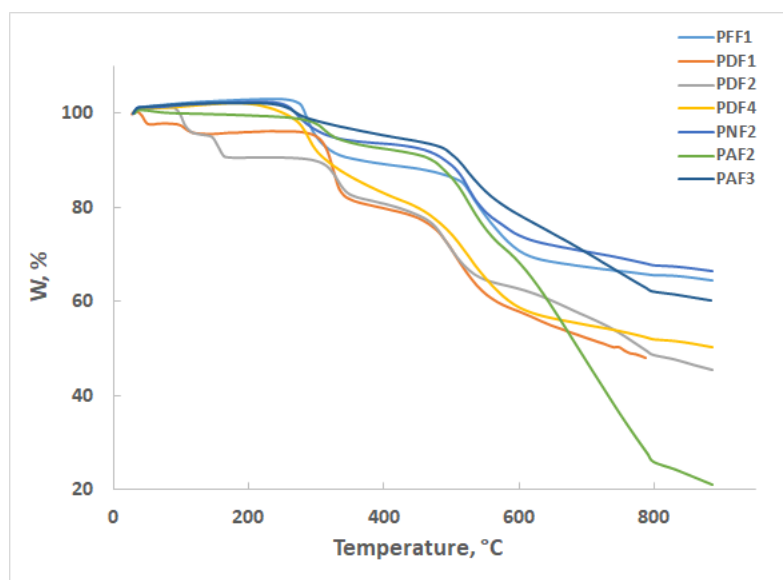


Figure III.20. TG curves for azopolysiloxanes substituted with different azo derivatives (PFF1: 4 – (phenylazo)phenol; PDF1, PDF2 and PDF4: 4 – (4'-diphenylazo)phenol; PNF2: 4 – (1'-naphthaleneazo)phenol; PAF2, PAF3: 4 – (2'-anthraceneazo)phenol).

All four types of azopolysiloxanes display characteristic degradation steps (two or three), depending on the azo derivative's chemical structure and the substitution degree.

The –N=N– link from the azo group is the weakest fragment from the thermal degradation point of view for all the samples studied. This first step starts at an average temperature of 275 °C and ends at about 341 °C. Degradation rates are quite different,

although correlation between them is not very clear (standard deviation for the temperature where degradation reaches the highest rate T_{peak} is $SD = 19\text{ }^{\circ}\text{C}$). More specifically, the order of their degradation rate is:

$$\text{PAF3} < \text{PNF2} < \text{PDF4} < \text{PFF1} < \text{PAF2} < \text{PDF1} < \text{PDF2}.$$

Table III.2. The degradation steps for azopolysiloxane samples.

Sample	Step	$T_{\text{onset}},\text{ }^{\circ}\text{C}$	$T_{\text{endset}},\text{ }^{\circ}\text{C}$	$T_{\text{peak}},\text{ }^{\circ}\text{C}$	W, %	Residue, %	ΔT
Linear polysiloxane	I	242	329	301	14.63	58.67	343
	II	502	585	534	26.69		
PFF1	I	270	324	292	14.25	62.61	358
	II	514	628	538	23.14		
PDF1	I	306	338	324	16.11	55.08	344
	II	474	550	506	21.92		
	III	614	650	627	6.89		
PDF2	I	303	346	330	9.78	≤ 58.38	≥ 497
	II	457	532	495	17.50		
	III	614	-	666	14.34		
PDF4	I	254	382	291	20.55	50.09	351
	II	471	605	525	29.36		
PNF2	I	252	333	276	8.93	65.29	359
	II	469	611	526	25.78		
PAF2	I	291	344	312	6.72	≤ 27.28	≥ 509
	II	476	557	527	23.01		
	III	612	-	693	42.99		
PAF3	I	251	318	270	7.76	≤ 60.05	≥ 549
	II	485	591	528	15.69		
	III	591	-	-	16.05		

T_{onset} = value of start temperature of the degradation step

T_{endset} = value of end temperature of the degradation step

T_{peak} = maximum value of temperature during the degradation step

W = weight loss during the degradation step

Residue = left weight of the sample at the end of test

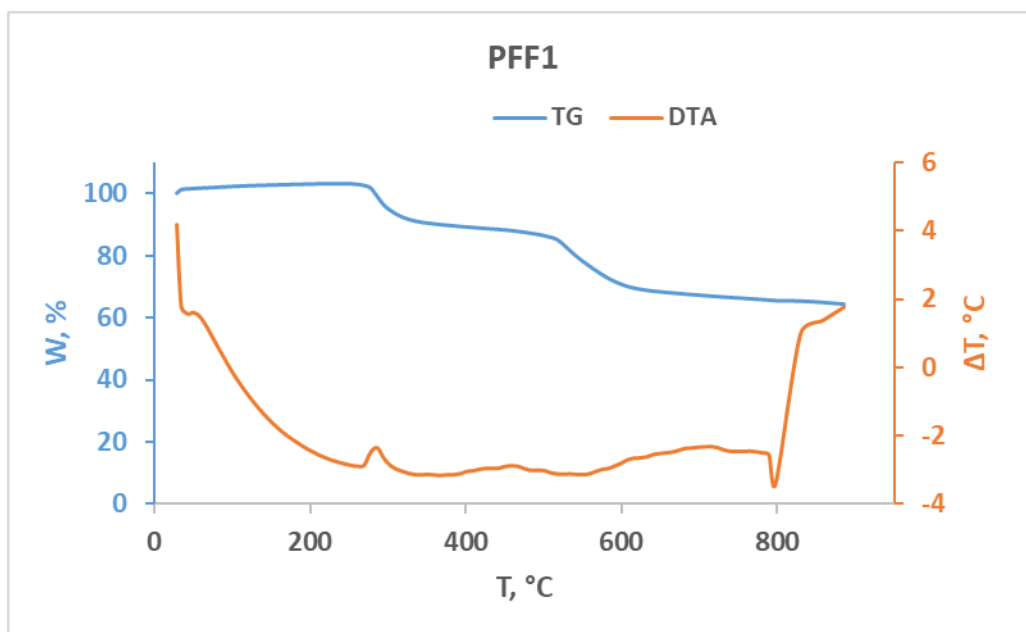
ΔT = temperature range between that covers all degradation steps

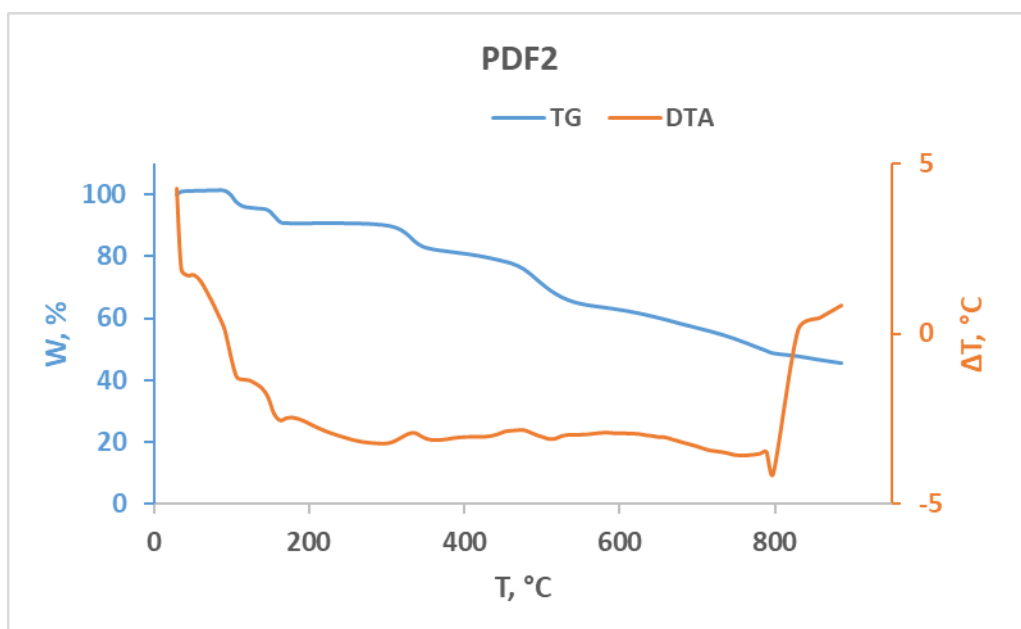
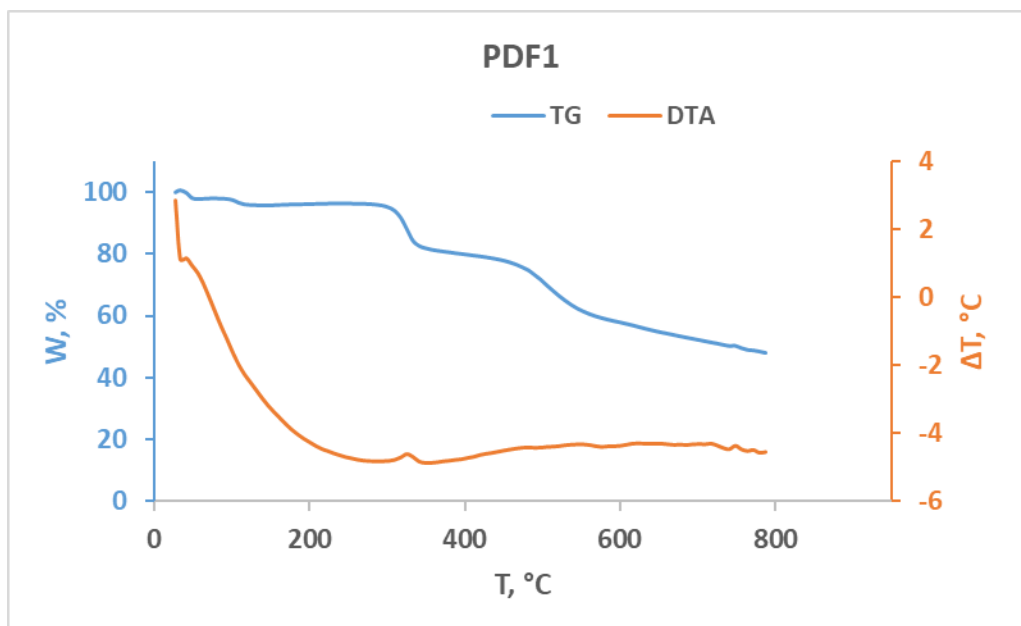
Sample PAF3 which contains the bulky (anthraceneazo)phenol in medium concentration ($S_d = 43\%$) has the lowest degradation rate in the first step, while PDF2 with 58 % (diphenylazo)phenol. Before substitution with azo derivatives, the polysiloxanes weakest fragment is chlorobenzyl group from the side chain. Compared to the azo moiety,

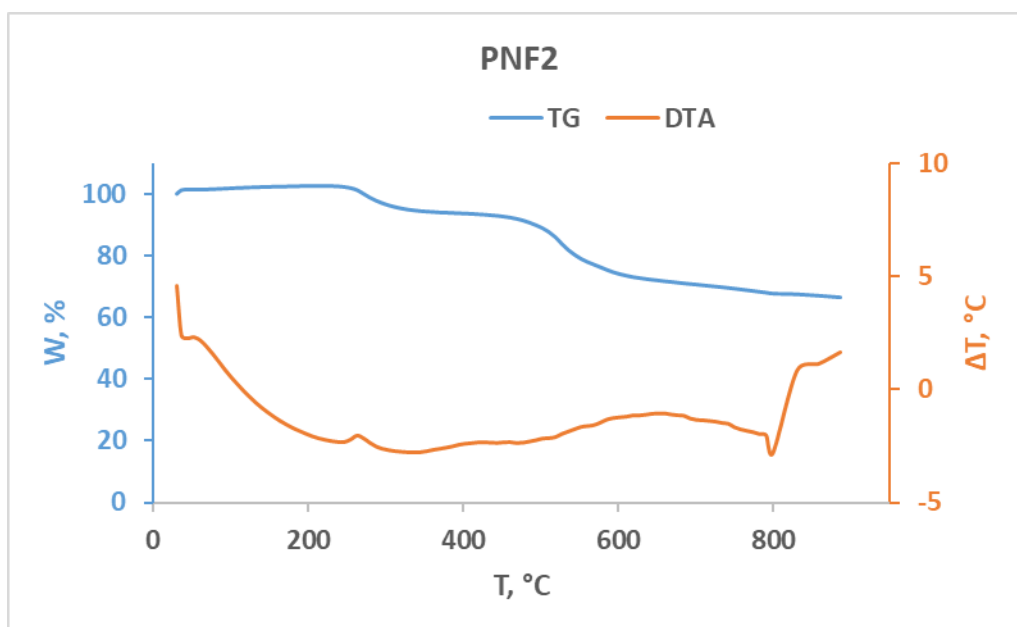
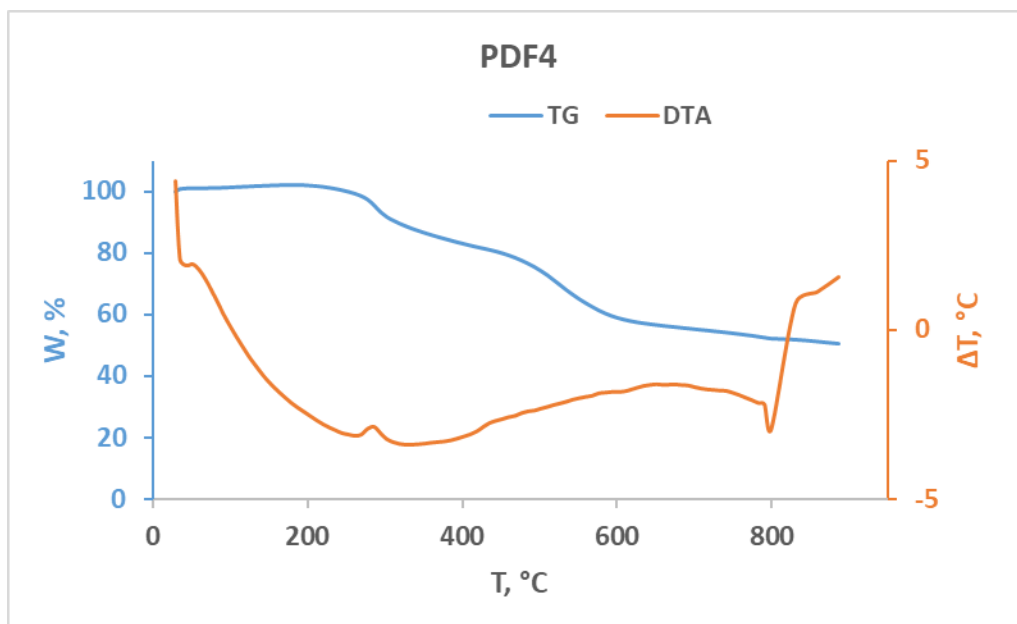
its thermal stability is a bit lower, which is why the first degradation step of linear polysiloxane onsets at 242 °C.

The second degradation step is also present to all azopolysiloxanes and it takes place in the average range of $< 478 - 582 > ^\circ\text{C}$. The third step appears only on some of the azopolysiloxanes: PDF1, PDF2, PAF2 and PAF3. These samples, except PDF1, disclose on the thermograms that the third step continues after the test finishes, at 890 °C, indicating that there is still more mass to be degraded.

The data presented in the table shows the mass loss steps, excluding the evaporation for the samples that were not well dried, in order to show the degradation accurately. The azopolysiloxanes that lost solvents in the first part of the heating process (PDF1 and PDF2) are better observed on the curves where the thermograms are depicted singularly for each sample. (*Figure III.21*).







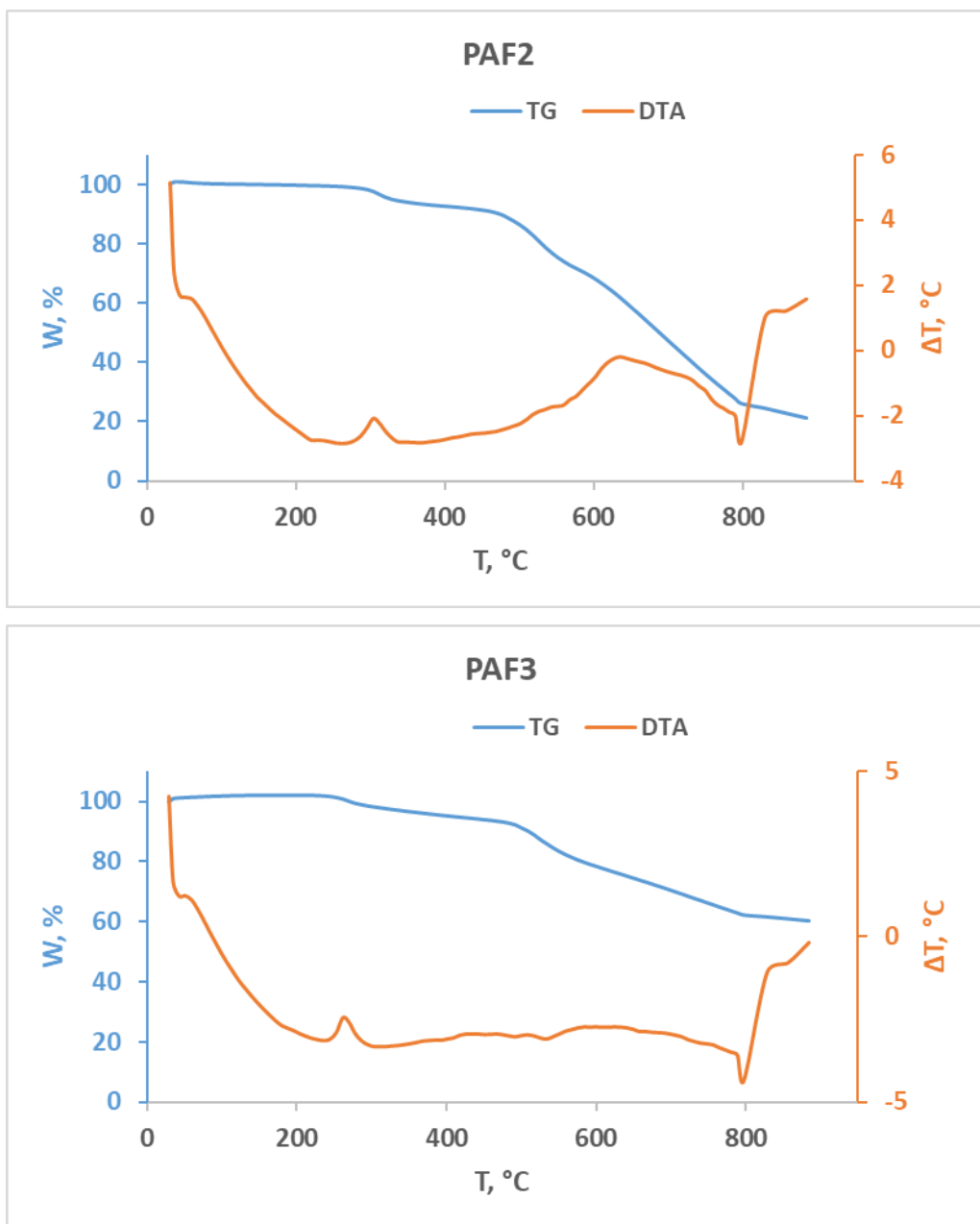


Figure III.21. Data from thermogravimetric TG and differential thermal analysis DTA for polysiloxanes substituted with different azo derivatives (PFF1: 4 – (phenylazo)phenol; PDF1, PDF2 and PDF4: 4 – (4'-diphenylazo)phenol; PNF2: 4 – (1'-naphthaleneazo)phenol; PAF2, PAF3: 4 – (2'-anthraceneazo)phenol).

We evaluate the glass transition temperature T_g from differential thermal analysis DTA curves for each sample (Table III.3.). The first process that can be observed in all samples in the temperature range $T = 34 - 51$ °C, where $\Delta T = 0$ °C, represents the change of azopolysiloxanes from glassy to amorphous state. Given the structural attributes of

macromolecular compounds, the transition occurs on a span of time and temperature rather than an instantaneous change.

Table III.3. Glass transition temperature (T_g).

Sample	PFF1	PDF1	PDF2	PDF4	PNF2	PAF2	PAF3
T_g , °C	42	38	47	43	43	47	47

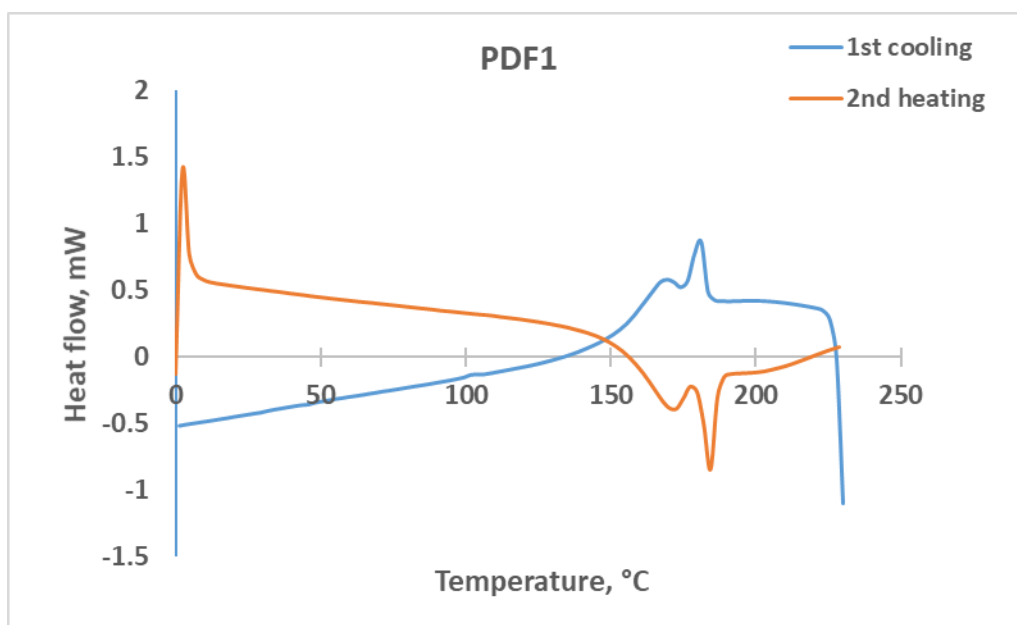
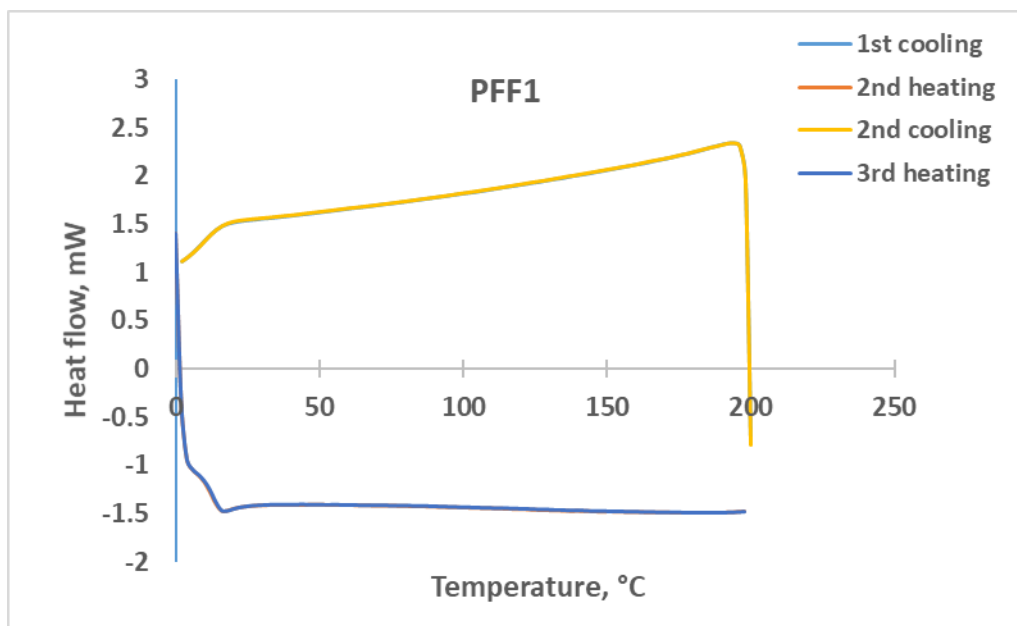
The DTA show that the first step specific to the degradation of azo links $-N=N-$ is an exothermic process for all azopolysiloxanes. Moreover, allure of the curves indicates that the onset degradation takes place with a release of thermal energy that rapidly drops after which the process slowly starts to consume energy.

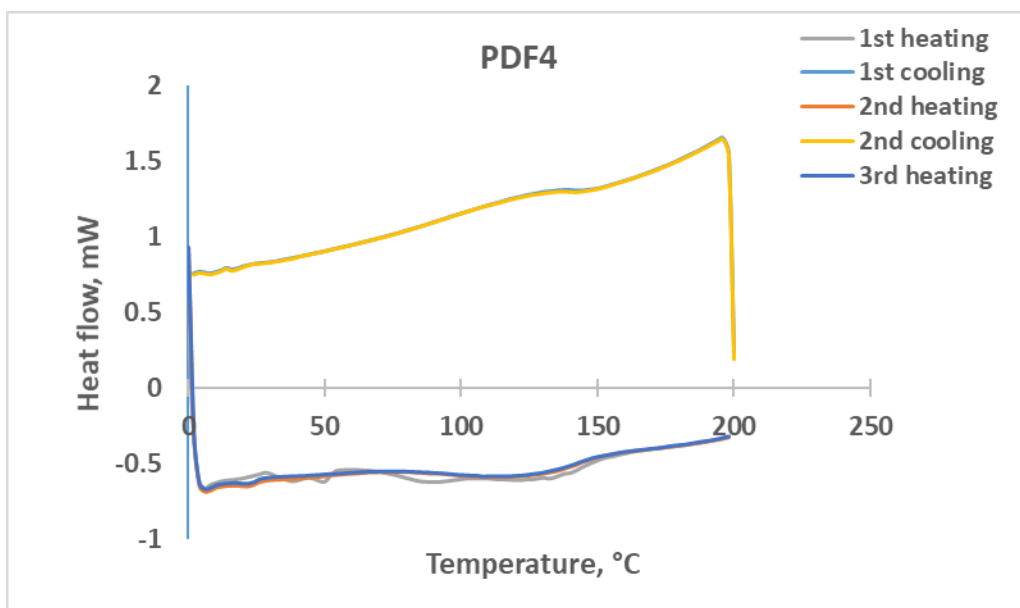
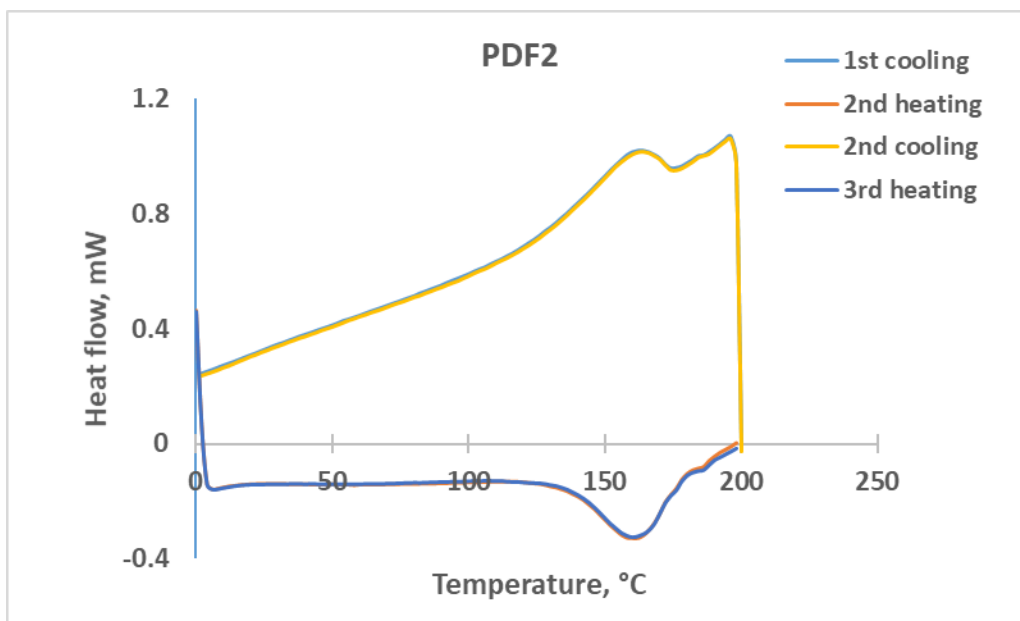
Another characteristic specific to all the azopolysiloxanes (except PDF1) is the endothermic peak that appears around 800 °C, towards the end of the degradation span covered in our test. This consume of energy takes place during the third degradation step (PDF2, PAF2 and PAF3) or during thermal stability (PFF1, PDF4 and PNF2). Summarizing our findings, the azopolysiloxanes studied present good thermal stability till around 275 °C, allowing the samples to be exposed to laser radiation for nanostructuration and also sterilized for biological cultures without any degradation process.

III.2.2. Differential thermal analysis

We perform differential scanning calorimetry on a Mettler Toledo DSC-1 Star System in N_2 atmosphere (15 mL/min), and the weight of the samples is 2.5 – 4.5 mg.

We investigate the azopolysiloxanes through DSC analyses in the temperature range underlined by the thermogravimetric tests, which indicated the upper limit of thermal stability of our samples. DSC data is registered for heating and cooling cycles with rate of 10K/min in the temperature ranges: $T = 0 - 230$ °C (PDF1), $T = 0 - 200$ °C (PFF1, PDF2, PDF4, PNF2), $T = -50 - 150$ °C (PNF2) and $T = -50 - 200$ °C (PAF4).





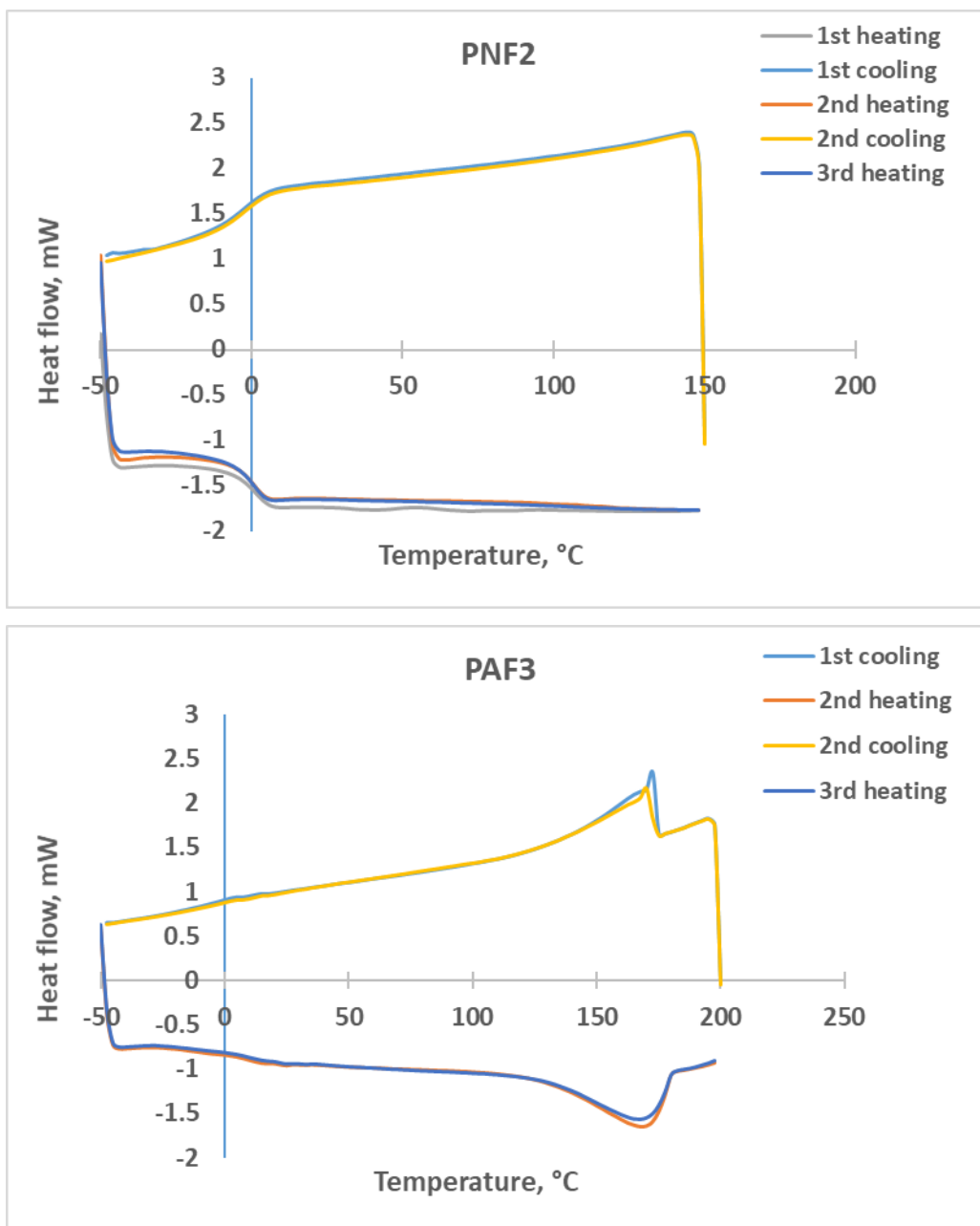


Figure III.22. DSC heating and cooling cycles for polysiloxanes substituted with different azo derivatives (PFF1: 4 – (phenylazo)phenol; PDF1, PDF2 and PDF4: 4 – (4'-diphenylazo)phenol; PNF2: 4 – (1'-naphthaleneazo)phenol; PAF2, PAF3: 4 – (2'-anthraceneazo)phenol).

PDF1 sample (84 % diphenylazo phenol) presents two first order transition in the temperature range $T = 160 - 200$ °C which is observed during both heating and cooling. The maximum heat flow of the two transitions appears at approximately the same values during heating and cooling (a difference of only 4 and 3 °C).

$$\text{First transition: } T_{\max}(\text{heating}) - T_{\max}(\text{cooling}) = 173 - 169 = 4\text{ }^{\circ}\text{C}$$

$$\text{Second transition: } T_{\max}(\text{heating}) - T_{\max}(\text{cooling}) = 184 - 181 = 3\text{ }^{\circ}\text{C}$$

Equation III.2.

Considering the fact that the azopolysiloxane crystalizes without supercooling needed, suggests that it passes through a liquid crystal phase transition. This represents a particular behavior for the azo derivatives that our group studied until now. Further investigation of this phenomenon is made through polarized optical microscopy (*Chapter III.3*).

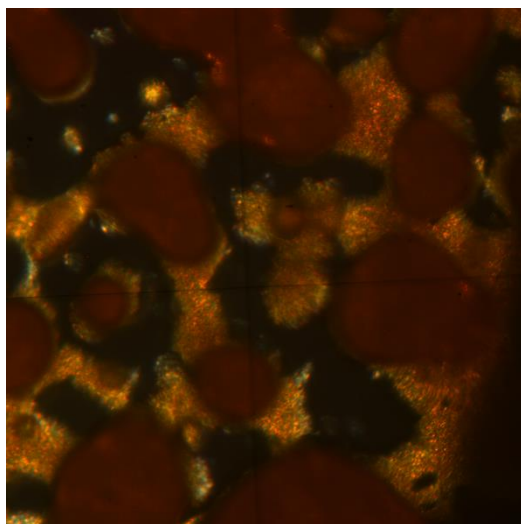
III.3. Liquid crystal state investigation

Optical microscopy in polarized light is used to identify and characterize mesophases in materials supposed to show liquid crystal properties. Liquid crystals are birefringent in polarized light which in connection with the sample's fluidity give information about the possible existence of mesophases. The moieties responsible for this particular behavior are called mesogens. Rigid aromatic cycles are a common structure found in mesogens, giving them the ability to align with each other. When linked to flexible chains, they achieve both fluid and solid state characteristics, resulting in the liquid crystal phase, the mesophase. Thermotropic liquid crystals are characterized by the fact that the mesophase is induced by temperature. When mesogens present orientational (directional) order, the phase is called nematic, while when they also have positional order, the smectic mesophase appears.

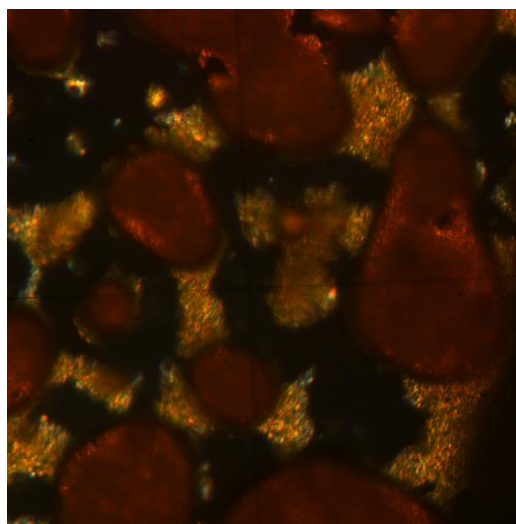
When analyzing mesophases, the sample's texture (microstructure) depends on the relative position of the mesogens and the light vector. To be observed, the mesogens have to be perpendicular on the light polarization vector, otherwise, they will disclose their birefringent property and the investigated field appears to be dark. When properly positioned, mesogens determine a light field, whose intensity is proportional with the material's birefringence.

Considering that azopolysiloxanes are special polymers, liquid crystal characteristics can be expected to be observed. Because PDF1 sample showed the two phase transitions on the DSC curve, we analyzed it for liquid crystal properties with polarized light

microscopy, using optical microscope Axioskop 40 Pol from Zeiss. The azopolysiloxane was heated with 20 °C/min in the temperature range $T = 20 - 265$ °C and cooled back with 10 °C/min.

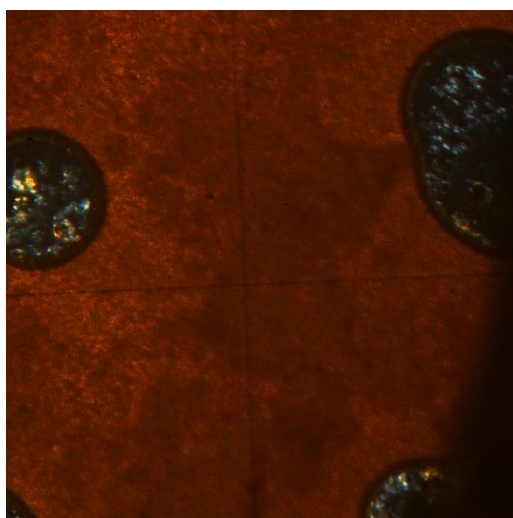


188 °C

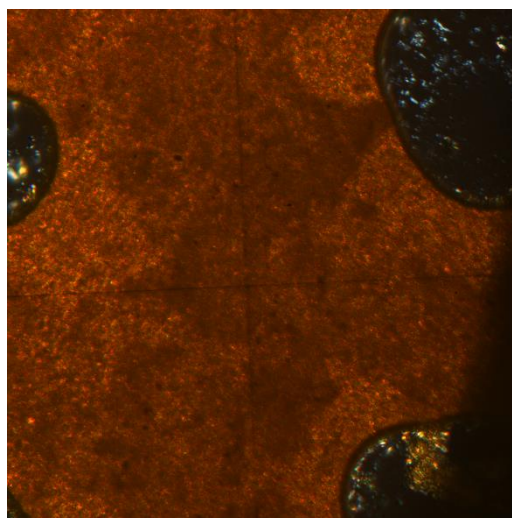


199 °C

Figure III.23. *Mesophases of PDF1 sample during heating.*



183 °C



169 °C

Figure III.24. *Isotropic phase of PDF1 sample during cooling*

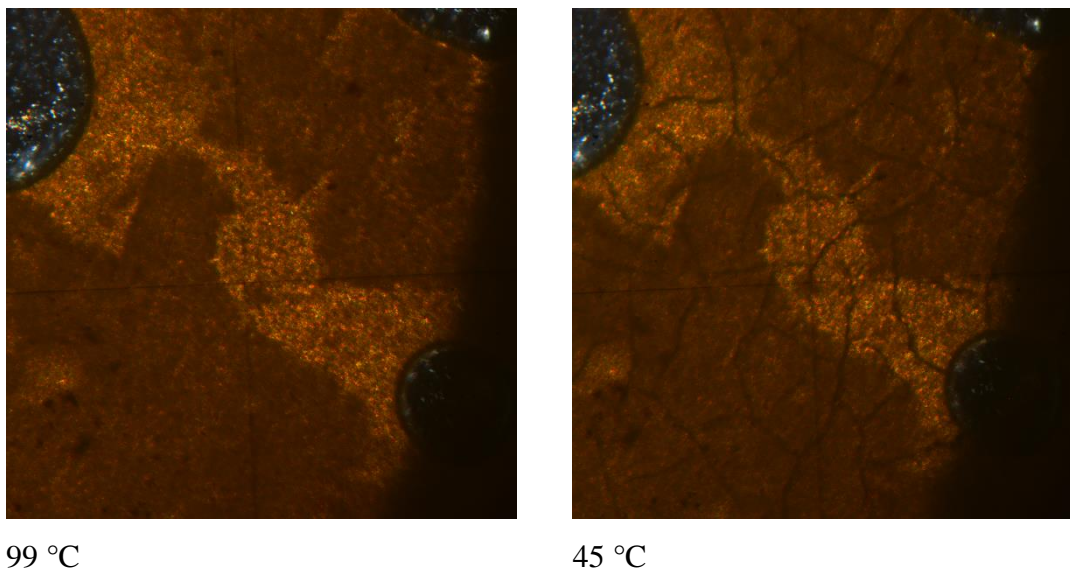


Figure III.25. *Isotropic phase of PDF1 sample during cooling*

Polymers are known to adopt different conformations depending on temperature and solvents. During heating, the polymer chains experience an extension, allowing their parallelization. On the contrary, lower temperatures cause the macromolecules to form random coils. Due to the random arrangement of coils, the chains are less probable to reorient in order to allow the formation of mesophases. In this frame, the appearance of crystal liquid properties in PDF1 sample can be observed during the heating process, but the formation of mesophase during cooling is not present.

III.4. Surface characterization

Evaluation of the surface's energy is required with respect to the azopolysiloxanic films applications. In the context of support for cell cultures, the films are immersed in a solution which provides necessary nutrients to the cells. Consequently, the films surface must be hydrophilic enough to enable contact with the solution. Moreover, surface nanostructuration of films is dictated by the azo derivatives and their interaction with the surrounding matter. Polysiloxanes have flexible main chains that allow mobility to the azo derivatives, an important aspect to consider when reorganization processes are to be desired (for the mass transport). The presence of azo derivatives on the films surface influences the

azopolysiloxanes response to irradiation. Knowing that polysiloxanes are intermediary hydrophobic compounds, assessment of the azopolysiloxanes surface properties can offer information about the distribution of azo derivatives towards the film surface

We perform contact angle measurements in static regime at room temperature with Drop Shape Analyzer – DSA100 goniometer from KRUSS. The analyzed azopolysiloxanic films (thickness $\delta = 400 - 600$ nm) are deposited on silanized glass substrates through spin coater technique. Sessile drop method was employed with 15 μ L volume of droplets, and at least 5 measurements for each sample. Estimation of the drop profile uses an equation for conical section. The contact angle is given by the derivate of this equation at the intersection point between the tangent of drop profile and the base line.

We summarize the results obtained on the analyzed films in the following table.

Table III.4. Average values of contact angle measurements.

Sample	Linear polysiloxane	PFF1	PDF4	PNF2	PAF4
Substituent	-	Phenyl azophenol	Diphenyl azophenol	Napthalene azophenol	Anthracene azophenol
Contact angle, °	83	86	98	92	93

Please note that even if polysiloxanes are regarded as hydrophobic materials in general due to their chemical structure, literature shows that the contact angle can largely vary from 115 ° to 54 °, passing thus from the hydrophobic domain to the hydrophilic one. This change in its surface properties depends on various factors like measuring temperature, time of exposure in air and humidity prior to measuring, molecular weight, substrate of deposition, film thickness. Under the conditions specified above, we obtained an 83 ° contact angle for the unmodified polysiloxane film. Azobenzene is also regarded as a hydrophobic molecule, but the surface energy within the different derivatives varies in function of their specific chemical structure, and their polarity implicitly. Thus, we can interpret our results in a relative manner, by comparing the linear unmodified polysiloxane to the one modified with different azo derivatives.

Given the fact that the measurement of contact angles of azopolysiloxanes samples are higher than the polysiloxane, the results suggest the presence of azobenzenic groups on the film's surface. Within all the samples, PDF4 (32 % diphenyl azophenol) shows enhanced

hydrophobicity. However, even if all samples show values little over 90° (the intermediary domain), allow good performance with regards to the biological applications, when films are to be immersed in an aqueous solution.

III.5. Conclusions

We synthesized a series of polysiloxanes modified with different azo derivatives of various substitution degrees (S_d). Starting from the classical azobenzene, **4 – (phenylazo)phenol**, we obtained the PFF set with 52, 61 and 99 % S_d . Following this, we designed new azobenzenes in order to obtain molecules with different geometries and sizes. **4 – (4'-diphenylazo)phenol** has three aromatic cycles in its structure, resulting in a longer molecule. Linking to the polysiloxane side chain, we form the next set of samples, called PDF ($S_d = 31, 32, 58$ and 84 %). We also design two azo derivatives with condensed aromatic nuclei (naphthalene and anthracene). PNF series is polysiloxane modified with **4 – (1'-naphthaleneazo)phenol** ($S_d = 31$ and 72 %), and PAF series has **(2'-anthraceneazo)phenol** ($S_d = 28, 30, 43$ and 84 %).

The azopolysiloxanes are further characterized to evaluate their thermal stability with regard to the nanostructuration process that subject the film samples under laser irradiation, but also to the sterilization condition needed for biological applications. We find that all the azopolysiloxanes investigated present thermal stability up to at least 251 °C, when the first degradation step begins. We also estimate the glass transition temperature, which lays in the $34 - 51$ °C range for all samples. Differential scanning calorimetry reveals a possible first order transition for PDF1 sample. Azobenzenes class is well known and studied for their mesogens properties, but as substituent in a polymeric system creates a new context. Nanostructuration requires good optical properties, thus amorphous polymers are preferred. Consequently, PDF1 is investigated through polarized light microscopy. We observed the appearance of mesophases in function of temperature. PDF1 displayed a mesophase in the temperature range $T = 188 - 199$ °C during heating.

Lastly, considering that when tested for suitability as support in cell cultures the azopolysiloxane films are immersed in an aqueous solution, we evaluated the surface energy of films deposited on silanized glass. The films present a contact angle around 90 °, which is the intermediate value between hydrophilic and hydrophobic domains. We estimate that the azo derivatives present at the film surface bring their contribution in lowering the surface energy (increase contact angle).

CHAPTER IV. Photoisomerization studies

IV.1. Photoisomerization capacity of different azopolysiloxanes

Photoisomerization studies offer important information about the azopolysiloxanes' capacity to answer to light stimuli. Azobenzenic molecules absorb light energy due to their chromophore group $-N=N-$ and change their configuration from trans to cis and backwards. These motions induce the rearrangement of surrounding matter. Thus, when linked to polymeric chains, this property can be exploited to drive mass transport processes which finally lead to SRG.

We evaluate the trans – cis isomers conversion in time while the films are exposed to UV or Vis light. We quest for the maximum value of isomers conversion and the necessary time to reach it, when the equilibrium sets in, namely the kinetics of cis conversion. After equilibrium, further irradiation of the sample determines the decrease of cis isomer, meaning the reverse process cis – trans isomerization is more intense.

The azo derivatives we synthesized have different light absorption bands for the two isomer configurations. The next picture displays the absorption spectra for the wavelength range $\lambda = 300 - 600$ nm where the azo derivatives are known to absorb (*Figure IV.1*). Measurements were registered on a Shimatzu UV-1700 spectrophotometer.

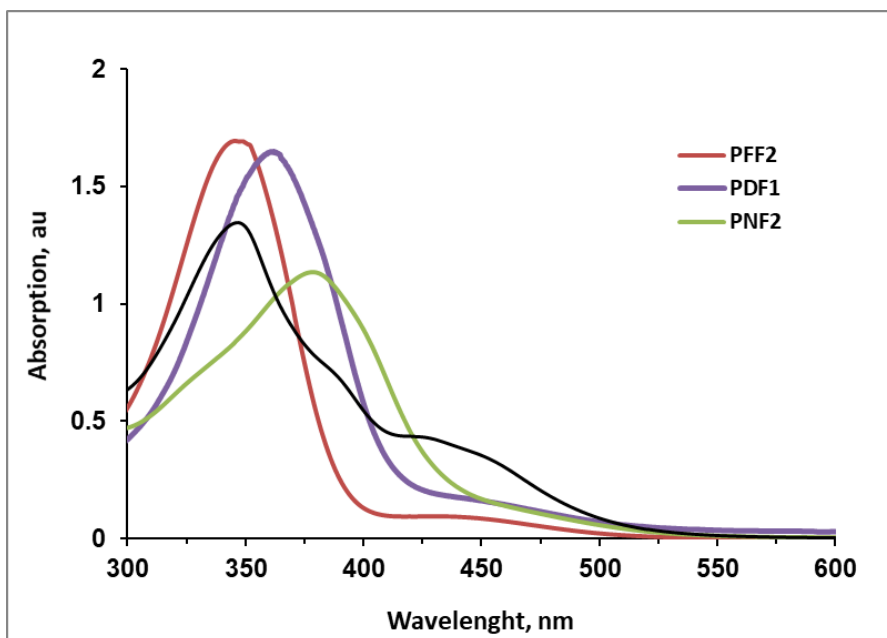


Figure IV.1. Absorption spectra of azopolysiloxane solutions displaying the characteristic maxima to the two isomers *trans* (first peak) and *cis* (second peak).

Trans isomer presents a maximum of absorption at different values, function of the chemical structure of the derivative, as listed below (Table IV.1.).

Table IV.1. Maximum absorption wavelength of *trans* isomer.

Sample	PFF2	PDF1	PNF2	PAF4
Substituent	Phenyl azophenol	Diphenyl azophenol	Napthalene azophenol	Anthracene azophenol
λ_{max} , nm	345	362	380	347

Evaluation of the *cis* – *trans* equilibrium is based on the fact that the two isomers have different absorption maximums. We monitor the *cis* conversion at $\lambda = 365$ nm for all the azopolysiloxanes, a wavelength that is found inside the *trans* absorption peak. Prior to measurements, the samples are held in the absence of light, thus we can assume that the azopolysiloxane is completely relaxed and all isomers are in *trans* configuration. Consequently, the *cis* conversion is calculated with the following formula (Equation IV.1).

$$cis \% = 100 - \left(\frac{100 \cdot A_{(t=0)}}{A_{(t=i)}} \right)$$

Equation IV.1.

where $A_{(t=0)}$ is the initial absorption measured at time $t = 0$ and $A_{(t=i)}$ is the absorption measured at time $t = i$.

The photoisomerization studies are performed on films of $\delta = 400 - 600$ nm thickness, deposited through spin – coating technique on silanized glass substrates. We use an UV lamp of 100 W equipped with a $\lambda = 365$ nm filter. For the irradiation in the Vis domain we use a light source of 12 W that presents a maximum absorption band at $\lambda = 451$ nm. The absorption is monitored throughout the irradiation experiment with a Boeco SI UV spectrophotometer.

IV.2. Isomerization under UV light

We carry photoisomerization tests on films of polysiloxanes substituted with different azo derivatives using two UV light intensities: $I = 4$ and 22 mW/cm^2 . Light intensity is known to be an influence factor in the azo materials capacity to answer to light stimuli, as well as the wavelength. We compare here the UV light induced isomerization for four different samples (*Figures IV.2. – 5*).

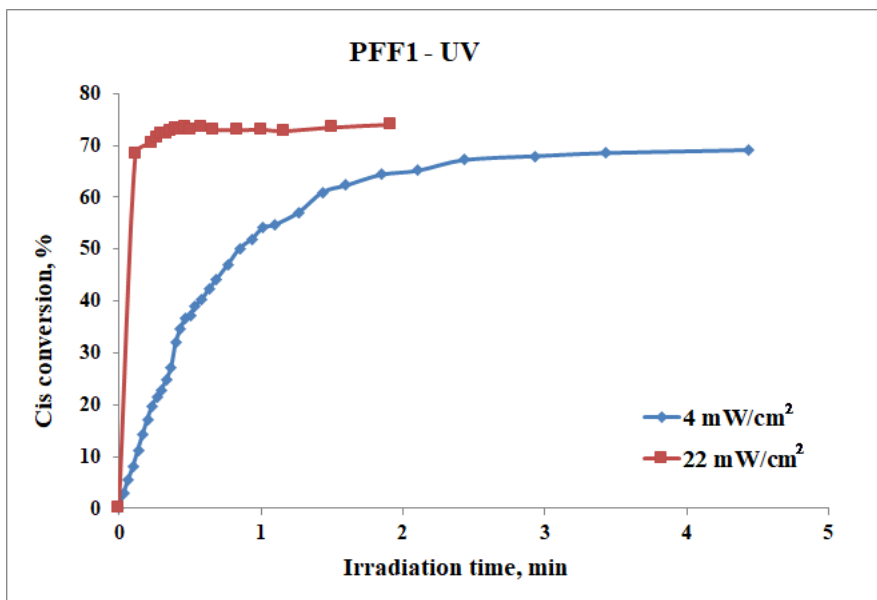


Figure IV.2. Isomerization kinetics under UV light of two intensities $I = 4$ and 22 mW/cm^2 for PFF1 sample (polysiloxane 99 % substituted with 4 – (phenylazo)phenol).

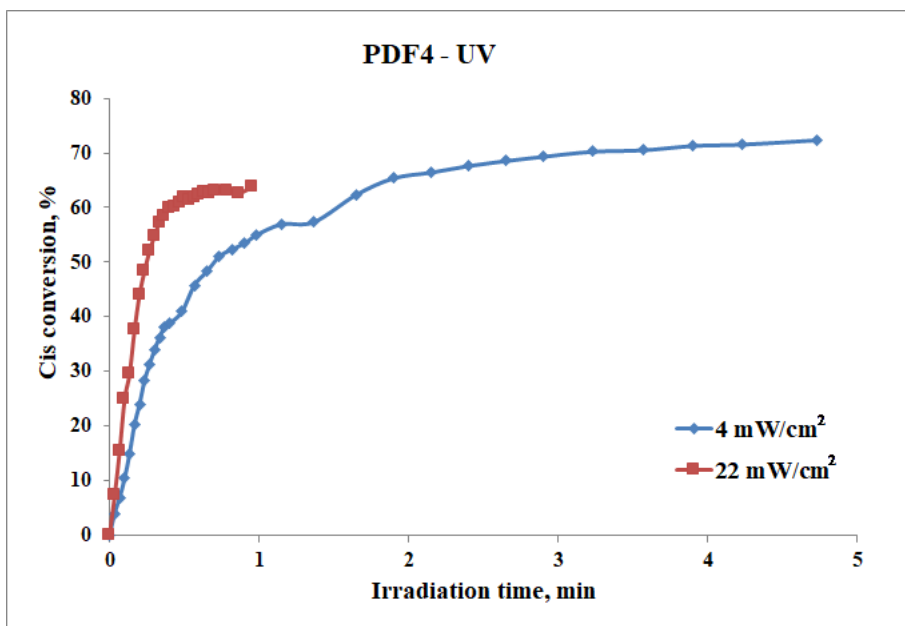


Figure IV.3. Isomerization kinetics under UV light of two intensities $I = 4$ and 22 mW/cm^2 for PDF4 sample (polysiloxane 32 % substituted with 4 – (4'-diphenylazo)phenol).

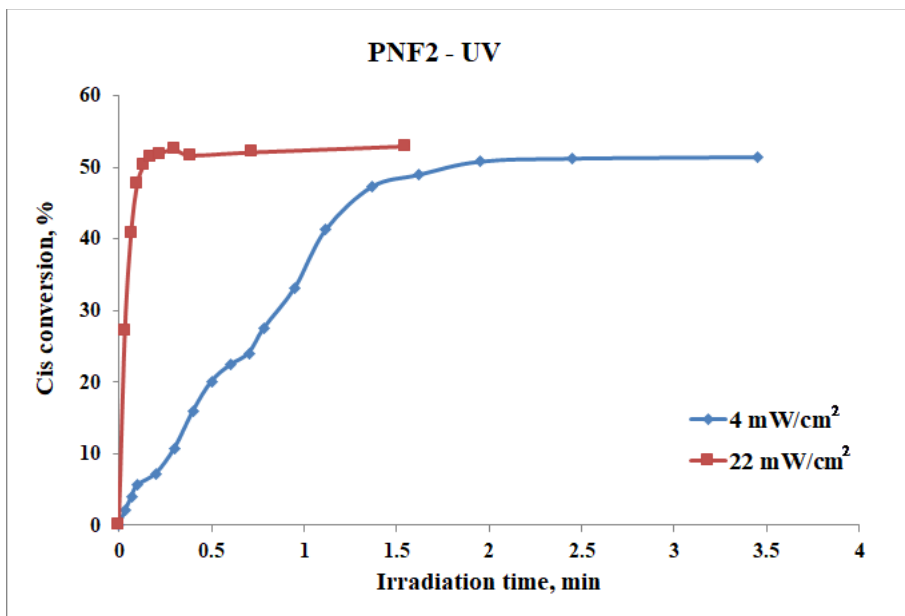


Figure IV.4. Isomerization kinetics under UV light of two intensities $I = 4$ and 22 mW/cm^2 for PNF2 sample (polysiloxane 31 % substituted with 4 – (1'-naphthaleneazo)phenol).

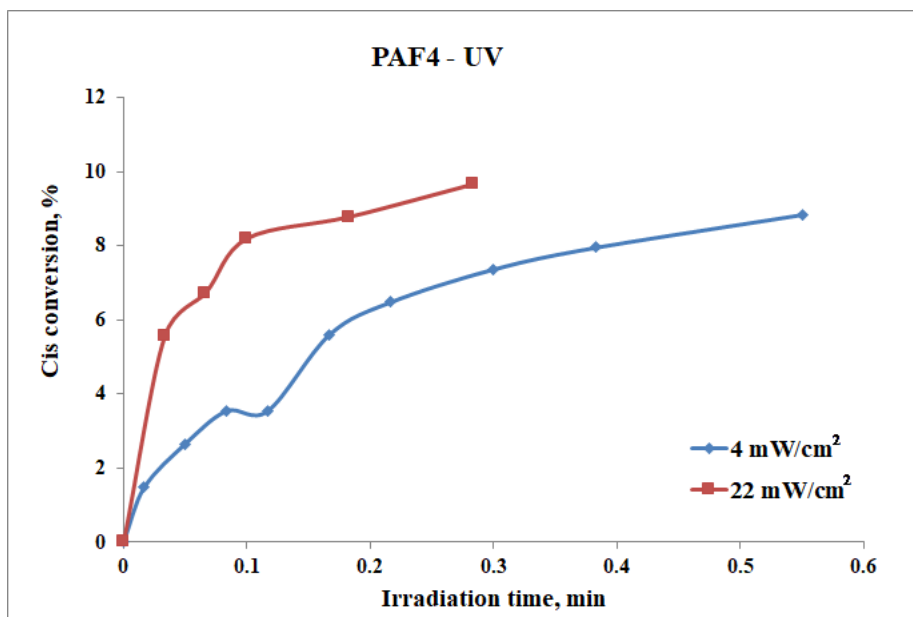


Figure IV.5. Isomerization kinetics under UV light of two intensities $I = 4$ and 22 mW/cm^2 for PAF4 sample (polysiloxane 28 % substituted with 4 – (2'-anthraceneazo)phenol).

Our studies reveal the progression in time of isomerization process of azobenzenes found on the side chains of polysiloxanes.

The cis conversion at equilibrium reaches different values for the four samples. PFF1 behavior shows a very fast increase in cis isomer up to 70 (4 mW/cm²) and 75 % (22 mW/cm²). In the first two – three minutes of irradiation, the conversion is already close to its maximum for both intensities, but the sample irradiated with lower intensity exhibits a delay in reaching the equilibrium. Lower intensity means lower power in the given time.

PDF4 has a similar answer in what regards the setting of equilibrium but opposite, highest cis conversion 76 % reaches corresponds to the lower intensity, while lowest cis conversion 64 % corresponds to the higher intensity. Again, the setting of equilibrium for low intensity lingers (irradiation time up to about 1 h).

PNF2 samples set cis equilibrium in a shorter time than the previous samples, PFF1 and PDF4, but cis conversion is also lower (51 % for 4 mW/cm² and 53 % for 22 mW/cm²). In about one minute, the conversion already reaches towards equilibrium.

PAF4 azopolysiloxane is the sample that has the smallest response to UV light irradiation, lower (9 % for 4 mW/cm² and 10 % for 22 mW/cm²). Also, the equilibrium

installs in a very short time, around half a minute. The substituent of PAF4, anthracene azophenol, is voluminous, thus a possible explanation could stand in the steric hindrance.

IV.3. Isomerization under Vis light

We perform another set of tests on the azopolysiloxane samples, using Vis light for irradiation (*Figures IV.6. – 9.*). As before, we compare two light intensities $I = 4$ and 22 mW/cm^2 .

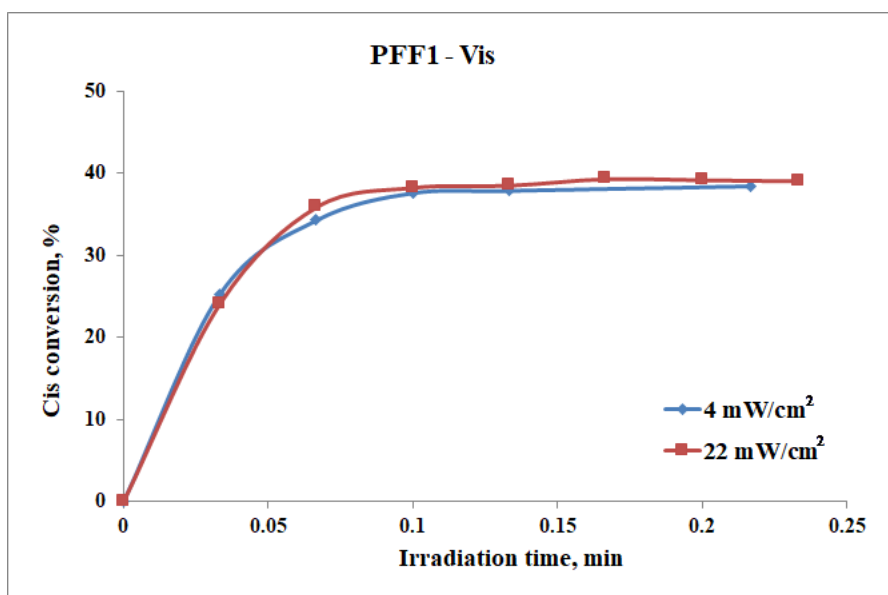


Figure IV.6. Isomerization kinetics under Vis light of two intensities $I = 4$ and 22 mW/cm^2 for PFF1 sample (polysiloxane 99 % substituted with 4 – (phenylazo)phenol).

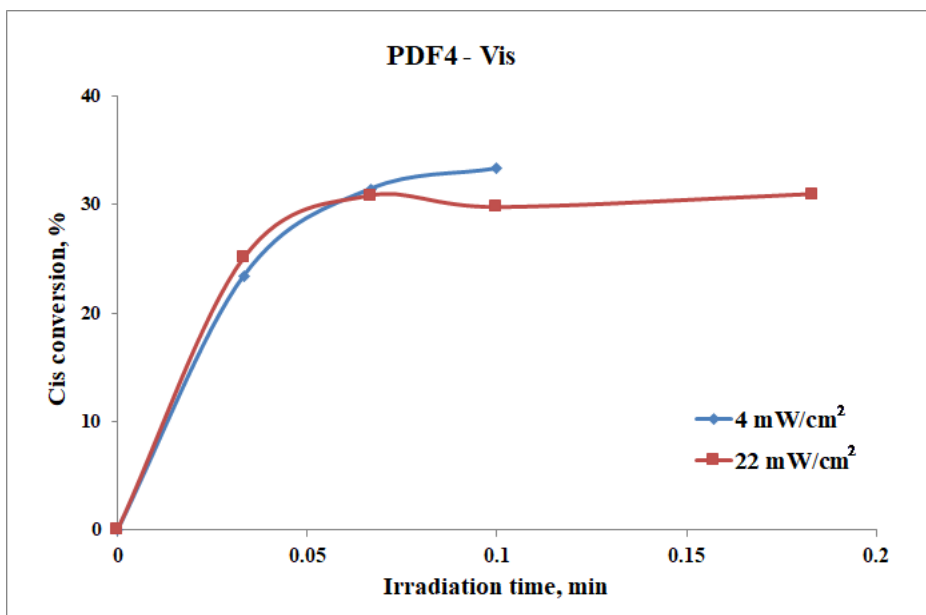


Figure IV.7. Isomerization kinetics under Vis light of two intensities $I = 4$ and 22 mW/cm^2 for PDF4 sample (polysiloxane 32 % substituted with 4 – (4'-diphenylazo)phenol).

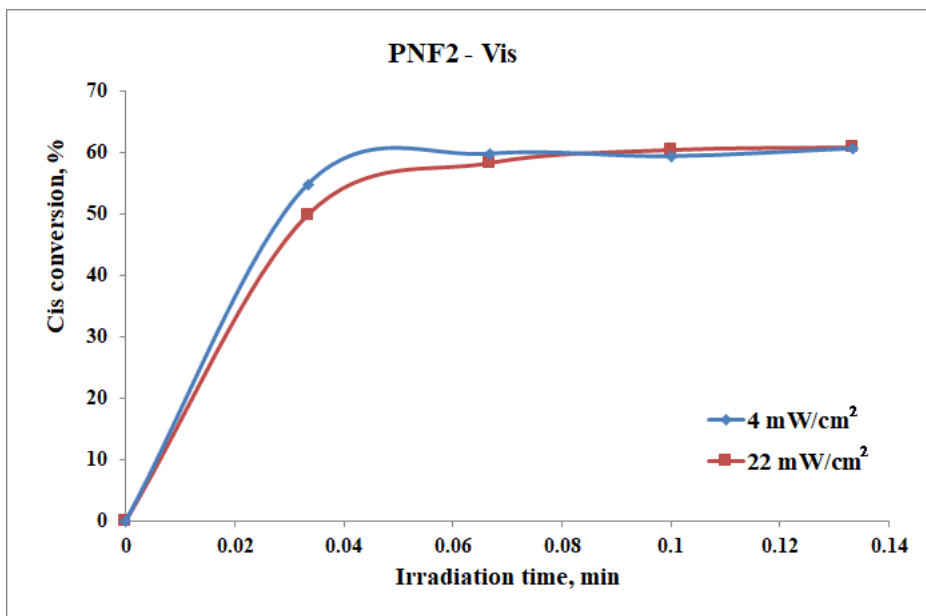


Figure IV.8. Isomerization kinetics under Vis light of two intensities $I = 4$ and 22 mW/cm^2 for PNF2 sample (polysiloxane 31 % substituted with 4 – (1'-naphthaleneazo)phenol).

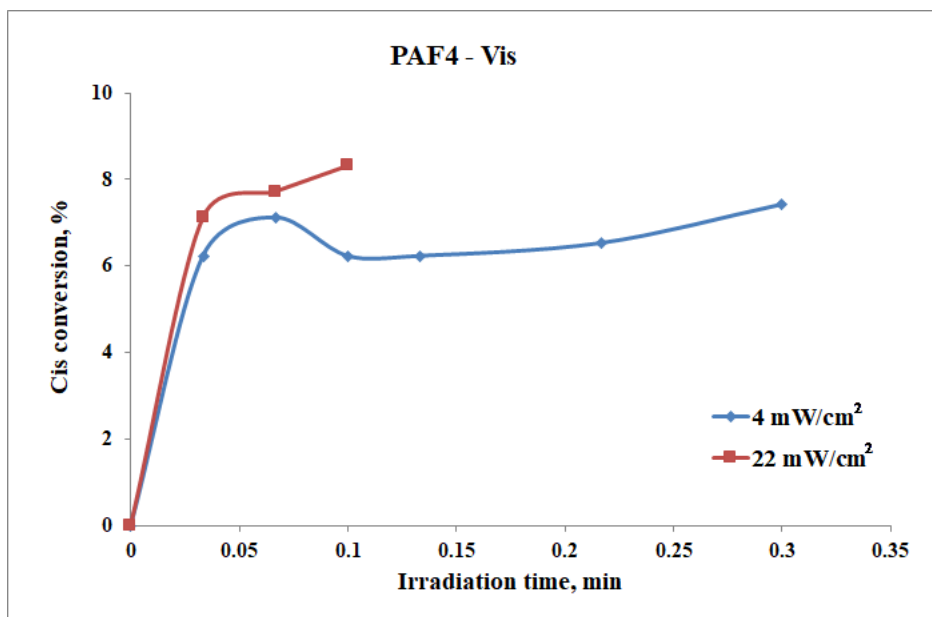


Figure IV.9. Isomerization kinetics under Vis light of two intensities $I = 4$ and 22 mW/cm^2 for PAF4 sample (polysiloxane 28 % substituted with 4 – (2'-anthraceneazo)phenol).

As general observation, irradiation in the Vis domain, determines a faster answer in azopolysiloxanes, all samples reach conversion equilibrium in less than half minute. However, the cis conversion is lower or about the same value than their UV counterparts. Exception from this rule is PNF2 sample that presents a distinct response, meaning that Vis irradiation enables a higher cis conversion than UV irradiation with no significant difference between the two intensities, 61 % in 8 s.

Light intensity causes no significant difference in the PFF1 sample either. Cis conversion, 38 % for 4 mW/cm^2 and 40 % for 22 mW/cm^2 .

PDF4 film's behavior is surprising; it presents 36 % cis conversion for low intensity and 31 % for high light intensity.

At last, PAF4 sample shows the weakest response, with a conversion of only 7 % (4 mW/cm^2) and 8 % (22 mW/cm^2).

IV.4. Conclusions

We test the photoisomerization capacity of the different azopolysiloxanes films deposited on a silanized glass substrate. We analyze polysiloxanes modified with azo derivatives PFF1: 4 – (phenylazo)phenol; PDF4: 4 – (4'-diphenylazo)phenol; PNF2: 4 – (1'-naphthaleneazo)phenol and PAF4: 4 – (2'-anthraceneazo)phenol. For irradiation two sources are used, in UV and Vis light wavelength domains, with two intensities $I = 4$ and 22 mW/cm^2 . Two samples, PFF1 and PDF4 reach the highest cis conversion when irradiated with UV light, while PNF2's cis conversion is favored by the Vis domain and PAF4 film presents the weakest capacity to photoisomerize. We see that the light intensity has lower influence than the irradiation domain. We summarize these findings in *Figure IV.10*.

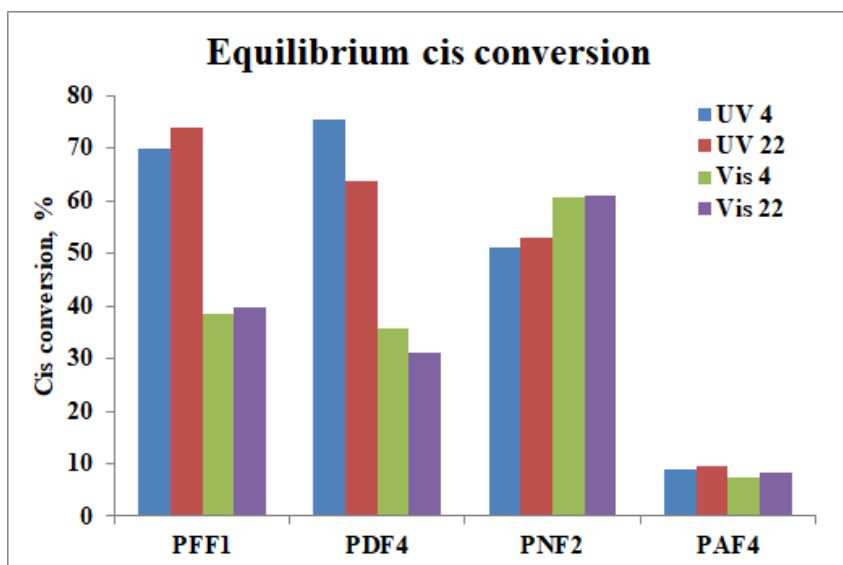


Figure IV.10. Cis conversion at equilibrium under UV and Vis light at two intensity values $I = 4$ and 22 mW/cm^2 .

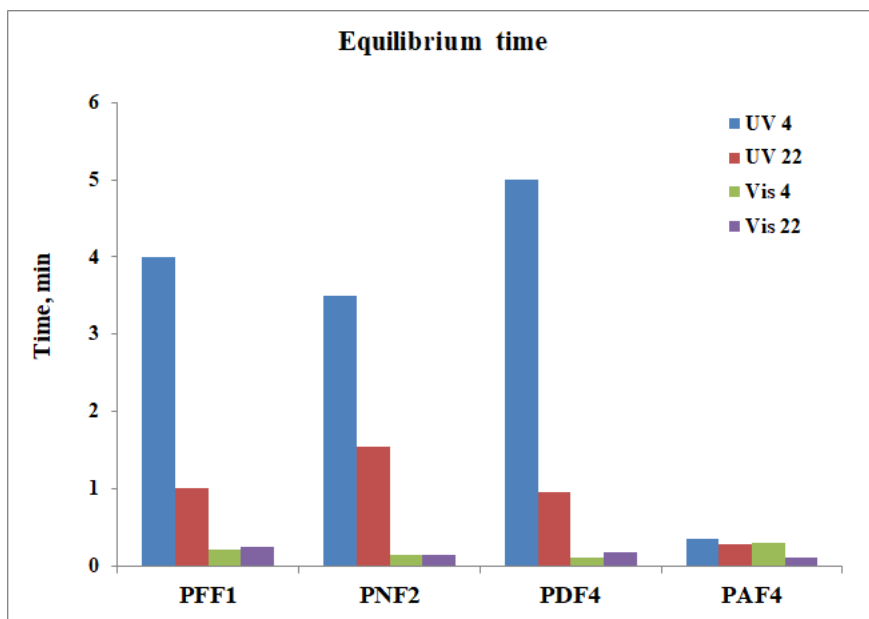


Figure IV.11. Necessary time to reach equilibrium under UV and Vis light at two intensity values $I = 4$ and 22 mW/cm^2 .

Regarding the time necessary to reach the cis conversion equilibrium, the differences are plain clear between UV and Vis domains. When irradiated with UV light, all the azopolysiloxanes need more time to reach equilibrium, from one minutes to 5 minutes. Even though this difference seems big, by looking at the kinetics for PDF4, which exhibits the longer time, 5 minutes, it can be observed that, in fact, after 2 minutes, the conversion is already close to its maximum, showing a very slow increase (around 5 percent) for the next 3 minutes. When Vis light is used for irradiation, the equilibrium usually sets in less than half a minute. *Figure IV.11.* displays this comparison between the studied samples.

CHAPTER V. Photochromic behavior

V.1. Strategy overview

The azopolysiloxanes photochromic behavior is investigated to gain insight into the complex mechanism that enables azopolymeric films to generate SRG under irradiation. For the nanostructures to form on the surface of the films, the material has to experience a mass displacement at micrometric level. Even if this phenomenon of mass transport has long been observed, no all-comprehensive model has yet been proposed and the subject is still under debate.

The present study is structured based on the different parameters of the irradiation setup, that is light intensity and the presence of assistance light. Various test are ran for the four azobenzene derivatives used as substituents on the polysiloxane main chain.

In the next table (*Table V.1.*), several characteristics referring to the azopolysiloxane and the obtained films are presented.

Table V.1. *Characteristics of film samples*

Sample	azobenzene derivative	Substitution degree, %
PFF3	4 – (4'-phenylazo)phenol)	99
PDF1	4 – (4'-diphenylazo)phenol)	84
PDF4	4 – (4'-diphenylazo)phenol)	32
PNF1	4 – (1'-naphthaleneazo)phenol)	72
PAF2	4 – (2'-anthraceneazo)phenol)	43

The sample's irradiation is done with an Ar⁺ laser (p-p polarization, wavelength $\lambda = 514.5$ nm, energy $h\nu = 2.41$ eV, beam diameter $\Phi = 1.75$ mm, . The *writing* beam is split and the two resulting beams meet on the film surface under a 13° angle, which gives a grating period $\Lambda = 2.4$ μm . Experiments have been carried out for two light intensities: $I_1 = 2.3$ W/cm² ($P_{\text{Ar}} = 14$ mW) and $I_2 = 4.2$ W/cm² ($P_{\text{Ar}} = 26$ mW). An additional light source, LDM405 laser diode module, in the violet/blue spectrum ($\lambda = 405$ nm, $P = 4$ mW, vertical polarization, $\Phi = 3 \times 5$ mm). This *assistance* light's wavelength is in between the absorption bands of the azobenzenes derivatives cis and trans forms, thus both isomers have equally chances to be excited by it. Being vertically polarized, it addresses to the azobenzenes that are perpendicular to its polarization plane, thus to the ones that are parallel to the polarization vector of the writing light. This way, the assistance light excites the azo molecules that are “invisible” to the writing beam and are thus “blocked”. Consequently, the blue light intensifies the photoisomerization process by constantly exciting azobenzenes that cannot be excited by the writing light and vice versa. The grating formation is probed with a *reading* beam from a He-Ne laser ($\lambda = 632.8$ nm and $h\nu = 1.96$ eV).

During the experiments, the assistance light, but also the writing light, are set ON and OFF to try to differentiate between different behaviors that the azopolysiloxanes present.

V.2. Photochromic behavior of PFF3: polysiloxane with 4 – (phenylazo) phenol

The film was prepared from a concentrated solution of polysiloxane 99 % substituted with 4 – (phenylazo)phenol) in 1,1,2 – trichloroethane (sample PFF3) through spin coating and left to dry at least 2 days before experiments. Films of 300 or 500 nm thickness were deposited on glass slides.

V.2.1. Set 1

The first set of irradiation experiments was carried on 500 nm thickness films with low and high light intensity (*Figures V.1. – 7.*), with the assistance light ON or OFF.

The azopolysiloxane films behave very differently in what regards their photochromic behavior, depending on both light intensity of writing beam and the presence

of blue assistance light. At low intensity $I = 2.3 \text{ W/cm}^2$, the presence of assistance light beam on the sample determines a cyclic writing – erasing phenomenon. The first order diffraction grows rapidly in the first 2 minutes of irradiation, then follows a first peak (difficult to observe on the whole scale, but clear on a larger scale), then a second, having a total of 7 peaks during irradiation under blue light assistance (*Figure V.1.*). Examining the evolution of local first order diffraction maxima during irradiation time (*Figure V.2.*), the peaks distribution can be approximatively fitted to an exponential growth.

$$y = 2.02e^{0.54x}$$

Equation V.1.

A change in this behavior takes place when the assistance light is switched OFF (blue down arrow on graph), disrupting this cyclic evolution. It suggests that without the supplementary blue light to reorient the azobenzene molecule in a position favorable to absorb the writing beam light, the grating process slows down and follows another mechanism. The writing – erasing processes competition is less intense. By switching OFF the writing light (green down arrow) also, we observe a fast decrease of the first order diffraction power.

Regarding the time evolution of first order diffraction for the sample irradiated without assistance light, the behavior follows a steady growth up until approx. half the value when assistance light is ON. No peaks are observed without the assistance light, suggesting that the writing process takes place undisturbed by the extra reorientation of azobenzene.

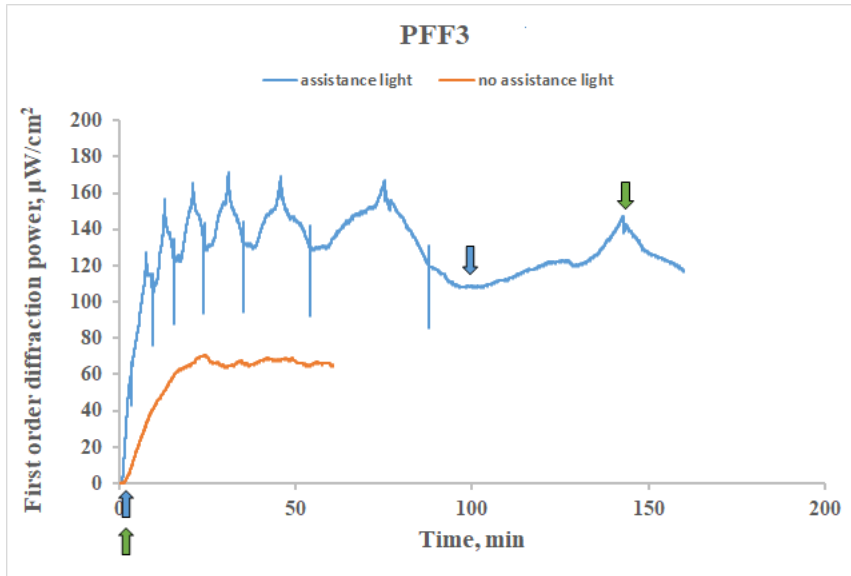


Figure V.1. First order diffraction power evolution in time at low intensity irradiation $I = 2.3 \text{ W}/\text{cm}^2$ with and without assistance light. Up/down arrows represent ON/OFF positions of writing light (filled with green) and assistance light (filled with blue).

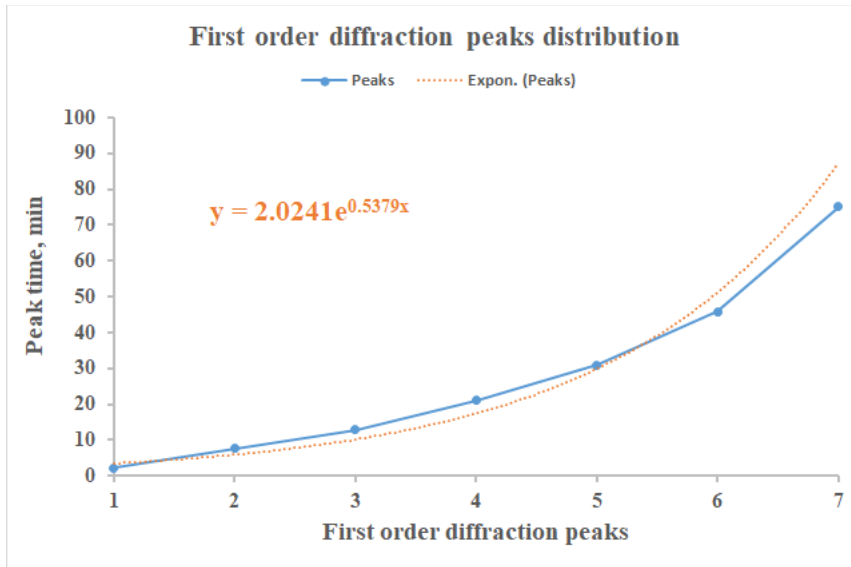


Figure V.2. Distribution of first order diffraction peaks at low intensity irradiation $I = 2.3 \text{ W}/\text{cm}^2$ with assistance light.

The diffraction efficiency (Figure V.3.) of irradiation assisted by blue light shows a rather steady evolution, rather than increasing steps, as the first order diffraction power. This behavior is assimilated to the increase of diffraction power in zeroth order, which represents the transmitted light through the sample. During irradiation, it can be observed that the

opacity of the film decreases, a fact that allows higher light transmittance. Due to this fact, the growth of both diffraction order powers (zeroth and first), the efficiency presents a more linear evolution. Without assistance light, no growth of zeroth order diffraction power (Figure V.4.) is registered. This determines a linear evolution of efficiency, after it reaches a plateau, like the first order diffraction envisions.

A very important aspect of the presence of assistance light during irradiation is not only in the evolution behavior, but also in the maximum diffraction efficiency values reached for both samples. The assistance of blue light during the writing process determines higher efficiency, maximum 0.89 %, compared with 0.27 %, the maximum reached without assistance light.

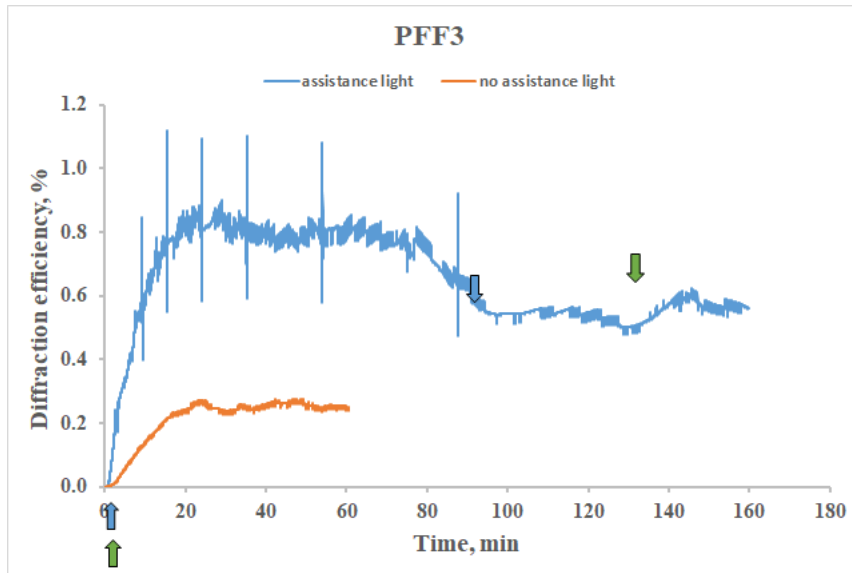


Figure V.3. Diffraction efficiency in time at low intensity irradiation $I = 2.3 \text{ W/cm}^2$ with and without assistance light. Up/down arrows represent ON/OFF positions of writing light (filled with green) and assistance light (filled with blue).

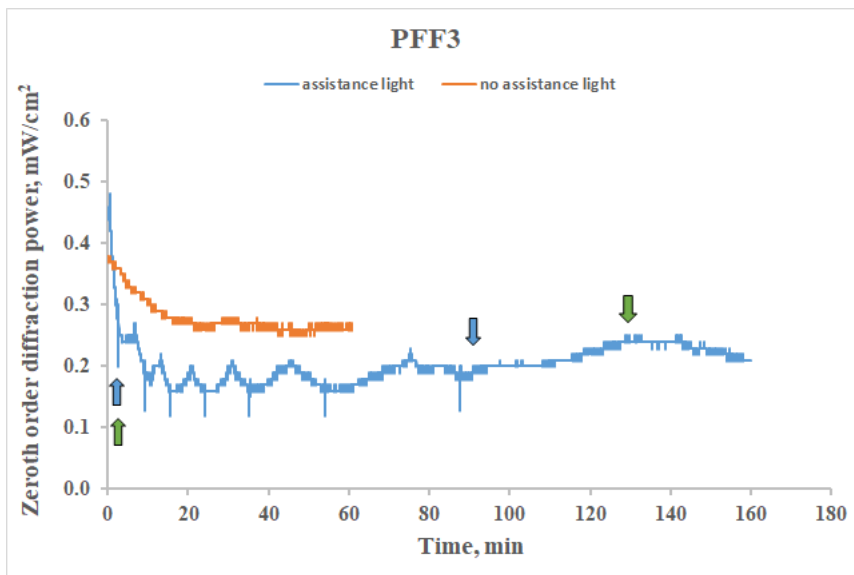


Figure V.4. Zeroth order diffraction power evolution in time at low intensity irradiation $I = 2.3 \text{ W/cm}^2$ with and without assistance light. Up/down arrows represent ON/OFF positions of writing light (filled with green) and assistance light (filled with blue).

Second part of this set of experiments uses light of higher intensity, $I = 4.2 \text{ W/cm}^2$ (Figures V.5. – 7.). The samples behave very differently compared to the ones irradiated at lower intensity. The maximum diffraction efficiency is reached when the assistance light is OFF, even if the time required is a bit longer than for the sample irradiated with the assistance light ON. Azobenzene reorientation induced by the blue light in polymer does not favor the writing of surface grating. Further difference from lower intensity results is observed in the allure of the curves. The kinetics is very similar for both samples: with or without assistance light, the diffraction efficiency (Figure V.6.) increases linearly then reaches a plateau, and after it starts to decrease. These findings show that irradiation with high intensity light triggers another response, which excludes competition between writing and erasure processes. An important aspect to mention is that when the assistance light is switched OFF, the diffraction efficiency comes to a stand and when it is switched back ON, it increases. In these circumstances, it is difficult to assign the specific role of assistance light in creating the SRG.

One possibility is that the time assigned to the experiment at high intensity, even though it is relatively long (1 hour), is not enough to catch eventual changes in the photochromic behavior.

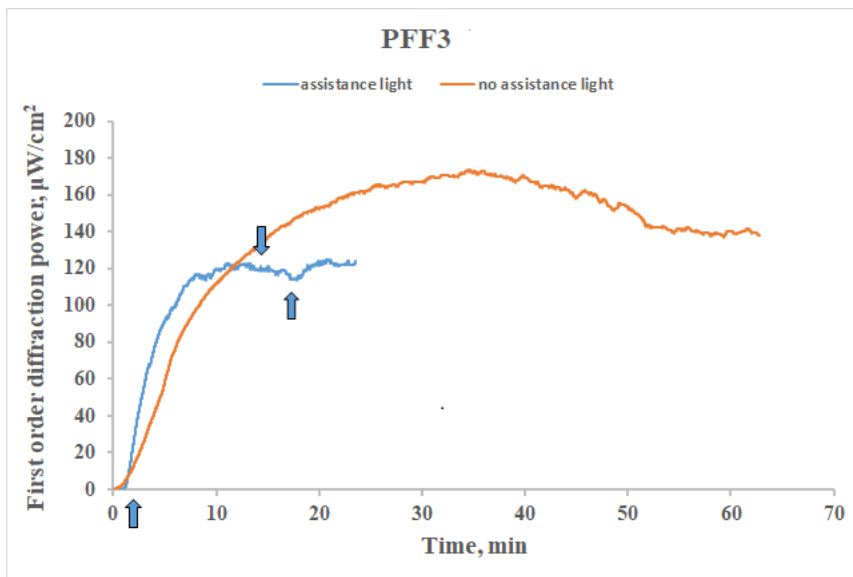


Figure V.5. First order diffraction power evolution in time at high intensity irradiation $I = 4.2 \text{ W/cm}^2$ with and without assistance light. Blue up/down arrows represent ON/OFF positions of assistance light.

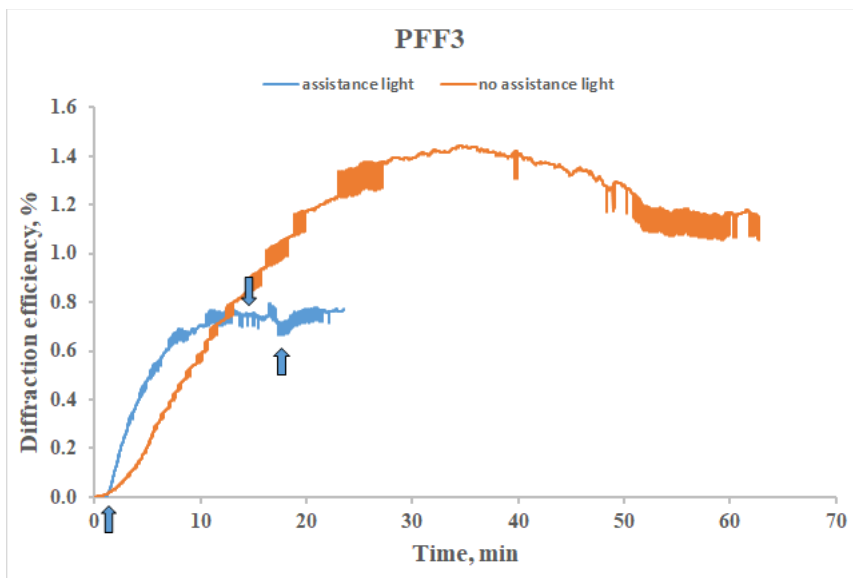


Figure V.6. Diffraction efficiency in time at high intensity irradiation $I = 4.2 \text{ W/cm}^2$ with and without assistance light. Blue up/down arrows represent ON/OFF positions of assistance light.

The main important difference in Set 1 experiments rests in the behavior relative to the presence of assistance light. While it favors grating inscription at low intensity, it seems to hinder it at higher intensity.

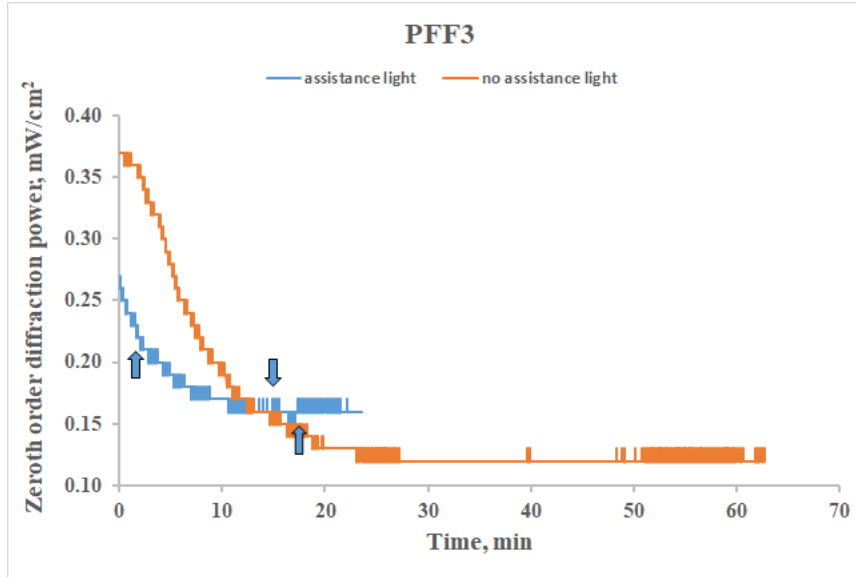


Figure V.7. Zeroth order diffraction power evolution in time at high intensity irradiation $I = 4.2 \text{ W/cm}^2$ with and without assistance light. Blue up/down arrows represent ON/OFF positions of assistance light.

Table V.1. Irradiation results for Set 1: PFF3 film of 500 nm thickness.

Property \ Light intensity, W/cm^2	2.3		4.2	
	Assistance ON	Assistance OFF	Assistance ON	Assistance OFF
Max η_D , %	0.86	0.26	0.78	1.44
t(Max η_D), min	27	25	21	35

Max η_D – maximum value of diffraction efficiency;

t(Max η_D) – time at which the maximum value of diffraction efficiency is reached.

V.2.2. Set 2

The second set of irradiation experiments (*Figures V.8. – 13.*) refers to PFF3 films of 300 nm thickness, irradiated at low intensity light with the assistance light ON and OFF.

First part of the experiment (*Figures V.8 – 10.*) in this set compares two samples, one irradiated in the presence of blue light, one without. To observe how the presence of blue light affects the behavior compared with the basic setup of green writing light, the assistance

light is set ON in the first part of the experiment for 15 minutes, then turned back OFF. Very important to note here however is that even though the films have been prepared to have the same properties, some inhomogeneity in the film must have perturbed the amplitude of the answer. One explanation for this issue lies in the film preparation step: different initial orientation of the azobenzenes, meaning that instead of a random orientation, there is a preferential direction. Even so, the qualitative interpretation is not affected by this downside. Proceeding on this track, the following conclusions can be drawn from these findings. The behavior of the sample irradiated without assistance light shows a sinusoidal evolution in time with a relative regularity, showing the existing of the two concurrent processes: writing and erasure.

By switching the assistance light ON when the peak of starts to form, we investigate its influence on the equilibrium state. Considering that when the first order diffraction power reaches maximum value (local or global), it finds a (meta-)stable state, we investigate the effect of this (meta-)equilibrium induced by the blue light. We find that the assistance light determines a disturbance of the azobenzene molecules that reflects in levelling the diffraction efficiency, by maintaining it around 0.188 ± 0.002 % for the 15 minutes that the assistance light stays ON. After switching it OFF, the sample's behavior displays a fast decrease of diffraction efficiency near zero values. After this sudden drop, the diffraction starts to increase. Following this increase, a new peak is reached, then a fast increase, like at the beginning of the irradiation. This complex behavior shows the various processes that take place inside the material, once the azobenzene are reoriented according to the assistance light.

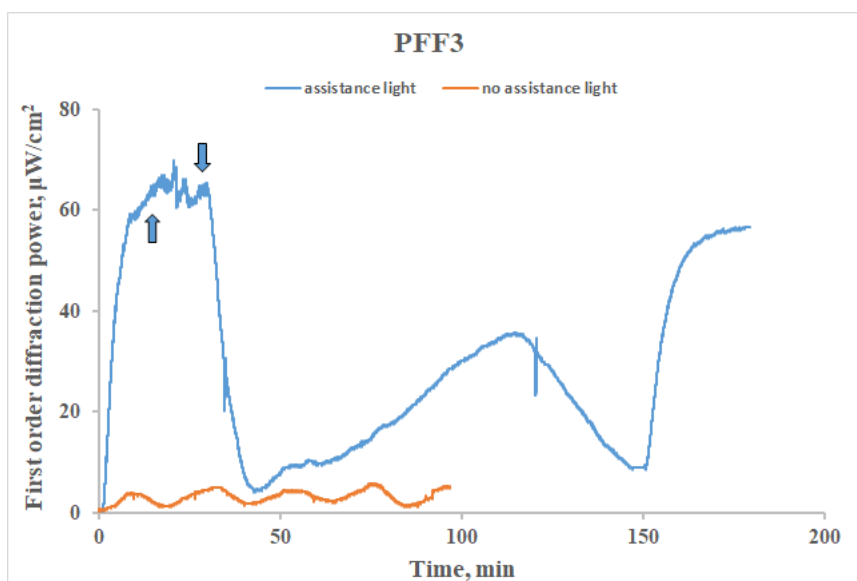


Figure V.8. First order diffraction power evolution in time at low intensity irradiation $I = 2.3 \text{ W/cm}^2$ with and without assistance light. Blue up/down arrows represent ON/OFF positions of assistance light.

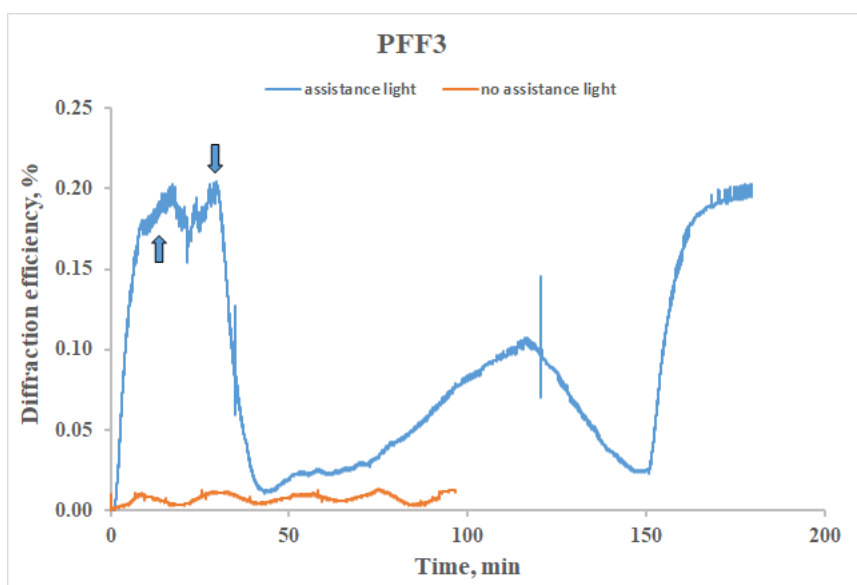


Figure V.9. Diffraction efficiency dependence on time at low intensity irradiation $I = 2.3 \text{ W/cm}^2$ with and without assistance light. Blue up/down arrows represent ON/OFF positions of assistance light.

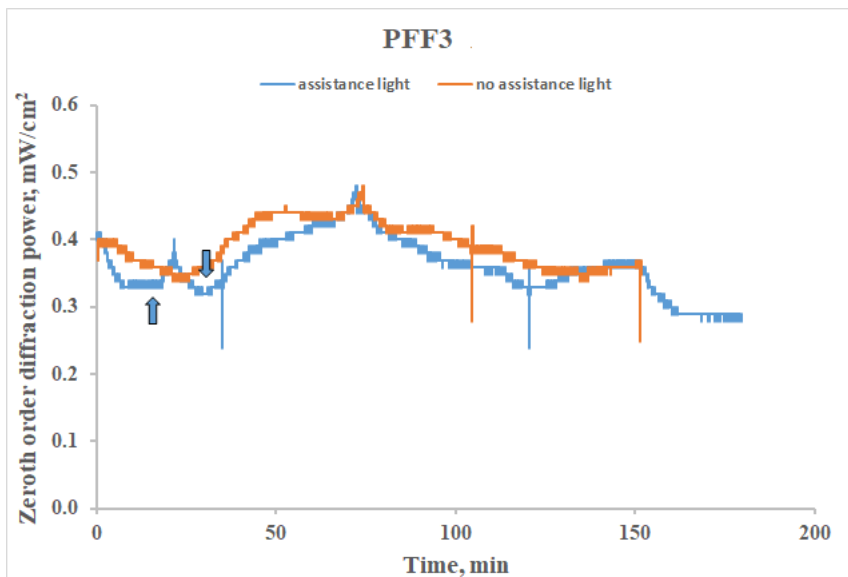


Figure V.10. Zeroth order diffraction power evolution in time at low irradiation intensity $I = 2.3 \text{ W/cm}^2$ with and without assistance light. Up/down arrows represent ON/OFF positions of assistance light (filled with blue) and writing light (filled with green; the orange outline shows the affiliation).

During and at the end of the experiment, 4 diffraction (red *reading* light) and self-diffraction (green *writing* light) can be observed, a clear sign of SRG inscription.

V.3. Photochromic behavior of PDF: polysiloxane with 4– (4'-diphenylazo) phenol

The films were prepared from concentrated solution of polysiloxane substituted 84 % (PDF1 sample) and 32 % (PDF4 sample) with 4– (4'-diphenylazo)phenol in a similar manner as PFF3 samples.

As specified in characterization of polysiloxane modified with this azobenzene derivative (*Chapter III*), solubility has raised significant issue, and obtaining a clear solution of high concentration was a challenging task. Chloroform was the best solvent from the ones tried, but depositing films from solutions of chloroform leads to another difficulty. The volatility of chloroform affects the optical properties of the films, affecting their transparency (the films become rather translucent). In these circumstances, the PDF films obtained in this study were not of the best optical quality. The unsuitable optical properties of the films

(especially PDF1 which has a higher substitution degree, 84 %) impedes a clear interpretation of the results.

Bearing this in mind, we mention that during the experiments, a large light halo could be observed on both PDF samples, an indicator that the total light diffraction has a significant component apart from the grating diffraction. Without the possibility to separate the diffraction due to the grating and the diffraction due to the intimal structure of the film, the resulting measured diffraction is highly probable to have large errors.

However, without attempting to make a quantitative analysis of these results, the following experiments present the behavior of two PDF film samples (*Figures V.11. – 13.*) with the intention to provide an idea about the possibilities of this azopolysiloxane to be used for SRG formation.

The first order diffraction dependence on time (*Figure V.11.*) displays an abrupt power increase with the ON setting of blue light. Irradiation with only the writing light does not affect the diffraction in the first minutes of the experiment. Only when adding the assistance light, the diffraction power increases. The large light halo that forms around the film sample and the lack of diffraction points of any order observed visually, suggest that the first order diffraction registered is mostly due to the unsuitable optical properties of the film. However, the exact fact that for the diffraction to experience a change during the experiment needed the supplementary assistance light, offers information about the existence of azobenzenes motion inside the polymeric film.

A note worth mentioned here is that the first order diffraction for PDF1 sample is much larger (another size range) than for PDF4 is due to the fact that the high substitution degree with azobenzene derivative contributed to the poor optical properties of the film.

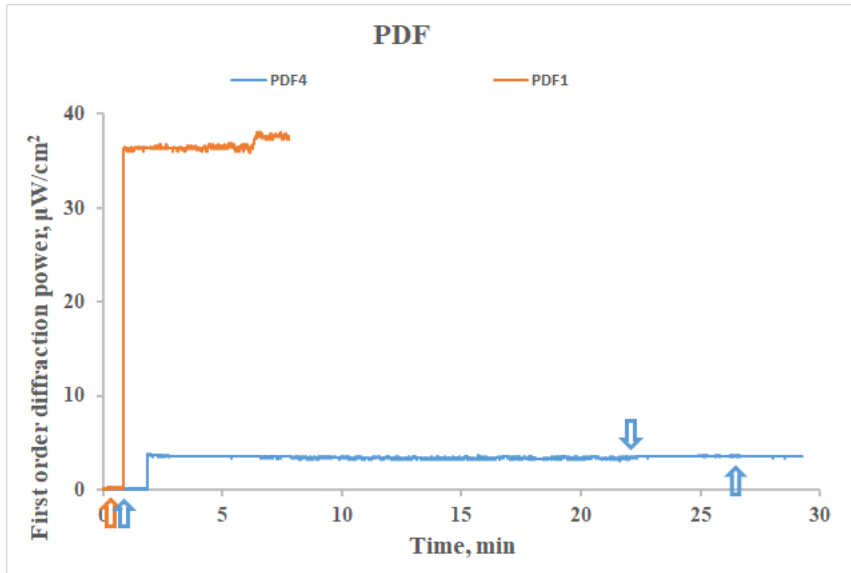


Figure V.11. First order diffraction power evolution in time for PDF1 and PDF4 samples at high intensity $I = 4.2 \text{ W}/\text{cm}^2$. Up/down-arrows represent ON/OFF positions of assistance light for PDF4 (blue outline) and PDF1 (orange outline).

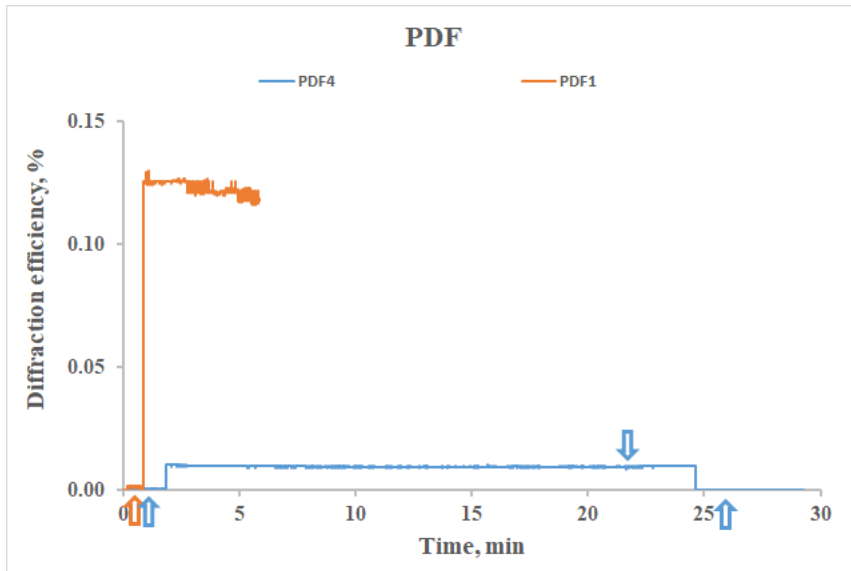


Figure V.12. Diffraction efficiency evolution in time for PDF1 and PDF4 samples at high intensity $I = 4.2 \text{ W}/\text{cm}^2$. Up/down-arrows represent ON/OFF positions of assistance light for PDF4 (blue outline) and (orange outline).

An observation that sustains the qualitative analysis statement of the presence of chromophores motion inside the film due to the light excitation from the blue spectrum wavelength is that the diffraction efficiency of PDF4 sample goes back to zero as soon as the assistance light is switched OFF.

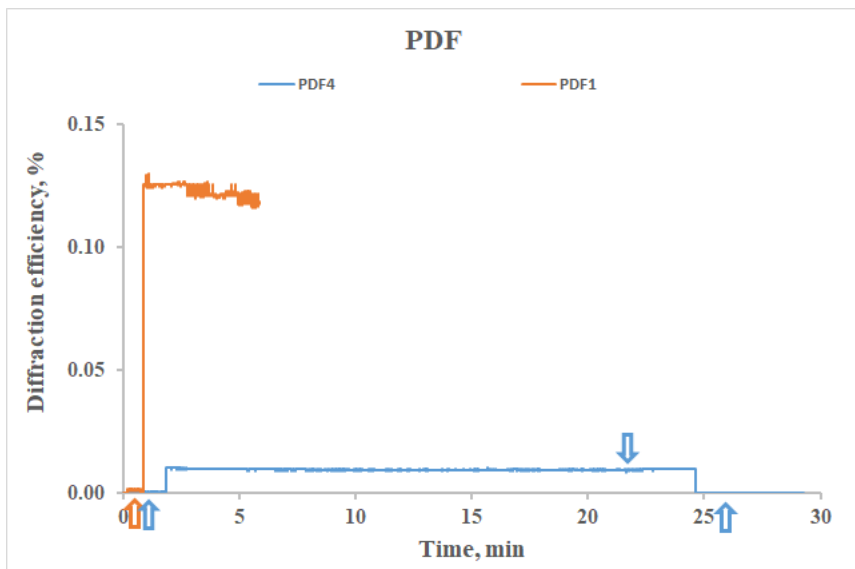


Figure V.13. Zeroth order diffraction power evolution in time for PDF1 and PDF4 samples at high intensity irradiation $I = 4.2 \text{ W/cm}^2$. Up/down-arrows represent ON/OFF positions of assistance light for PDF4 (outlined with blue) and PDF1 (outlined with orange).

The main conclusion that can be drawn from the behaviour of PDF1 sample is that the writing and erasing processes being concurrent, the rate of each are very similar, thus one can not prevail on the other. The result is the impossibility of SRG forming under these conditions.

V.4. Photochromic behavior of PNF1: polysiloxane with 4-(1'-naphthaleneazo)phenol

The films were prepared from a concentrated solution of polysiloxane 72 % substituted with 4 – (1'-naphthaleneazo)phenol (PNF1) in the same manner as the previous samples and have 500 nm thickness.

This experiment is focused on the influence of assistance light on the mass transport that leads to SRG. In this regard, in the last part of the experiment the assistance light is switched ON and OFF several times.

Under irradiation, PNF1 sample shows a complex behavior. The first order diffraction (Figure V.14. and detail, Figure V.15.) shows a steep increase of diffraction power while the sample is irradiated in the presence of blue light. The power reaches maximum value within 10 minutes of irradiation and starts to slowly decrease in the next 80 minutes. The final part of the test is reserved to control the blue light in such a way to observe the sudden changes in the photochromic behavior due to the azobenzenes blue light absorption.

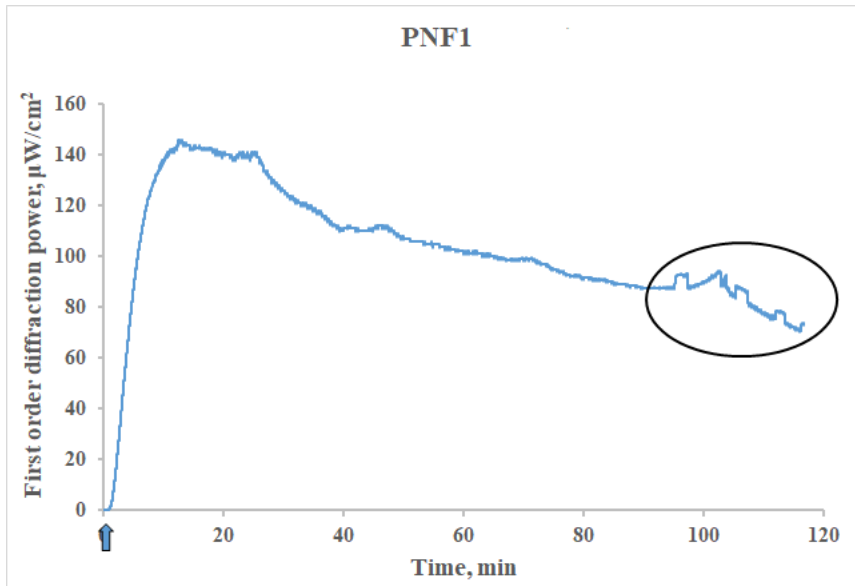


Figure V.14. First order diffraction power evolution in time at high intensity irradiation $I = 4.2 \text{ W/cm}^2$ with assistance light. Blue up-arrow represents the ON position of assistance light.

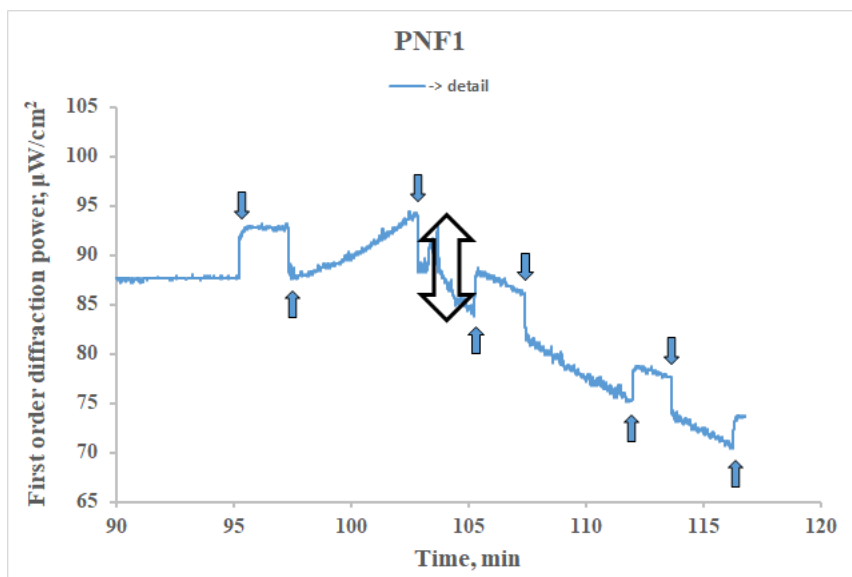


Figure V.15. Detail for Figure V.14. Blue up/down arrows represent the ON/OFF positions of assistance light and the up-down arrow represents a succession of approx. 1 second ON-OFF cycles.

Evolution of the first order diffraction (and the diffraction efficiency on that matter (Figure V.16. and detail Figure V.17.) shows a complex response to the presence of assistance light. After the SRG writing with assistance light reaches a maximum, the process seems to reverse and the diffraction follows a steady continuous decrease. By switching OFF the blue light, the process experiences a relatively low but abrupt enhance and remains constant until the assistance light is switched back ON. This effects an instantaneous decrease about the same amount as the previous increase. This suggests that by making available to photoisomerization less chromophores, favors SRG formation.

The predominant behavior that can be observed in the final part of the experiment, is that switching ON the assistance light, almost always (except the first ON) the azopolysiloxane's first answer is a sudden increase (although not too large, compared to the integral behavior) of first order diffraction power.

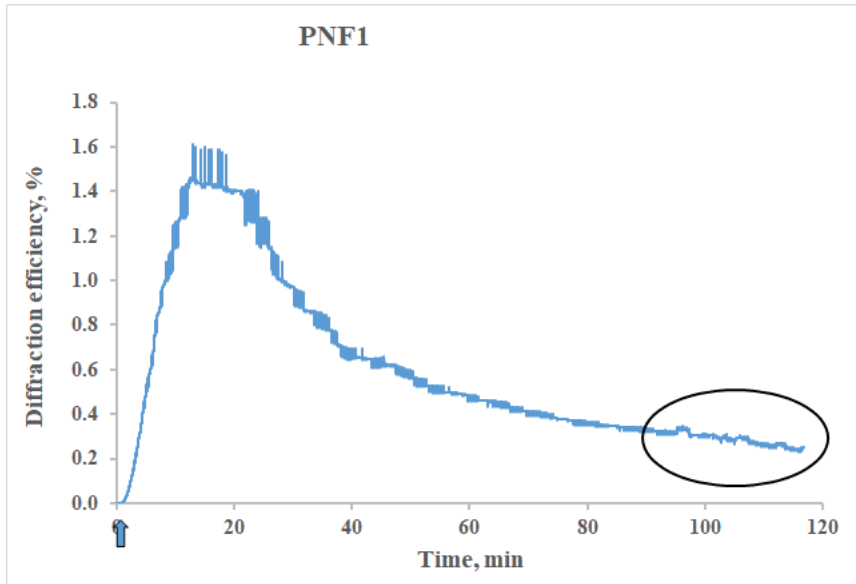


Figure V.16. Diffraction efficiency dependence on time at high intensity irradiation $I = 4.2 \text{ W/cm}^2$ with assistance light. Blue up-arrow represents the ON position of assistance light

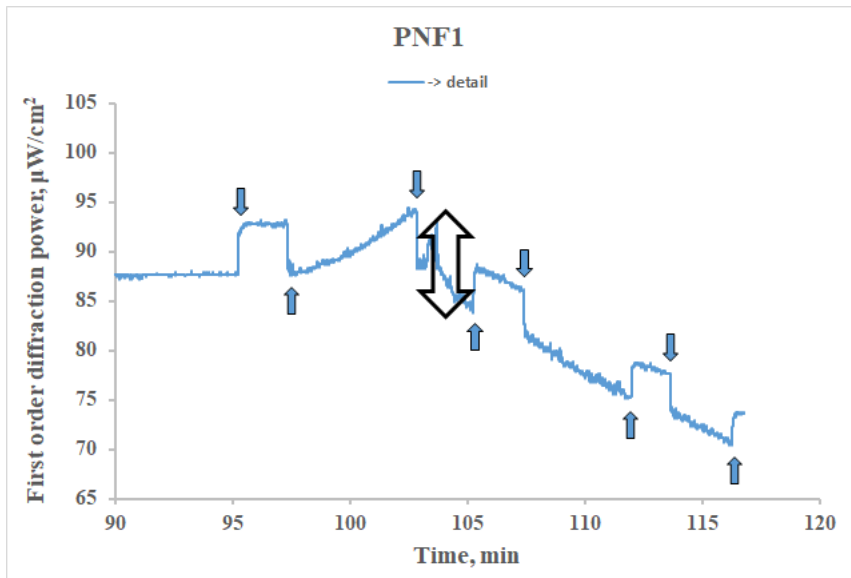


Figure V.17. Detail for Figure V.16. Blue up/down arrows represent the ON/OFF positions of assistance light and the up-down arrow represents a succession of approx. 1 second ON-OFF cycles.

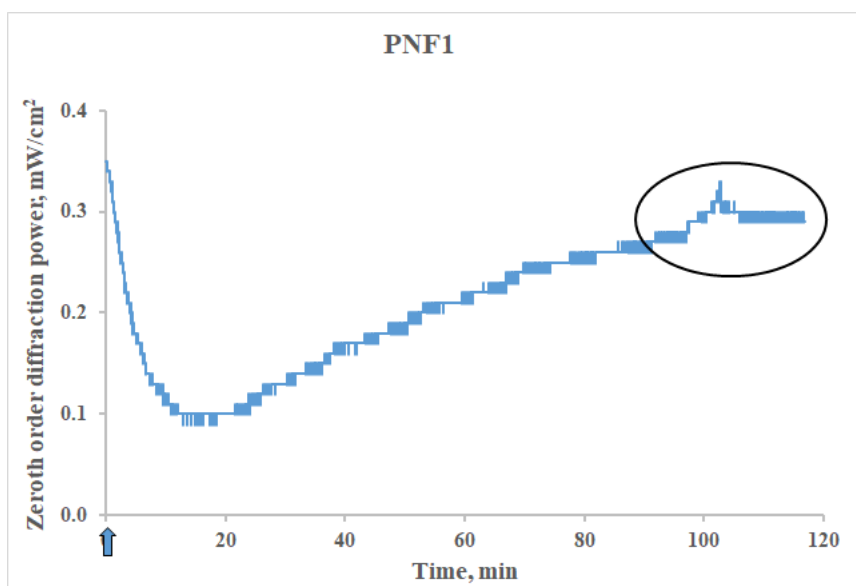


Figure V.18. Zeroth order diffraction power evolution in time at high intensity irradiation $I = 4.2 \text{ W}/\text{cm}^2$ with assistance light. Blue up-arrow represents the ON position of assistance light

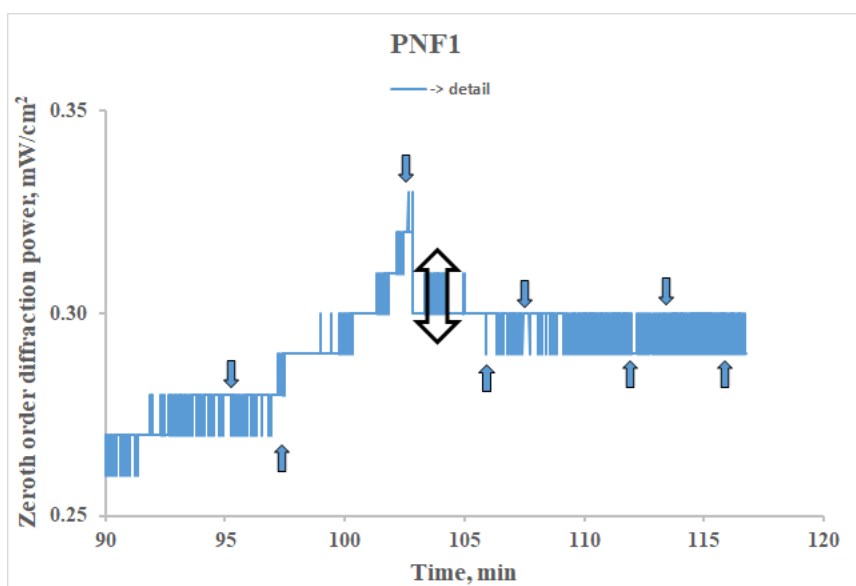
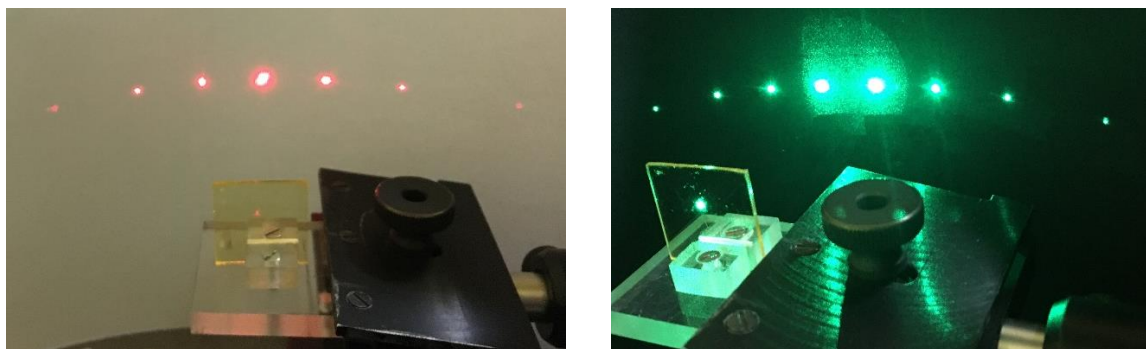


Figure V.19. Detail for Figure V.18. Blue up/down arrows represent the ON/OFF positions of assistance light and the up-down arrow represents a succession of approx. 1 second ON-OFF cycles.

At the end of this experiment, three clear diffraction orders and four self-diffraction orders can be observed. The self diffraction that can be observed in the picture confirms the formation of a diffraction grating.



a) diffraction orders

b) self-diffraction orders

Figure V.20. Pictures of diffraction and self-diffraction

V.5. Photochromic behavior of PAF2: polysiloxane with 4-(2'-anthraceneazo)phenol

The films were prepared from concentrated solution of polysiloxane substituted 43 % with 4- (2'-anthraceneazo)phenol in a similar manner as the other samples.

This azobenzene derivative, even more voluminous than 4- (4'-diphenylazo)phenol, poses the same problems when linked to polysiloxane. The corresponding azopolysiloxane, PAF2 compounds encounter solubility issues to the point that affects the films quality.

Below are discussed the experiments on PAF2 films and the results are to be carefully considered within the same high errors framework, as the PDF results. The light halo is very prominent in these experiments also.

The evolution of first order diffraction in time (*Figure V.23*), displays no answer until the two lights (writing then assistance) are switched ON. The reading beam “sees” no diffraction until these lights are switched ON and start affecting the sample’s molecular structure. The low increase of the diffraction power when the writing light hits the sample continues with an abrupt increase when the second light, the assistance light, is also set ON. This dramatic change shows the light affect the material’s structural order, but the exact

phenomenon it is difficult to grasp. The diffraction registered could be due to the refraction index modification, due to polarization grating, or surface grating.

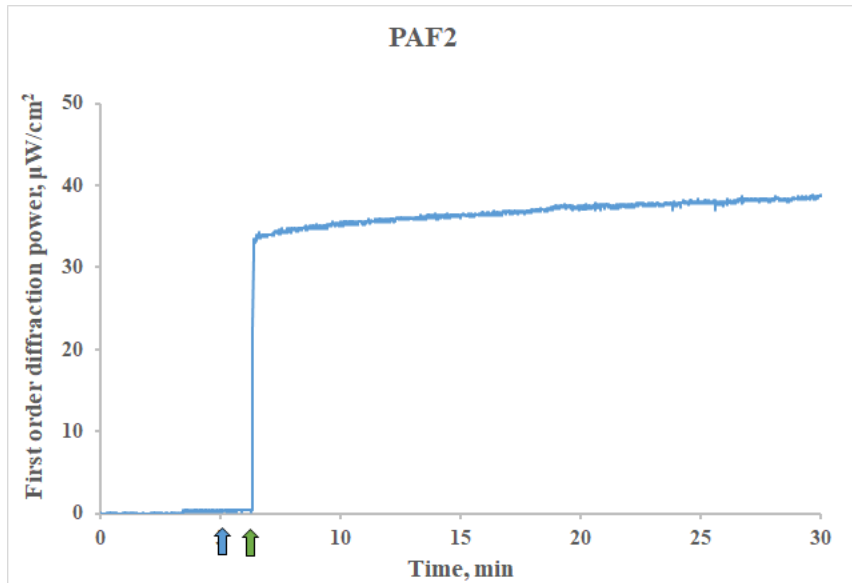


Figure V.23. First order diffraction power evolution in time at high intensity irradiation $I = 4.2 \text{ W/cm}^2$ with assistance light. Up-arrows represent the ON position of assistance light (color blue) and writing light (color green).

The modification of zeroth order diffraction (Figure V.25.) seems to be attributed not only due to the changes of light diffraction, but also due to a change in the film's optical properties. This statement is sustained by the visual observation of an increase of the film's transparency. In the frame discussed, the diffraction efficiency (Figure V.24.) gives very little information on the actual process that takes place during irradiation.

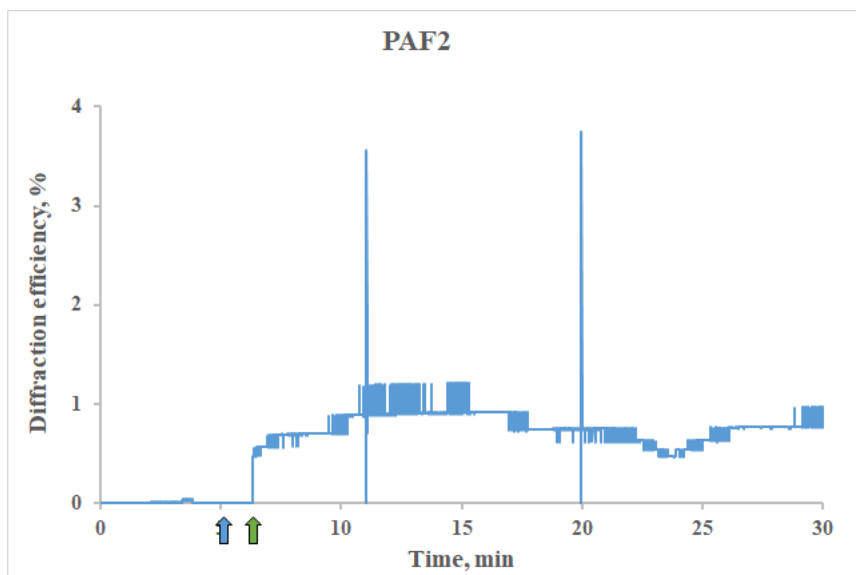


Figure V.24. Diffraction efficiency dependence on time at high intensity irradiation $I = 4.2 \text{ W/cm}^2$ with assistance light. Up-arrows represent the ON position of assistance light (color blue) and writing light (color green).

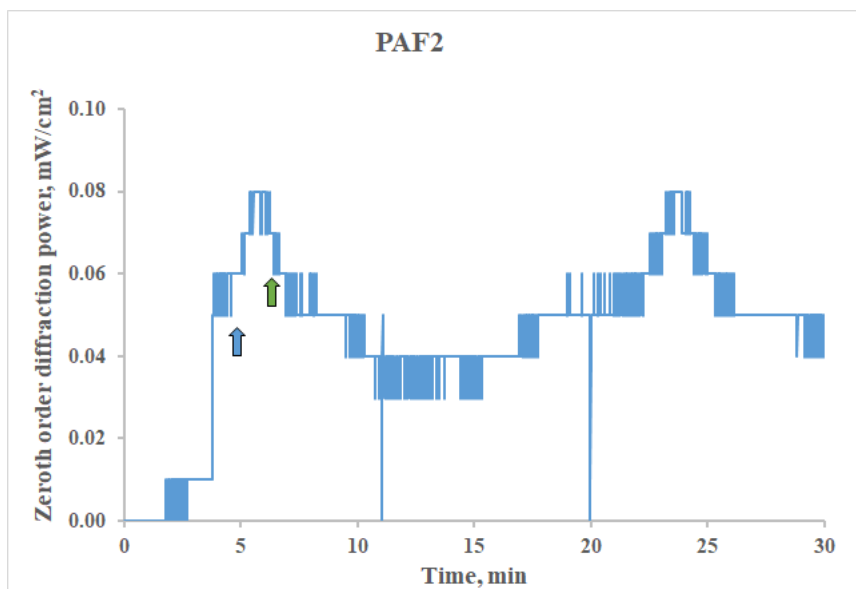


Figure V.25. Zeroth order diffraction power evolution in time at high intensity irradiation $I = 4.2 \text{ W/cm}^2$ with assistance light. Up-arrows represent the ON position of assistance light (color blue) and writing light (color green).

PAF2 azopolysiloxane behaves very much like PDF samples. The competition between the writing and erasing process is very tight, thus formation of SRG is impeded, and no diffraction grating can be observed on the surface of the films.

V.6. Conclusions

Polysiloxanes substituted with various azo groups are investigated for the ability to form SRG. The behaviour of the samples differs in diffraction efficiency, showing that PFF and PNF azopolysiloxanes are more suitable for SRG obtaining than PDF and PAF azopolysiloxanes.. The sinusoidal evolution along with the less regulated increases and decreases of diffraction efficiency, show that there is a competition between the writing and erasing processes during irradiation. Correlating the results of all the samples, one aspect stands out with certainty: there are at least two mechanisms responsible the mass transport than enables SRG inscription. The assistance blue light intensifies the isomerization process, changing the dynamics of matter reorganization. The inconsistency of its effect on the diffraction efficiency makes it difficult to pronounce on what the exact mechanisms are involved. These results are in good agreement with the findings of previous research (Hurduc, Macovei, Paius, Ibanescu, *et al.*, 2013), that show evidential observations of the existence of different mass transport processes that influence the SRG inscription capacity.

CHAPTER VI. Experimental technique

VI.1. Materials and methods

VI.1.1. Linear polysiloxane synthesis

Polysiloxane obtaining has two steps: polycondensation of monomer, when a hydrolysate results, then its cationic equilibration.

Step1 Hydrolysate synthesis

A volume of 40 mL dichloromethane and 30 g of fine grounded ice are introduced in a 500 mL three necks flask and left for stirring 10 minutes. In a by-pass funnel, 10 mL acetone and the monomer dichloro-4-[(chloromethyl)-phenyl]ethyl-methylsilane are mixed together and slowly dripped into the flask (approx. 60 minutes). Then the obtained mixture is left for stirring 15 more minutes. The synthesis is carried in N₂ atmosphere and the temperature is kept at 0 – 5 °C during the whole reaction.

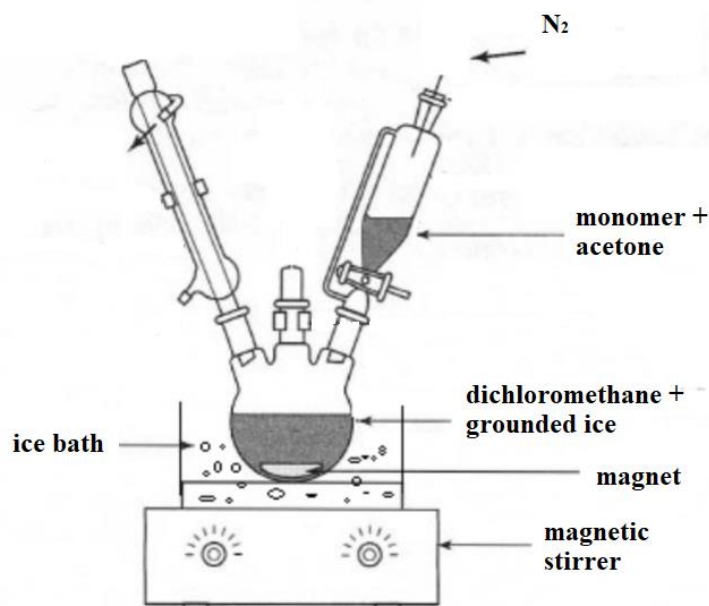


Figure VI.1. Installation for hydrolysate synthesis.

After the hydrolysis reaction ends, the mixture is then transferred into a separation funnel. The organic phase is collected ($d = 1.32$) and let dry over night after adding magnesium sulfate for anhydization. The monomer is passed through filter paper to clear out the magnesium sulfate and then the remaining solvents, acetone and dichloromethane are first removed at rotary evaporator and then with a vacuum pump at room temperature. The obtained hydrolysate is used in step 2 to synthesize the polysiloxane.

Step 2 Polysiloxane synthesis

A quantity of 6 g of hydrolysate and 0.1 g DVDS are introduced in a 50 mL flask and left for stirring 10 minutes. 3 – 4 drops of triflic acid are carefully added under strong stirring. The reaction is carried at room temperature for 48 – 72 hours. The viscosity increase during the polymer formation may cause stirring problems, which are solved by adding a few drops of dichloroethane. The reaction mixture is then precipitated in an Erlenmeyer drop by drop under vigorous stirring in methanol and left for maturation 2 – 3 hours. The precipitate is then left for deposition overnight. The two fractions are separated due to the solubility differences in methanol. The cyclic polysiloxane is soluble in methanol, thus it is removed along with the methanol through filtration. This filtration is repeated 3 – 5 times. The linear

polysiloxane is then collected from the filter paper with dichloromethane and left to dry at room temperature. Rotary evaporator or vacuum pump can also be used.

VI.1.2. Azobenzene derivatives

The azo derivatives were obtained through a classical reaction of diazotization immediately followed by phenol coupling, starting from different primary aromatic amines (1-naphthylamine and 2-aminoanthracene). The classic 4 – (phenylazo)phenol was purchased as such, while for 4-(4'-biphenylazo)phenol synthesis obtaining the corresponding amine, 4-aminobiphenyl, was necessary. All reactive and solvents were purchased from Sigma Aldrich or Chemical Company and used as such.

VI.1.2.1. 4-(4'-biphenylazo)phenol

As mentioned, 4 – aminobiphenyl was synthesized in two steps: nitration of biphenyl, followed by the reduction of formed 4 – nitrobiphenyl. Then, 4-(4'-biphenylazo)phenol is obtained through a classical method, diazotization and phenol coupling.

Step 1: 4-nitrobiphenyl synthesis (nitration)

In a 250 mL flask, 15 g of biphenyl and 60 mL acetic acid are stirred at 60 °C for about 30 minutes till the complete dissolution of biphenyl. Then, solution of 32 mL fuming nitric acid and 48 mL acetic acid is added into the flask and kept for about 24 – 32 h at room temperature with continuous stirring. It results a mixture of 2-nitrobiphenyl (soluble) and 4-nitrobiphenyl (insoluble, so that it precipitates). The flask content is filtered on a Gooch crucible and washed with approx. 10 mL of acetic acid. The 4-nitrobiphenyl is oven-dried at room temperature, when a white snowy powder is obtained.

Step 2: 4-aminobiphenyl synthesis (reduction)

A mixture of 2 g (10 mmol) of 4-nitrobiphenyl and 50 mL of ethanol is refluxed in a 250 mL two-neck flask at 80 °C for about 30 minutes, till the complete dissolution of the nitro derivative. A sodium sulphide solution is prepared from 7.2 g (30 mmol) of $\text{Na}_2\text{S} \cdot 9\text{H}_2\text{O}$, 25 mL of water and 25 mL of ethanol, then slowly added (small volumes every 2-3 minutes) in the flask through the available neck. The mixture is kept refluxing with stirring for about 20 h more (overnight). During the reaction, the formation of amino group is checked

through Thin Layer Chromatography, using as eluent the solvents: dichloromethane and ethyl acetate 20:1. The developing is carried out by slowly dripping hydrochloric acid into a concentrated aqueous solution of sodium nitrite. The red colouring of aminobiphenyl corresponding spot, confirms the presence of the amino group. The mixture is filtered on a Gooch crucible and washed with water, then dried at room temperature.

Step 3: 4-(4'-biphenylazo)phenol synthesis (diazotization and phenol coupling)

A suspension of 2 g (11.8 mmol) of 4-aminobiphenyl and 15 mL of water is prepared on a magnetic stirrer. After a fine suspension is formed, 3.6 mL of hydrochloric acid 36% are added. An ice bath is applied to keep the temperature at 1-3 °C while a solution of 0.8142 g (11.8 mmol) NaNO₂ and 4.4 mL of water is added drop by drop. The mixture is kept on the magnetic stirrer for 30 more minutes at 1-3 °C. Afterwards, the coupling reaction can be performed, by adding the obtained mixture into a solution of 1.1468 g (12.2 mmol) of phenol, 3.0452 g (22.4 mmol) CH₃COONa * 3 H₂O and 15.3 mL of water in small volumes. The mixture is kept at room temperature over night, when a suspension is formed. The pH of the suspension is corrected, if needed, with hydrochloric acid till 2-4, then filtered on a Gooch crucible and washed with water. The oven drying at 70 °C can last too long, in which case is advised the following proceeding. The compound is dissolved in diethyl ether and then anhydrous NaSO₄ is added to retain the water. The solution is filtered and the diethyl ether is removed with a rotary evaporator from the filtrate. The residue is purified through chromatography with a SiO₂ column, using as eluent the solvents: dichloromethane and hexane 20:1.

VI.1.2.2. 4 – (1'-naphthaleneazo)phenol synthesis

A mixture of 5 g of 1-naphthylamine, 100 mL H₂O and 10.5 mL HCl 32 % is refluxed in a 250 mL flask until complete solubilization of the amine, when a white precipitate of naphthylamine, chloride is obtained. Then, the mixture is slowly poured in a 500 mL Berzelius that contains water and ice, under continuous stirring. The temperature of the mixture is kept approx. 0 °C by adding ice in the glass. Further, 2.42 g NaNO₂ solved in 5.7 mL of H₂O is slowly dripped in the previously obtained mixture, maintain the temperature around 0 °C by placing the container on an ice and salt bath. After complete solubilization, the contain of the glass is dripped in an aqueous solution of CH₃COONa * 3 H₂O 20 % and

3.58 g of phenol. This operation is performed also on an ice bath and under continuous stirring. A viscous black compound is formed on the bottom of the glass, along with particles in suspension. The formed solid is extracted with ethyl acetate in a separation funnel. The action is repeated until complete extraction and after, anhydrous Na_2SO_4 is added to remove traces of water. The solvent is removed from 4 – (1'-naphthaleneazo)phenol at rotary evaporator. The purification is done on Al_2O_3 chromatography column with ethyl acetate and hexane (1:1).

VI.1.2.3. 4-(2'-anthraceneazo)phenol synthesis

2 g of 2-aminoanthracene in 100 mL H_2O and 0.5 mL HCl 32%. is left for reflux 30 minutes in a 250 mL flask until a fine suspension forms, 2-aminoanthracene clorhydrate. In a 500 mL Berzelius, a water and ice mixture is prepared and the container is placed on an ice and salt bath. The suspension is poured in the Berzelius and left to reach at least 0 °C. Then, a solution formed from 2.42 g NaNO_2 in 5.7 mL H_2O is added by releasing the solution under the suspension level with a pipette. The mixture is left for stirring maintaining the temperature around 0 °C until complete homogenization and after is transferred in a dropping funnel. Separately, 130 mL aqueous solution of $\text{CH}_3\text{COONa} \cdot 3 \text{H}_2\text{O}$ 20 % is mixed with 3.58 g of phenol and placed on an iced bath. The funnel mixture is slowly dropped in this mixture and left stirring for maturation one more hour. The precipitate is then filtered on a Gooch crucible and purified through column chromatography with silica gel, using a mixture of dichloromethane and ethyl acetate (20:1). The final product, is a black glassy compound (m. p. = 225 0 °C).

VI.1.2.4. Sodium salts

All the azobenzene derivatives are transformed into sodium salts so they can be connected on the polysiloxane's side chain to the chlorobenzyl group. The azobenzene derivatives and NaOH are introduced in equimolecular rates and are left for reflux in acetone 5 hours under vigorous stirring. During the reaction, acetone can be added if the mixture is too viscous. The azo salts precipitate in the reaction media and acetone is removed at rotary evaporator. Remaining solvent is removed at room temperature leaving the compound in a well vented area for a few days so that the unreacted NaOH gets deactivated.

VI.1.3. Azopolysiloxanes synthesis

Polysiloxane is modified by nucleophilic substitution SN_2 of the chlorobenzyl side group with the azo derivatives.

The molecular rate between the azobenzene derivative salts and polysiloxane is adjusted in function of the desired substitution degree. The usual synthesis recipe starts with 0.3 g of polysiloxane in 4 mL DMSO, which are placed in an ultrasound bath for 5 minutes to ensure complete solubilization. Then, 0.1 g TBA is added and the flask is placed again in the ultrasound bath. The azo salt is the last to be added and the mixture is refluxed at 80 – 85 °C for 5 hours under continuous stirring. Depending on the substitution degree and the azobenzene derivative, the resulting compound is a thick glue – like paste or a fine powder. The product is filtered or separated, then washed thoroughly several times with methanol to remove any traces of unreacted low molecular mass compounds. The final azopolysiloxane is collected with dichloromethane, then dried at room temperature. Traces of remaining solvents are removed with the vacuum pump, then the reaction yield is calculated.

VI.2. Methods and instruments

VI.2.1. Spectroscopy

For the chemical analysis of the compounds in this study, some of the most common techniques of spectroscopy are employed: resonance spectroscopy (1H and ^{13}C NMR) to confirm the chemical structure of our compounds and absorption spectroscopy (UV and Vis) to measure the concentration of cis isomer of azobenzene derivatives in solution and films.

VI.2.1.1. 1H and ^{13}C NMR

This characterization method is based on the magnetic properties of atomic nuclei. Placed in a magnetic field, the samples are excited with radio waves and the intramolecular magnetic field of an atom from the molecule changes the resonance frequency and produces a nuclear magnetic resonance signal that is then detected and interpreted. The resulted fields offer information about the electronic structure of the atomic nuclei (1H and ^{13}C) and affiliated functional group, thus the method is used to identify molecular compounds.

Analysis for this thesis was performed on RMN Bruker Avance DRX 400 MHz spectrometer. 15 – 50 mg of sample is dissolved in 0.4 – 0.8 mL of deuterated chloroform. The spectra are registered using TMS as standard and processed with MestReC and ACD/NMR Processor Academic Edition software.

VI.2.1.2. UV-Vis

Ultraviolet – visible spectroscopy uses electromagnetic radiation from a part of UV wavelength and full Vis spectrum range, where atoms and molecules undergo electronic transitions from the ground state to the excited state. The spectrophotometer measures the light intensity before and after passing through a sample, and evaluates the sample's absorption based on the calculated transmittance. Compounds absorb light irradiation of specific wavelengths in specific amounts, depending on their internal structure, thus the spectrum is uniquely characteristic to a specific compound.

In azobenzene molecules, UV-Vis absorption is due to the chromophore groups –N=N– that change their relative spatial arrangement when irradiated and result in forming configurational isomers *cis* and *trans*. The two isomers have different absorption maxima, which were registered with Shimatzu UV-1700 in solution (chloroform) for each azobenzene derivative. Exploiting the different absorption bands of *cis* and *trans* isomers, the photoisomerization process is monitored for azopolysiloxane films. The measurements were carried on Boeco S1 UV spectrophotometer.

VI.2.2. Spin coating technique

Spin coating is a technique used for homogeneous solution deposition on different substrates. The films are deposited from a concentrated solution of azopolysiloxane in 1,1,2-trichloroethane or chloroform. The solutions are kept at ultrasound bath for 1 – 5 hours at room temperature or 45 °C and then filtered on microfilters with pores of 0.45 or 1 µm in diameter. Rotation speed and time were adapted depending on the aimed film thickness. Then, the films were left to dry at room temperature in a well-vented area for 2 days.

VI.2.3. Thermal analysis methods

VI.2.3.1. Thermal gravimetric analysis

Thermogravimetry measures the mass of a sample during temperature changing with constant rate to identify thermal reactions. The mass loss of a sample in function of temperature or time is registered on a TGA curve and shows the degradation steps. The first derivative of this curve, the DTG is used to evaluate phase transitions from the inflexion points.

Thermogravimetric analysis is used for azopolysiloxanes in the present thesis to determine the thermal stability and distinguish phase transitions, namely the glass transition temperature. The tests are performed with Mettler Toledo TGA – SDTAR851e on a range of temperature $T = 25 - 890\text{ }^{\circ}\text{C}$ with a heating rate of 10 and 15 K/min.

VI.2.3.2. Differential thermal analysis

Differential scanning calorimetry measures the temperature difference between a reference the analyzed sample, as the temperature increases or decreases. The sample's behavior is registered in a DTA curve that shows exothermic and endothermic processes in the material. The method allows for calculation of heating capacity and identifying of phase transitions and thermal transitions of order I and II.

Studies in the present thesis are performed on a Mettler Toledo DSC-1 Star System in N_2 atmosphere (15 mL/min), and the weight of the samples is 2.5 – 4.5 mg. DSC data is registered for heating and cooling cycles with rate of 10K/min in the temperature ranges: $T = -50 - 230\text{ }^{\circ}\text{C}$.

VI.2.4. Contact angle

The surface properties in terms of hydrophobic/hydrophilic are measured with contact angle method. The static technique is represented by the deposition of a water droplet on the surface, when the contact angle θ_c is considered to form at the intersection point between the three phases: solid, liquid, and gas. The tangential method used to evaluate the droplet's 2D projection for angles $\theta_c = 10 - 100$ assumes that the ensemble formed by the droplet's projection and her shadow on the surface is an ellipse. The profile is adjusted to a

general equation for conic section. The equation's derivative at the intersection point represents the slope at the three phases contact point, thus the contact angle. This method is suited for the samples characterized in this thesis.

The surface properties of azopolysiloxane films were evaluated with Drop Shape Analyzer – DSA100 goniometer from Kruss. The analyzed azopolysiloxanic films (thickness $\delta = 400 - 600$ nm) are deposited on silanized glass substrates through spin coating technique. Sessile drop method was employed with 15 μ L volume of droplets, and at least 5 measurements for each sample.

VI.2.5. Optical microscopy with polarized light

Liquid crystal properties with polarized light microscopy due to the fact that liquid crystals are birefringent in polarized light and depending on the sample's fluidity, it can give information about the possible existence of mesophases. To be observed, the mesogens have to be perpendicular on the light polarization vector, otherwise, they will disclose their birefringent property, and the investigated field appears to be dark. When properly positioned, mesogens determine a light field, whose intensity is proportional with the material's birefringence.

Azopolysiloxanes were analyzed using optical microscope Axioskop 40 Pol from Zeiss. The azopolysiloxane was heated with 20 °C/min in the temperature range $T = 20 - 265$ °C and cooled back with 10 °C/min.

VI.2.6. Laser irradiation

Interference laser irradiation is used to induce nanostructures on the film surfaces, SRG. The gratings have been induced using an Ar laser (514.5 nm wavelength) and probed through the diffraction of a HeNe beam (632.8 nm wavelength). Two laser beams meet on the film surface and form an interference pattern that translates into a sinusoidal relief pattern (the SRG) with specific amplitude and period, characteristics that depend on the interference angle between the two beams. Regarding the experimental setup, the light wavelength, polarization, and intensity are influence factors for SRG formation.

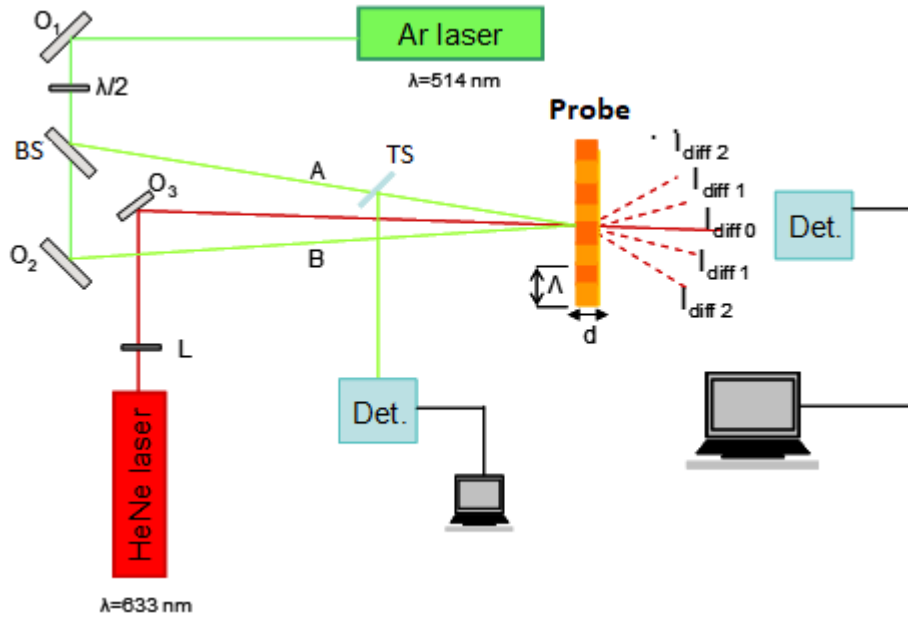


Figure VI.2. Schematic illustration of laser setup.

The light source for SRG inscription is a Ar^+ laser that emits a beam (also called *writing beam*) of $\lambda = 514.5$ nm wavelength with p-p linear polarization. As SRG inscription needs interference, the laser beam is split in two equal beams by BS beam splitter, then one beam is reflected by O1 mirror to meet the other on the film surface. Position of BS beam splitter and O1 mirror can be modified in order to control the angle between the two interfering beams. A second light source, He-Ne laser is used to monitor the SRG inscription by sending a laser beam (also called *reading beam*) of $\lambda = 632.8$ nm wavelength on the film surface close to the normal incidence (it is not coplanar with the writing beams). A supplementary light (also called *assistance light*) was added to enhance the photoisomerization of azobenzenes.

The Ar^+ green writing beam has the following characteristics: p-p polarization, wavelength $\lambda = 514.5$ nm, energy $h\nu = 2.41$ eV, beam diameter (regulated by a diaphragm) $\Phi = 1.75$ mm. The beam is split in two equal beams and we use two different intensities in our experiments: $I_1 = 2.3$ W/cm² ($P_{\text{Ar}} = 14$ mW) and $I_2 = 4.2$ W/cm² ($P_{\text{Ar}} = 26$ mW).

The He-Ne red reading beam has wavelength $\lambda = 632.8$ nm and energy $h\nu = 1.96$ eV.

The blue assistance light is emitted by a LDM405 – laser diode module (from Thorlabs) with vertical polarization, wavelength $\lambda = 405$ nm, power $P = 4$ mW, and diameter of radius spot $\Phi = 3 \times 5$ mm.

2nd PART
Simulation Studies

CHAPTER VII. Simulation framework and calculations

VII.1. Framework

All calculations in the herein thesis are performed using software developed by prof. Teboul (University of Angers).

Molecular dynamics simulations are employed to simulate the behavior of supercooled liquids under the influence of a flapping motor. The simulated system is comprised of one *molecular motor* diluted in the environmental medium made up of 500 molecules that are referred to as *host molecules*. To address a material in bulk, the system consists of a simulation cell with periodic boundaries conditions.

The molecular motor is source of perturbation in the system when the isomerization is ON and the motor experiences successive folding/unfolding cycles. Thus, the system simulated is out of equilibrium.

We use the NVT ensemble, and the temperature is controlled with a Berendsen thermostat, for which we use the coupling parameter $\tau = 5 \cdot 10^{-15} \text{ s}$.

We integrate the Newton's equation of motion with the Gear prediction – correction algorithm with the quaternion method for a time step of $\Delta t = 10^{-15} \text{ s}$.

VII.2. Simulated systems

VII.2.1. Host molecules - the environment

The host molecules that portray the viscous medium are represented in our calculations by methyl methacrylate (*MMA*) monomers, or by a simplified model of a diatomic molecule.

VII.2.1.1. Diatomic host molecule model

The simplified model of the host molecules consists of two atoms ($i = 1,2$). Interaction between atoms is simulated according to 12 – 6 Lennard-Jones potential:

$$V_{ij} = 4\varepsilon_{ij} \left(\left(\sigma_{ij}/r \right)^{12} - \left(\sigma_{ij}/r \right)^6 \right)$$

Equation VII.1.

where ε is the depth of the potential well, σ is the (finite) distance between i and j atoms at which the potential is equal to zero, and r represents the distance between any two atoms. While the ε gives the strength of the interaction between i and j atoms, σ settles the distance at which the two i and j atoms can draw (thus is sometimes called Van der Waals) and it measures the distance between the i and j atoms' center of masses.

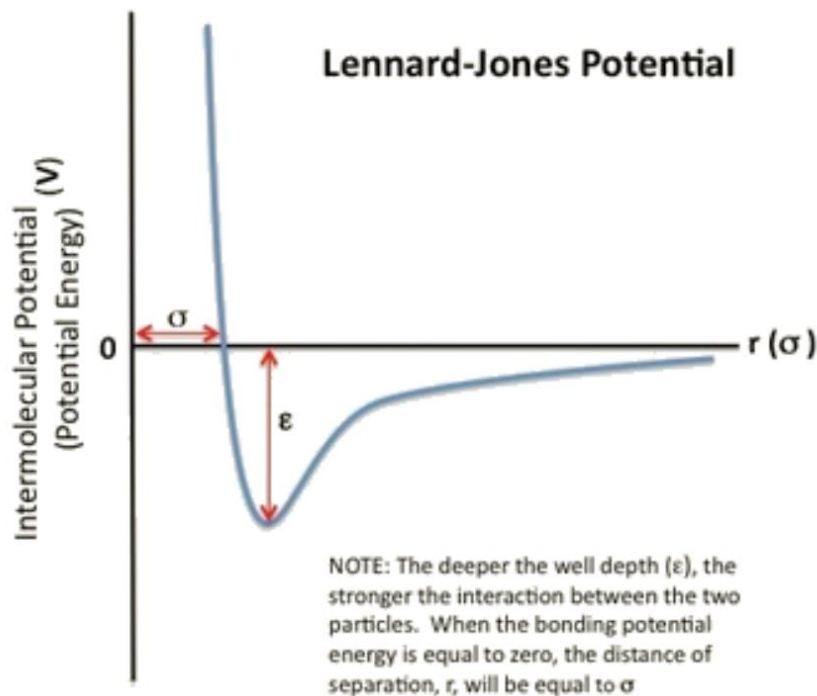


Figure VII.1. Lennard-Jones potential.

These parameters describe the environment's properties, are chosen to mimic the aimed viscosity and offer a stable medium inside the range of temperature and density used. The system does not crystallize, not even for long run times.

The following parameters values fit our simulated system:

$$\varepsilon_{11} = \varepsilon_{12} = 0.5 \text{ kJ mol}^{-1}$$

$$\varepsilon_{22} = 0.4 \text{ kJ mol}^{-1}$$

$$\sigma_{ij} = \alpha \sigma_{ij}^0,$$

Equations VII.2.

where $\sigma_{11}^0 = \sigma_{12}^0 = 3.45 \text{ \AA}$, $\sigma_{22}^0 = 3.28 \text{ \AA}$ and α is a parameter that defines the different hosts used.

The 2 atoms are rigidly bonded at a $d = \alpha d^0$ distance, where $d^0 = 1.73$. As mentioned, α is a factor that enables the construction of different hosts. The distance d between the atoms varies from one motor to another, and it is always smaller than σ_{33} in order to have continuity in the molecule. The atoms mass remains constant through the different hosts, i.e. Argon mass $m_{Ag} = 40 \text{ g/mol}$. At this setup there is an exception which will be mentioned in the corresponding section.

VII.2.1.2. Methyl methacrylate coarse grained model

The methyl methacrylate monomer (MMA) is modeled with coarse-grained method. The general geometry is maintained by designing a four center molecule (4 out of the 5 carbon atoms are detained) (*Figure VII.2.*). The mass of MMA molecule is $m = 100 \text{ g/mole}$.

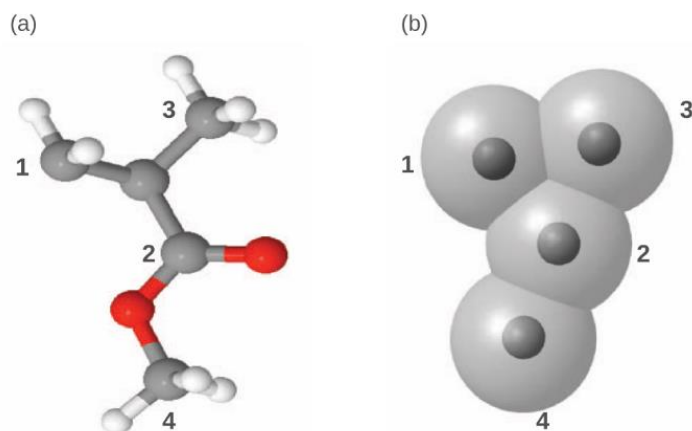


Figure VII.2. Representation of methylmethacrylate molecule in (a) all atom model and (b) coarse grained model with rigid bodies (Accary and Teboul, 2012).

The 12 – 6 Lennard Jones is again used to describe the interatomic potentials and has the following parameters (*Table VII.1.*). Interactions between different grains i and j take place conforming the following equation.

$$\varepsilon_{ij} = (\varepsilon_{ii} - \varepsilon_{jj})^{0.5} \text{ and } \sigma_{ij} = (\sigma_{ii} - \sigma_{jj})^{0.5}$$

Equations VII.3.

Table VII.1. Lennard Jones parameters for MMA coarse grained model

Grain	ε (kJ/mol)	σ (Å)
1	1.765	3.336
2	0.129	4.543
3	2.293	3.457
4	2.858	3.336

VII.2.2. Molecular motor – the isomerizing azobenzene

In the same manner as the host molecules, the motor is defined by an idealized motor with a simplified rectangular shape. Disperse Red 1 (DR1) molecule is also used, but mostly to verify and justify the choosing of a model molecular motor.

The idealized molecular motor plays the role of the azobenzene like molecules in experimental setups. The herein used model is built starting from minimum 3 parallel rows of 2 atoms each. The distance between both rows and columns are varied, and the number of rows increased, do that the motor's size is tuned to different sizes. As imagined, this assembly gives shape to a rectangular motor of various lengths and widths. The row number is always

Argon mass is again applied for all the atoms in the motor. The 12 – 6 Lennard-Jones potential is again used for the interaction between the motor atoms, with the parameters:

$$\varepsilon_{33} = 0.996 \text{ kJ mol}^{-1}$$

$$\sigma_{33} = 3.045 \text{ Å}$$

Equations VII.4.

Interactions of motor – host atoms comply with the following rule:

$$\varepsilon_{ij} = (\varepsilon_{ii} - \varepsilon_{jj})^{-0.5} \text{ and } \sigma_{ij} = (\sigma_{ii} - \sigma_{jj})^{-0.5}.$$

Equations VII.5.

Considering the simplified geometry of this molecular motor, the isomerization is modeled as a folding at mid length $L = L_T/2$ up to a 60° angle between the arms. Here, L_T defines the total length of the motor. The reverse motion flattens the molecule back into its initial form, describing the unfolding. Repetitive folding/unfolding cycles mimic the trans-cis isomerization process that takes place in azobenzenes, as a result of luminous excitation.

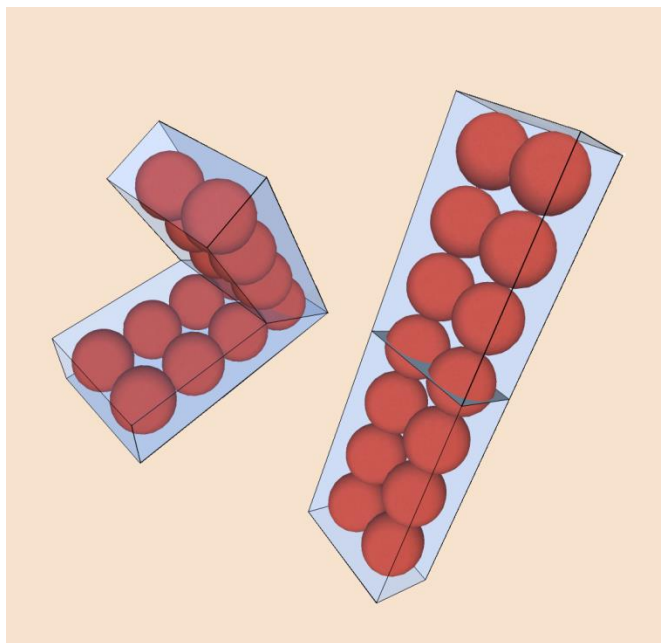


Figure VII.3. Representation of a simplified motor built of seven rows with two atoms each in **left side**) folded form – cis and **right side**) unfolded flat form – trans; bordered in parallelograms to guide the eye; orthogonal plan to the longitudinal axis represents the mid length to visually differentiate the two moving arms.

Particularities on the isomerization process are to be described as they will play an important role in the present work. The isomerization period T_f (sometimes noted τ_p) represents the time needed for a complete cycle to take place. Isomerization ensues from the following steps (*Figure VII.4.*):

1. Folding – the motor moves its two arms with a constant rate, closing them up to a 60° angle in a time τ_f (sometimes noted t_{iso}).

2. Stationary phase – the motor holds its folded form for a characteristic time $t = (T_f - 2\tau_f)/2$.

3. Unfolding – the motor open its two arms by following the reverse uniform movement of folding in a τ_f time.

4. Stationary phase – the motor remains in the flat starting position, resting for a characteristic time $t = (T_f - 2\tau_f)/2$.

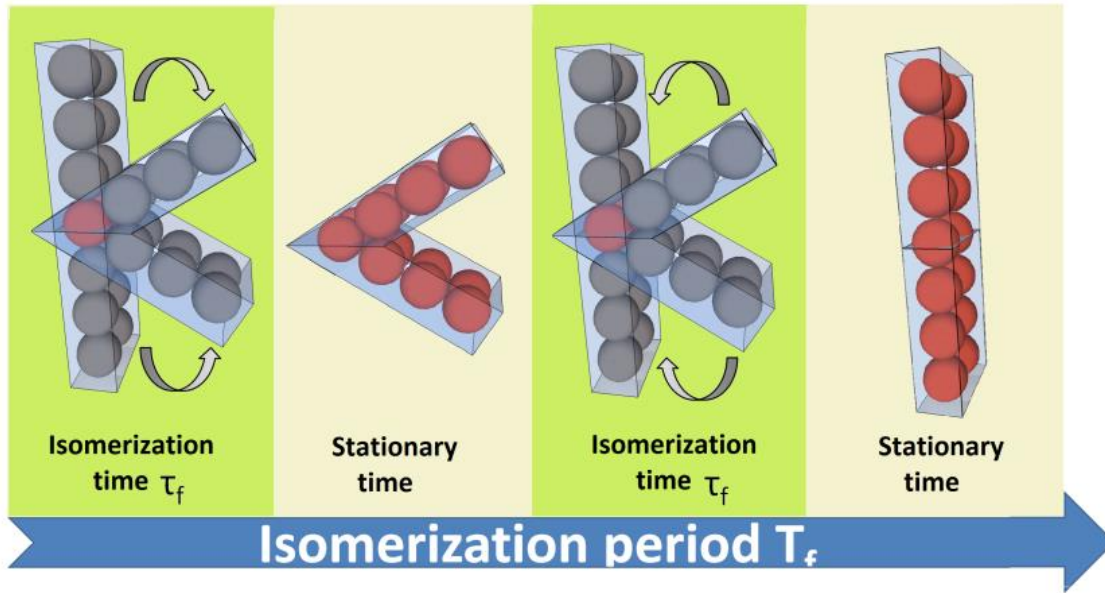


Figure VII.4. Representation of the four successive isomerization steps in one complete isomerization cycle.

The isomerization process disregards the medium's viscosity. In order to attribute this ability to the motor, the model is coerced into strictly respecting the programmed times. During simulation, when the isomerization is ON, the motor folds and unfolds without taking into account the possible hindrance from surrounding molecules related to viscosity. (Figure VII.5.).

This is in agreement with experimental parameters (Singleton *et al.*, 2012): the isomerization pressure is very high, over 1 GPa. Moreover, the photofluidisation process observed experimentally (Hurduc *et al.*, 2013), supports this idea. The isomerization cycles continue succeeding under continual energy supply.

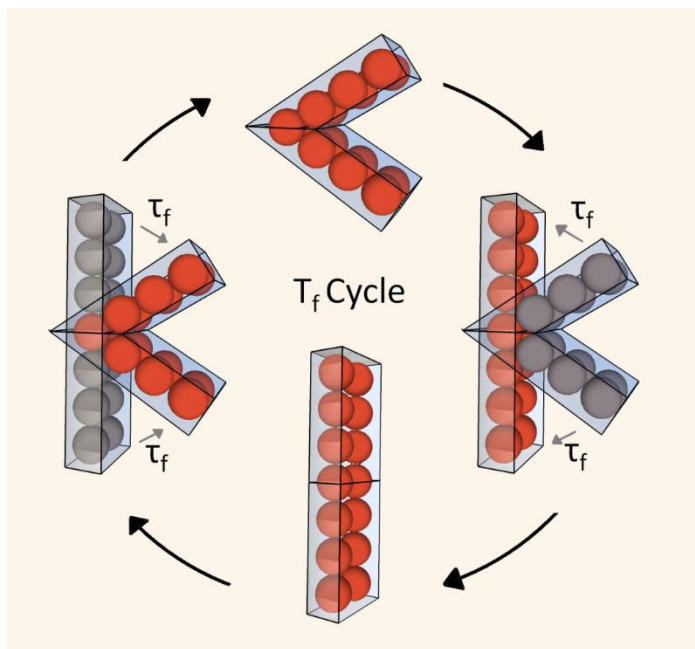


Figure VII.5. Schematic illustration of isomerization cycle.

VII.3. Results validation

VII.3.1. Use of idealized molecules

Often, molecular simulations appeal to simplified models of the system studied. The idea behind this approach is justified by the computational time, which is correlated with the number of simulated atoms/particles. Thus, the most used method is to use coarse grained models, which group together several atoms.

The most important aspect when using simplified models, is to keep a proper balance between results accuracy and computational time needed for the simulation.

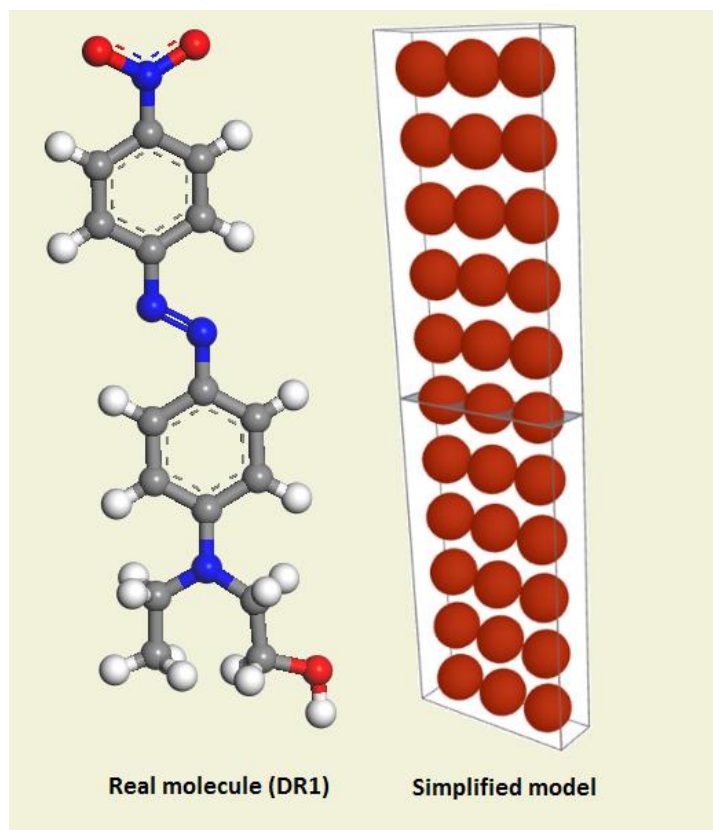


Figure VII.6. Comparison representation of DR1 molecule and an idealized motor molecule in the trans flat configuration.

In this work, several models are used for simulation. Firstly, the azobenzene like molecule, often refers to as molecular motor, is represented by a simplified model, i.e. a rectangular planar (when in trans configuration) molecule, having the corresponding azo moiety at the mid length, parting the motor in two symmetrical arms. The trans to cis isomerization process is thus idealized through a folding motion which brings together the two arms at a constant rate to a 60° angle. Consequently, the cis to trans isomerization is mimicked by the unfolding of the molecule, reaching the flat initial shape.

Figure VII.7. depicts a comparison between the results obtained when using as motor the real dye DR1 molecule and when using idealized molecules, choosing for this purpose two sizes of the simplified rectangular model: *i*) length $L = 12.4 \text{ \AA}$ and width $W 5.4 \text{ \AA}$ and *ii*) length and $L = 11.4 \text{ \AA}$ and width $W 3.9 \text{ \AA}$. The results are comparable for the host diffusion induced by isomerization.

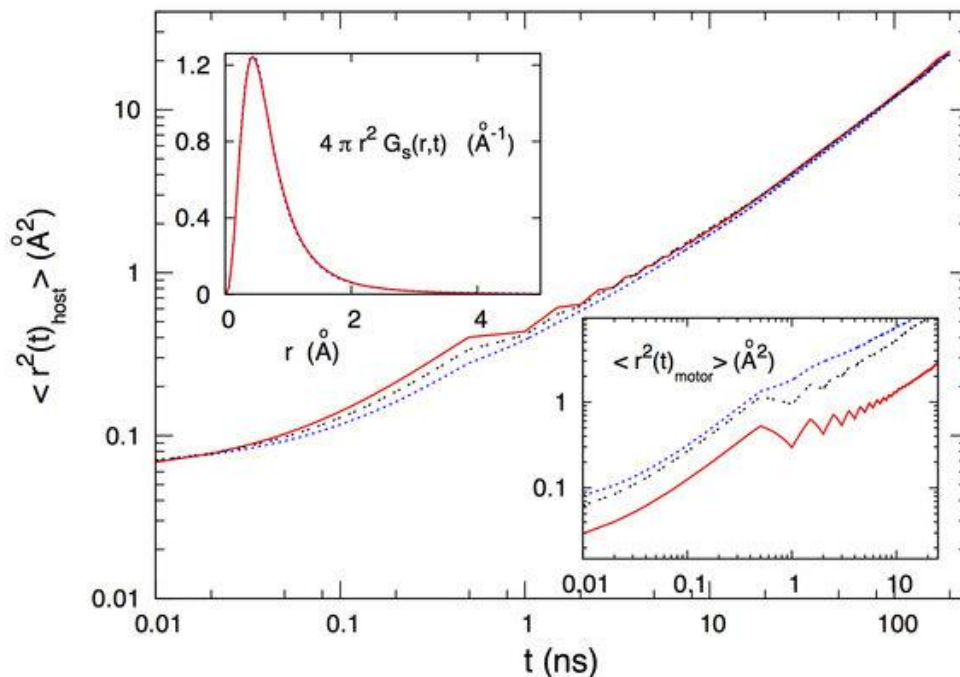


Figure VII.7. Mean square displacements $\langle r^2(t)_{\text{host}} \rangle$ for host (host 1, $\sigma = 3.45 \text{ \AA}$, $l = 5.1 \text{ \AA}$, and $T = 10 \text{ K}$) while the motor is DR1 molecule (red continuous line) or idealized molecules: $L = 12.4 \text{ \AA}$, $W = 5.4 \text{ \AA}$ (black dashed line) and $L = 11.4 \text{ \AA}$, $W = 3.9 \text{ \AA}$ (blue dotted line). The oscillations match the isomerization period and show the displacement induced by each isomerization, which on the long run translates in the host's diffusion. **Bottom inset:** Mean square displacements $\langle r^2(t)_{\text{motor}} \rangle$ for the motor under the same conditions and representations. Note: there is only one motor molecule in the simulation cell, thus the result is less accurate than for the host (500 molecules). As before, the oscillations correspond to the displacement with each isomerization. **Upper inset:** Van Hove correlation function $G_s(r, t)$ ($t = 400 \text{ ps}$) for the host.

All three MSD curves depict how the medium molecules start to escape the cage formed by the surrounding molecules at a time $t = 0.2 \text{ ns}$ (finale of MSD plateau), reaching the same diffusion on longer times $t > 10 \text{ ns}$. Thus, the different motors induce similar diffusive behaviour, showing that not only the idealized shape, but also the simplified isomerization movement are of reduced significance in what regards the motor's capacity to induce diffusion of medium host molecules. Analyzing the Van Hove function (Figure VII.3. upper inset), the conclusion judgement is that the probability to encounter a molecule at a time t at distance r from its previous position is the same for the three motors (the real DR1 and the two simplified models).

Regarding the motor diffusion, pictured in *Figure VII.7. bottom inset*, the MSD curves show that diffusion is dependent on the motor's size and shape. As an observation, using logarithmic scales, the MSD slope does not reflect the diffusion coefficient D (as in linear axis). It is the height of MSD curves that offers information on the diffusion magnitude. The motor's isomerization induced diffusion is larger for the two idealized models than for the real DR1. This suggests the possibility to design motors that diffuse faster, a subject investigated in *Chapter I.X.* of this thesis.

VII.3.2. Time period between two successive trans – cis isomerizations τ_p

Experiments often use very small intensities, which results in a very large τ_p , so it is important to verify for our particular systems that we are in the same regime as experiments. (Even though in other papers we verified the period influence on the isomerization effects, i.e. the isomerization to be enough distanced in time so that an isomerization does not affect the next one.)

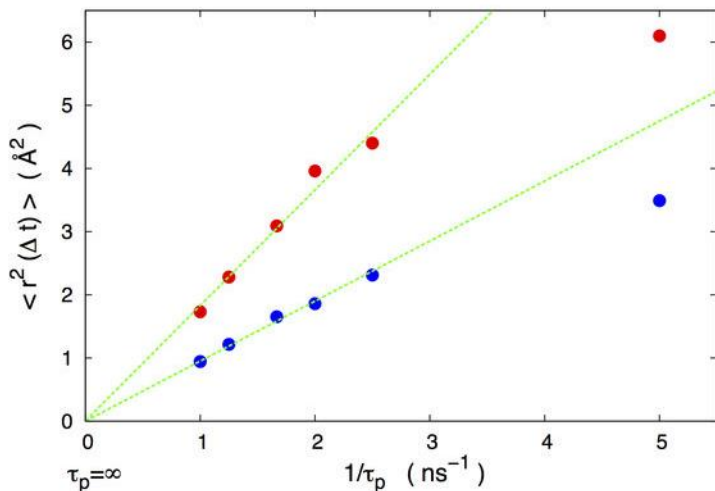


Figure VII.8. Host mobility $\langle r^2(\Delta t) \rangle$ ($\Delta t = 10$ ns) as function of period τ_p i.e. the time between two trans – cis isomerizations (the low thermal mobility is subtracted) for i) host 1 (red circles): $\alpha = 1$, $\sigma_{11} = 3.45$ Å, $\rho = 2.42$ g/cm³, and $T = 10$ K ($T < T_g$) and ii) host 2 (blue circles): $\alpha = 1.32$, $\sigma_{11} = 4.56$ Å, $\rho = 1.63$ g/cm³, and $T = 80$ K ($T > T_g$). The motor is $L = 15.4$ Å long and $W = 3.9$ Å wide.

In experimental studies of azobenzene containing materials, the irradiation light is often of very low intensity, determining a large mean time period τ_p . In simulations, these times are not feasible, thus it is desirable to shorten this time period. The important aspect in this matter is to ensure that the isomerizations act like separate stimuli and they do not affect each other's effects. To verify that the time period used for the calculations resides in the same physical regime as in experimental studies, various time periods are tested for the different host molecules tested.

In the linear response theory, response is proportional to stimulus if the stimuli are sufficiently low and rare enough to act separately. Accordingly, when in the linear regime, the time periods used in the calculations of this work should be relatable to the majority of experiments. The host mobility for two different hosts (host 1 and host 2) (*Figure VII.8.*) is proportional to the inverse of the time period $1/\tau_p$ for frequencies as large as $f = 1/\tau_p$ 2.5 ns^{-1} , i.e. periods $\tau_p \geq 400 \text{ ps}$. Thus, the two periods compared in the *Figure VII.4.*, $\tau_p = 400$ and 600 ps , are both included in the linear response regime. At larger frequencies though a decrease in the medium viscosity around the motor determines saturation.

CHAPTER VIII. Diffusion studies on different motor sizes

VIII.1. Study framework

In this work section, the aim is focused on finding the parameters that have significant influence on the molecules motion found in the vicinity of an isomerizing motor. For this purpose, we use an idealized model for the molecular motor (rectangular form) to study how isomerization induced mass transport depends on the motor's dimensions.

The calculation is performed for a system of one molecular motor of various sizes and 500 host molecules. We use two types of host molecules, each constituted of two atoms ($i=1,2$) that interact with Lenard-Jones potentials.

$V_{ij} = 4\varepsilon_{ij} \left((\sigma_{ij}/r)^{12} - (\sigma_{ij}/r)^6 \right)$, with the parameters: $\varepsilon_{11} = \varepsilon_{12} = 0.5 \text{ kJ mol}^{-1}$, $\varepsilon_{22} = 0.4 \text{ kJ mol}^{-1}$ and $\sigma_{ij} = \alpha \sigma_{ij}^0$, where $\sigma_{11}^0 = \sigma_{12}^0 = 3.45 \text{ \AA}$, $\sigma_{11}^0 = 3.28 \text{ \AA}$ and α is a constant that defines our different hosts. We used mainly two hosts, that we call host1 ($\alpha = 1$) and host2 ($\alpha = 1.32$). The atoms are rigidly bonded by fixing the interatomic distance to $d = \alpha d^0$, with $d^0 = 1.73 \text{ \AA}$. We model the motor with a rectangular shape constituted of rows of Lenard-Jones atoms with the parameters: $\varepsilon_{33} = 0.996 \text{ kJ mol}^{-1}$ and $\sigma_{33} = 3.405 \text{ \AA}$. For the motor atoms, as well for the host atoms, we used the mass of Argon. The host interacts with the motor by the following rule: $\varepsilon_{ij} = (\varepsilon_{ii}\varepsilon_{jj})^{0.5}$ and $\sigma_{ij} = (\sigma_{ii}\sigma_{jj})^{0.5}$. We evaluate the glass transition temperature T_g of the host to be $T_g \approx 28 \text{ K}$, from the change of slope of the potential energy as a function of temperature. As we use Lenard-Jones atoms, the potentials are versatile and the modification of the ε results in a modification of the temperatures (e.g. glass transition temperature, melting temperature) by the same amount.

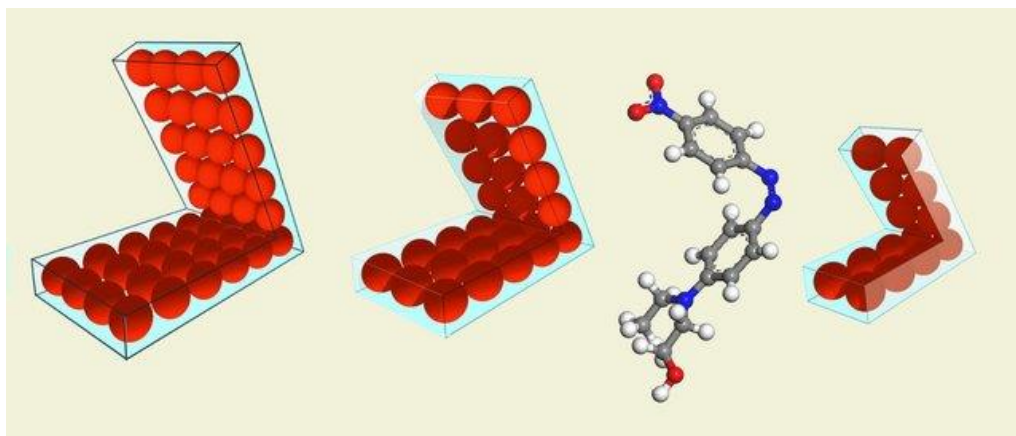


Figure VIII.1. Representation of an idealized model motor in three different sizes, along with Disperse Red 1 molecule, both in cis (folded) configuration. The parallelograms in the illustration are just for guiding purposes.

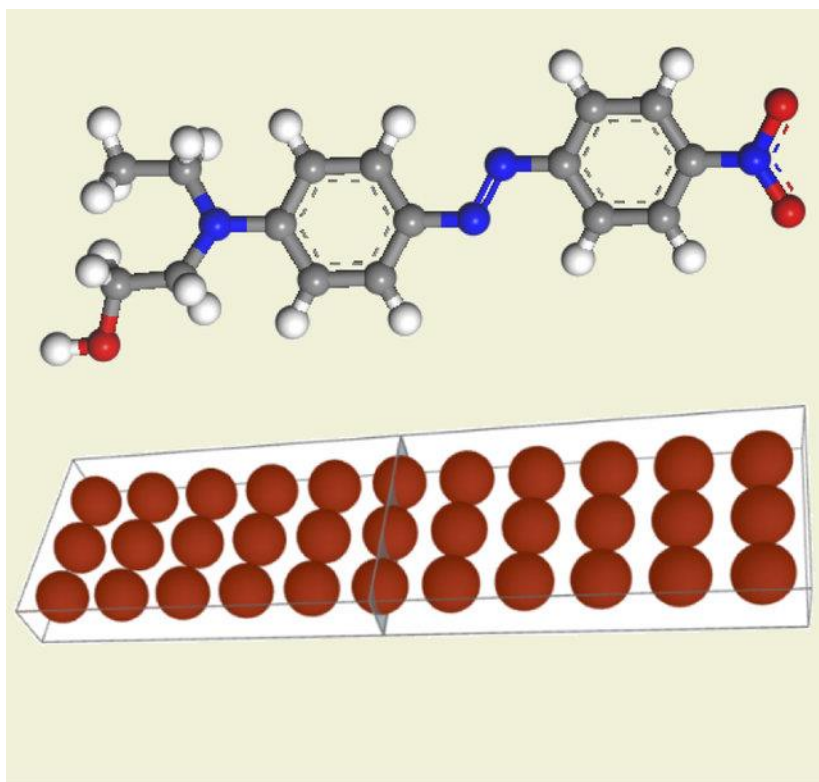


Figure VIII.2. An idealized model motor, along with the Disperse Red 1 molecule in trans (flat) configuration. The parallelograms in the illustration are just for guiding purposes.

Summarizing the calculation system, we have the following parameters.

Host 1 ($\alpha = 1$):

$$\sigma_1 = 3.45 \text{ \AA}, \sigma_1 = 3.28 \text{ \AA}, d = 1.73 \text{ \AA}, l = 5.1 \text{ \AA};$$

$$T_g \approx 28 \text{ K}, \text{ simulation temperature } T_{\text{sim}} = 10, 40 \text{ K};$$

Host 2 ($\alpha = 1.32$):

$$\sigma_1 = 4.554 \text{ \AA}, \sigma_1 = 4.330 \text{ \AA}, d = 2.284 \text{ \AA}, l = 6.7 \text{ \AA};$$

$$T_g \approx 28 \text{ K}, \text{ simulation temperature } T_{\text{sim}} = 40, 80 \text{ K};$$

Motor:

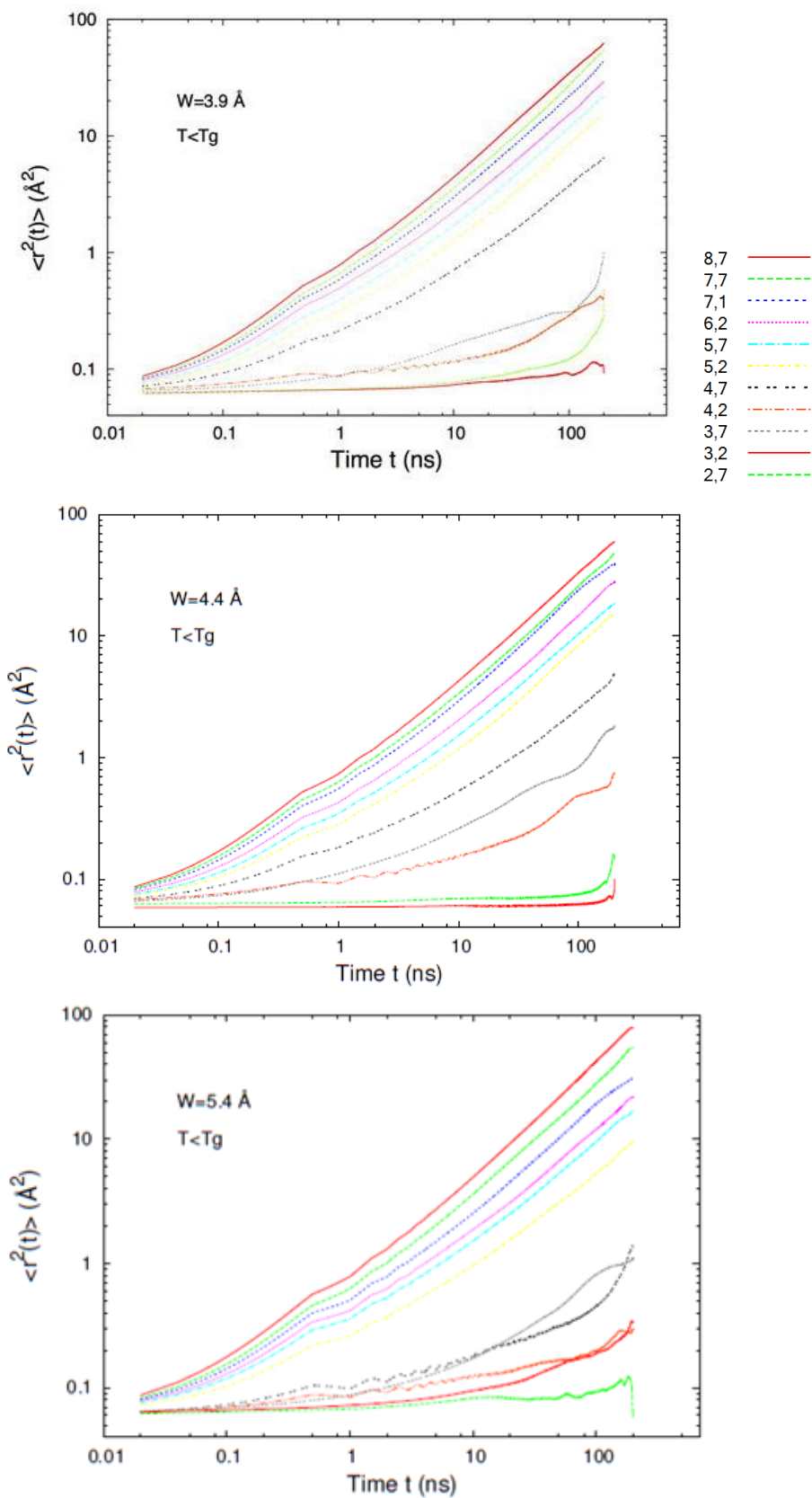
$$11 \text{ lengths } L = L_T/2 = 2.7, 3.2, 3.7, 4.2, 4.7, 5.2, 5.7, 6.2, 7.1, 7.7, 8.7 \text{ \AA};$$

$$5 \text{ widths } W = 3.9, 4.4, 5.4, 7.4, 9.4 \text{ \AA}.$$

VIII.2. Influence of the motor's arm length on the host diffusion

Diffusion is calculated by using the position of mass centers of molecules. Thus, saving positions as a function of time allows the diffusion evaluation by relating it to the mean square displacement (MSD), according to Einstein's theory of Brownian motion. The mean square displacement evolution dependence on time is interpreted according to the Stokes-Einstein law for Brownian motion, which states a linear increase of MSD with time $\lim_{t \rightarrow \infty} \langle r^2(t) \rangle = 6Dt$, where r is the vector of distance covered by a particle in the time interval t , and D is the diffusion coefficient.

The MSD evaluation at $T = 10 \text{ K} < T_g$ shows that the medium's motions depend on the motor's arm length. Long motors, starting from $L_T = 9.4 \text{ \AA}$, induce diffusive motions into the host molecules. In systems with shorter motors, the isomerization generates only oscillating motions in the medium's molecules. These motions correspond to the oscillations inside the cages formed by the nearest neighbors.



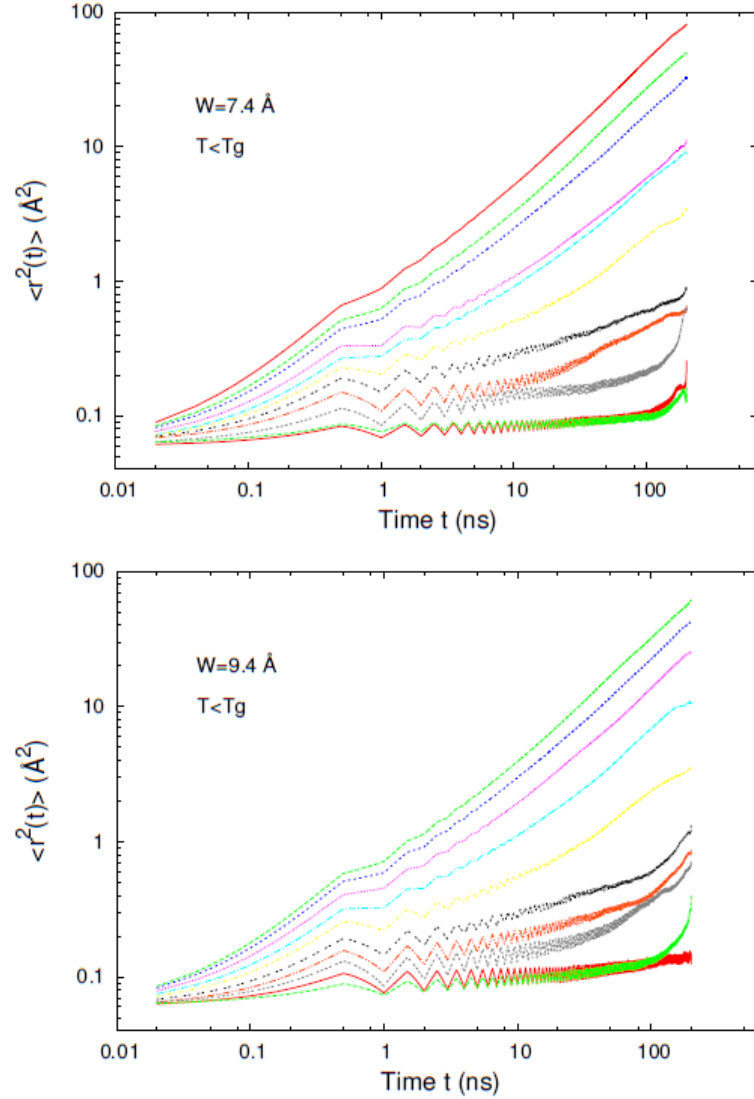
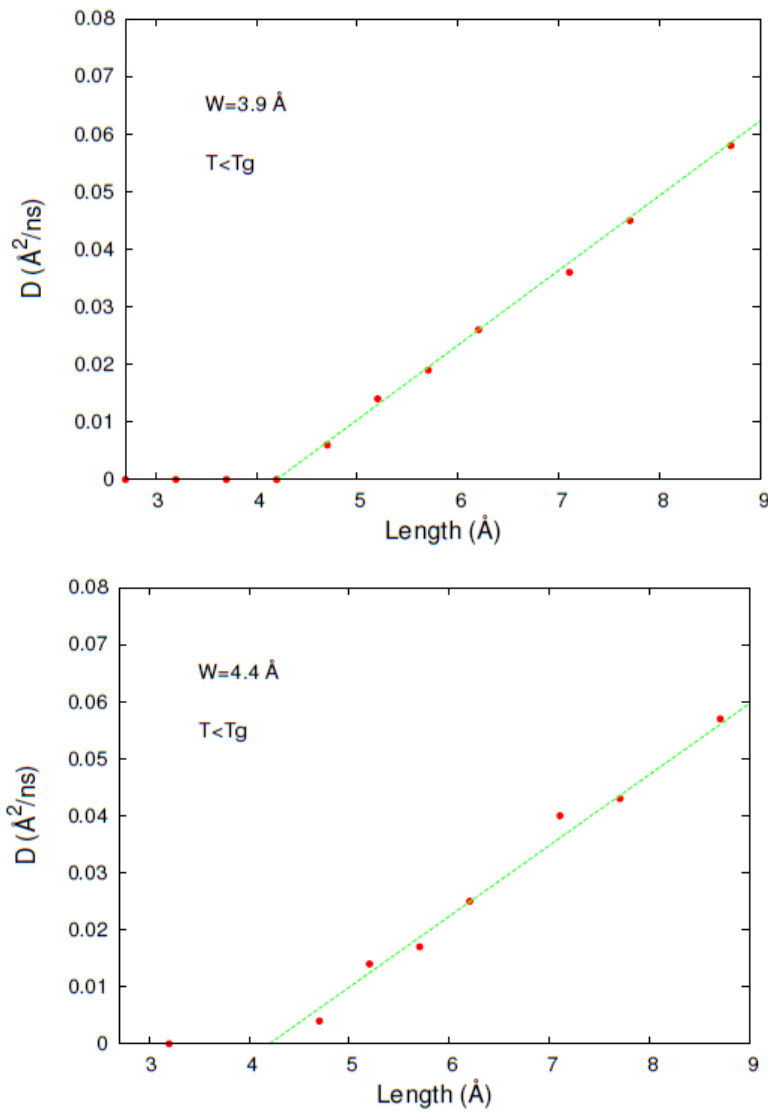


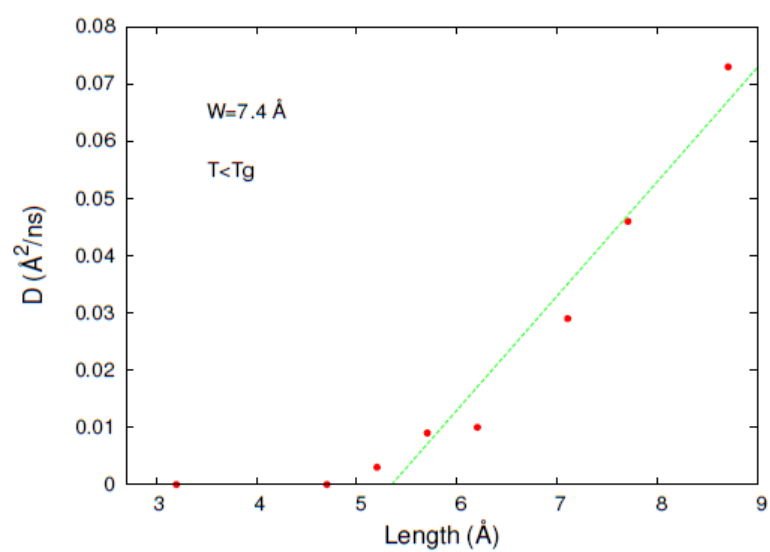
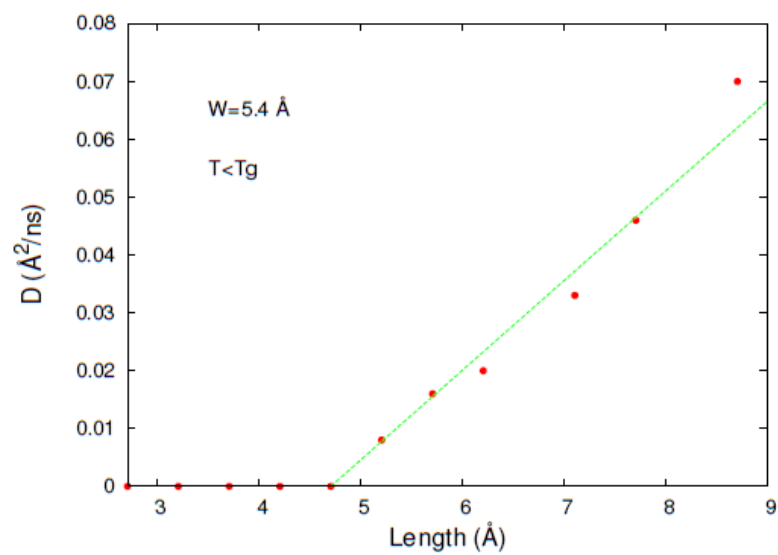
Figure VIII.3. Mean square displacement of host 1 molecules, plotted for all motor's widths $W = 3.9, 4.4, 5.4, 7.4, 9.4 \text{ \AA}$ at $T = 10 \text{ K} < T_g$. The curves represent the different lengths of the motor's arm $L = L_T/2$.

Analyzing how motors of all widths need approximately the same minimum arm length, in order to create diffusive motion in the surrounding medium, it appears that there is a length threshold.

To further observe this behavior, the diffusion coefficient D is calculated and displayed as a function of the arm length, L . The results clearly show a length threshold followed by a linear increase. In conformity with our simulation set up, the system's evolution is to be explained within the frame of the linear response theory. According to it, a small perturbation induces a linear response.

Previous research (Accary and Teboul, 2013) of molecular dynamics on a system of DR1 diluted in MMA, that there are two different dynamical regimes that depend on the isomerization period τ_p . The two regimes are correlated in the experiments with two physical behaviors that take place at low or high light intensity. The linear response regime takes place at large isomerization periods, when the stimuli is small enough, so the diffusion increases linearly with the isomerization rate $f = 1/\tau_p$. The saturation regime corresponds to small isomerization periods that lead to bigger stimuli, resulting in important perturbations that affect the host, thus the diffusion coefficient reaches saturation.





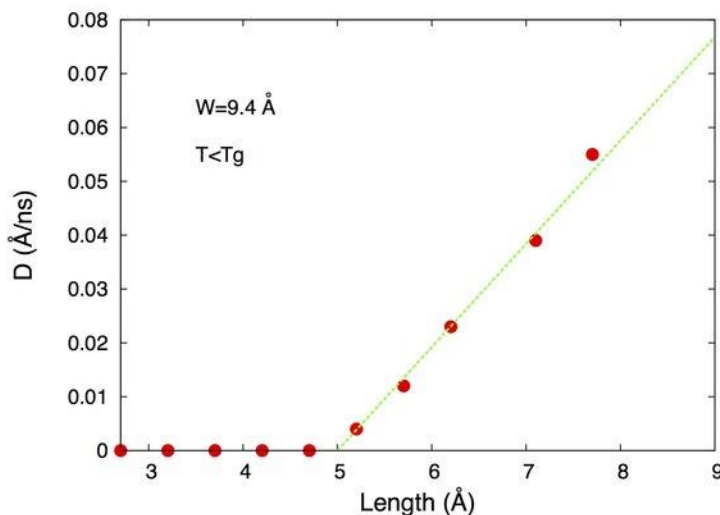


Figure VIII.4. Host 1 diffusion coefficient versus the motor's arm length $L = L_T/2$ for all the constant widths $W = 3.9, 4.4, 5.4, 7.4, 9.4 \text{ Å}$ at $T = 10 \text{ K} < T_g$.

These results find the motor's arm length threshold $L_{threshold} \approx 5 \text{ Å}$. Considering the host's dimension, $w = 3.4 \text{ Å}$, and $l = 5.1 \text{ Å}$, it can be observed that the threshold value matches the host molecule's size.

The non-Gaussian parameter $\alpha_2(R, \tau_p, t) - \tau_p$ is the isomerization period T_f —measures the deviation from typical Brownian motions as a result of spontaneously emerging cooperative motions of molecules. Thus, the parameter is dependent on the applied stimulus, i.e. it increases with the motions induced by the isomerization. Evaluation of α_2 is performed over an area defined of radius $< 10 \text{ Å}$ around the center of mass of the motor.

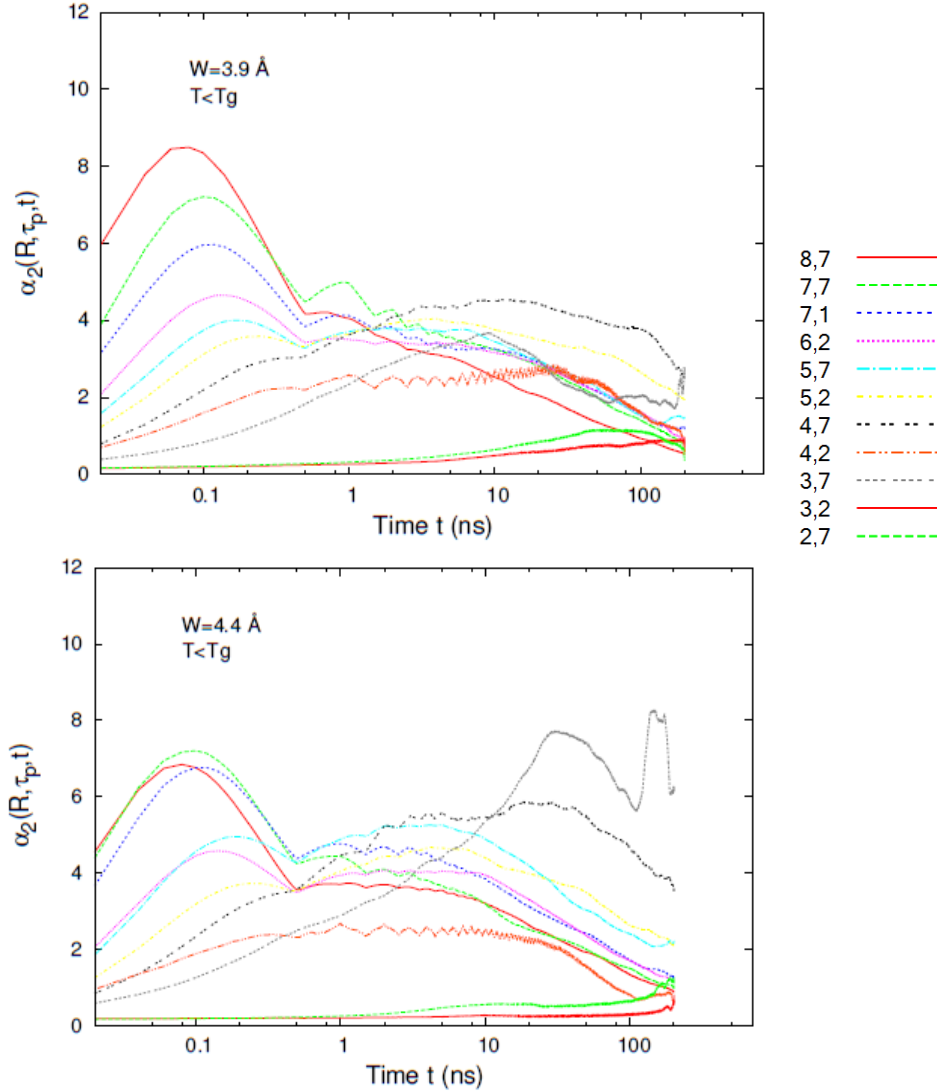


Figure VIII.5. The non-Gaussian parameter α_2 of host 1 molecules inside the simulation box versus the motor's arm length $L = L_T/2$ for the constant widths $W = 3.9$ and 4.4 \AA at $T = 10 \text{ K} < T_g$.

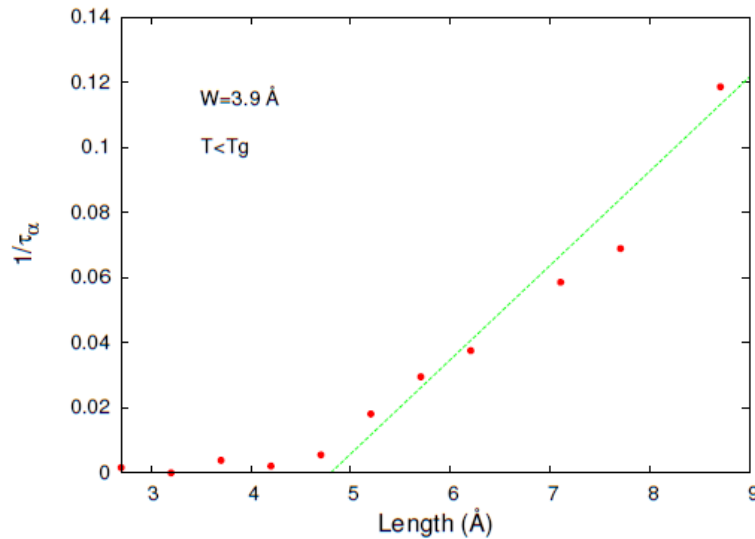
The dependence of $\alpha_2(R, \tau_p, t) - \tau_p$ is the isomerization period T_f versus time on the motor's arm length can be quantified through the time t^* where α_2 reaches maximum amplitude: $\alpha_2(t^*) = \alpha_{max}$.

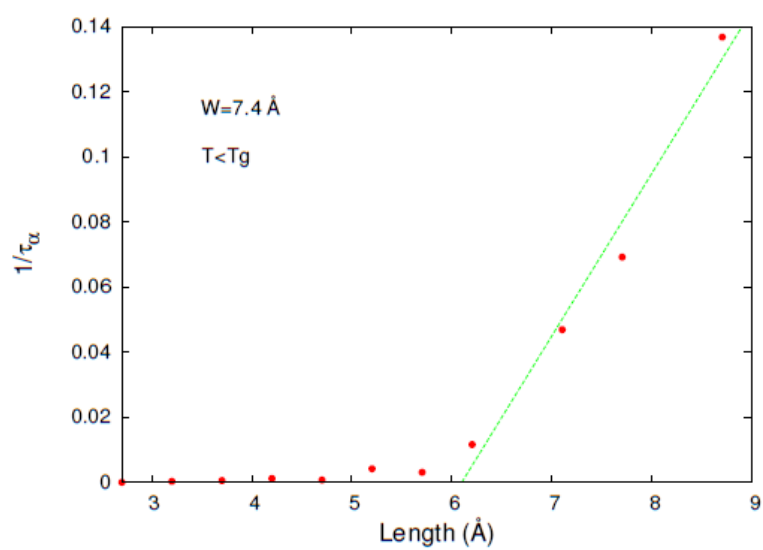
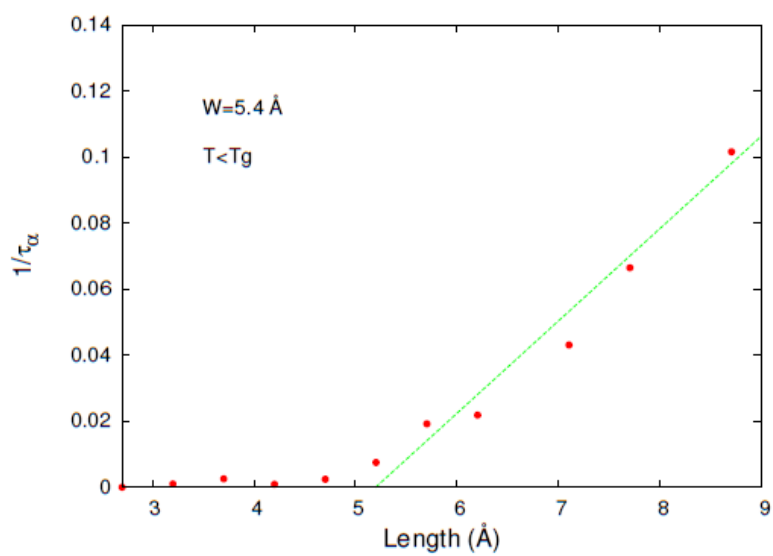
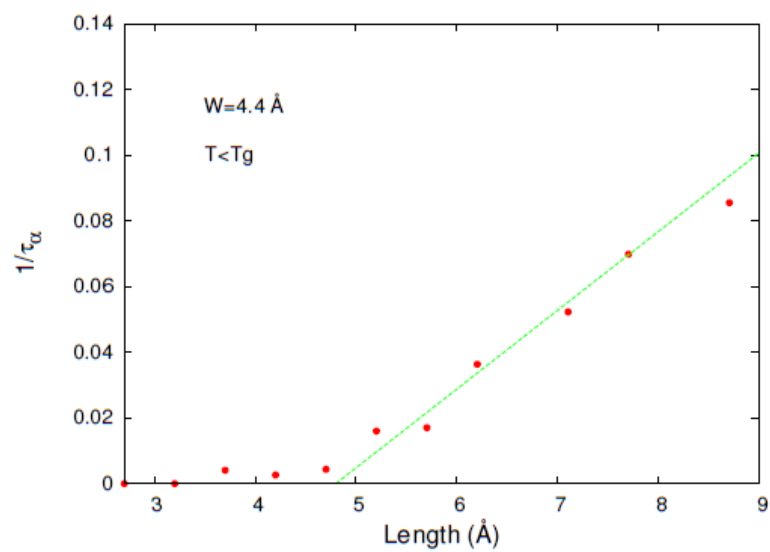
In accordance with the results for diffusion, along with the decrease of the motor's arm length, the amplitude of α_2 also decreases. Longer motors have a higher effect on the molecules displacement, which in turn influences the deviation from Brownian motion. Thus, dynamic heterogeneities in the medium molecules experience a rise along with the diffusion.

According to Einstein – Smoluchowski equation $D = \frac{kT}{\xi}$, diffusion is influenced by the friction coefficient ξ , which implies the system's viscosity and a particle's (here molecule) form and size. T represents the absolute temperature, and k is the Boltzmann constant.

Information about the system's viscosity is drawn from the α structural relaxation time τ_α . This parameter is obtained from the incoherent intermediate scattering functions (IISF), and it is defined by the relation $F_s(Q_{max}, \tau_\alpha) = e^{-1}$, where Q is the wave vector. When $Q = Q_{max}$, the wave vector corresponds to the maximum of the static structure factor $S(Q)$. The time in which IISF decreases by a factor of $1/e$ represents the α structural relaxation time τ_α .

Depicting the inverse of the α relaxation time $1/\tau_\alpha$ as a function of the arm's length, the appearance of the threshold is again observed, followed by the linear increase. As the relaxation time offers information on viscosity, the obtained data indicates that the medium's viscosity decreases only above a threshold value. Below the L value, there is no effect on the viscosity. It is necessary to be noted that the effect on viscosity manifests intermittently, according to the trans – cis isomerization, translated here through folding/unfolding.





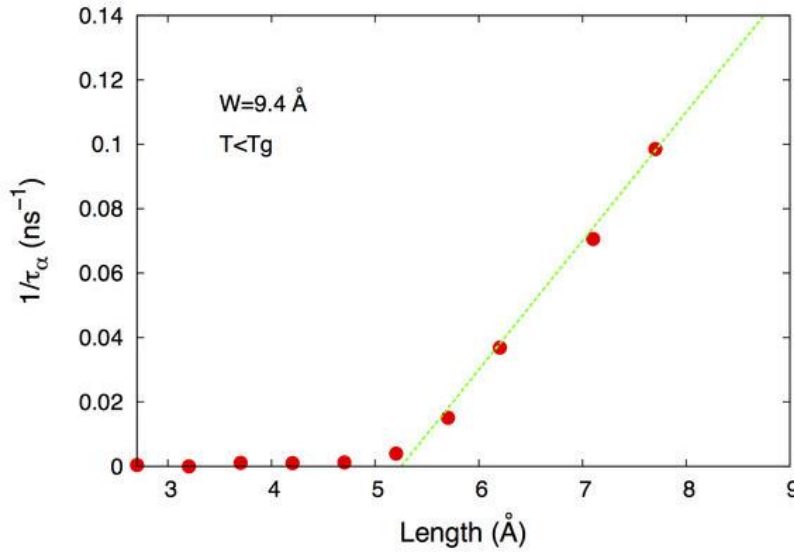


Figure VIII.5. Average α relaxation time τ_α of host 1 molecules inside the simulation box versus the motor's arm length $L = L_T/2$ for all the constant widths $W = 3.9, 4.4, 5.4, 7.4, 9.4$ Å at $T = 10$ K $< T_g$.

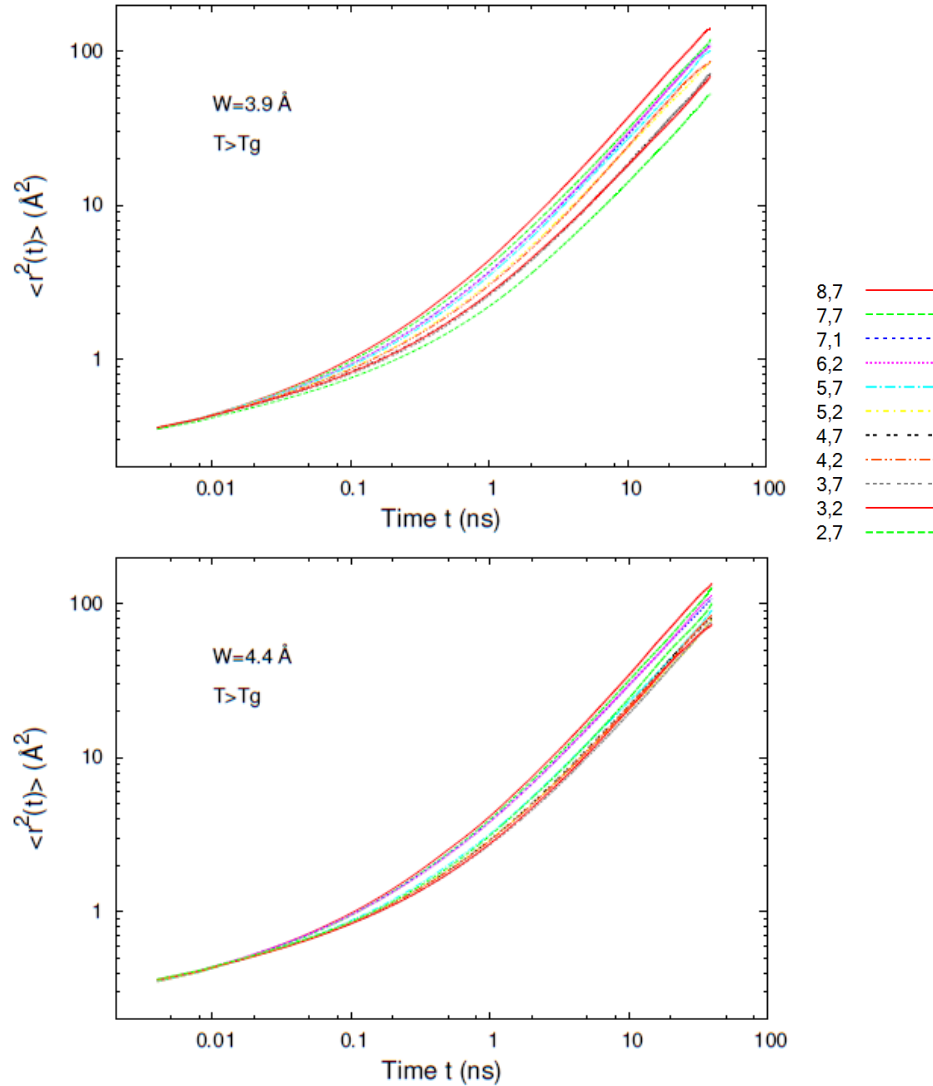
Regarding the isomerization induced mass transport, there are at least two theories that predict the existence of a threshold. According to the cage breaking theory, the motor needs to perform a thrust upon the host molecules, so that they can reach at least the nearby cage. The distance range from one cage to the next one represents, thus, the minimum length necessary to induce diffusion. In accordance with the pressure gradient theory, the driving force has to surpass the material's constitutive stress and this crossover is also associated with the minimum length of the arm.

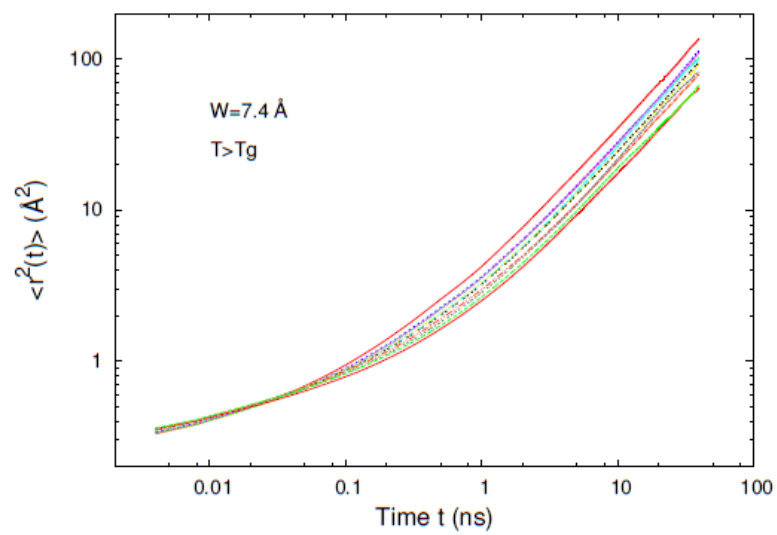
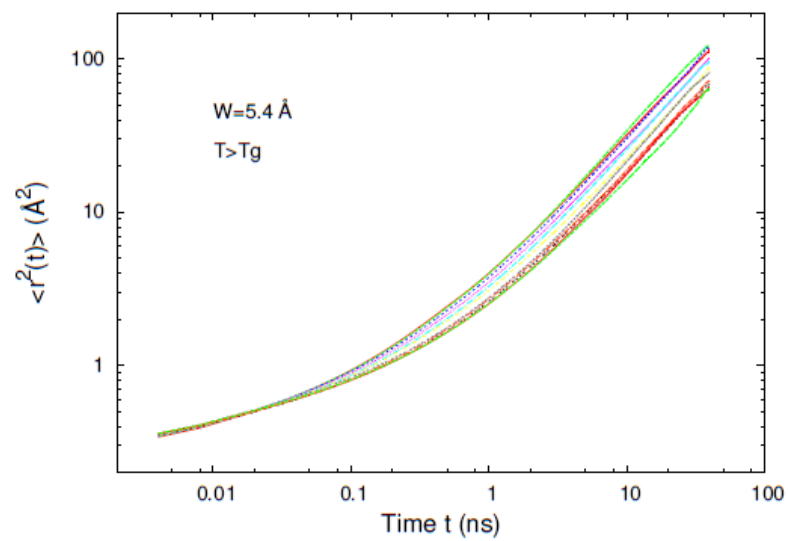
The different mass transport theories proposed have different responses to temperature influences. For example, in the cage breaking theory, the temperature would not be expected to have a significant influence on the motor's arm length threshold, since the distance between a molecule and its first neighbors that form the cage is independent of temperature. Thus, the minimum distance that the host molecules have to be pushed to is always the same, no matter the temperature. Meanwhile, for theories with constraints, the constraints are expected to grow with the temperature increase, which in turn will raise the threshold values. Performing calculations at different temperatures offer the possibility to investigate the temperature's involvement in the diffusion behavior.

Since the results presented above correspond to simulations at $T = 10\text{ K} < T_g$, we also wanted to see the behavior at higher temperatures, and we modeled the same system at $T = 40\text{ K} > T_g$.

We find the material responds in the same manner, with the specification that diffusion never totally cancels due to thermal energy. To highlight the isomerization induced diffusion, thermal diffusion thus has to be subtracted from the total diffusion.

For this purpose, simulations are run with and without isomerization. When the system to be calculated has a motor that does not perform the isomerization specific motion, the simulation is referred to here as being *off*. In the same manner, when the motor isomerizes inside the medium, the simulation is called *on*.





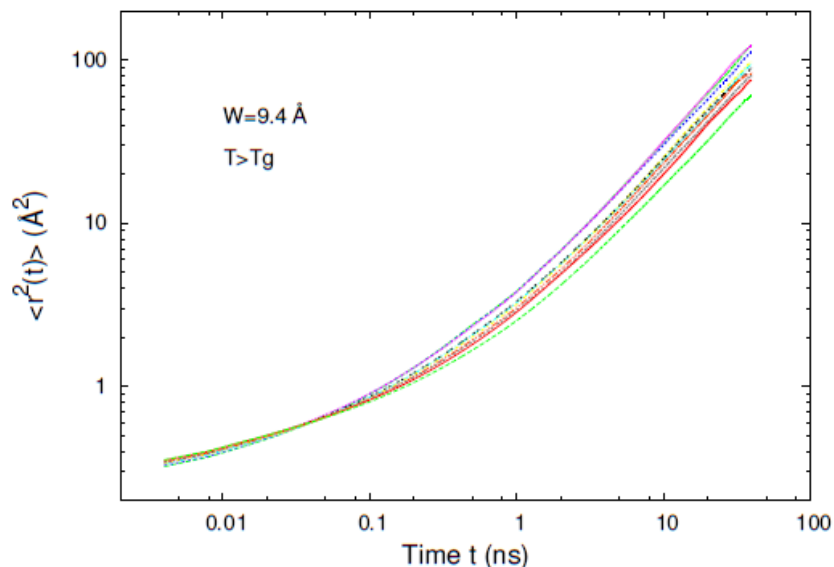
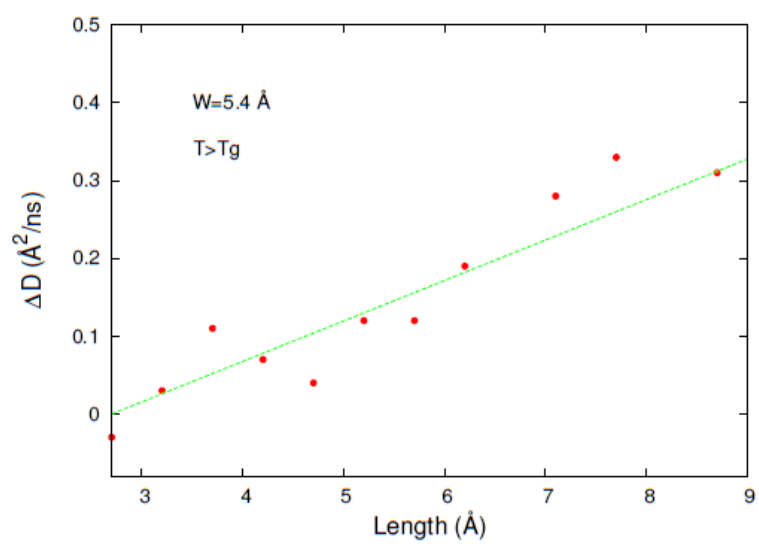
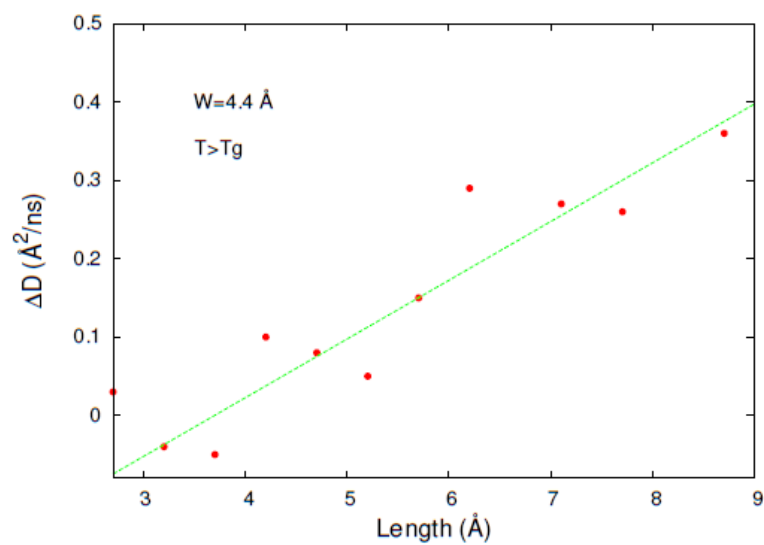
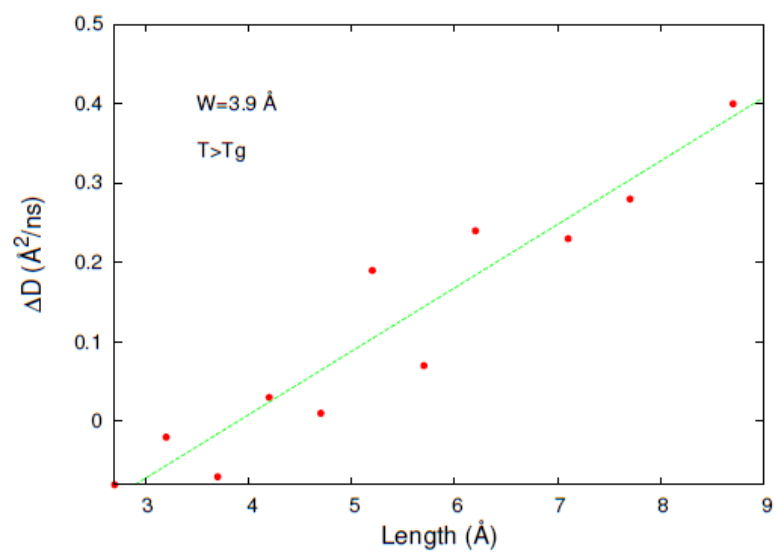


Figure VIII.6. Mean square displacement of host 1 molecules plotted for all motor's widths $W = 3.9, 4.4, 5.4, 7.4, 9.4 \text{ \AA}$ at $T = 40 \text{ K} > T_g$ with isomerization on. The curves represent the different lengths of the motor's arm $L = L_T/2$.

The host's diffusion at the higher simulation temperature $T = 40 \text{ K}$ is similar to the one found for low temperature $T = 10 \text{ K}$. But, as already mentioned, thermal energy intervenes, so thermal diffusive motions are always present in the system, masking an eventual threshold of the motor's arm length.

The diffusion coefficient is calculated here as the difference between the simulation *on* and *off* $\Delta D = D_{on} - D_{off}$.



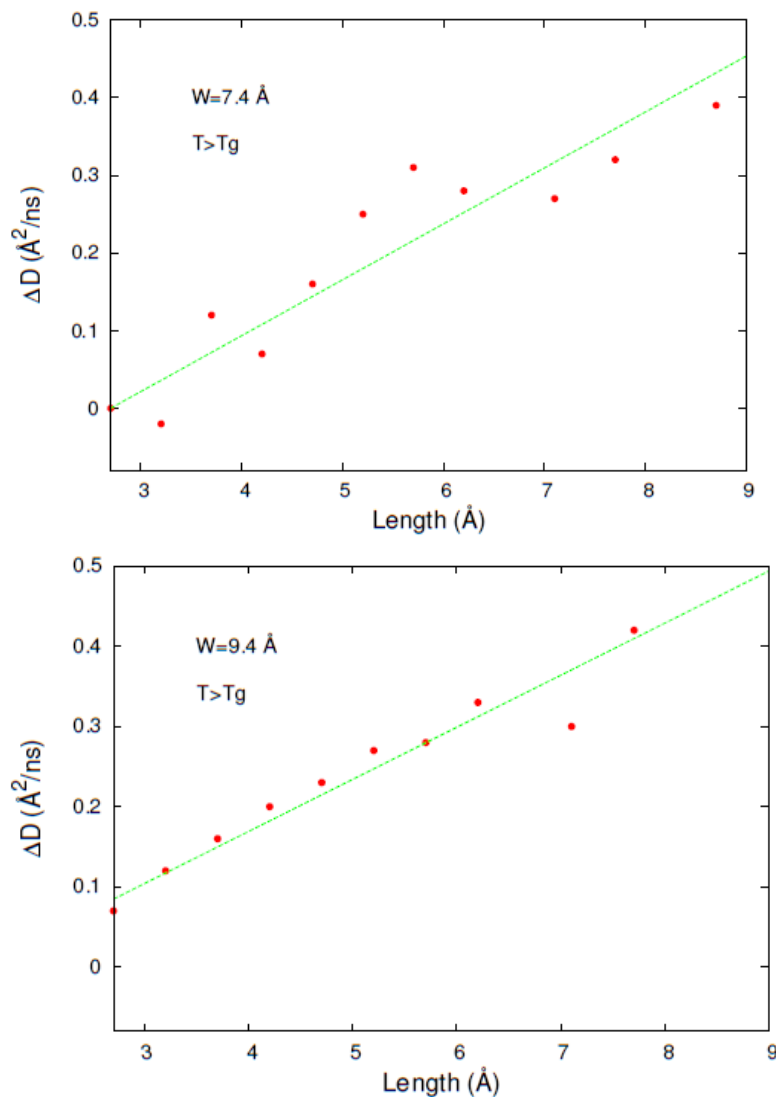
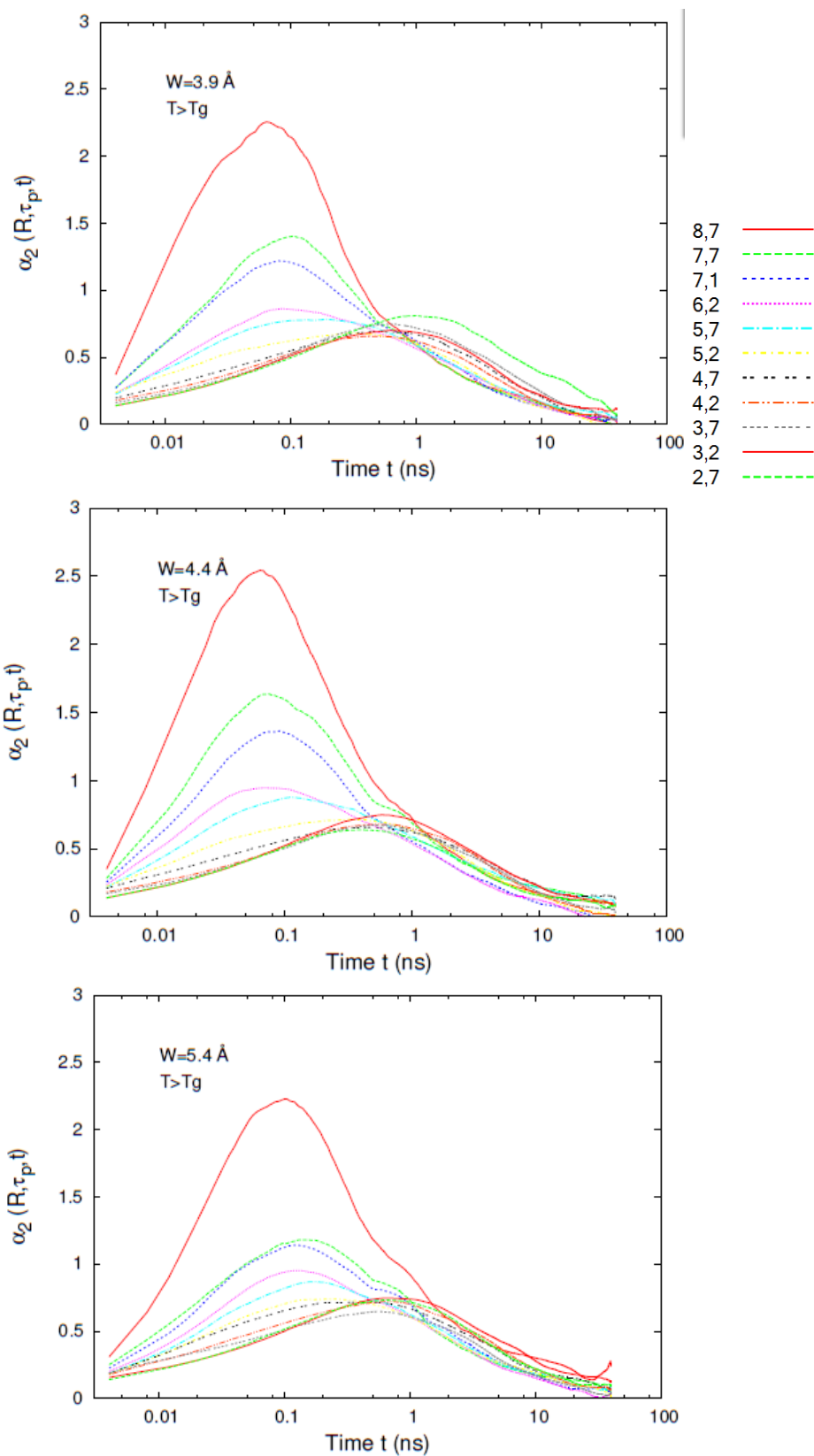


Figure VIII.7. Host I diffusion coefficient versus the motor's arm length $L = L_T/2$ for all the constant widths $W = 3.9, 4.4, 5.4, 7.4, 9.4 \text{ \AA}$ at $T = 40 \text{ K} > T_g$ with isomerization on.

As for the low temperature simulations $T = 10 \text{ K}$, a linear dependence is found between the motor's arm length and the host's diffusion. The difference is that the threshold is not observed.

Calculation of α_2 parameter is again performed to investigate the correlation between the spontaneously emerging cooperative motions of the host molecules and the motor's arm length.



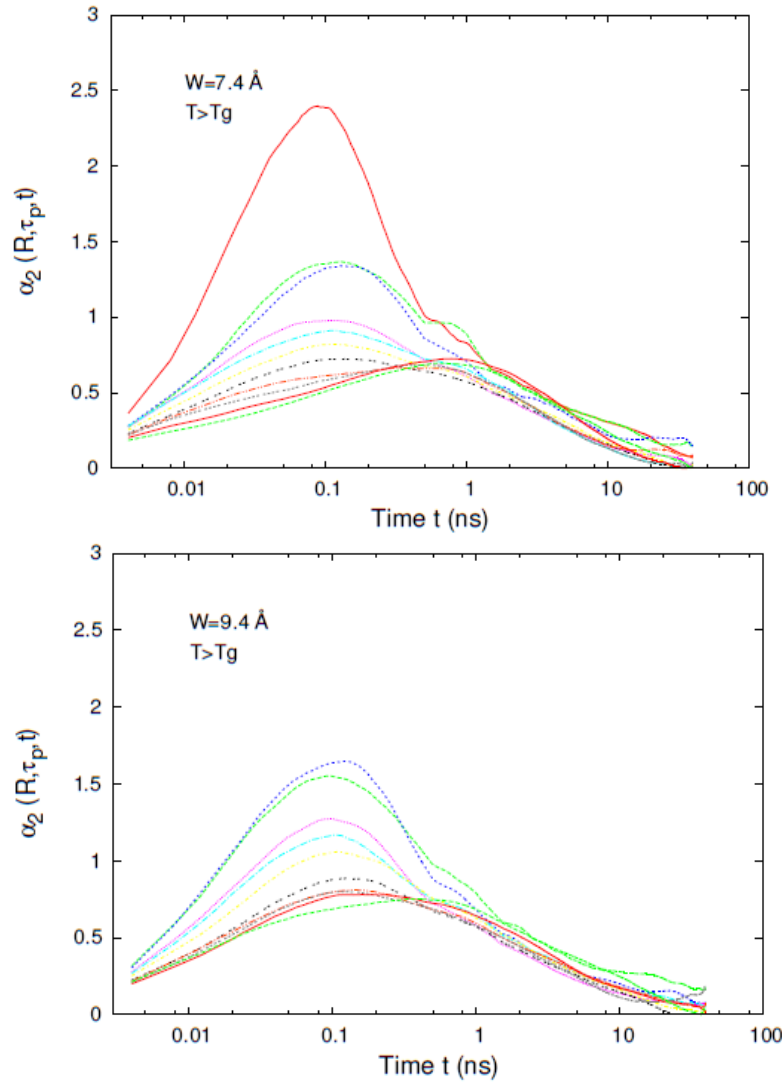
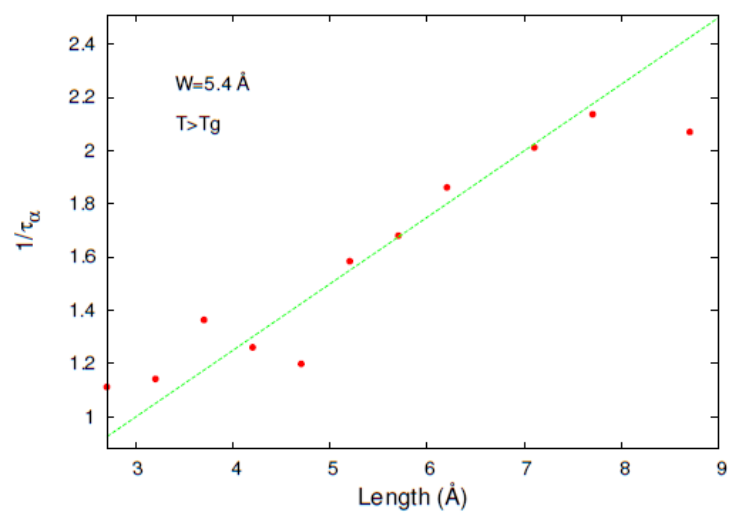
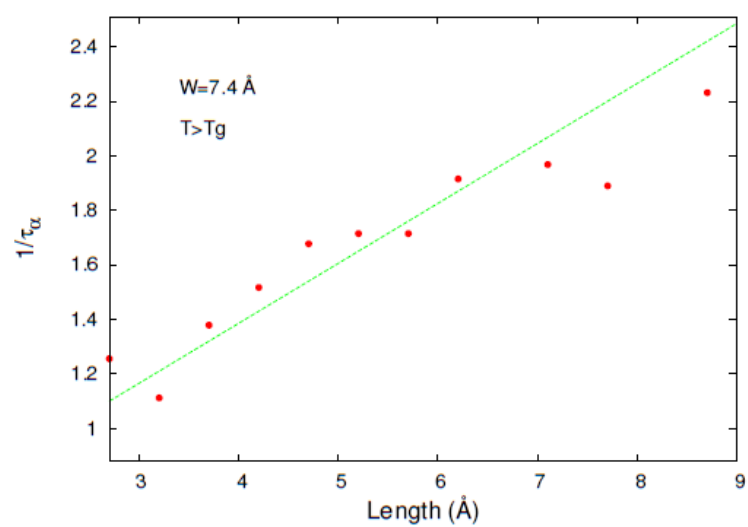
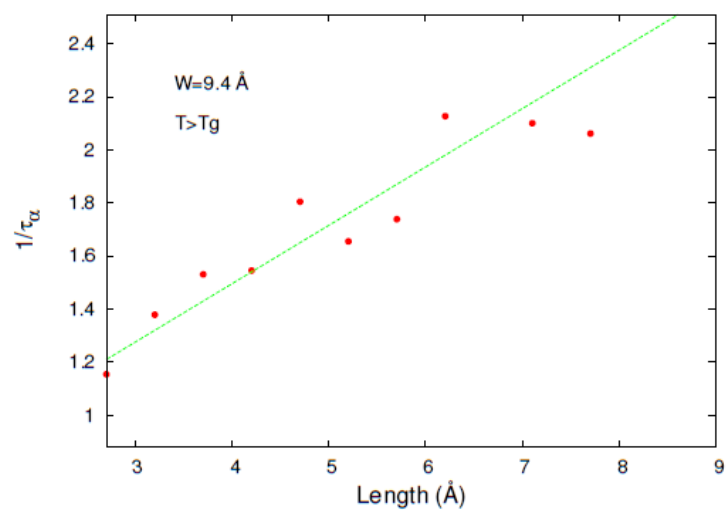


Figure VIII.8. The non-Gaussian parameter α_2 of host 1 molecules versus the motor's arm length $L = L_T/2$ for all the constant widths $W = 3.9, 4.4, 5.4, 7.4, 9.4 \text{ \AA}$ at $T = 40 \text{ K}$ with isomerization on.

Like in the case of the low temperature simulations, the α_2 parameter experiences a growth along with the motor's arm length. These results show that increased diffusion is linked to more cooperative motions in the medium molecules.

Viscosity is also investigated and displayed as the inverse of the α relaxation time $1/\tau_\alpha$.



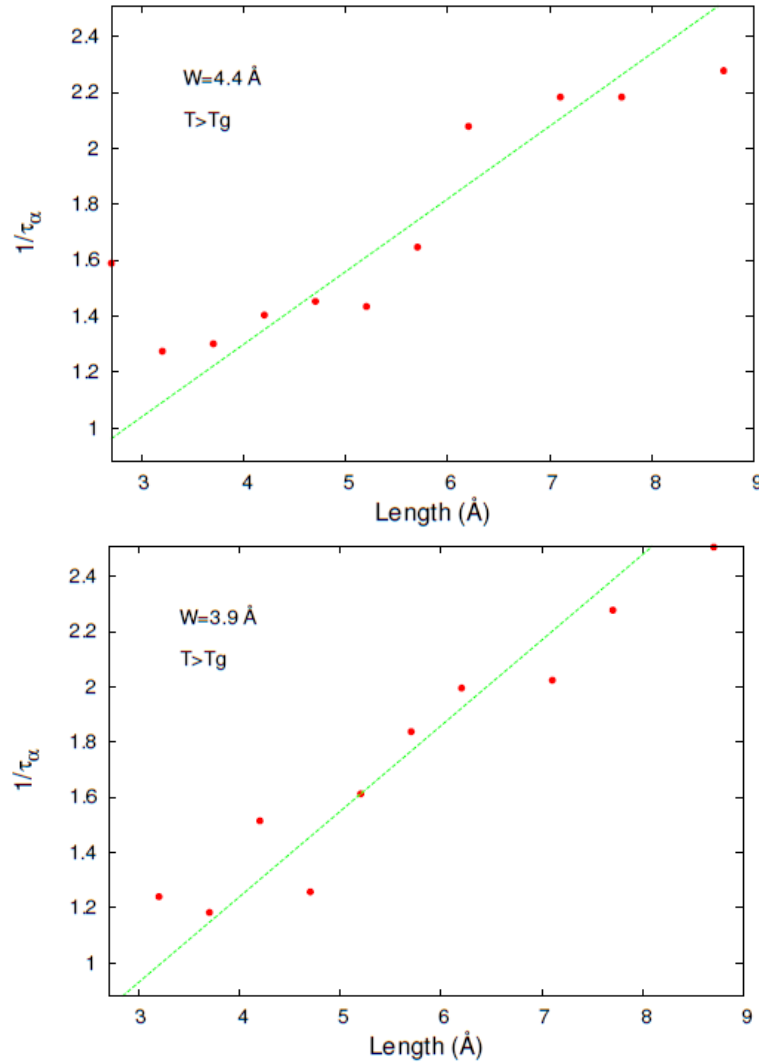
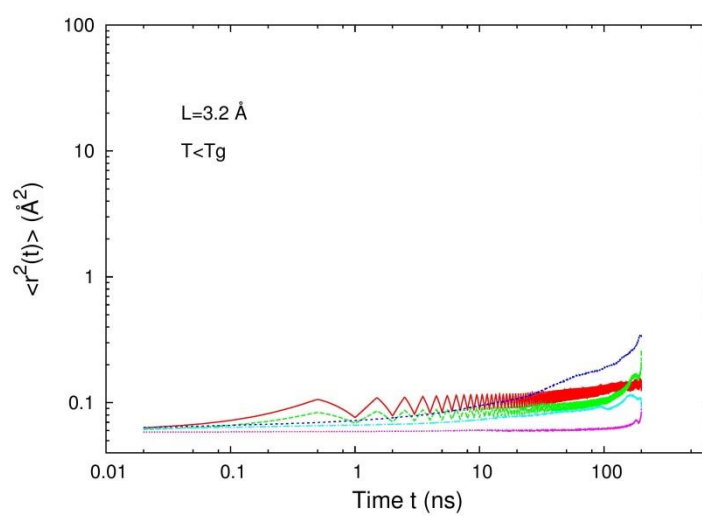
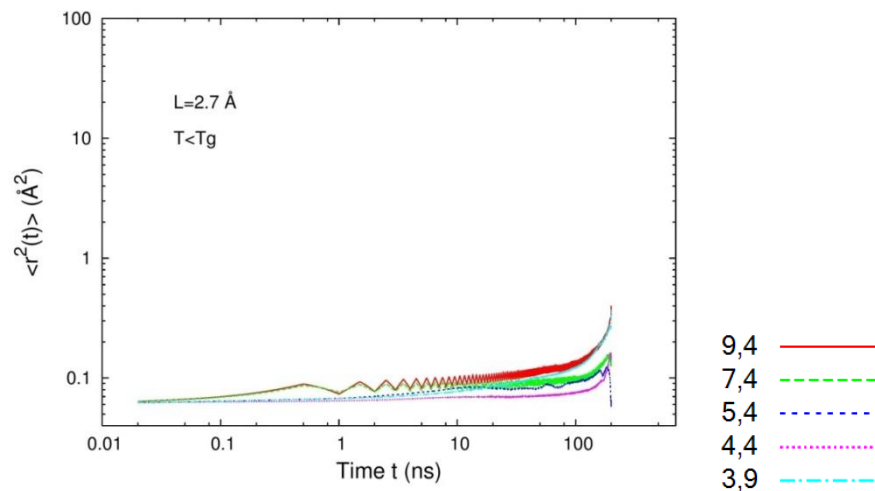


Figure VIII.9. Average α relaxation time τ_α of host molecules inside the simulation box versus the motor's arm length $L = L_T/2$ for all the constant widths $W = 3.9, 4.4, 5.4, 7.4, 9.4$ Å at $T = 40$ K with isomerization on.

The results show that an increase in the motor's arm length comes with the viscosity decay, just as seen for low temperature.

VIII.3. Influence of motor width on the host's diffusion

The effect of the motor's width on its capacity to induce diffusion of the surrounding matter is also studied. Graphs of the MSD dependence on the motor's width are presented for a few different motor lengths, to show how the diffusion evolves with the width increase. In contrast with the results for the arm length, no threshold is expected for the motor's width.



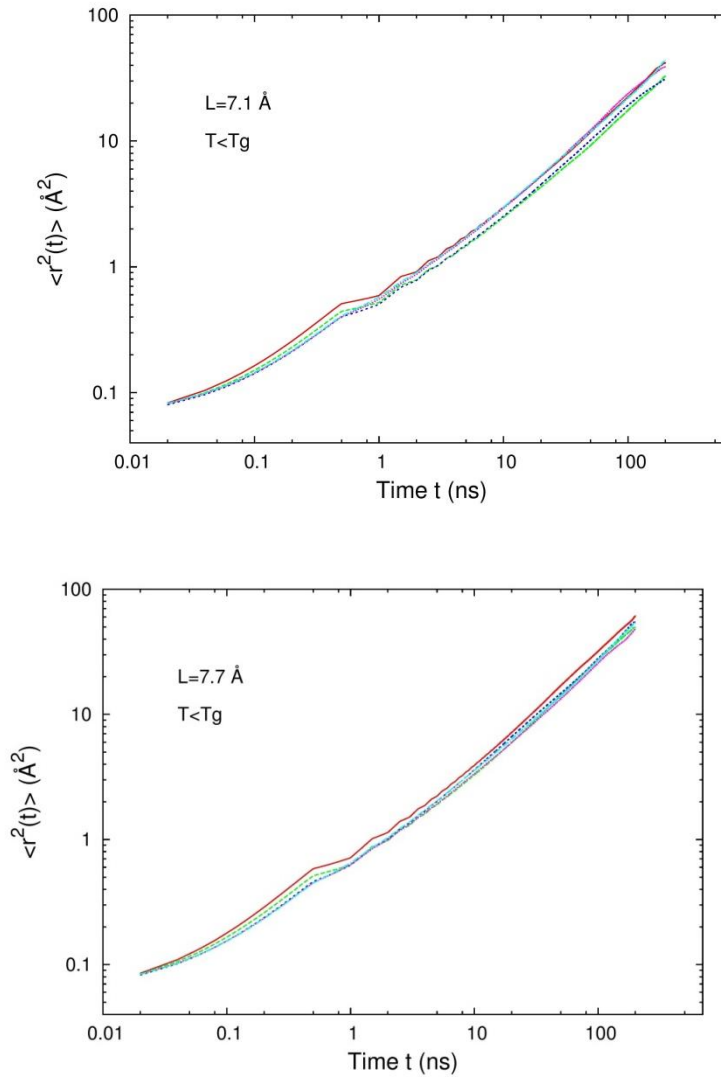


Figure VIII.10. Mean square displacement of host 1 molecules plotted for the arm lengths $L = L_T/2 = 2.7, 3.2, 7.1, 7.7 \text{ \AA}$ at $T = 10 \text{ K} < T_g$. The curves represent the different motor's widths.

For analyzing the behavior under the width's influence, it is sufficient to concentrate on the long motors, with $L_T > \delta$, that do induce diffusion. In agreement with the expectations, MSD evolution over time for different widths is almost the same, no matter how wide the motor is.

The MSD of the system with a $L = 2.7 \text{ \AA}$ long motor shows the free motion of host molecules. The staggering rate of the curve is due to the repeated isomerization phenomenon,

which creates small perturbations. The apparent increase at the end of the simulation time is explained by the fact that, at longer times, the perturbations tend to be larger, along with a precision decrease. Thus, the host molecules present no diffusion, just as stated in the previous results, where this small length $L = 2.7 \text{ \AA}$ is found to be below the threshold. In what concerns the large motor, $L = 7.7 \text{ \AA}$, the plot shows a clear diffusion, as the length is well above the threshold. What is to be noted here is that diffusion varies insignificantly with the width. Comparing the narrowest motor $W = 3.9 \text{ \AA}$ with the widest $W = 9.4 \text{ \AA}$, which is more than double, the results show that diffusion is almost constant.

What follows from this behavior is that within the range of widths studied, the motor's width has nearly no influence on diffusion. For large widths, however, a strong modification of the threshold is to be expected.

For further investigation, the previously found length thresholds are displayed for all the widths tested. To gain more insight into this matter, a new set of calculations was made for host 2 also. The length threshold corresponding to host 2 was found in the same manner as for host 1. The results for both hosts are depicted together and show that diffusion stays in the same range of threshold, unaffected by the motor's width. A threshold $\delta = 4.8 \pm 0.5 \text{ \AA}$ corresponds to host 1 and $\delta = 5.9 \pm 0.6 \text{ \AA}$ to host 2.

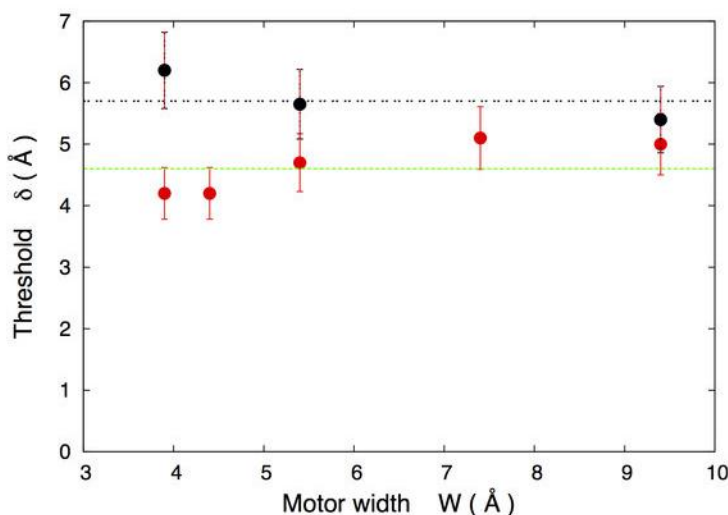


Figure VIII.11. Threshold on the motor's length versus the width. Red circles correspond to simulations with host 1 at $T = 10 \text{ K}$ and black circles are for host 2, $T = 40 \text{ K}$.

This finding agrees with the cage breaking model, which enables the following statement: Augmenting the motor's surface on the lateral only increases the number of molecules encountered in its way while folding/unfolding. Thus, while the number of pushed molecules increases, the distance's amplitude remains unaffected. To describe a clearer picture of the situation, doubling the motor's width should amount to having two motors, with respect to the diffusion. According to the linear response theory, there should be a relation of linear increase proportionality between diffusion and width. As the herein results do not find this behavior, there is one cue that can be noted: The motor's motion creates a perturbation in the neighboring molecules, diminishing, thus, its capacity to boost more molecules (i.e. to increase the number of pushed molecules) by adding more width.

VIII.4. Evaluation of different parameters concerning the host molecules

The analysis outcome on diffusion – motor size dependence revealed that diffusive motion in a host is enabled only if the motor's arm length extends over a certain reference value. The appearance of this threshold calls for more investigation, in order to find a connection to the various scales implied in the medium's molecules. Considering the host's 1 threshold, $\delta = 4.8 \pm 0.5 \text{ \AA}$, the maximum distance that the molecules can be pushed by the motor is $l\theta' = 5 \pm 0.5 \text{ \AA}$.

Firstly, a dimension related to the free motion of the host is analyzed. The free-volume theory takes into account this motion, stating that it is enabled by the free space that is created with each isomerization. The MSD plateau at low temperature $\langle r_{\text{plateau}}^2 \rangle = 0.06 \text{ \AA}^2$ gives the magnitude that a molecule can move freely inside its cage formed by the neighboring molecules $L_{\text{cage}}^{\text{host}} = \sqrt{\langle r_{\text{plateau}}^2 \rangle} = 0.25 \text{ \AA}$. In the same manner, the motor's free motion is evaluated: $\langle r_{\text{plateau}}^2 \rangle = 0.94 \text{ \AA}^2$ with $L_{\text{cage}}^{\text{motor}} = 0.97 \text{ \AA}$. These values prove to be way too low to be held responsible for diffusion.

A second lead is the link between diffusion and the host size, according to the cage breaking theory. Between the size of the host 1 molecules, 5.1 \AA long and 3.45 \AA wide, and

the threshold value, there is a clear comparability. In addition, the radial distribution function is evaluated to withdraw information about the system's structure.

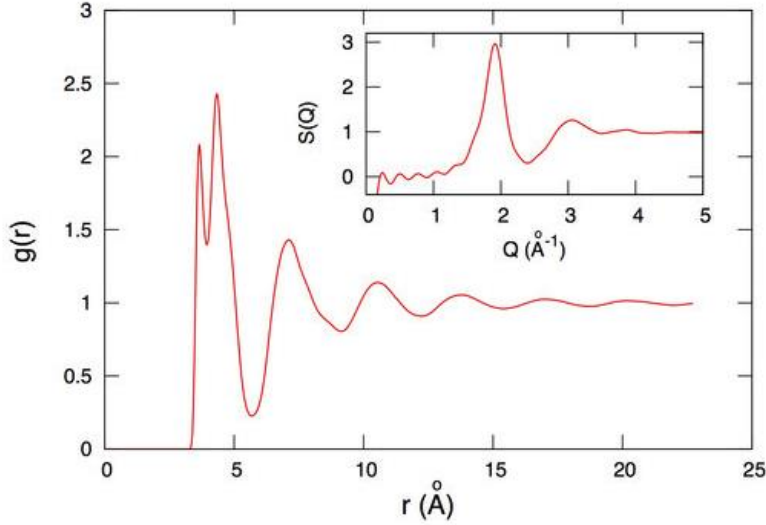


Figure VIII.12. Radial distribution function $g(r)$ between the centers of mass of host 1 molecules. Inset: Structure factor $S(Q)$. $T = 10$ K $< T_g$.

Peaks in $g(r)$ disclose the position of neighboring molecules. Thus, the first peak, situated at $r_0 = 3.7$ Å shows the distance until the closest neighbor and the second peak $r_1 = 4.4$ Å shows the next nearest neighbor. The first minimum in this function, $r_{min} = 5.7$ Å corresponds to the value of the mean force potential's barrier $V_{mf} = -kT \log(g(r))$. This represents the length that needs to be outdistanced by a molecule, in order to leave the cage that it is confined into by its neighboring molecules. In the cage breaking model, this translates into the minimum distance that a molecule has to be pushed to derive into diffusive motion. Now, this calculation of $r_{min} = 5.7$ Å, along with the prior discussed parameters - host molecule's length $l = 5.1$ Å and the motor's arm displacement $\theta l' = 5$ Å - offers a first picture of the molecular movement in the material. To measure the spatial correlation between the positions of the molecules, the structure factor $S(Q)$ is analyzed. The curve shows a first peak at $Q_0 = 1.92$ Å⁻¹, leading to the global correlation length $L_{global} = \frac{2\pi}{Q_0} = 3.3$ Å.

The induced host mobility is evaluated as a function of the host molecules distance to the motor. Calculation of this three-dimensional variation is performed considering the space around the motor as being layered into concentric spheres of 2 Å thickness each.

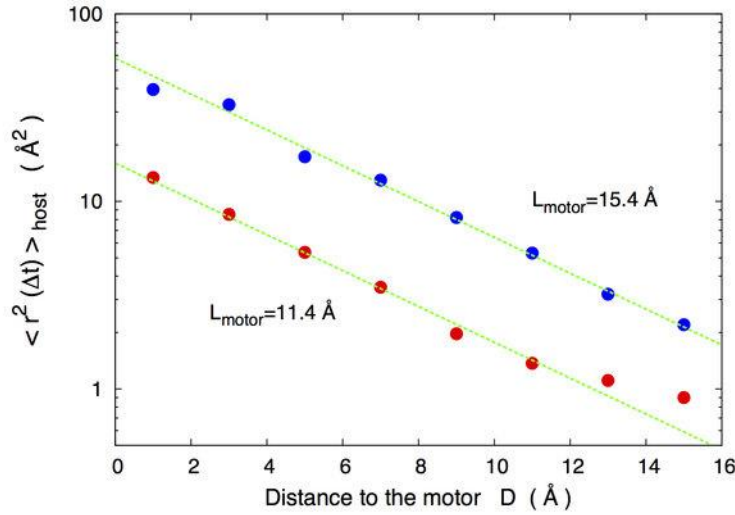


Figure VIII.13. Local host mobility $\mu = \langle r^2(\Delta t) \rangle$ ($\Delta t = 10 \text{ ns}$) versus the distance D from the motor, for two different motor molecules. Host 2 with $\sigma = 4.56 \text{ Å}$ and $\alpha = 1.32$, $T = 40 \text{ K}$.

The host mobility decreases exponentially with the distance to the motor $\mu = \mu_0 e^{-D/R_0}$, with $R_0 = 4.55 \text{ Å}$. It is to be noted that here the host size is $\sigma = 4.56 \text{ Å}$, thus $R_0 \approx \sigma$. Similar to the previously found results, new connections can be made to different theories of the isomerization induced mass transport. The gradient pressure theory assumes that the substantial decrease of the driving force implies a $\mu = 1/4\pi r^2$ decrease. Moreover, as the gradient pressure must surpass the material's constitutive constraint to induce diffusion, the model presumes a distance threshold. This would mean that at distances $r > r_{\text{threshold}}$, diffusion stops.

VIII.5. Threshold dependence on the host molecule size

As the previous results found a link between the threshold of the motor's arm length and the host molecule size, the following simulations will refer only to this linkage, in order to bring more clarity.

Instead of varying the size of the motor, the host's size will vary, while the motor remains the same in all calculations, i. e. the DR1 molecule. The algorithm used to obtain the different hosts can be seen as building a series of molecules that grow in size by multiplying the σ_{ij} parameters of Lennard-Jones potential, as well as the l distance between the two atoms, with the α constant. The simulation box is rescaled in the same manner. According to the calculations, diffusive motions in the host stop once its size is $\sigma > 5.4 \text{ \AA}$ and $l > 8 \text{ \AA}$. The DR1's lightest arm is $l_{arm} = 7.8 \text{ \AA}$, a value that matches the host's length. Thus, the host size dictates the motor's length threshold.

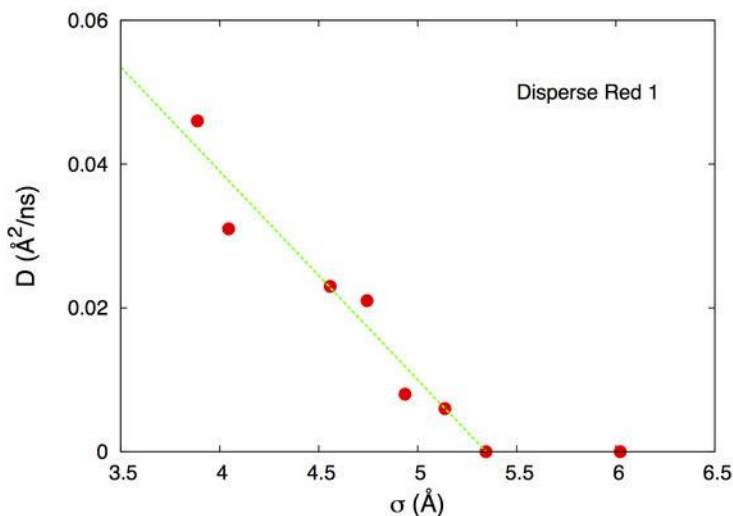


Figure VIII.14. Host diffusion coefficient versus the size of the host molecule, for a constant motor (the real DR1).

The following calculations treat the threshold dependence on the host size for an ideal simplified motor. The different hosts are built respecting the same procedure as before, i.e. a wide range of hosts is obtained with the help of the same α multiplying factor. Different motor's lengths are tested for each host, in order to find the threshold. Once found, the thresholds are displayed versus the σ size of the host molecule.

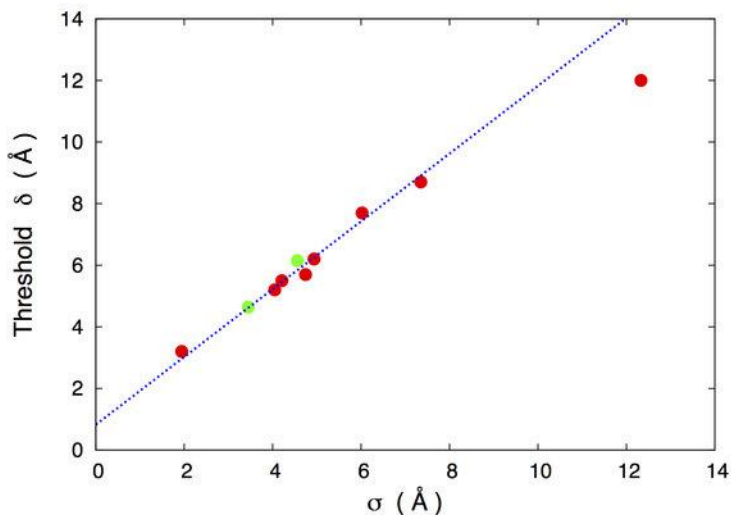


Figure VIII.15. Threshold values δ on the motor's length versus the size σ of host molecules. Green circles correspond to thresholds obtained from simulations at $T = 10$ K and red circles $T = 40$ K. The fitted line corresponds to a threshold $\delta = 1.1\sigma + 0.75$ Å.

Results show that the threshold is proportional to the host's molecule size, clarifying the direct link between a motor's capacity to induce diffusion in host molecules, depending on how big they are relative to the motor's length.

The r_{min} value versus the size of the host shows the same dependence as the threshold.

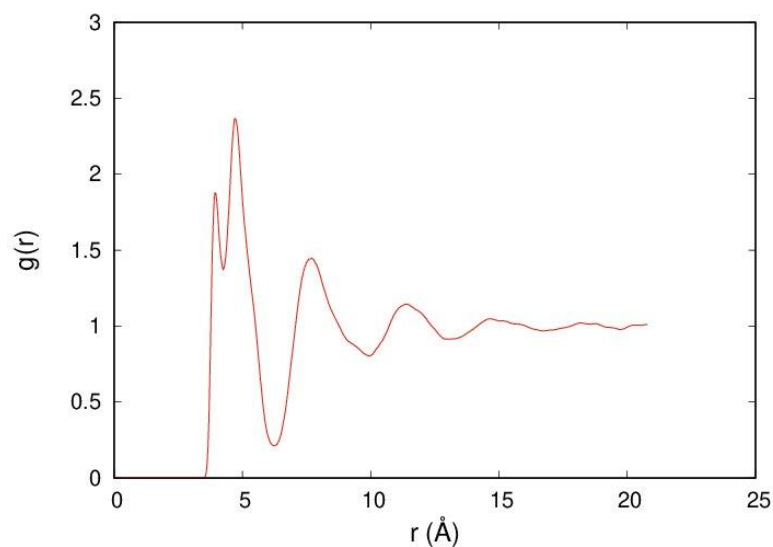


Figure VIII.16. Radial distribution function $g(r)$ for $\sigma = 4.045$ Å

The radial distribution function $g(r)$ for $\sigma = 4.045$ Å shows $r_{min} = 6.26$ Å.

VIII.6. Conclusions

With this study, we aimed to find the meaningful parameters in terms of influence on the molecules motion found in the proximity of an isomerizing motor.

Our results show the existence of a threshold for the motor size for the diffusion of host molecules to occur. The dimension of the threshold is in direct relation with the host molecule size. Accordingly, the motor's size relative to the host size is a significant parameter for the mass transport mechanism, a conclusion that agrees well with the cage breaking model. Moreover, the motor's width does not influence in a significant manner the thresholds values, supporting the cage breaking model. The finding is valid for both DR1 molecules, as well for our simplified molecular motor.

The mass transport presents a linear increase with the motor's length, according to the linear theory, showing that this behavior is within the linear regime. This response is related to the increase of the number of host molecules pushed by the motor. Our results show that the isomerization induced motions are exponentially decreasing with the distance to the motor and link this comportment to cooperative motions.

CHAPTER IX. Isomerization rate influence on host's diffusion

IX.1. Study framework

A short description of the system used for these calculations: one motor ($L_T = 15.4$ Å and $W = 4.4$ Å, $m = 560$ g/mole) and 500 methyl methacrylate molecules. The density is set constant (NVT ensemble) at $\rho = 1.65$ g/cm³ (see detailed system in *Chapter VII*).

As the present study addresses the characteristic times in an isomerization cycle, *Figure IX.1.* depicts the different stages that a molecular motors passes through, starting from the stable form – trans, to the less stable one, - cis. The folding time τ_f represents the time in which the motor actively changes its configuration (from trans to cis), and the time period T_f represents the time necessary to one isomerization cycle (trans – cis – trans).

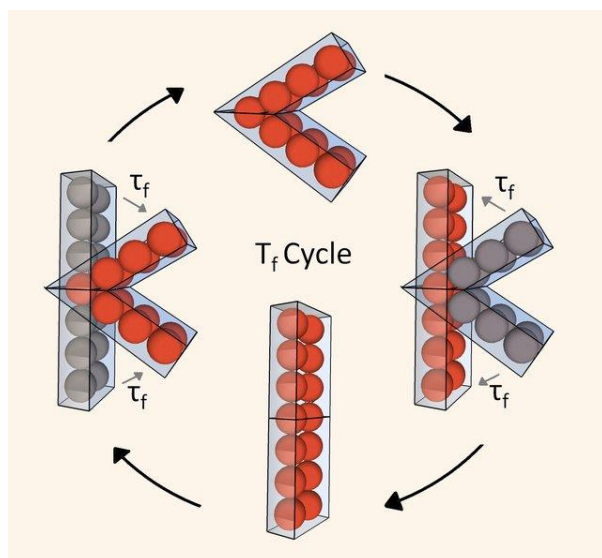


Figure IX.1. Schematic illustration of the simplified molecular motor passing through the 4 stages of one isomerization cycle during in the time period T_f : uniform trans—cis conversion (folding) in the specific time τ_f ; stationary phase in cis form; uniform cis—trans conversion (unfolding) in the specific time τ_f ; stationary phase in trans form.

Folding time τ_f and time period T_f represent the important parameters in this study, thus a first security check is done to ensure they are appropriately used.

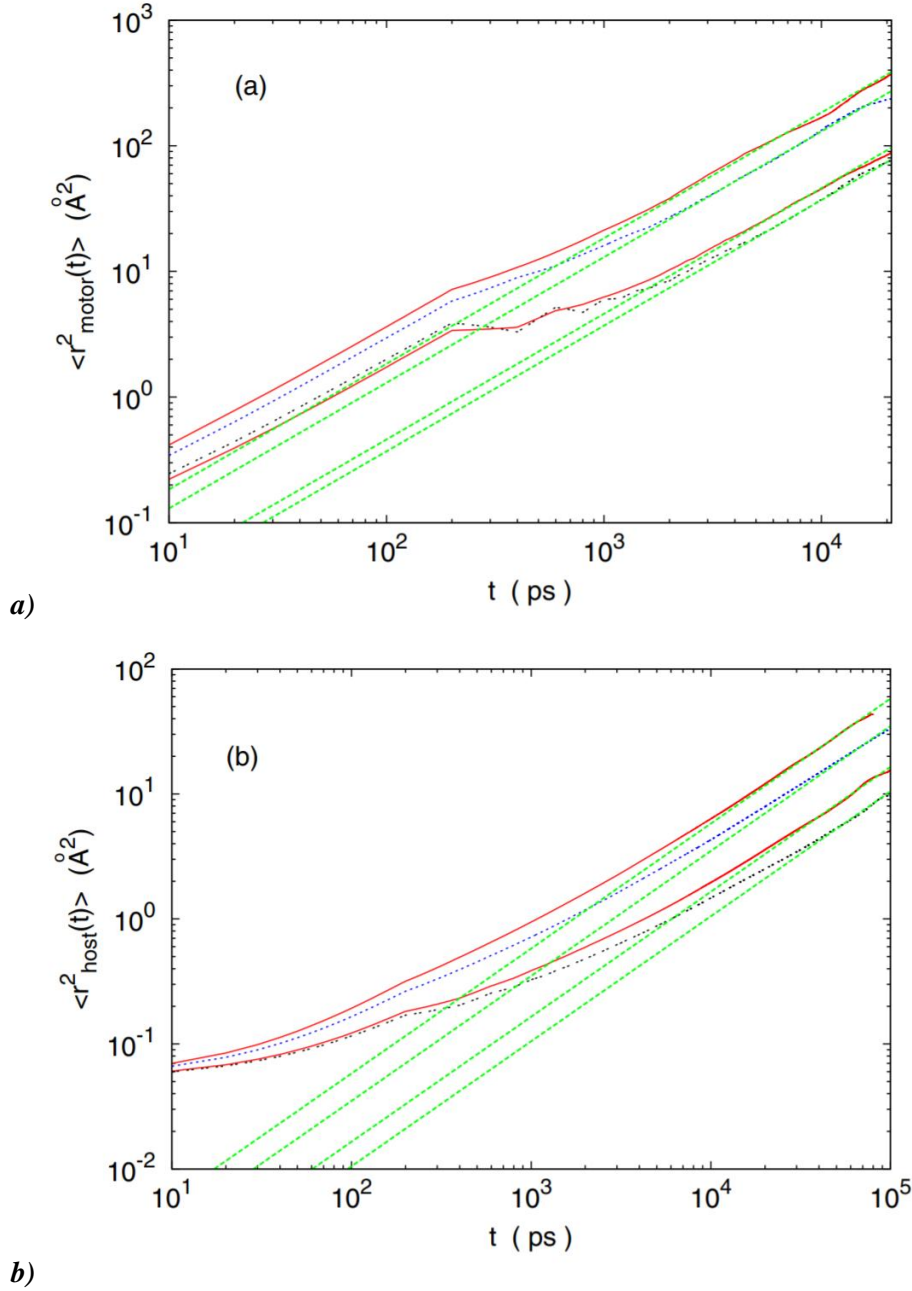


Figure IX.2. Mean square displacement of the (a) motor and (b) host molecules for various folding times. From top to bottom $\tau_f = 3 \cdot 10^{-2} \text{ ps}$, $4 \cdot 10^{-2} \text{ ps}$, $2 \cdot 10^{-2} \text{ ps}$ and 2 ps . The dashed lines represent linear fits of the mean square displacements $\langle r_{\text{motor}}^2(t) \rangle$ and $\langle r_{\text{host}}^2(t) \rangle$.

The study begins by certifying the existence of diffusive motions in the simulated system. The verification is performed for various folding times τ_f , ranging from $\tau_f = 3 \cdot 10^{-2} \text{ ps}$ to 2 ps .

The fit lines (*Figure IX.2.*) for the motor and host molecules show that the mean square displacements $\langle r_{motor}^2(t) \rangle$, $\langle r_{host}^2(t) \rangle$ evolve linearly with time at large time scales. This finding attests that the motions of the molecules are diffusive for the folding time τ_f range tested $\tau_f = 3 \cdot 10^{-2} \text{ ps}$ to 2 ps .

Investigation of the molecules' diffusion starts with ensuring that the time period T_f chosen is enclosed in the linear response range. This regime assures the absence of interference between two consecutive isomerizations, such that each isomerization acts on an unperturbed medium. Using only one motor inside the simulation box ensures that this low motor concentration gives rise to the smallest possible perturbation of the host material for a given folding period T_f .

IX.2. Diffusion behavior dependence on the isomerization rate

Comparing the diffusion coefficient (*Figure IX.3.*) for the two folding periods, $T_f = 600 \text{ ps}$ and $T_f = 400 \text{ ps}$, the behavior is shown to be superposed, confirming that the system's response is proportional to the number of foldings per second. This places the chosen time periods T_f into the linear regime, where the response is proportional to the perturbation $D = \alpha/T_f + D_{th} = \alpha/T_f$. Thus, there is no cumulative effect to influence the behavior of the system molecules.

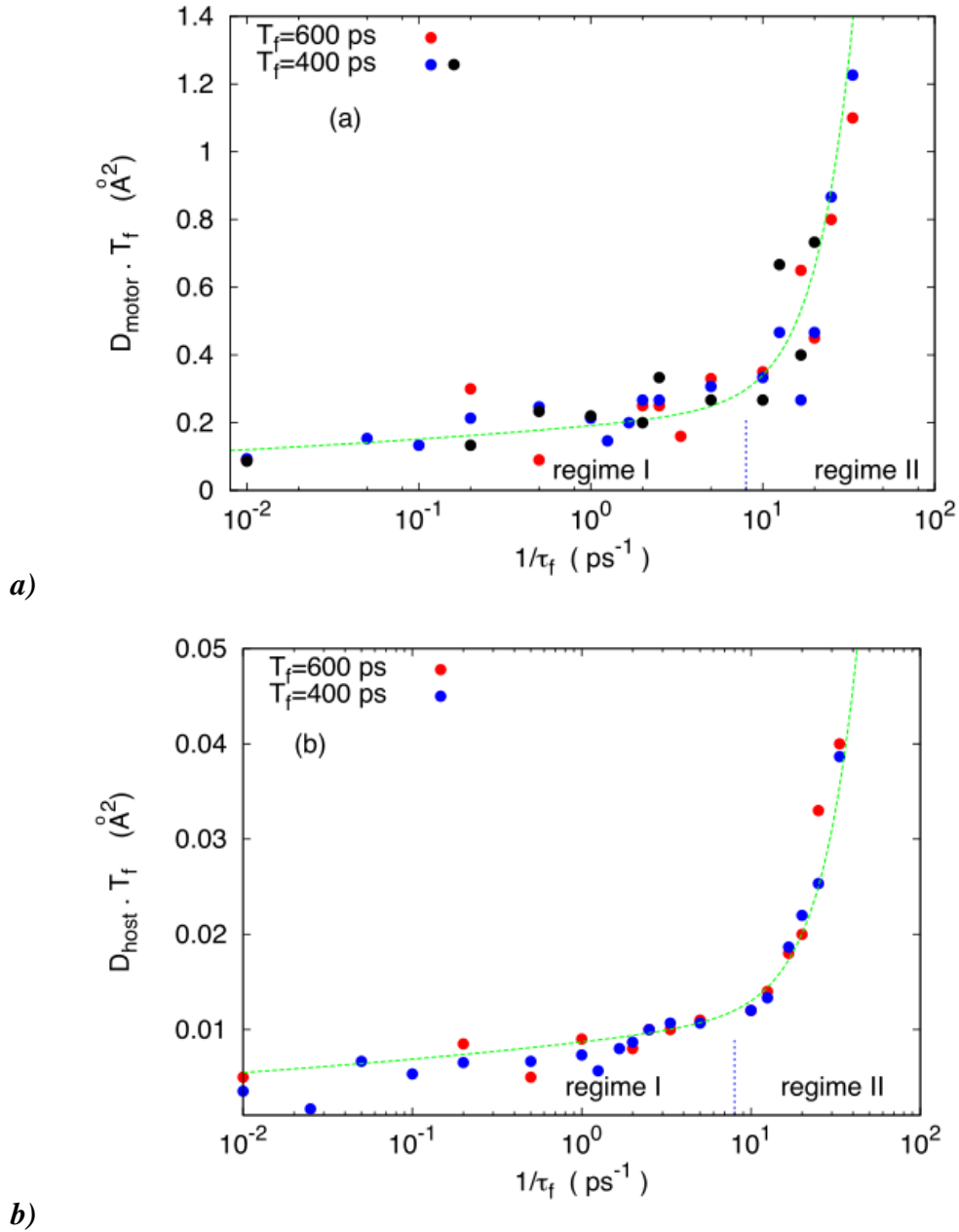


Figure IX.3. (a) Motor's diffusion coefficient multiplied by the folding period $D_{motor} \times T_f$ versus the inverse of the folding time $1/\tau_f$. Blue, red, and black circles correspond to two different folding periods. Black circles indicate large simulation boxes. The short blue dotted line represents $\tau_f = 1.25 \cdot 10^{-1}$ ps and separates the two regimes. The green dashed line is a fit corresponding to $D_{motor} = a\tau_f^{-0.1} + b\tau_f^{-2}$ (as T_f is constant).

The temperature is $T = 140$ K. (b) The same figure, but for the hosts 'averaged diffusion D_{host} . The green fitted line corresponds to $D_{host} = e\tau_f^{-0.1} + f\tau_f^{-2}$

The evolution of diffusion with the folding time τ_f differentiates between two types of dependency relations. Analyzing the fit line, two time regimes are shown.

Regime I corresponding to slow foldings, i.e. large folding times $\tau_f > 1.2 \cdot 10^{-1} \text{ ps}$. Diffusion coefficient progresses slowly with $1/\tau_f$, after the following relation: $D_{motor} \approx \tau_f^{-0.1}$.

Regime II corresponding to fast foldings, i. e. short folding times $\tau_f < 1.2 \cdot 10^{-1} \text{ ps}$. Diffusion coefficient shows a fast growth with $1/\tau_f$, respecting the following equation: $D_{motor} \approx \tau_f^{-2}$.

The difference in the diffusion's response manner quantified in the two regimes suggests that there is a difference in the responsible physical mechanism also. Knowing that $\delta v \approx L/(2\tau_f)$, the momentum variation during the folding process is $\delta p \approx nm\delta v$, where n is the number of pushed host molecules during one folding, and m is the mass of one host molecule. According to this, the medium, formed by host molecules, generates an instantaneous force $F \approx \delta p/\tau_f \approx nmL/(2\tau_f^2)$.

Results show that the host molecules have a similar diffusion response as the motors. However, the motor's diffusion is almost 4 times higher than the hosts', pointing that the medium's motions are driven by the motor's motions.

IX.3. Investigation on the forces acting on the motor

Further, to investigate the behavior in these two regimes, the force acting on the motor is studied. The evolution of the force exerted on the motor by the surrounding medium during one folding is evaluated for different folding times τ_f belonging to the two regimes previously found.

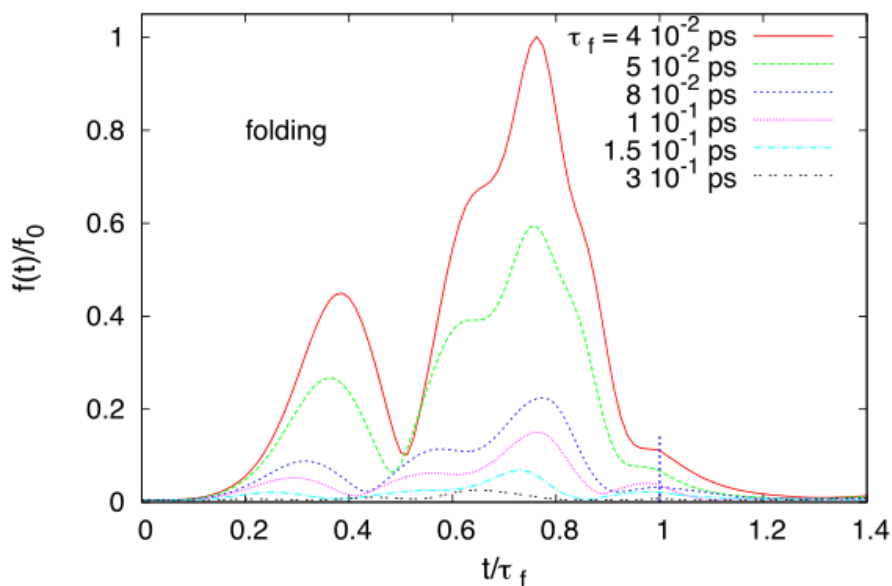


Figure IX.4. Time evolution of the force acting on the motor during the folding process for various folding times τ_f . The force persists during a short time after the end of the folding (marked by the small blue dotted line), due to the perturbation of the host medium.

The force that opposes to the motor's folding (*Figure IX.4.*) shows that its evolution follows the rise of a peak, reaching a minimum around half of the folding time, then the rise of a higher second peak. In its folding motion, the motor encounters resistance from the surrounding shell formed by host molecules. The maximum resistance is met in the second part of the folding time. Evaluation of this force evolution during the unfolding act shows similar results.

Displaying the maximum force reached during folding for the various folding characteristic time allows an investigation of the force evolution during the two regimes found for the diffusion behavior.

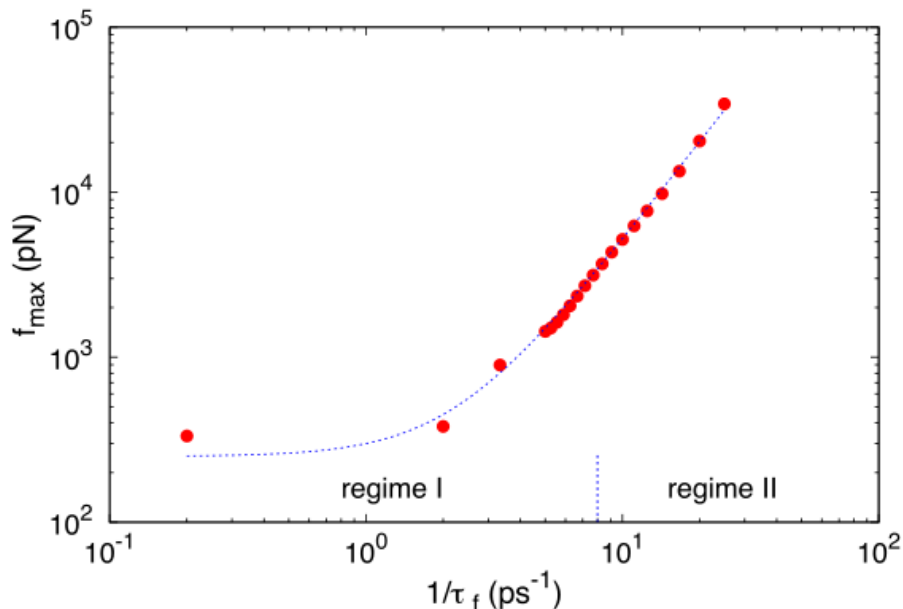


Figure IX.5. The maximum value of the force acting on the motor during the folding process versus the inverse of folding characteristic time $1/\tau_f$. The maximum values of the force evolve as τ_f^{-2} but a change from this behavior arises for slow foldings (first points of the curve: $\tau_f > 200$ ps i.e. regime I). The dashed blue line is a fit of $f = a + b\tau_f^{-2}$.

In *regime II* (Figure IX.5.), the force evolves strongly with $1/\tau_f$, following the same relation as the diffusion: $f_{\max} \approx \tau_f^{-2}$. This result points that diffusion is proportional to the maximum of the force. Thus, in *regime II*, the diffusion behavior of the motor and the host molecules seems to be governed by the force induced by the motor's folding. Regarding the theories proposed to explain the azobenzene isomerization—induced mass transport, this finding is in agreement with the gradient pressure model.

Regime I is characterized by a weak dependence of the maximum force on the folding time. Consequently, the motor's and host molecules' diffusion exhibits a slight dependence on the force exerted during one folding. Linking this behavior to the possible mechanisms that generate massive mass transport, two theories are known to be based on the employing of a relatively small force in order to induce diffusion. In the cage breaking model, a minimum force is needed, just enough for the host molecules nearby the motor to pierce the shell of neighboring host molecules. As for the other model in agreement with this result, the diffusion anisotropy theory advocates for the motor's slithering through the medium, a motion that needs small forces.

IX.4. Defining efficiency of the isomerization frequency

The study of diffusion dependence on the isomerization rate, i.e. with the folding time τ_f , showed the presence of two time regimes, in which diffusion is differently influenced by how fast or slow the motor performs its isomerization motion. The force developed by the motor during isomerization indicates a similar trend. Linking the diffusion behavior with the maximum force exerted on the motor, more mechanisms can be considered responsible for the conduct specific to each regime.

In this context, the interpretation of the system's answer benefits from a detailed look at the molecules' displacement during the isomerization process. To distinct the molecules' motion during an isomerization cycle with its specific steps, the square displacement of the motor and host versus time is displayed. To note here is that the square displacements are not averaged over time. In addition, as the simulation box contains more than one host molecule, a configurationally averaging is needed (the result is averaged over all 500 molecules) when evaluating the square displacement of host molecules.

The square displacement for the motor versus time is displayed, comparing two different folding times τ_f , one situated in the *regime I* range ($\tau_f = 5 \text{ ps}$), and one in the *regime II* ($\tau_f = 5 \cdot 10^{-2} \text{ ps}$). Similarly, the square displacement configurationally averaged on all host molecules analyzes the molecular motion in the two time regimes.

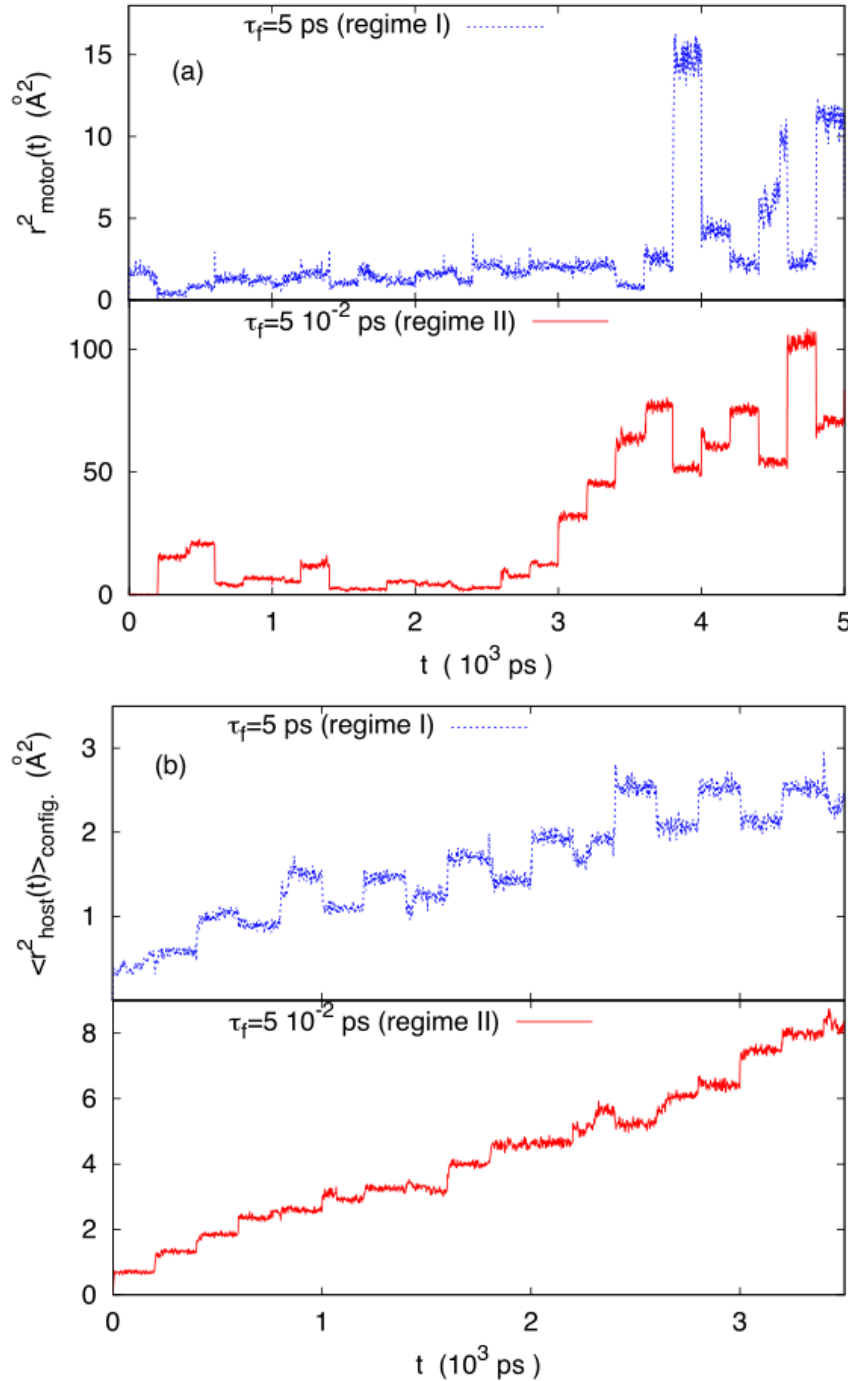
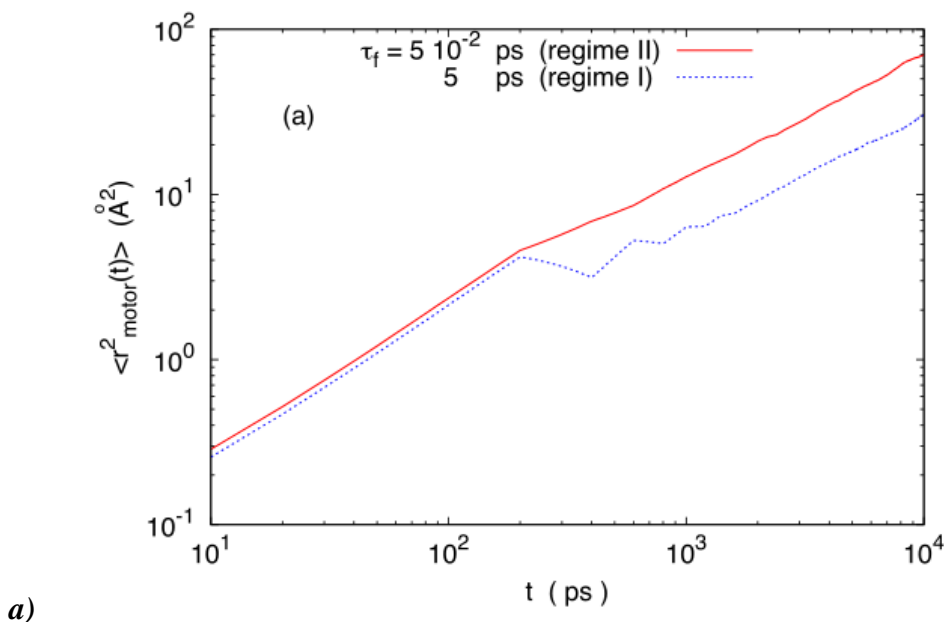


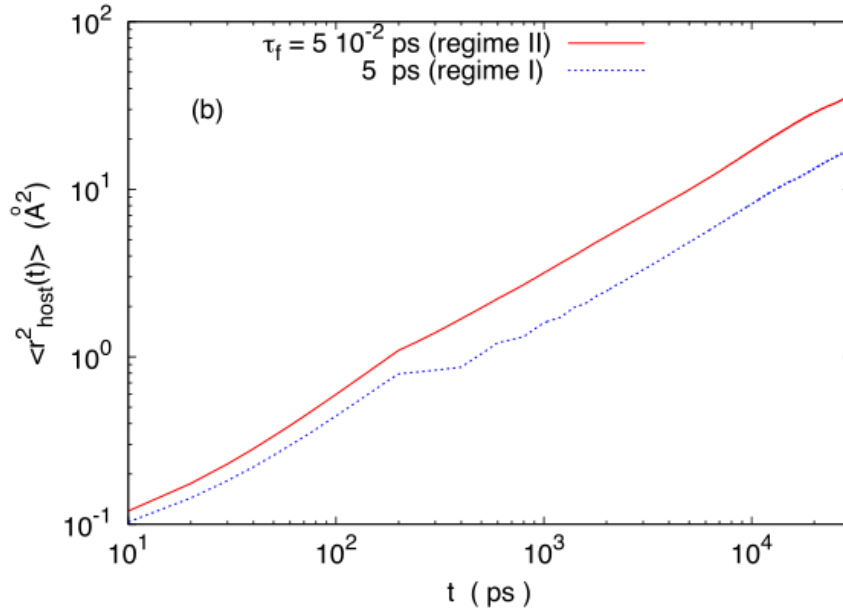
Figure IX.6. (a) Square displacement of the motor $r^2(t)$ versus time t . The blue line corresponds to regime I ($\tau_f = 5$ ps). The red line corresponds to regime II ($\tau_f = 5 \cdot 10^{-2}$ ps); the square displacement is rescaled by a factor of 1/5 for better visual clarity. The time period is $T_f = 400$ ps. The data is not averaged on time origins. (b) Configurationally averaged square displacement of the host molecules $\langle r^2(t) \rangle_{\text{config}}$ from around the motor (at a distance $R < 10$ \AA) versus time t . The time period is $T_f = 400$ ps. The data is not averaged on time origin, but is averaged on medium molecules.

The results for *regime I* reveal that the displacement of the motor and host molecules follows a rectangular trend. This evolution pattern is caused by the fact the motion induced by a motor's folding is counteracted by the sequent unfolding. Thus, the motions in *regime I* are hardly efficient in inducing diffusion. In the long run, the few steps where the folding induced motion is not totally counterbalanced by the unfolding contribute to the displacement seen for long times.

In *regime II*, the displacement for both motor and host molecules shows that most motions during the folding process are not reversed by the unfolding, each motion contributing thus to fast diffusion. Some steps for the motor's square displacement are quite high, while the host's displacement evolves with constant steps. This difference confirms that the host diffusion is induced by the motor's motion. Consequently, reframing the *regime I* behavior indicates that responsible for the slow dynamics in the host is the motor's incapability to reach high enough displacements in order to divert the host molecules' direction during the unfolding process. Overall, compared to the displacement in *regime I*, the *regime's II* displacement steps are proved to be more efficient.

Looking at the mean square displacements evolution in the two regimes, helps fill in the previous findings. Results show resembling behaviors for the motor and the hosts' molecules, thus they are discussed together without differentiating between the two.





b)

Figure IX.7. (a) Mean square displacement of the motor $\langle r_{\text{motor}}^2(t) \rangle$ versus time t . Continuous red line: regime II ($\tau_f = 5 \cdot 10^{-2}$ ps); Dashed blue line: ($\tau_f = 5$ ps). These data are averaged on time origins. (b) Mean square displacement of the host molecules $\langle r_{\text{host}}^2(t) \rangle$ versus time t . Continuous red line: regime I ($\tau_f = 5 \cdot 10^{-2}$ ps); Dashed blue line: ($\tau_f = 5$ ps). These data are averaged on time origins.

The mean square displacements in the two regimes display a similar evolution up until around 200 ps, which represents half of the time period $T_f/2 = 200$ ps, right before the unfolding process starts to take place. After this time, displacement in regime II continues to increase, reaching diffusion in at long times. Meanwhile, in regime I, the displacement shows an oscillating trend caused by the successive folding—unfolding processes, determining a lower growth rate with time.

To conclude, the fact that the displacements corresponding to the two regimes part their ways after the short time $T_f/2 = 200$ ps, i.e. only one folding process, suggests that the distinction between *regime I* and *regime II* is due to a particularity in the motor's mobility. This characteristic refers to the probability of the reverse motion to take place during unfolding. This probability is further investigated by defining the motor's efficiency as a way to quantify its ability to induce diffusion.

The efficiency of the motor's mobility is evaluated after the following relation:

$$\varepsilon = \frac{\langle r^2(pT_f) \rangle}{(2p \langle r^2(T_f/2) \rangle)}$$

Equation IX.1.

where p represents the number of periods.

The efficiency ε can be described as a probability quantity that considers the two opposite events:

1. The motor always returns to its initial position: $\varepsilon = 0$.
2. The motor has the same probability as in the Brownian random motion to return to its initial position: $\varepsilon = 1$.

To note in this case is that with the equation used the efficiency value can be higher than 1 ($\varepsilon > 1$), but the chances for this event (i.e. the motor's probability of returning to its initial position is higher than in the Brownian random motion) are low, as the motor's direction is not biased.

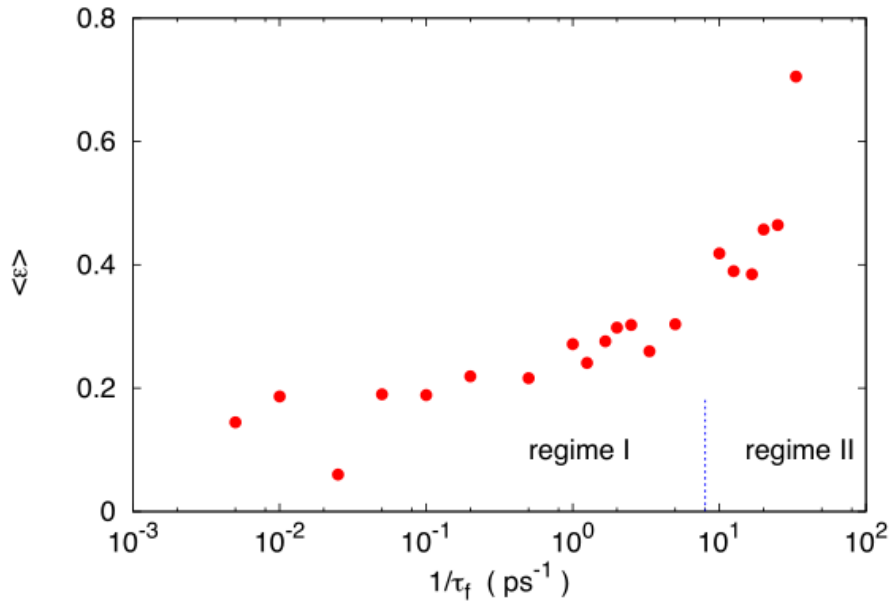


Figure IX.8. The efficiency of the mobility of the motor defined as versus the folding time τ_f . The time period is $T_f = 400$ ps and the number of periods $p = 5$. An efficiency of mobility of 1 means that the motor has the same probability of returning to its initial position as in the Brownian random motion, and an efficiency of 0 means that the motor always returns to its initial position (i.e. the unfolding process reverses the motion induced by the folding).

The evolution of efficiency ε with the folding time τ_f shows the same trend as the evolution of motion driven by folding. The growth of efficiency ε with the inverse of folding time $1/\tau_f$ reveals that in *regime II* the motor possesses a higher efficiency than in *regime I*. This trend can be responsible for the differences in the motor's motion previously observed in the two regimes.

This conduct needs further analysis in order to paint a clearer picture of the underlying causes.

To know how much the motor moves during a folding process, while disregarding what happens during unfolding, the squared displacement averaged on all the half period times $\langle r^2(T_f/2) \rangle$ is shown. By depicting this mean square displacement versus time along with the efficiency's ε evolution, a comparison between the two is enabled.

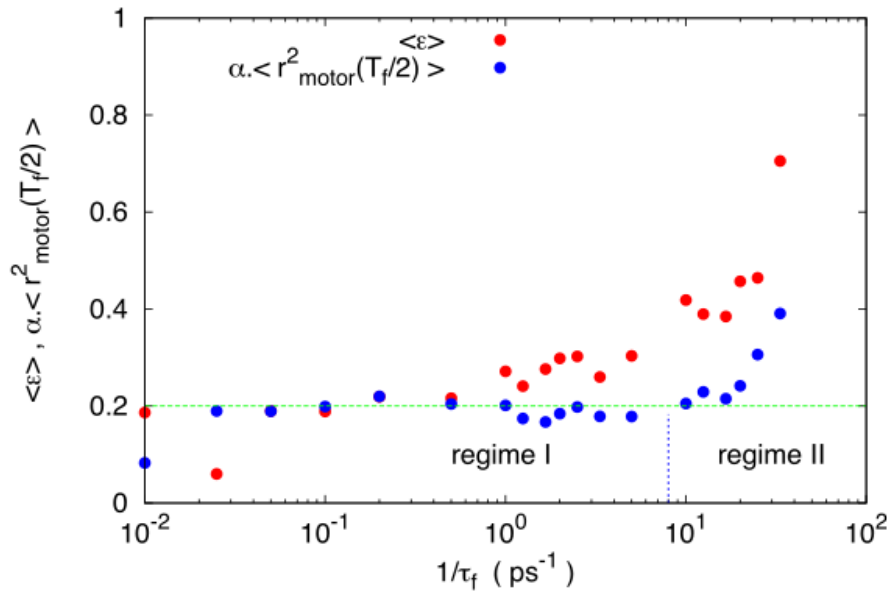


Figure IX.9. Comparison between the efficiency of the mobility ε evolution versus the inverse of folding time $1/\tau_f$ and the motor's motion after one folding only $\langle r^2(T_f/2) \rangle$. The mean square displacement $\langle r^2(T_f/2) \rangle$ is multiplied by a factor $\alpha = 5.3 \cdot 10^{-2} \text{ \AA}^{-2}$ to help compare the two parameters. The green dashed line represents a guideline to show the mean square displacement approximately constant up to $1/\tau_f = 20 \text{ ps}^{-1}$ (i.e. $\tau_f \geq 5 \cdot 10^{-2} \text{ ps}$).

The motor's mean square displacement acquired in one folding $\langle r^2(T_f/2) \rangle$ and the mobility's efficiency ϵ have a resembling behavior with time. Also, these two plots show the same evolution as the overall motion in the system. But the displacement increases more slowly with time, compared to the efficiency. Due to this distinction, it can be said that the main contribution to the global motion belongs to the motor's efficiency of mobility ϵ . Thus, the efficiency is at the core of all the differences observed between the two regimes. By folding fast (regime II), the motor attains a trajectory well distinguishable from the opposite path that follows (driven by the unfolding process that succeeds it). The distinct progression of the motor while folding and unfolding that is induced by the isomerization rate is the aspect most responsible for the displacement behavior studied here.

IX.5. Conclusions

In this section of the thesis, the photoinduced displacement of molecules in a viscous medium is studied, as a function of the characteristic folding time τ_f of the molecular motor. Two time regimes are found: *regime I* when the motor folds slowly, and *regime II* for fast folding. In *regime I*, the diffusion slowly increases with τ_f , while in *regime II*, the diffusion augments with τ_f ($D \approx \tau_f^{-2}$), which leads to the idea that there two mechanisms that can be differentiated. The displacement of the motor during folding in the first regime is reversed by a backwards displacement during the unfolding. This phenomenon is not characteristic to the second regime: when the motor folds fast, the induced displacement has a totally different trajectory than when it unfolds, thus globally, the motions in *regime II* are more efficient.

These findings agree well with fluctuation theorems regarding time reversal mechanisms. By fast folding, the motor generates higher entropy and is more efficient in inducing diffusion. This study results can serve as a starting point to design more efficient motors.

CHAPTER X. Studies on the motor's motion

X.1. Study framework

This study uses one simplified molecular (its characteristic are specified for each study in this chapter) and host 1 molecules (detailed system construction in *Chapter VII*)

The following parameters are used for the 500 idealized diatomic host 1 molecules:

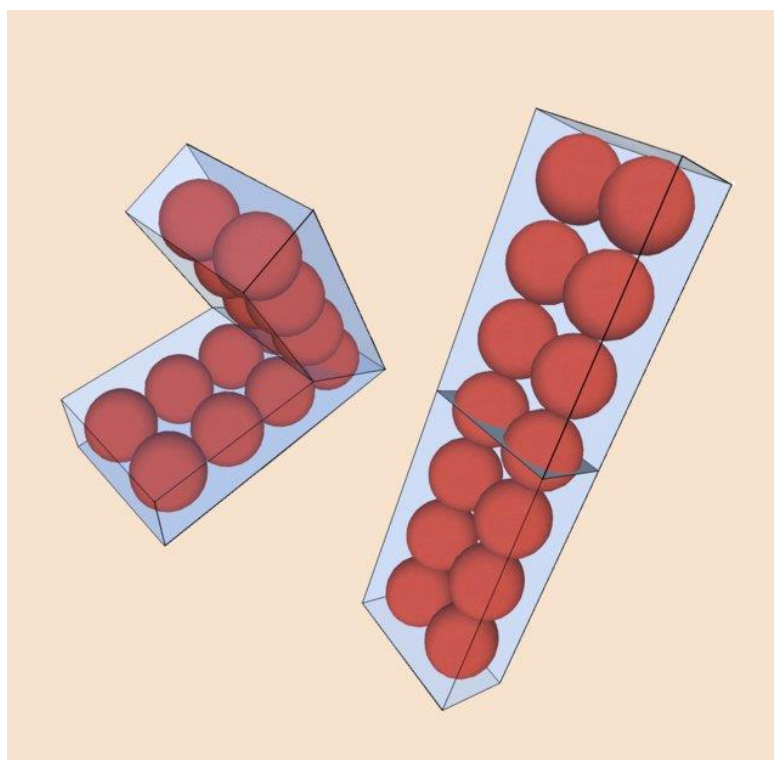


Figure X.1. Picture of the molecular motor built of two ranks of seven atoms each, illustrated in the folded (cis) and flat (trans) configuration. The contouring parallelogram is intended just as a guideline for the eye.

X.2. Characteristic diffusion for motor and host molecules

The studied system consists of one molecular motor embedded in a glassy material. Between the motor and the host molecules that make up the surrounding medium, there is a significant difference in size. It is known that diffusion is influenced by both the size and mass of the particles. Thus, by changing these parameters, differences in the diffusion process may be expected to arise. When heading to a thorough study of the motor's motion, knowledge of the diffusion particularities can offer a good start point.

In this section, the physical mechanism of diffusion of both the system's components (motor and host molecules) is analyzed. Throughout this chapter, most of the studies are discussed in the context of a comparison between the mass of the host and the motor. Thus, the relative mass of the two components is expressed through the motor's mass on the host's mass ratio $M_{\text{motor}}/m_{\text{host}}$ or shortly M/m .

The self Van Hove correlations functions $G_s(r,t)$ paints a picture about the dynamics in the system, by calculating the density of probability that a particle i has moved a distance r in a time t . The Van Hove functions for the motor and the host are evaluated for two different mass ratios: $M_{\text{motor}}/m_{\text{host}} = 5.25$ and $M_{\text{motor}}/m_{\text{host}} = 0.42$ (Figures X.2 and X.3).

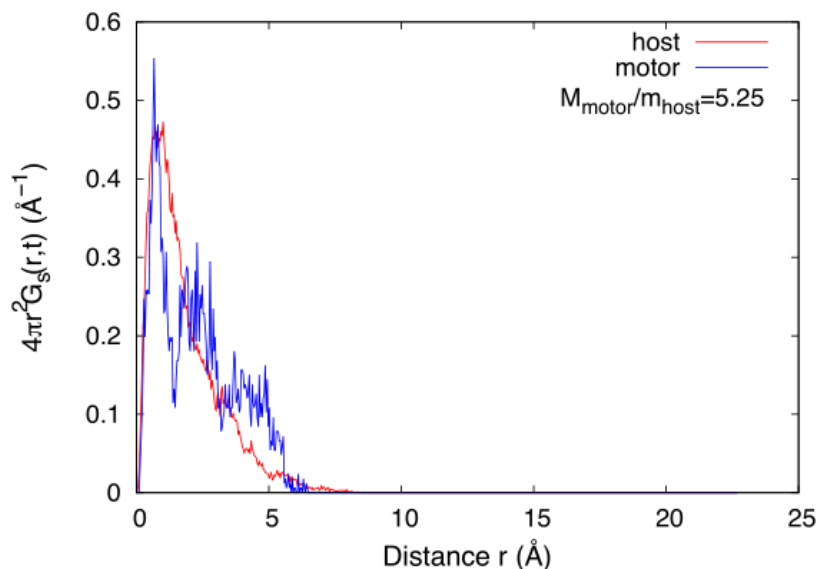


Figure X.2. The self Van Hove correlation functions $G_s(r,t)$ for the motor (length $L = 9.4 \text{ Å}$) and host molecules at time $t = 700 \text{ ps}$. The mass ratio between the motor and the host is $M_{\text{motor}}/m_{\text{host}} = 5.25$.

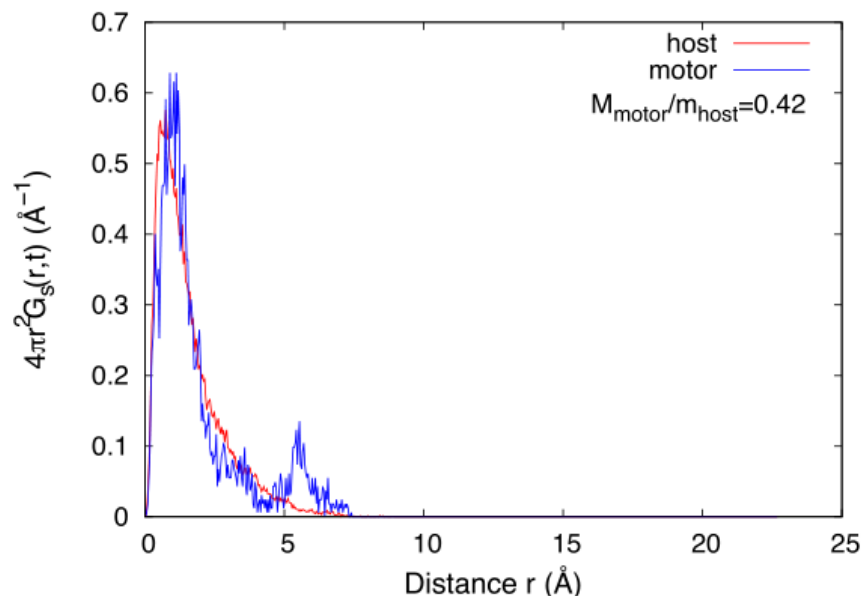


Figure X.3. The self Van Hove correlation functions $G_s(r,t)$ for the motor (length $L = 9.4 \text{ \AA}$) and host molecules at time $t = 700 \text{ ps}$. The mass ratio between the motor and the host is $M_{\text{motor}}/m_{\text{host}} = 0.42$.

Both systems (mass ratio 5.25 and 0.42) indicate the same results. The self Van Hove functions for the host show a typically liquid evolution, displaying a continuous trend that characterizes the diffusive motions in liquids. On the contrary, the correlation functions for the motor reveal a jagged curve. The peaks are due to the hopping motions specific to diffusion in solids. Thus, in one system, there are two different physical mechanisms that preside diffusion. This behavior is assigned here to the size difference between the motor and host molecules. While the dynamics in the host is propelled through liquid-like diffusion motions, the motor's diffusion takes place through leaping-like motions. In its motion, the motor encounters more molecules than the host, given its larger size. This means that its diffusion requires simultaneous multiple rearrangements of the host molecules, which hinders a continuous evolution. So the fast folding will make the motor to leap from its position to the nearby position. Concerning the host motions, its diffusion could be explained as following. The motor's fast folding determines the surrounding molecules to rearrange in order to accommodate its new position (some by clearing the path and some by diffusing to the new nearby created voids). This mechanism implies that regardless of the motor's leap length, the host molecules will still move to the nearby position, and no further. Another explanation considers that the host molecules move as consequence of the forces induced by

the folding movement. Further analysis of the obtained results confirms the first explanation. Accordingly, the self correlation functions indicate that, through its hopping motions, the motor reaches positions that are often larger than the hosts' nearby molecules motions ($r < 6 \text{ \AA}$). So, a large or small leap empowers the same displacement in the host molecules.

X.3. Influence of the relative molecular masses on diffusion

The previous results show that when a larger mass is used for the host molecules, the motor takes larger leaps. In this subchapter, this parameter is thus varied in order to study its effect on the motor's motion.

As the force increases with the mass, a first step is the evaluation of the force that the host molecules exert on the motor. The force is defined as the following:

$$F = \delta p / \delta t \approx nm v / \tau \approx nm L / \tau^2,$$

where $n(L)$ represents the number of host molecules that pushed the motor during the folding.

$$n \approx \rho L^2 e \Delta \theta / 2,$$

with $\Delta \theta = \pi - \theta$, where θ represents the folded motor's opening angle, $\rho = N/V$ the medium's density, τ is the characteristic folding time, L and e the motor's length and width respectively, and m the host molecule's mass.

The previous work about the influence of the isomerization rate (discussed in chapter IX) showed that (within the parameters used in the present study, i.e. the time period $T_f = 600 \text{ ps}$ and characteristic folding time $\tau_f = 1 \text{ ps}$), diffusion is proportional to the maximum of the force, as both force and mobility evolve the same with $1/\tau_f$. Consequently, increasing the mass of the host molecule m should result in a growth of the elementary motion of the motor. These findings highlight the possibility of using the molecular mass m of the environmental molecules as a way to adjust the motor's motion.

The problem of efficiency of the motor's motion ε was previously investigated in this work (see *Chapter IX*) in order to evaluate the motor's ability to induce the hosts' diffusion. In the present chapter, efficiency is discussed in the framework of Purcell's scallop theorem. Applying this theorem to the azobenzene-like motors, they should not be able to move further in any given direction because the displacement achieved during folding is

reversed by unfolding. The scallop theorem is developed for reduced scales models of Newtonian fluids with low Reynolds number, e.g. fluid mechanics in cells, in the absence of Brownian noise. The herein studied system is subjected to microscopic fluctuations of the Brownian noise, given the large period used in the simulation $T_f = 600 \text{ ps}$ (also discussed in *Chapter IX*). Moreover, the system does not constitute a continuous medium at the nanoscale.

However, this theorem raises a concern regarding the use of this flapping (open/close) motions as a way to move inside a medium. Accordingly, the motor is prone to undo the folding, i.e. closing, displacement. To analyze the probability of this event to occur, the motor's motion efficiency ε is again used.

The two time regimes of the motor's diffusion, i.e. I and II, suggested two different mechanisms to lay at the origin of diffusion: one is based on the efficiency ε of the motor's motion and one on the distance that the motor is pushed with each folding; considering these, diffusion is thus described by the efficiency of the motor's motion by which it induces the actual displacement through the folding process:

$$\langle r^2(nT_f) \rangle = 2n\varepsilon \langle r^2(T_f/2) \rangle.$$

As stated before, the efficiency is defined by the equation:

$$\varepsilon = \frac{\langle r^2(nT_f) \rangle}{(2n \langle r^2(T_f/2) \rangle)}$$

where $n \geq 1$ represents the number of periods, and T_f is the time period. Here, $n = 4$. By this definition, when $\varepsilon = 0$, the motor always returns to its initial position, which is what the scallop theorem sustains. On the contrary, for $\varepsilon = 1$, the motor's motion follows a Markovian process, describing the motor's probability to return to its initial position equal to that in a typical random Brownian motion. Note that within this equation, $\varepsilon > 1$ is also possible, but since the moving direction of the motor is not subject to any bias, the chance for the efficiency to take values higher than 1 is low.

In this context, the efficiency ε is analyzed for different mass ratios m/M in order to establish a correlation between the two (*Figure X.4*).

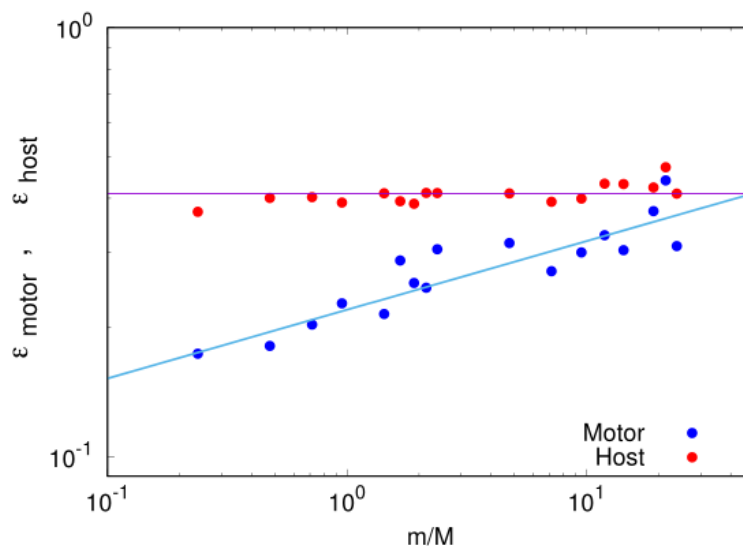


Figure X.4. The motor's and host molecules' dependence on the host to motor mass ratio m/M . The motor's mass is kept constant $M = 420 \text{ g/mol}$ while varying the host's mass. The motor's length is $L = 15.4 \text{ \AA}$.

The variation of efficiency ε shows that for the host molecules, the mass ratio m/M does not represent an influencing parameter. On the contrary, the variation of efficiency ε with the mass ratio m/M presents a growth along with the host molecule's mass m increase. A pertinent interpretation of this behavior is that a motor that is lighter than the surrounding molecules is more prone to change its direction after it takes a folding—induced leap. Thus, the unfolding motion will not counterbalance the displacement achieved through folding. An environment of massy host molecules leads to a higher diffusion and mobility for the motor.

Regarding the second mechanism that was found to play a role in the diffusion, this can be evaluated through the elementary mean square displacement $\langle r^2(T_f/2) \rangle$ (Figure X.5). The average motion is elementary, meaning that it takes into consideration only the first half of the time period, which corresponds to the folding.

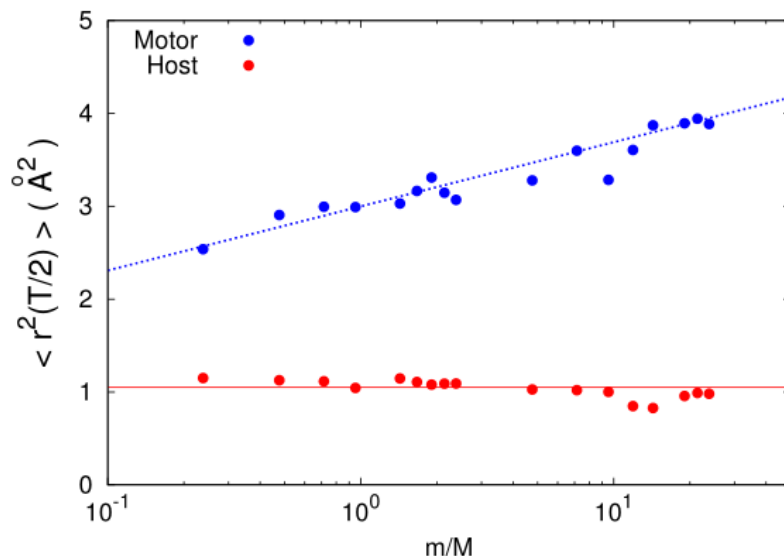


Figure X.5. Elementary displacements $\langle r^2(T_f/2) \rangle$ (i.e. mean square displacement for one folding) versus the mass ratio m/M for the host and the motor (constant mass $M = 420$ g/mol and length $L = 15.4$ Å).

The evolution of the average elementary displacements for both host and motor is quite similar to that of the efficiency. While the elementary displacement for the host $\langle r_{host}^2(T_f/2) \rangle$ shows that the mass ratio m/M does not influence it, the elementary displacement for the host $\langle r_{motor}^2(T_f/2) \rangle$ reveals an increase with the host's mass. This result suggests that the displacement's growth comes along with enlarging the force exerted on the motor by the massy host molecules.

These findings state that mobility and diffusion of the motor experience an increase with the host molecule's mass. This behavior is enabled by an increase of the motor's motion efficiency ϵ and of the displacement induced by one folding.

X.4. Influence of the molecular sizes ratio on diffusion

After studying the influence of the motor/host molar masses ratio M/m on diffusion, another parameter (easy known in experiments) is evaluated for its influence, i.e. molecular sizes ratio.

The findings show that there is a threshold for the motor's relative size. By folding, a motor shorter than the threshold will not result in any significant motion. As the threshold

for the motor is almost equal to the one for the host, this suggests a possible correlation between the two.

Analyzing the variation of the motor's mobility with the motor's length L for different hosts mass, a growth in mobility is revealed. The motor's mobility follows either a continuous, either a step by step increase with the motor's length. The host's mobility is also influenced by the motor's length, which is in agreement with previous studies within this work (see chapter VIII), i.e. larger motors induce larger host's mobility. Thus, the motor's length can serve as a parameter to control its mobility.

Mobility μ is defined here as the mean square displacement $\langle r^2 \rangle$ at a certain time Δt as follows:

$$\mu = \langle r^2(\Delta t) \rangle, \text{ with } \Delta t = 10 \text{ ns.}$$

The simulated system follows a Markovian process at times larger than the time period T_f , linking the mobility μ to the diffusion coefficient D , according to Einstein's formula for diffusion:

$$\lim_{\Delta t \rightarrow \infty} \langle r^2(\Delta t) \rangle = 6D\Delta t.$$

Following the introduction of these notions, the motor's and host's mobility is analyzed as a function of the motor's length L for three different motor/host mass ratios M/m (Figure X.6., X.7., X.8.). Calculation of the host's mobility takes into account the molecules surrounding the motor up until a $r < 10 \text{ \AA}$ radius.

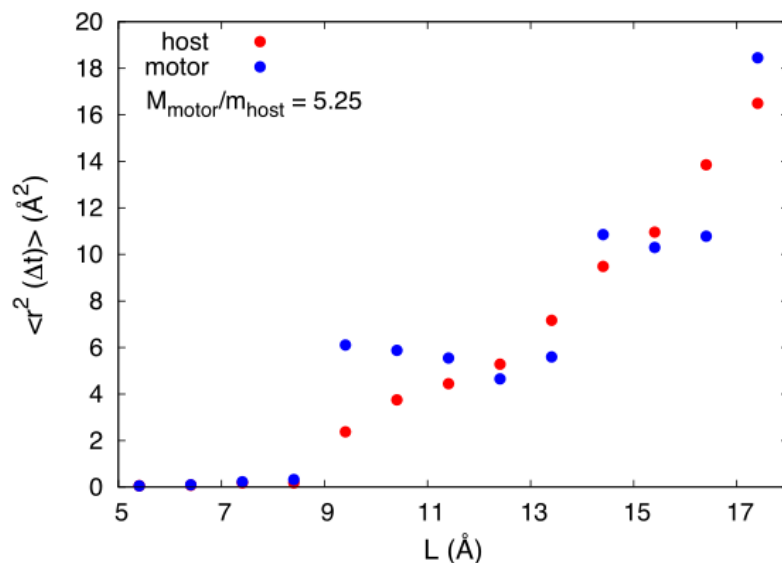


Figure X.6. Motor and host mobilities $\mu = \langle r^2(\Delta t) \rangle$ ($\Delta t = 10$ ns) versus the motor's length L . Mass of the motor is larger than the host's. Calculation of host molecules mobility $\langle r^2(\Delta t) \rangle_{\text{host}}$ is restricted on a $r < 10$ Å radius around the motor.

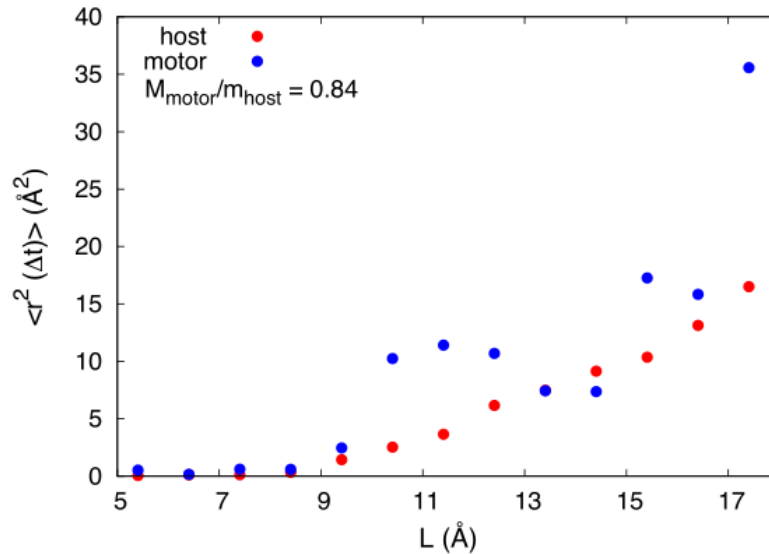


Figure X.7. Motor and host mobilities $\mu = \langle r^2(\Delta t) \rangle$ ($\Delta t = 10$ ns) versus the motor's length L . Mass of the motor and host are almost equal. Calculation of host molecules mobility $\langle r^2(\Delta t) \rangle_{\text{host}}$ is restricted on a $r < 10$ Å radius around the motor.

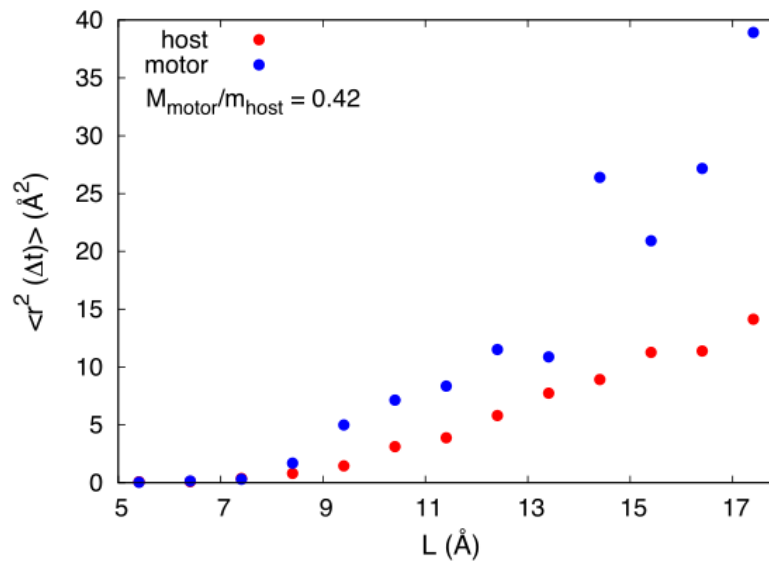


Figure X.8. Motor and host mobilities $\mu = \langle r^2(\Delta t) \rangle$ ($\Delta t = 10$ ns) versus the motor's length L . Mass of the motor is lower than the host's. Calculation of host molecules mobility $\langle r^2(\Delta t) \rangle_{\text{host}}$ is restricted on a $r < 10$ Å radius around the motor.

The mobility's evolution indicates the existence of more dynamical regimes.

Firstly, for short motors, the evolution shows that the motor lacks the efficiency to induce its motion, but also the host's motion. Thus, the results indicate the appearance of a threshold value for the motor's length, below which the motor folds inefficiently $L < L_{th} = 8.4 \text{ \AA}$. A shorter motor implies a decrease in the forces applied to it, which instead lowers its capacity to move through the medium by hopping from one place to another.

Secondly, longer motors will encounter more host molecules in its motion, which translates to a higher force exerted by the medium. When this force is large enough to enable the motor to hop to a new position, it means that the motor's length threshold is surpassed $L > L_{th} = 8.4 \text{ \AA}$. From this point on, the mobility's evolution shows an influence of the motor/host molecular mass ratio M/m . When the motor is heavier than the host molecule, the mobility's dependence on the motor's length displays a growth in steps. By contrast, lighter motors ($M \approx m$ and $M < m$) do not show this type of increase. The step like ascendance of the mobility is related to the structure of the environment, i.e. the first set of neighbors, the second, and the third. The force generated on the motor by the surrounding molecules will experience thresholds than need to be overpassed in order for the motor to take a leap further than the distance to the first neighbor, the second, and finally the third. Knowing that the force depends on the host's mass m and the motor's length L , by increasing L while m remains constant, the force rises at first, and then it reaches a plateau, i.e. the threshold corresponding to the first layer of neighbors and so on. As previously stated, the motor/host mass ratio appears to make a difference in the evolution of the mobility. For lighter motors, the growth of the mobility does not display anymore the steps discussed before. Thus, increasing the host's mass m seems to diminish the steps up to a point when they cannot be detected anymore.

To better understanding of the rise of threshold in the evolution of the mobility versus the motor's length, it is helpful to analyze the corresponding mean square displacement (*Figures X.9. and X.10.*). Thus, the motors whose lengths correspond to the start ($L = 9.4 \text{ \AA}$) and the end point ($L = 13.4 \text{ \AA}$) of the first plateau from *Figure X.6.* - when the motor is heavier than the host - are studied in detail with respect to their square displacement averaged on time (*Figure X.9.*).

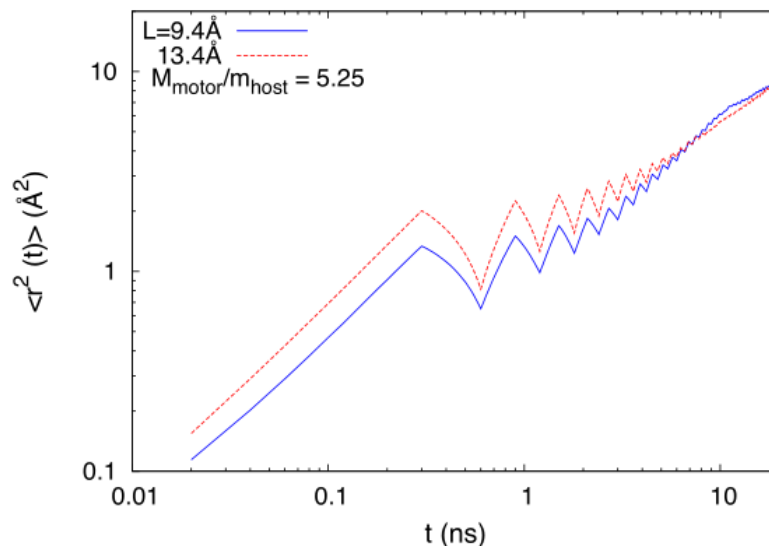


Figure X.9. Comparison of the motor's mean square displacement $\langle r^2(t) \rangle$ for two different motor sizes $L = 9.4 \text{ \AA}$ and $L = 13.4 \text{ \AA}$ found in a medium of light molecules. These correspond to the beginning and end of the first mobility plateau when mass of the motor is larger than the host's (Figure 6)

For the case in which the motor is heavier than the host molecule (Figure X.9.), the mean square displacement for the two lengths ($L = 9.4 \text{ \AA}$ and $L = 13.4 \text{ \AA}$) tends to reach the same values at large times. This explains the plateau seen in the mobility, which begins with the mobility of the motor $L = 9.4 \text{ \AA}$ and ends with $L = 13.4 \text{ \AA}$. However, on short time scales, there is a difference between the two mean square displacements. The large motor achieves a higher displacement during the folding than the short one, as seen in the difference between the heights of the peaks. However, during unfolding, the mean square displacements are quite close to merging, as indicated by the low difference between the minimums. The results show that the motors with lengths situated in the plateau range $[9.4, 13.4] \text{ \AA}$ induce an inefficient increase in motion. In this length segment of the evolution, the force increases with length, but not enough to make a difference in the overall diffusion. Once the motor's length is greater than the end of the plateau ($L = 13.4 \text{ \AA}$), the applied force increases so to enable the motor to take greater leaps.

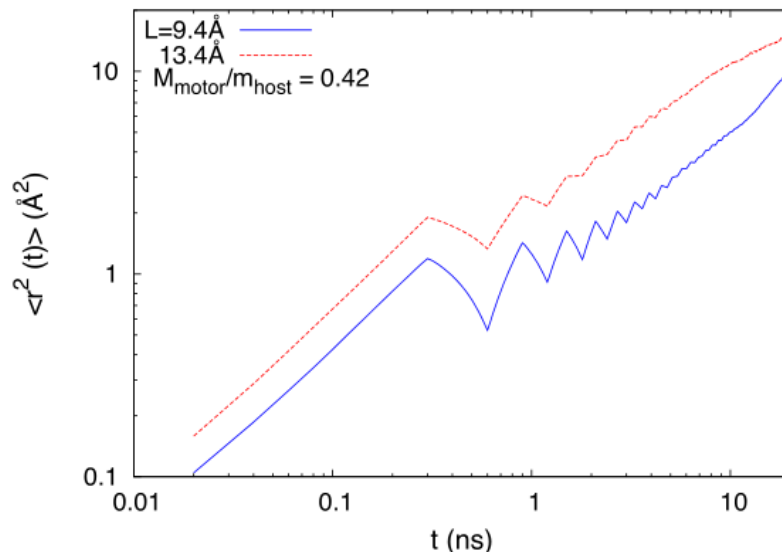


Figure X.10. Comparison of the motor's mean square displacement $\langle r^2(t) \rangle$ for two different motor sizes, $L = 9.4 \text{ \AA}$ and $L = 13.4 \text{ \AA}$ found in a medium of heavy molecules. These correspond to the beginning and end of the first mobility plateau when mass of the motor is lower than the host's in Figure X.6.

When the same analysis is performed for the case where the motor is lighter than the host molecule (Figure X.10.), the mean square displacement evolution for the two motor lengths ($L = 9.4 \text{ \AA}$ and $L = 13.4 \text{ \AA}$) reveal their distinct evolution during the whole simulation time. This picture is in agreement with the corresponding mobilities, where no plateau is observed. The force overcomes the threshold and causes the motor to hop to a new stable position. This way, the mean square displacement of the large ($L = 13.4 \text{ \AA}$) motor reaches a greater value than the short one ($L = 9.4 \text{ \AA}$).

To understand the motion that lays at the origin of the mobility behavior for motors smaller than the threshold, the mean square displacements for both motor and host are displayed (Figures X.11. and X.12.).

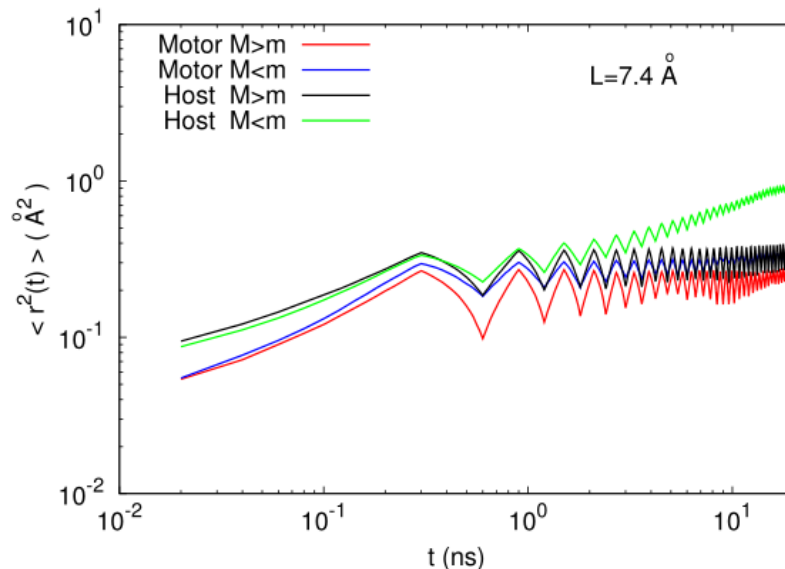


Figure X.11. Mean square displacement $\langle r^2(t) \rangle$ of the motor and host molecules surrounding the motor ($R < 5 \text{ \AA}$) for various host's masses. The motor's length $L = 7.4 \text{ \AA}$ is below the threshold.

As expected from the mobility values, the mean square displacement shows that there is no diffusion when the motor is below the threshold, i.e. $L = 7.4 \text{ \AA}$ (Figure X.11.). The evolution discloses oscillations caused by the motor's displacement during folding, as well as the nearby host's ($R < 5 \text{ \AA}$). The host molecule's oscillations are greater than the motor's due to its relatively smaller size. Moreover, the host influences the motor's motion through its molecular mass. During folding, heavy hosts act with greater forces on the motor, which in turn induce larger displacements.

The motor's and host's mean square displacements induced by a motor larger than the threshold value $L = 13.4 \text{ \AA} > L_{th}$ are depicted together for two host masses for comparison. (Figure X.12.)

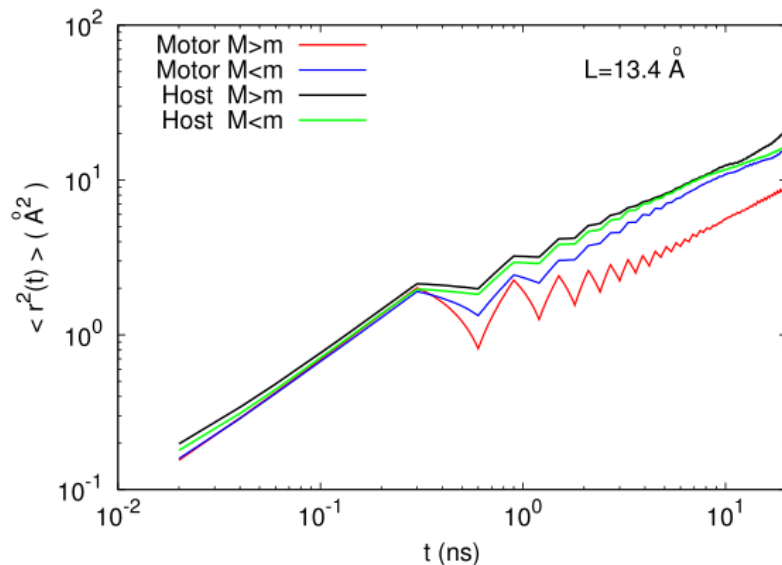


Figure X.12. Mean square displacement $\langle r^2(t) \rangle$ of the motor and host molecules surrounding the motor ($R < 5 \text{ \AA}$) for various host's masses. The motor's length $L = 13.4 \text{ \AA}$ is above the threshold.

The first peaks of the displacements that correspond to the first folding are almost overlapped for host and motor and also for both host masses. After this moment in time, the evolutions start to differ between them, meaning that the distinction is made starting with the unfolding that follows. According to the efficiency ε previously defined, the differences that arise are caused by distinct efficiencies of the motor's motion. Lighter motors are more prone to change their direction with each leap, a characteristic that gives them effectiveness. Moreover, the host's displacement is even greater, showing a stronger influence. Considering that the mean square displacements for host and motor are shown to have the same value after the first folding (first peaks), a correlation between their motions can be made, i.e. the host follows the motor's displacement.

In what regards the motor's efficiency variation with its length, this parameter was studied for both massy and light host molecules. The results are plotted together for comparison (Figure X.13).

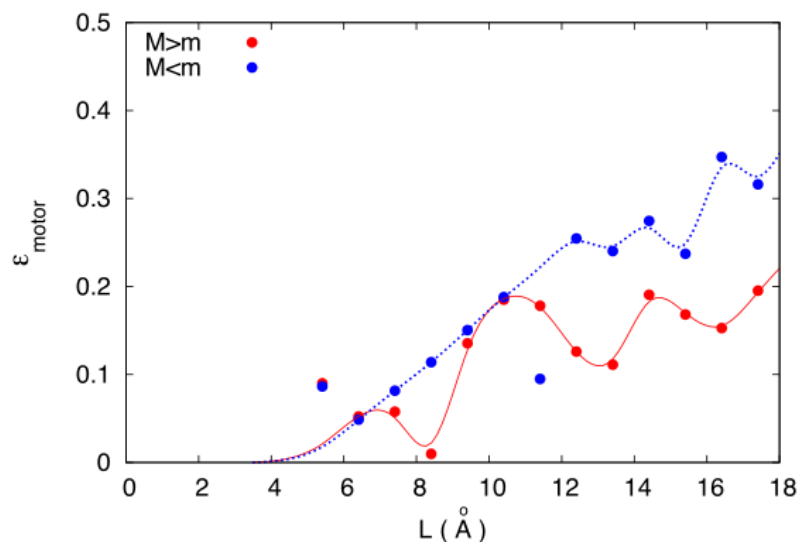


Figure X.13. Motor's efficiency coefficient $\varepsilon_{\text{motor}}$ versus the motor's length L for when the host is lighter or heavier than the motor. The fit lines are intended to serve as eye guidelines.

The data shows that the efficiency presents large fluctuations when the host molecule is lighter than the motor. Up to a motor's length of $\approx 10 \text{ \AA}$, the efficiency is approximately the same for both light and heavy hosts. After this length value, despite the oscillations, the motor displays a larger efficiency, when in hosts with greater mass. This finding is in consensus with the evolution of mean square displacements for the motor of $L = 13.4 \text{ \AA}$ from Figure X.12. A light motor that moves in a medium formed by heavier host molecules constitutes favorable conditions for the motor to shift its direction after each leap, a fact which raises its probability to move forward by exploring more space (i.e., not returning to its previous position). When found in the host with larger mass, the motor's efficiency experiences continuous growth, clarifying why the mobility for large host masses shows no steps. On the opposite hand, when the motor is found in a medium of light molecules, the efficiency dependence on the motor's length reaches a plateau after the length $L \approx 10 \text{ \AA}$ is exceeded. The oscillations are correlated with the steps observed in the motor's mobility. The force threshold previously discussed detains the displacement's growth, thus the evolution can either stay constant or decline.

Further understanding of this behavior requires a view into the motor's elementary displacement, i.e. the mean square displacement after one folding only (Figure X.14.).

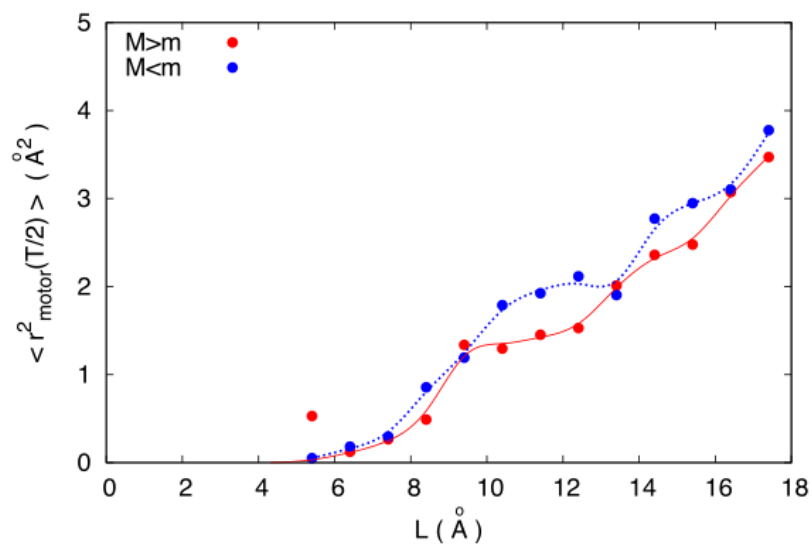


Figure X.14. Motor's mean square displacement after one folding only $\langle r_{\text{motor}}^2(T_f) \rangle$ versus the motor's length L for when the host is lighter or heavier than the motor. The fit lines are intended to serve as eye guidelines.

Results display the appearance of several plateaus for both host molecules, light and heavy. The difference is that when the motor is found in the host molecules with larger mass, the displacements are larger, just how the force variation showed that massy molecules exert a higher force on the motor.

Looking at the host molecule's efficiency coefficient $\varepsilon_{\text{host}}$, a continuous increase with the motor's length can be observed (Figure X.15).

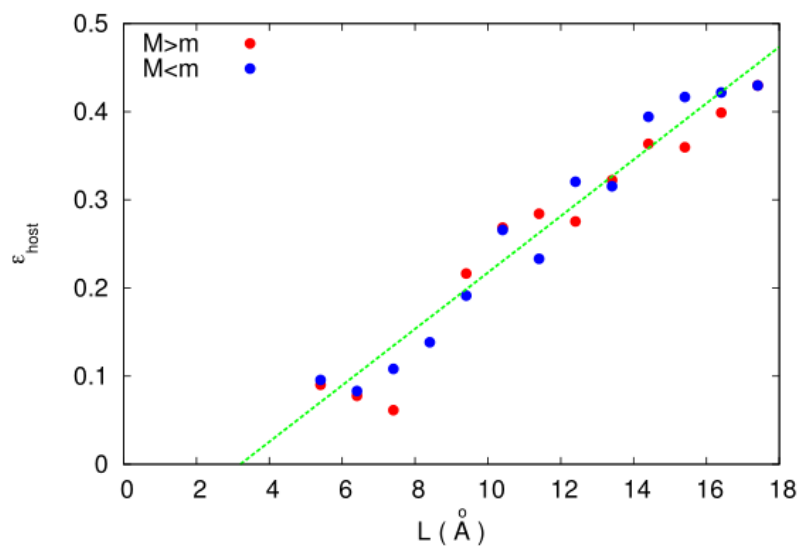


Figure X.15. Host's efficiency coefficient $\varepsilon_{\text{host}}$ versus the motor's length L for when the host is lighter or heavier than the motor.

The continuous increase of the host's efficiency evolution determines the continuous trend in the mobility, i.e. no steps. The behavior holds for both large and low masses, making the host's diffusion independent on its mass.

Like for the motor, the elementary displacement is also investigated (*Figure X.16*).

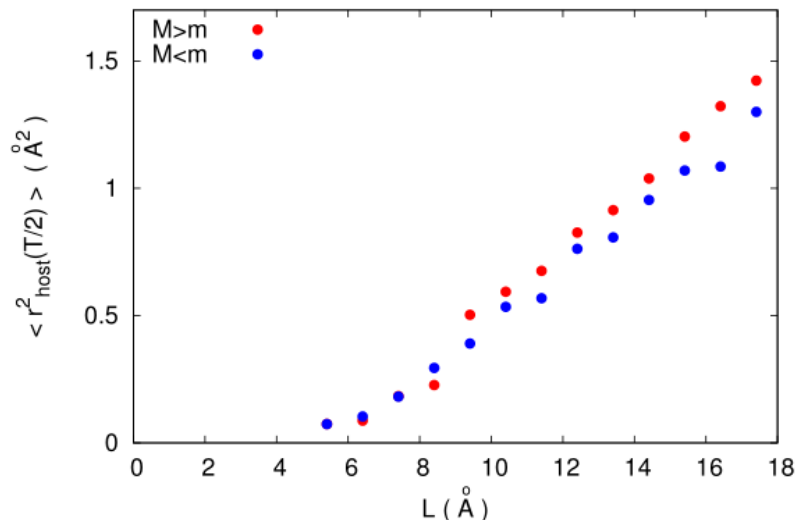


Figure X.16. Host's mean square displacement after one folding only $\langle r_{\text{host}}^2(T_f) \rangle$ versus the motor's length L for when the host is lighter or heavier than the motor.

The host molecule's mean square displacement for one folding shows also a continuous increase with the motor's length, with very little differences between the two host masses. However, the slightly lower displacement of the heavier host is compensated by the efficiency, thus the total displacement of the host is almost the same for both light and heavy host molecules, like it is shown in the first part of the study.

X.5. Conclusions

This section of the thesis studies the isomerization induced displacement of molecules in a viscous environment. The purpose is to identify relevant parameters that can be used to optimize the motor's diffusion. Our results show that a heavy host molecule or light small host molecules are both aspects to take into consideration when wanting to increase the motor's photoinduced displacement.

Different kinetics are found for the motor and host molecules. The motor moves in repetitive hopping steps like solids do, and the host molecules move in a typical manner to liquids.

The hopping motions of the motor determines the appearance of force thresholds. A minimum force is for the motor to reach a stable position when moving inside the environment. In turn, this leads to a threshold for the motor size: a minimum size is necessary for the motor to induce significant displacement.

CHAPTER XI. Conclusions

We synthesized a series of polysiloxanes modified with different azo derivatives, starting from the classical azobenzene, *4-(phenylazo)phenol*, which forms the forms PFF set of samples. Following this, we designed new azobenzenes in order to obtain molecules with different geometries and sizes. Derivative *4-(4'-diphenylazo)phenol* has three aromatic cycles in its structure, resulting in a longer molecule. We call azopolysiloxane batch with this azo group PDF. Next, we design two azo derivatives with condensed aromatic nuclei (naphthalene and anthracene). Polysiloxane substituted with *4-(1'-naphthaleneazo)phenol* is coded as PNF and the polysiloxanes modified with *(2'-anthraceneazo)phenol* are called PAF.

The azopolysiloxanes are further characterized to evaluate their thermal stability with regard to the nanostructuration process that subject the film samples under laser irradiation, but also to the sterilization condition needed for biological applications. We find that all the azopolysiloxanes investigated present thermal stability up to at least 251 °C, when the first degradation step begins. We also estimate the glass transition temperature, which lays in the 34 – 51 °C range for all samples. Differential scanning calorimetry reveals a possible first order transition for PDF1 sample.

We test the photoisomerization capacity of the different azopolysiloxanes films deposited on a silanized glass substrate. All azopolysiloxanes show a suitable cis conversion under UV and Vis light, except PAF films, which present cis conversion at equilibrium under 10 %.

Polysiloxanes substituted with various azo groups are investigated for the ability to form SRG. The behaviour of the samples differs in diffraction efficiency, showing that PFF and PNF azopolysiloxanes are more suitable for SRG obtaining than PDF and PAF

azopolysiloxanes. The wavy variation of diffraction efficiency, shows that there is a competition between the writing and erasing processes during irradiation. Correlating the results of all the samples, one aspect stands out with certainty: there are at least two mechanisms responsible the mass transport than enables SRG inscription. The assistance blue light intensifies the isomerization process, changing the dynamics of matter reorganization. In spite of that, the inconsistency of its effect on the diffraction efficiency makes it difficult to pronounce on what the exact mechanisms are involved. These results are in good agreement with the findings of previous research (Hurdac, Macovei, Paius, Ibanescu, *et al.*, 2013), that show evidential observations of the existence of different mass transport processes that influence the SRG inscription capacity.

Molecular modeling studies are performed, where the azobenzene is referred to as molecular motor is subjected to a simplification that is proved to keep all relevant characteristics of real azo-groups. Molecular dynamics is employed to simulate the behavior of supercooled liquids under the influence of the isomerizing motor. The simulated system is comprised of one molecular motor diluted in the environmental medium made up of 500 molecules that are referred to as host molecules. To address a material in bulk, the system consists of a simulation cell with periodic boundaries conditions.

The host molecules that portray the viscous medium are represented by methyl methacrylate *MMA* monomers or by a simplified model of a diatomic molecule. In the same manner, the motor is defined by Disperse Red 1 molecule, or by the idealized motor with simplified rectangular shape.

In the study of diffusion on different motor sizes, we aimed to find the meaningful parameters in terms of influence on the molecules motion found in the proximity of an isomerizing motor. Our results show the existence of a threshold for the motor size in what regards the diffusion of host molecules. The dimension of the threshold is in direct relation with the host molecule size. Accordingly, the motor's size relative to the host size is a significant parameter for the mass transport mechanism, a conclusion that agrees well with the cage breaking model.

Another approach to study the photoinduced displacement of molecules in a viscous medium is studied, was to consider the influence of the characteristic folding time τ_f of the molecular motor, which is associated with the isomerization rate. Two time regimes are

found: *regime I* when the motor folds slowly, and *regime II* for fast folding. In regime I, the diffusion slowly increases with τ_f , while in regime II, the diffusion augments with τ_f ($D \approx \tau_f^{-2}$), which leads to the idea that there are two mechanisms to can be differentiated. The displacement of the motor during folding in the Ist regime is reversed by a backwards displacement during the unfolding. This phenomenon is not characteristic to the II_{nd} regime: when the motor folds fast, the induced displacement has a very different trajectory than when it unfolds. Thus, globally, the displacement motion in regime II are more efficient.

Focusing on the motor's motion inside the surrounding medium, we compare investigate the influence of the mass ratio between the molecular motor and the host molecules. Our results show that a heavy host molecule or light small host molecules are both aspects to take into consideration when wanting to increase the motor's photoinduced displacement.

While the experimental part on the photochromic behaviour studies the capacity to inscribe SRG in real time and setting, both writing and erasing processes are captured. This suggests the existence of two mechanisms responsible for the mass transport phenomena. The complex dynamics of the diffraction efficiency evolution impedes an assignment to specific mechanisms. The simulation studies focus on the diffusion capacity of azobenzene like molecules, a process that involves only the writing phenomena when correlated with actual irradiation experiments. Analysis of the diffusive behaviour as function of the azobenzene size or the isomerization frequency, finds agreement with several models: the cage breaking, induced pressure gradient and translational diffusion. Both experimental and simulation study methods concede on a photo fluidization process that occurs as a result of the azobenzene isomerization.

SCIENTIFIC ACTIVITY

Published papers in ISI – indexed journals

1. *“How does the motion of the surrounding molecules depend on the shape of a folding molecular motor?”* Ciobotarescu S., Hurduc N., Teboul V., Phys. Chem. Chem. Phys., 18, 14654-14661 (2016).
2. *“Folding time dependence of the motions of a molecular motor diluted inside an amorphous medium”* Ciobotarescu S., Bechelli S., Rajanson G., Migirditch S., Hester B., Hurduc N. and Teboul V., Phys. Rev. E 96, 062614 (2017).
3. *“Optimizing the motion of a folding molecular motor in soft matter”* Rajanson G., Ciobotarescu S. and Teboul V., Phys. Chem. Chem. Phys., 20, 10077-10085 (2018).

Published papers in BDI – indexed journals

1. *“Conformational analysis of polysiloxanes substituted with azobenzene”* Ciobotărescu S., Epure E.-L. and Hurduc N., Bul. Inst. Polit. Iași, 63, 41-49 (2017).

Other published papers

1. *“Understanding how light fueled molecular motors induce motion in the surrounding medium”*, Ciobotărescu S., Atlas of Science, December 6 2016.

Oral communications

1. Student Scientific Circles, April 25-27 2013, Iași, Romania, “*Azopolymeric films for cellular cultures*”, Ciobotărescu S., Hurduc N.
2. International Session Stream Summer School, July 8-13 2013, Iași, Romania, “*Polymeric films as support for cell cultures*”, Ciobotărescu S., Epure E.-L.
3. Student Scientific Session, May 8-10 2014, Iași, Romania, “*Nanostructurable azopolisiloxanes for biological applications*”, Ciobotărescu S., Păiuș C.-M.
4. 2nd International Conference on Chemical Engineering, November 5-8 2014, Iași, Romania, “*Self-assembling behavior of amphiphilic azopolysiloxanes modified with quaternary ammonium groups*”, Epure E.-L., Ciobotărescu S., Hurduc N.
5. 1st Conference of Doctoral Schools, May 29-30 2017, Iași, Romania, “*Conformational analysis of polysiloxanes substituted with azobenzene*” Ciobotărescu S., Epure E.-L.
6. 12th International Symposium from Romania for Cosmetic Products and Fragrances “Nature – Health – Beauty”, May 30 – June 2 2017, Iași, Romania, “*Molecular modeling for the evaluation of cosmetic ingredients*” Ciobotărescu S., Epure E.-L. Hurduc N.
7. Scientific Session, May 14-18 2018, Iași, Romania, “*Conformation dynamics in azobenzene modified polysiloxanes bulk, as a result of isomerization process*”, Căluian A., Ciobotărescu S.
8. 2nd Conference of Doctoral Schools, May 23-24 2018, Iași, Romania, “*Experiments and simulations on azopolymers used as substrate for cell cultures*” Ciobotărescu S., Epure E.-L.
9. 4th International Conference on Chemical Engineering, 31 October – 02 November 2018, Iași, Romania, “*Understanding the Structure - Mass Transport Relationship in Azopolymers* ” Ciobotărescu S., Epure E.-L., Teboul V., Hurduc N.

Project member

1. INOBIOPACK – *“Inovative eco-friendly antimicrobial bio nanomaterials for food and medicine packaging”*, PN-II-RU-TE-2014-4-1828, “Petru Poni” Institute of Macromolecular Chemistry, Romania, research assistant Jul 2016 – Aug 2016.
2. NanoAzoSurf – *“Filme azo-polimerice nanostructurate utilizate drept suport în culturi celulare”*, PN III-PCE nr. 31/2017, “Gheorghe Asachi” Technical University of Iasi, research assistant Sept 2017 – Nov 2019.

Research stages

1. *University of Angers*, Angers, France, Erasmus student, Jan – May 2015.
2. *University of Angers*, Angers, France, Erasmus student Jan – Jul 2016.
3. *University of North Dakota*, North Dakota, USA, research assistant, Nov 2016 – Apr 2017.
4. *University of Angers*, Angers, France, Erasmus student, Apr – May 2019.

Titre : Synthèse, modélisation moléculaire et comportement photochrome de polysiloxanes contenant des groupements azos sous différentes formes

Mots clés : azobenzène, polysiloxane, modélisation moléculaire, relief de surface.

Résumé : La présente thèse représente une étude complexe des azopolysiloxanes photosensibles et rejoint les techniques théoriques et expérimentales. Le thème tourne autour du phénomène de transport de masse des azopolymères induit par la photoisomérisation des azobenzènes. La conversion *trans* – *cis* de l'azobenzène et de ses dérivés est un processus réversible actionné par la lumière, qui permet le réarrangement de la matière environnante au niveau nano et micro. Cette propriété est exploitée pour fabriquer des réseaux de relief de surface (SRG) avec caractéristiques géométriques spécifiques.

Les présentes études visent à comprendre ce mécanisme complexe, sujet à une grande controverse parmi les différents groupes de recherche. Les paramètres qui contrôlent le processus sont traités et analysés. L'étude expérimentale comprend la synthèse et la

caractérisation de quatre azopolysiloxanes qui sont ensuite analysés pour leur capacité d'obtenir des SRG. Le comportement photochromique est évalué par des expériences d'irradiation à différentes intensités lumineuses, en présence ou l'absence d'une lumière d'assistance qui devrait intensifier l'isomérisation.

La simulation informatique se concentre sur la diffusion des molécules dans le système: une molécule de type azobenzène (moteur moléculaire) diluée dans le milieu hôte. Des calculs de modélisation moléculaire sont effectués pour des moteurs de différentes longueurs et avec différents temps d'isomérisation (isomérisation rapide ou lente) afin de définir la relation entre ces paramètres et la diffusion.

Fournir des informations expérimentales et théoriques sur les azopolymères, est trop important pour comprendre la formation de SRG.

Title : Synthesis, molecular modeling and photochromic behaviour of polysiloxanes containing azo-groups with different geometries

Keywords : azobenzene, polysiloxane, molecular modeling, surface relief.

Abstract : The herein thesis represents a complex study of photosensitive azopolysiloxanes and rejoins both theoretical and experimental techniques. The theme revolves around the azopolymer's mass transport phenomenon induced by the photoisomerization of azobenzenes. *Trans*- to *cis* conversion of azobenzene and its derivatives is a reversible light actuated process that enables the rearrangement of surrounding matter at nano and micro level. This property is exploited to fabricate surface relief gratings (SRG) with certain geometrical features.

The present studies are directed to comprehension of this complex mechanism, subject to great controversial among different research groups. The parameters that control the process are addressed and analyzed.

Experimental study comprises the synthesis and characterization of four azopolysiloxanes which are then analyzed for the capacity to obtain SRG. Photochromic behaviour is evaluated through irradiation experiments at different light intensity, in the presence or absence of an assistance light that supposedly intensifies isomerization.

Computer simulation focuses on diffusion of the molecules in the system: one azobenzene – like molecule (molecular motor) diluted in the host medium. Molecular modeling calculations are performed for motors with different lengths and with various isomerization times (fast or slow isomerization) in order to define the relation between these parameters and diffusion.

Providing experimental and theoretical info on azopolymers is part of the SRG formation insight.